Biologically Inspired and Rehabilitation Robotics 2020

Lead Guest Editor: Liwei Shi
Guest Editors: Yong Yu, Nan Xiao, Dongming Gan, and Wei Wei

Biologically Inspired and Rehabilitation Robotics 2020

Biologically Inspired and Rehabilitation Robotics 2020

Lead Guest Editor: Liwei Shi
Guest Editors: Yong Yu, Nan Xiao, Dongming Gan, and Wei Wei

Contents

Editorial

Biologically Inspired and Rehabilitation Robotics 2020

Liwei Shi [iD],[1] **Yong Yu,**[2] **Nan Xiao,**[1] **Dongming Gan** [iD],[3] **and Wei Wei** [iD][4]

[1]*The Institute of Advanced Biomedical Engineering System, School of Life Science, Beijing Institute of Technology, No. 5, Zhongguancun South Street, Haidian District, 100081 Beijing, China*
[2]*Kagoshima University, Kagoshima, Japan*
[3]*Purdue University, West Lafayette, IN 47907, USA*
[4]*Soochow University, Suzhou, China*

Correspondence should be addressed to Liwei Shi; shiliwei@bit.edu.cn, Dongming Gan; dongming.gan@ku.ac.ae, and Wei Wei; weiwei0728@suda.edu.cn

Bioinspired methods are becoming increasingly important in the face of the complexity of today's demanding applications. Biological inspiration in robotics is leading to complex structures with sensory-motor coordination, in which learning often plays an important role in achieving adaptation. In addition, rehabilitation robotics has produced exciting new ideas and novel human assistive devices in the growing field of biomedical robotics. The science and technology of rehabilitation robotics will progress through the collaboration among robotic researchers, medical doctors, and patients.

This special issue focuses on the theoretical and technological challenges of evolutionary transformation from biological systems to intelligent robots. There were 14 original research papers that were finally accepted in this special issue after formal peer reviews. The accepted papers can be further classified into two related topics including rehabilitation and human assisting systems and bioinspired manipulator system for fine manipulation, surgery, robotics, and human-robot interaction applications.

Among the rehabilitation and human assisting systems, a big focus was on the lower limb and upper limb applications. H. Woo et al. investigated how climbing assistance by a robotic exoskeleton affects energy consumption. Despite lack of individual optimization, assistive joint torque applied to the hip and knee joints reduced metabolic cost and cardiovascular burden of stair climbing in healthy young males. The prediction of sensor data can help the exoskeleton control system to get the human motion intention and target position in advance, so as to reduce the human-machine interaction force. S. Zha et al. designed a human motion capture system to acquire human walking joint data and proposed a method for optimizing parameters of Takens' nonlinear prediction algorithm. Compared with the original Takens prediction algorithm, the prediction angle obtained by the improved prediction PSO-Takens algorithm was more closely related to the actual motion angle data of the human body, with a smaller error rate and smooth features. Robotic exoskeletons (RE) for motor rehabilitation can provide the user with consistent, symmetrical, goal-directed repetition of movement, and balance and stability. K. K. Karunakaran et al. evaluated the therapeutic effect of RE training on the loading/unloading and spatial temporal characteristics in adolescents and young adults with chronic ABI. Results showed improved step length, speed, and an overall progression towards healthy bilateral loading, with linearity of loading showing a significant therapeutic effect ($p < 0.05$). These results suggested that high dose, repetitive, consistent gait training using RE has the potential to induce recovery of function in adolescents and young adults diagnosed with ABI. K. Park et al. implemented the optimal design of a motorized prosthetic leg and evaluation of its performance for stair walking. Developed prosthetic leg includes two degrees of freedom on the knee and ankle joint designed using a virtual product development process for better stair walking. The DC motor system was introduced to imitate gait motion in the knee joint, and a spring system was applied at the ankle joint to create torque and flexion angle. The motorized prosthetic leg was

optimally designed while maintaining structural safety under boundary conditions based on the human walking data, and its knee motions were synchronized with normal human gait via a PD controller. The results from this study might help amputees in their rehabilitation process and be applied to the area of biped robots that try to mimic human motion. The upper limb rehabilitation robots can be developed as an efficient tool for motor function assessments. Circle drawing has been used as a specific task for robot-based motor function measurement. C. Wang et al. used the robot-assisted and constrained circle drawing movements for upper limb to increase the consistency of muscle synergy features. In upper limb rehabilitation training by exploiting robotic devices, the qualitative or quantitative assessment of human active effort is conducive to altering the robot control parameters to offer the patients appropriate assistance, which is considered an effective rehabilitation strategy termed as assist-as-needed. Accordingly, a shoulder passive torque prediction method based on a backpropagation neural network (BPANN) was proposed to expand the shoulder passive torque-angle relationship by S. Li et al. Experiments were carried out to measure the kinematics and torques on the shoulder joint of 3 healthy subjects, and the measurement data was used as training set and testing set of a three-layer BPANN to test the prediction effect. Surface electromyography- (sEMG-) based hand grasp force estimation plays an important role with a promising accuracy in a laboratory environment, yet hardly clinically applicable because of physiological changes and other factors. J. Wang et al. proposed an easy-to-implement method to quantitatively estimate muscle fatigue and evaluated the effect of muscle fatigue on hand grasp force estimation. The experiment results demonstrated that the incorporation of muscle fatigue metrics explicitly in the grasp force estimation had a substantial impact on the performance.

Biology systems have showed good references and inspiration for engineers to develop new manipulation, robot system, and sensing systems. X. Ma et al. proposed a new catheter operating system of the surgical robot and designed a new mechanical structure of force feedback to measure the near-end force during the operation. A new controller, BP neural network PID controller, was designed by X. Ma et al., which could improve the axial and rotary motion accuracy of the system in remote operation. Simulation results show that the proposed BP neural network PID controller has good dynamic response quality. In addition, the robot of neurointerventional surgical has been continuously investigated and improved though 10 animal experiments. The robot system can realize the cooperative operation of the guidewire, and the catheter and has a force feedback system with good accuracy and stability. And various mechanical performance indexes basically meet the needs of vascular intervention surgery. J. Jiang et al. designed a passive ultrasound probe position and posture adjustment mechanism to assist doctors performing prostate scans and puncture interventions. In this paper, the forward kinematic analysis of the mechanism, the simulation of the centering effect, the development of the physical prototype, and related experimental research were presented.

Therefore, this special issue presents the most recent advances in modeling, design, analysis, control, implementation, and therapeutic testing of the human assistive rehabilitation systems, bioinspired prosthesis, manipulators, surgical robots, and sensing systems. We hope the knowledge and information will be good references and basis for further development in those fields for human centered science and technology.

Conflicts of Interest

The editors declare that they have no conflicts of interest regarding the publication of this special issue.

Liwei Shi
Yong Yu
Nan Xiao
Dongming Gan
Wei Wei

Research Article

Upper-Limb Muscle Synergy Features in Human-Robot Interaction with Circle-Drawing Movements

Cheng Wang [1] **Shutao Zhang** [2] **Jingyan Hu** [2] **Zhejing Huang** [3]
and Changcheng Shi [2]

[1]*Emergency Trauma Surgical Department, Ningbo First Hospital, Ningbo, Zhejiang 315010, China*
[2]*Cixi Institute of Biomedical Engineering, Ningbo Institute of Materials Technology and Engineering, Chinese Academy of Sciences, Ningbo, Zhejiang 315300, China*
[3]*Rehabilitation Department, Ningbo Yinzhou No. 2 Hospital, Ningbo, Zhejiang 315192, China*

Correspondence should be addressed to Changcheng Shi; changchengshi@nimte.ac.cn

Cheng Wang and Shutao Zhang contributed equally to this work.

The upper-limb rehabilitation robots can be developed as an efficient tool for motor function assessments. Circle-drawing has been used as a specific task for robot-based motor function measurement. The upper-limb movement-related kinematic and kinetic parameters measured by motion and force sensors embedded in the rehabilitation robots have been widely studied. However, the muscle synergies characterized by multiple surface electromyographic (sEMG) signals in upper limbs during human-robot interaction (HRI) with circle-drawing movements are rarely investigated. In this research, the robot-assisted and constrained circle-drawing movements for upper limb were used to increase the consistency of muscle synergy features. Both clockwise and counterclockwise circle-drawing tasks were implemented by all healthy subjects using right hands. The sEMG signals were recorded from six muscles in upper limb, and nonnegative matrix factorization (NMF) analysis was utilized to obtain muscle synergy information. Both synergy pattern and activation coefficient were calculated to represent the spatial and temporal features of muscle synergies, respectively. The results obtained from the experimental study confirmed that high structural similarity of muscle synergies was found among the subjects during HRI with circle-drawing movement by healthy subjects, which indicates healthy people may share a common underlying muscle control mechanism during constrained upper-limb circle-drawing movement. This study indicates the muscle synergy analysis during the HRI with constrained circle-drawing movement could be considered as a task for upper-limb motor function assessment.

1. Introduction

The upper-limb rehabilitation robots can provide continuously haptic assistance or resistance to stroke patients with motor impairments in order to help them restore the motor function of upper limbs [1]. Since it was early developed in the 1990s [2], the upper-limb rehabilitation robot has been gradually recognized as an effective medical device which could assist some stroke patients to restore or improve their motor functions of upper limbs [3]. Besides training, rehabilitation robots have a potential to be considered as an objective rehabilitation assessment tool due to a plenty of sensors

could be integrated into robotic systems and motor functions (i.e., range of motion, force, velocity, and muscle tone and strength) of upper limbs could be quantitatively detected and analyzed [4, 5]. Those assessment results can be obtained after training and provided to physicians locally or remotely in order to optimize the rehabilitation therapy. Moreover, some assessment results are also analyzed during the training process and provided to patients in order to visualize the rehabilitation progresses and enhance their training motivation.

Circle-drawing is one of typical human-robot interaction (HRI) tasks which are widely applied to quantitatively

(a)

(b)
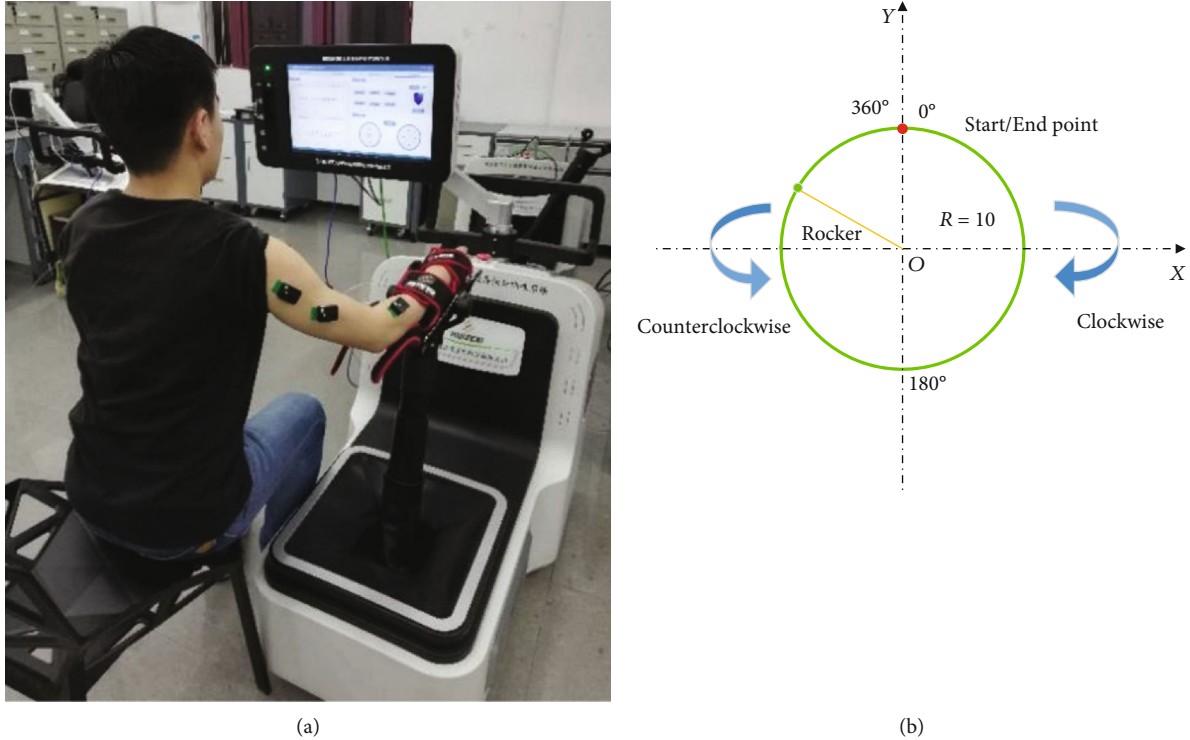
FIGURE 1: Setup and experimental design. Participants were asked to keep their upper body stable, and their forearm was tied to the joystick of EULRR. (a) Participants sit on the left side of EULRR to implement circle-drawing movement by using their right hands; (b) the illustration of clockwise and counterclockwise circle-drawing movements with constraint of EULRR system.

evaluate upper-limb motor function by using rehabilitation robots [5]. The ability to accurately implement this movement task is related to coordination of both elbow and shoulder joints. Therefore, circle-drawing-related kinematic (i.e., roundness, area, averaged speed, and jerk) and kinetic (HRI force) parameters measured by motion and force sensors embedded in the rehabilitation robots have been widely studied as the potential assessment metrics for upper-limb motor functions [4, 6, 7]. However, the muscle synergies characterized by multiple surface electromyographic (sEMG) signals in upper limbs during HRI with circle-drawing movements are rarely investigated.

Tropea et al. compared the muscle synergies of upper limbs in stroke patients and healthy subjects and observed that the difference can reflect the functional deficit induced by the neural damages [8]. Scano et al. clustered the muscle synergies of stroke patients into five groups and found a deep characterization and relationship with clinical assessment methods [9]. The previous studies strongly suggested that muscle synergy analysis may be a potentially promising method for assessing motor function stroke patients. However, it remains unclear whether the consistency of normal or abnormal muscle synergy patterns in upper limbs for stroke patients is good enough for rehabilitation assessments. The main challenge is the multiple degree-of-freedom and redundancy for upper-limb movements, which may cause a large variation of muscular activation patterns.

Hence, in this study, the end-effector upper-limb rehabilitation robot (EULRR) which was developed in the lab

was used as a tool to assist and confine the circle-drawing movements and measure the outcome of HRI tasks. The robot-assisted and constrained circle-drawing tasks for upper-limbs movement were used to increase the consistency of muscle synergy features. Both clockwise and counterclockwise circle-drawing tasks were implemented by all healthy subjects using right hands. The sEMG signals were recorded from six muscles in upper limb, and nonnegative matrix factorization (NMF) analysis was utilized to obtain muscle synergy information. Both synergy pattern and activation coefficient were calculated to represent the spatial and temporal features of muscle synergies, respectively. Reconstructed sEMG data were compared with the raw data in order to verify the effectiveness of NMF algorithm. The muscle synergy features of upper limb in HRI with two directions of circle-drawing movements were analyzed, and the consistency of muscular activation patterns was discussed.

2. Methods

2.1. Participants. Twelve healthy adults (10 males and 2 females and with average ages of 25 ± 1 years old) and two stroke patients (2 females, 67 and 39 years old, Brunnstrom stages III and IV) were involved in this study, who are all right-hand dominant, with no known neurological diseases, no muscular or skeletal impairments history of the upper limbs and the trunks, and no functional abnormalities. Before starting the experimentations, all the subjects signed an informed consent. The study was approved by the
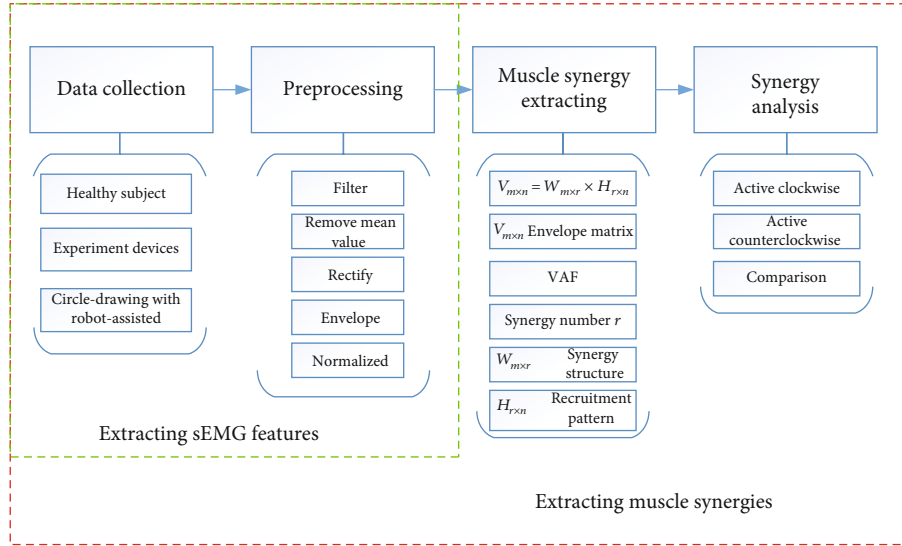
FIGURE 2: The illustration of sEMG data preprocessing and muscle synergy analysis.

Ningbo Institute of Materials Technology & Engineering, Chinese Academy of Sciences. Informed consent was acquired from each subject.

2.2. EULRR System and sEMG Acquisition Device. The EULRR system mainly consists of motor, belt, reducer, frame, rocker, sensor, and a tray with a grip in space coordinates. The system has 5DOF in total: the rocker moves along the three axes; the rotation DOF of tray turns around Z-axis and Y-axis. The movement of X/Y direction is transmitted to the reducer by the X/Y shaft motor through the belt pulley and then transmitted to the frame by the reducer. The movement of Z direction is transmitted by the Z shaft motor through the pulley to the inside of the screw [10]. A 6-axis force/torque sensor is attached between the tray and the end of rocker to measure the force/torque exerted by the subjects. sEMG signal acquisition equipment uses TRIGNO wireless sEMG system (Delsys Inc., Massachusetts, USA) which has 16 4-channel sEMG and acceleration acquisition sensor, wireless transmission range is up to 20 m, sensor delay is less than 500 μs (less than a sampling period), sEMG signal sampling rate is about 2000 Hz, baseline noise is less than 750 nV, it has 16-bit signal resolution, and sensor electrode is Ag-AgCl electrode with high conduction efficiency.

2.3. Upper-Limb Circle-Drawing Movement Tasks. After the sEMG electrode placement, the participants were asked to sit on the left side of the EULRR system and carried out all the tasks by using their right hands in the horizontal plane, as shown in Figure 1. In order to avoid unnecessary muscle compensation, they were informed to keep trunk steady and only use the upper limbs to complete the full circle-drawing movement by moving the joystick of EULRR, which constrained the circle radius of 10 cm. All subjects were instructed to carry out a series of trials (10 times per task). Subjects were asked to perform ten counterclockwise and clockwise circle-drawing movements from the start point arranged along the circular trajectory in a horizontal plane

by holding a handle of joystick with a self-comfortable speed in different directions. Before starting the experiment, subjects performed a simple learning process under the guidance of instructors in order to complete the tasks smoothly.

2.4. sEMG Data Acquisition. During the circle-drawing tasks, the sEMG signals were recorded from six upper-limb muscles including anterior deltoid (AD), posterior deltoid (PD), biceps brachii (BB), triceps brachii (TB), flexor carpi radialis (FCR), and extensor carpi radialis (ECR). Electrodes were placed in accordance with the guidelines of sEMG for noninvasive assessment of muscles (SENIAM) [11]. Each recorded site was cleaned with alcohol and scrub cream before placing the electrodes. All the data were collected at the sampling rate of 2000 Hz.

2.5. Muscle Synergy Analysis. The collected sEMG signals were preprocessed according to the following steps before extracting muscle synergies: band-pass-filtering (20-400 Hz), subtracting signal mean values to remove direct current offsets, then rectified, and enveloped. Each row of the preprocessed sEMG matrix ($V_{m\times t}$, where m is the number of muscles and t is the recorded time) [12] was normalized with respect to its submaximal [13] and sampled into 1000 points. Because we rectified the EMG data, all components of the synergy are nonnegative is reasonable. NMF algorithm [12, 14] was chosen here to extract synergy pattern matrix $W_{m\times r}$ and activation coefficient matrix $H_{r\times n}$. So the synergy decomposition as the equation $V_{m\times n} = W_{m\times r} \times H_{r\times n}$. A vector of $W_{m\times r}$ represents the relative weighting of muscles in each module, and the coefficient $H_{r\times n}$ represents the neural command that specifies how much each synergy will contribute to a total muscular activity pattern [15]. During the extraction, the number of synergy vector (r) was increased successively from one to six, and for each iteration of r, the NMF was repeated 20 times, and the repetition with the lowest residuals of reconstruction was selected.

The mean sEMG signals 10

(a)

The mean sEMG signals 10

(b)
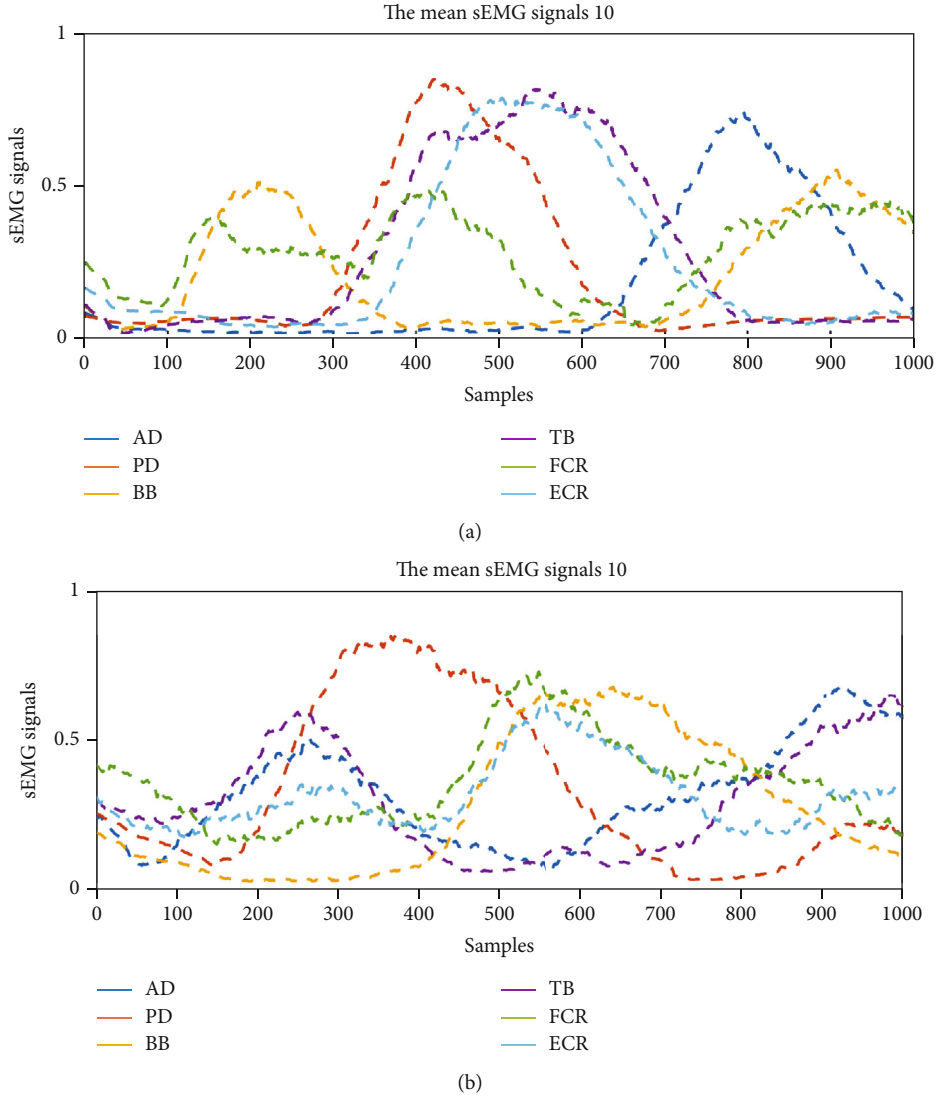
FIGURE 3: The typical sEMG results of six muscles in upper limb during the HRI with circle-drawing movements. (a) The sEMG results for counterclockwise circle-drawing movements; (b) the sEMG results for clockwise movements.

Various methods have been used to determine the appropriate number of muscle synergies underlying a given dataset [16, 17]. The criterion of variance account for (VAF) [18–20] was adopted here in the following equation:

$$\text{VAF} = 1 - \frac{\sum_{i,j}(V - V_r)_{ij}^2}{\sum_{i,j}V_{ij}^2},\tag{1}$$

in which V_r is the reconstructed EMG matrix and the V is the initial EMG matrix. The number of synergy vectors (N) that sufficiently recaptured the original EMGs was then defined as the minimum number (r) when VAF exceeded 90% in more than half of the subjects in both groups. We checked the goodness of reconstruction of global and individual muscle's EMG at N synergy components, which is sensitive to both shape and amplitude of the signals [21].

In summary, the muscle synergy features were analyzed in different movement directions of circle-drawing during human-robot interaction in healthy and stroke subjects. This study mainly includes sEMG data collection during circle-drawing movement with the EULRR assisted, sEMG data preprocessing, and muscle synergy extraction and analysis. The first two parts can be used to obtain the processed sEMG signals. The muscle synergy features can be obtained by analyzing those processed sEMG data. The procedure of sEMG data preprocessing and muscle synergy analysis is shown in Figure 2.

3. Results

3.1. sEMG Results during Circle-Drawing Movement. The mean and normalized sEMG signal envelopes of 10 times of counterclockwise and circle-drawing movements are shown in Figure 3. The sEMG features in the process of HRI with circle-drawing movements were analyzed. The sEMG result for the counterclockwise circle-drawing movements is shown in Figure 3(a). Firstly, the BB and TB were
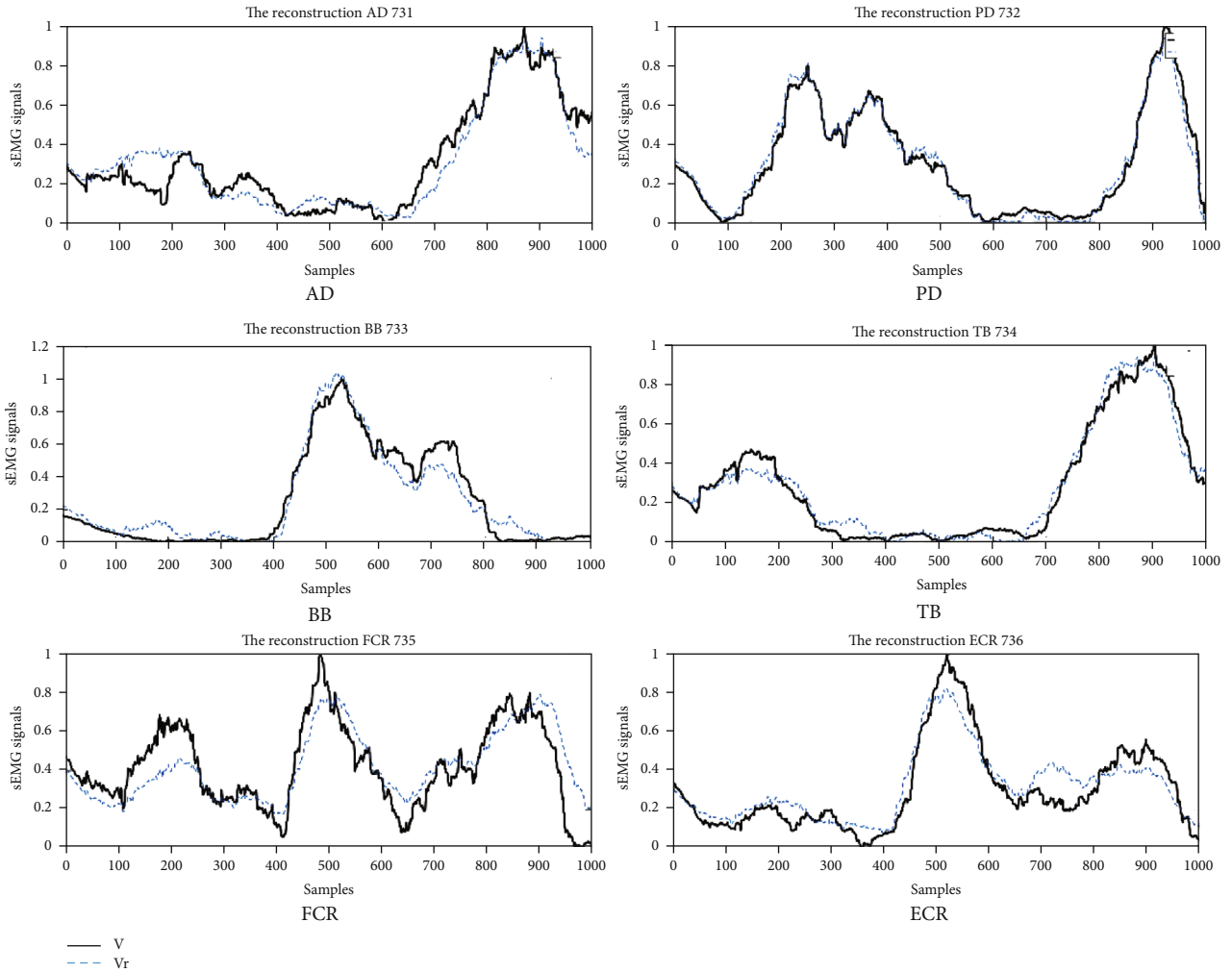
FIGURE 4: The comparison of raw and reconstructed sEMG data from factorized matrices.

activated in pairs and showed a negative correlation, which might indicate that TB contraction (relaxation) and BB relaxation (contraction) happened simultaneously and BB was activated slightly earlier at temporal domain. Secondly, the AD and PD were activated in pairs and showed a negative correlation. PD was activated slightly earlier at temporal domain. The sEMG result for the clockwise circle-drawing movements is shown in Figure 3(b). Firstly, the BB and TB were activated in pairs and showed a negative correlation. TB was activated slightly earlier at temporal domain. Secondly, the AD and PD were activated in pairs and showed a negative correlation. AD was activated slightly earlier at temporal domain.

3.2. The Results of Muscle Synergy Analysis. In the current study, we used VAF > 90% as the threshold to determine the number of muscle synergies. The mean VAF of all healthy subjects' 10 times circle-drawing movement demonstrated three muscle synergies can be appropriate for the sEMG data analysis. In Figure 4, the black solid curves represent the raw sEMG data, and the blue dotted line represents the reconstructed sEMG data. It can be seen that

three types of muscle synergies were sufficient to reconstruct the original sEMG signal. According to the analysis on two stroke patients' data, two muscle synergies can be extracted from the raw sEMG data.

We used the model of time-invariant synergies to extract the muscle synergies [22]. A typical muscle synergy analysis result of counterclockwise circle-drawing movement tasks by healthy subjects is shown in Figure 5. The W represents synergy patterns, and H represents activation coefficients, and targeted muscle numbers 1-6 represent AD, PD, BB, TB, FCR, and ECR, respectively. The results demonstrated that the first synergy pattern mainly includes AD, and the corresponding activation coefficients were mainly activated at the ending of movements for all subjects. The second synergy pattern mainly includes BB, FCR, and ECR; meanwhile, the corresponding activation coefficients were mainly activated at the beginning of movements. The third synergy pattern mainly includes PD and TB; meanwhile, the corresponding activation coefficients were mainly activated at the middle process of movements.

Figure 6 shows a typical muscle synergy analysis result for clockwise circle-drawing movements conducted by the

(a)

(b)

(c)
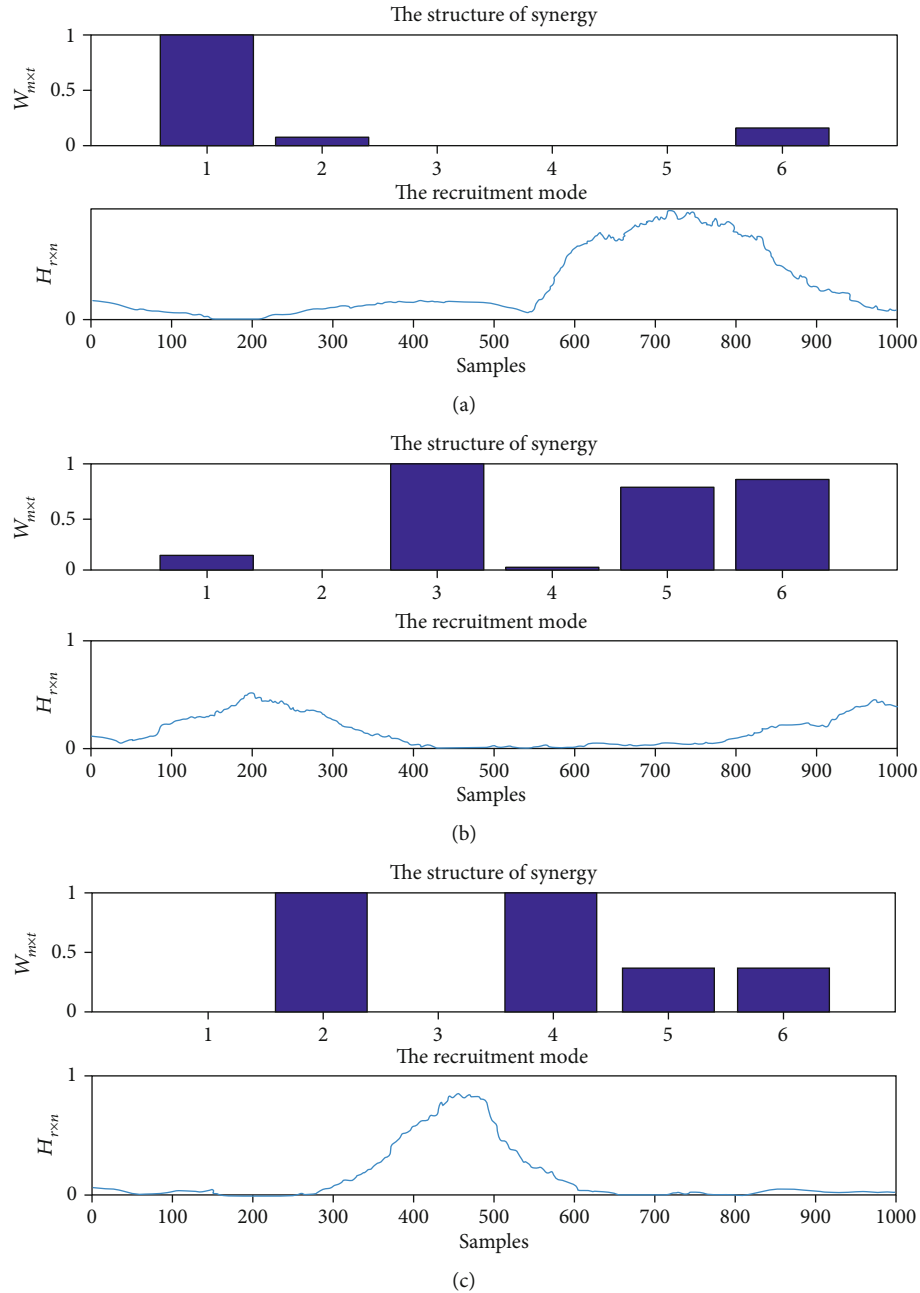
FIGURE 5: The typical results of muscle synergies of upper limbs for healthy subjects during the HRI with counterclockwise circle-drawing movements. (a) The synergy pattern and activation coefficients for the first synergy; (b) the synergy pattern and activation coefficients for the second synergy; (c) the synergy pattern and activation coefficients for the third synergy. The structure of synergy represents the synergy pattern of muscle synergies, and the recruitment mode represents the activation coefficients of muscle synergies.

healthy subjects. The results indicated the first synergy pattern includes AD, and the corresponding activation coefficients were mainly activated at the ending of movements. The second synergy pattern mainly includes BB, FCR, and ECR; meanwhile, the corresponding activation coefficients were mainly activated at the middle process of movements. The third synergy pattern includes PD and TB; meanwhile, the activation coefficients were mainly activated at the beginning of movements.

Figure 7 shows a typical muscle synergy analysis result for counterclockwise circle-drawing movements implemented by stroke subjects. The first muscle synergy pattern includes AD, BB, and FCR which are all flexion muscles, and the corresponding activation coefficients were mainly activated at the ending of movements. The second muscle synergy pattern includes PD, TB, and ECR which are all extensor muscles, and the corresponding activation coefficients were activated from the beginning to the middle

(a)

(b)

(c)
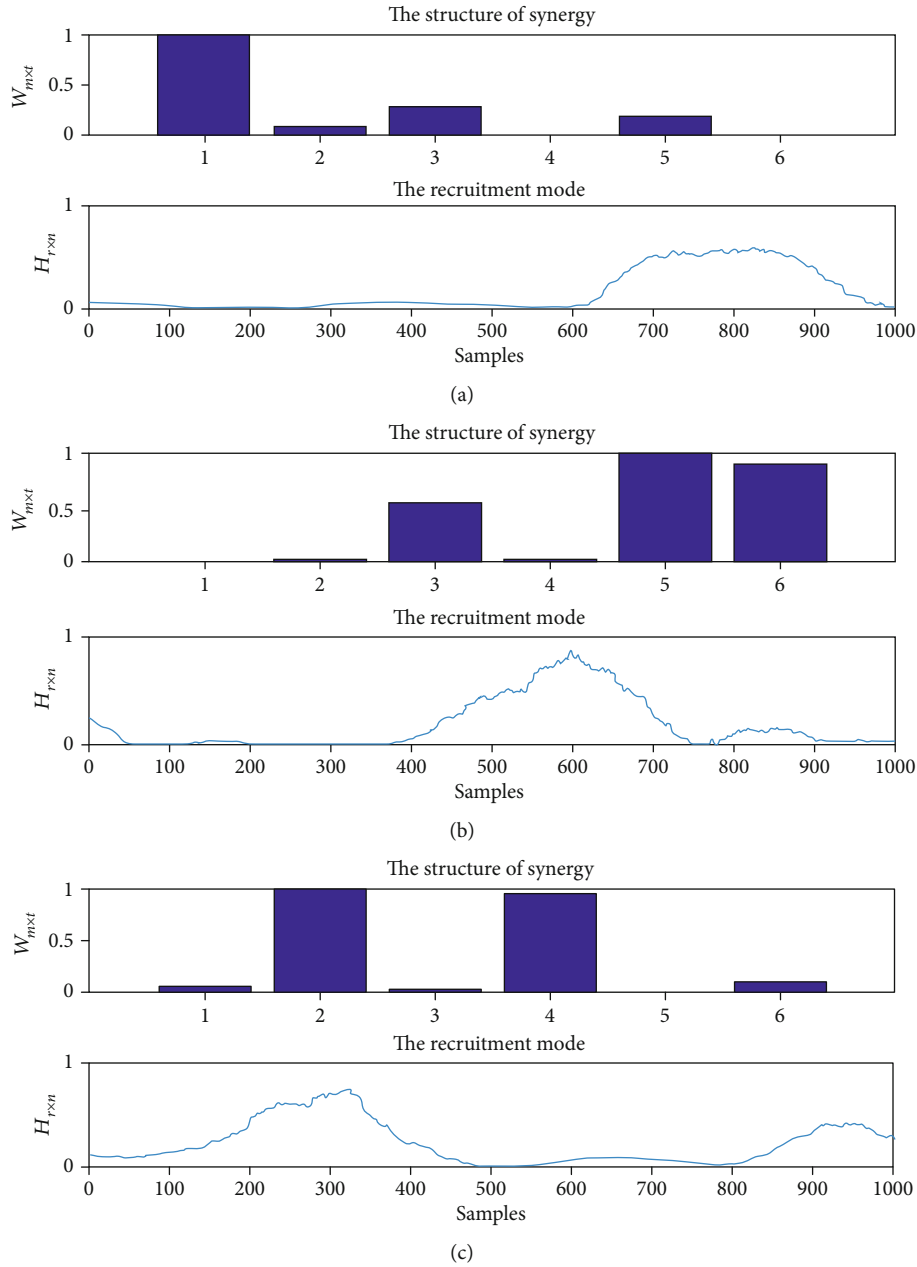
FIGURE 6: The typical results of muscle synergies of upper limbs for healthy subjects during the HRI with clockwise circle-drawing movements. (a) The synergy pattern and activation coefficients for the first synergy; (b) the synergy pattern and activation coefficients for the second synergy; (c) the synergy pattern and activation coefficients for the third synergy. The structure of synergy represents the synergy pattern of muscle synergies, and the recruitment mode represents the activation coefficients of muscle synergies.

processes of movements. Compared to the results for the healthy subjects, the curve of activation coefficients for stroke patients has four peaks which might be induced by impaired muscular function of patients.

Figure 8 shows a typical muscle synergy analysis result for clockwise circle-drawing movements implemented by stroke subjects. The first muscle synergy pattern includes PD, TB, and ECR which are all extensor muscles, and the corresponding activation coefficients were mainly activated at the ending of movements. The second muscle synergy pattern includes BB, TB, FCR, and ECR; meanwhile, the cor-responding activation coefficients were activated at the beginning of movements.

4. Discussion

Upper-limb rehabilitation robot could provide high-intensity, repetitive, task-specific, and interactive exercises for stroke patients. The robot could be effective to achieve the desired training functions, informing the subject to complete the task as well as enabling them to reduce unnecessary muscle activation [23]. Besides the training, the rehabilitation
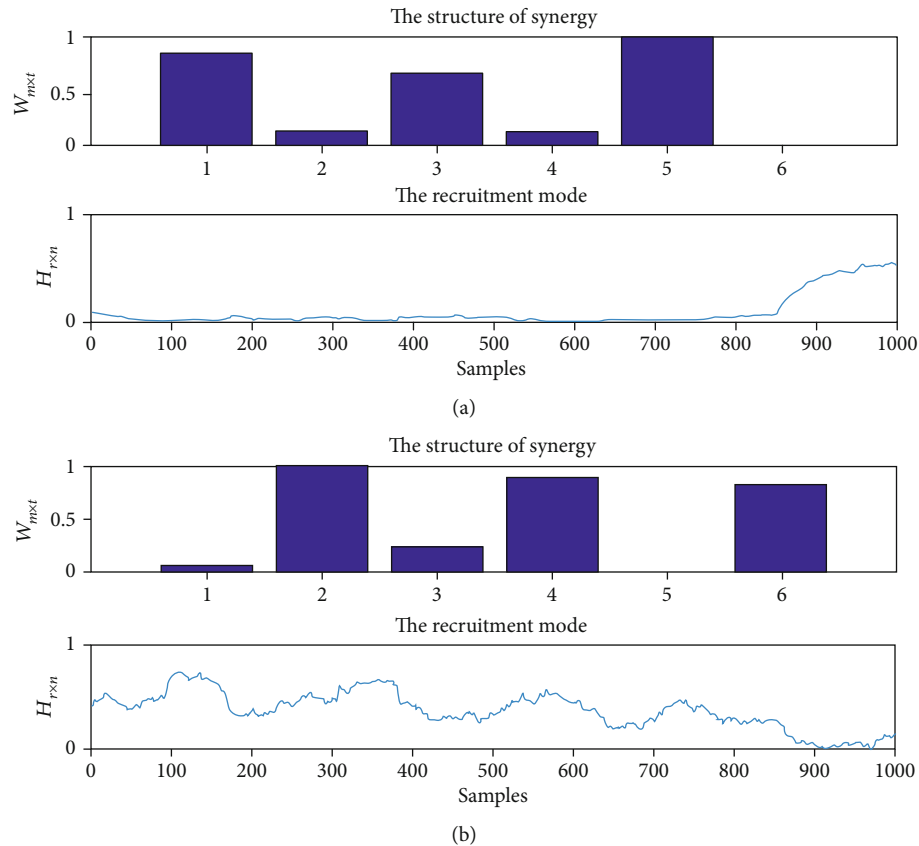
FIGURE 7: The typical results of muscle synergies of upper limbs for stroke patients during the HRI with counterclockwise circle-drawing movements. (a) The synergy pattern and activation coefficients for the first synergy; (b) the synergy pattern and activation coefficients for the second synergy. The structure of synergy represents the synergy pattern of muscle synergies, and the recruitment mode represents the activation coefficients of muscle synergies.

robot also can be developed as an efficient assessment tool for patients' upper-limb motor functions [24].

The structure of muscle synergy for a specific task may contain useful information on the residual ability of neuromuscular control in the poststroke patients. Stroke patients often have upper-limb problems due to abnormally high spasticity of muscles in the shoulder and elbow joints [25, 26]. Circle-drawing movement requires the coordination of both shoulder and elbow joints with multijoint movements. This task can be considered as a kind of task-specific, rhythmic, interactive training as well as an objective, reliable means of monitoring the change progress of patient's upper-limb motor function. Regarding the clinical practice, some kinematic indexes including circle area and roundness can give useful objective information regarding arm function of stroke survivors [6]. During robot-assisted rehabilitation process, it needs to promote the patients' muscle synergy to enhance the biomechanical functions of patients' upper limbs. Muscle synergy is helpful to increase understanding of the mechanisms involved in restoration of upper-limb function poststroke patients.

In this study, the constrained circle-drawing movements for upper limb were used as a task for motor function assessment. The results obtained from the experimental studies

confirmed that high structural similarity of muscle synergies was found among the healthy subjects during HRI with circle-drawing movement, indicating that the healthy people may share a common underlying muscle control mechanism during constrained upper-limb circle-drawing movement. It was found that the muscle activation patterns regarding counterclockwise and clockwise circle-drawing movements demonstrated a complementary mode, which indicated that the activation coefficients of muscle synergies may be affected by the moving directions.

The results of muscle synergy analysis for stroke patients demonstrated the number of muscle synergy decreases when compared with the healthy subjects. The similar phenomenon was also found by Cheung et al., and this reduction of synergy number may be due to the neural function changes after patients' cortical damage [19]. The activation coefficients of muscle synergy for stroke patients were also found to be different when compared with the healthy subjects. There were more peaks in the activation coefficient curve, especially during the HRI with counterclockwise circle-drawing movements. This feature of activation coefficients might be related to the abnormal motor function of patients' upper limbs as well as their discontinuity of circle-drawing movements. This study indicates the muscle synergy analysis
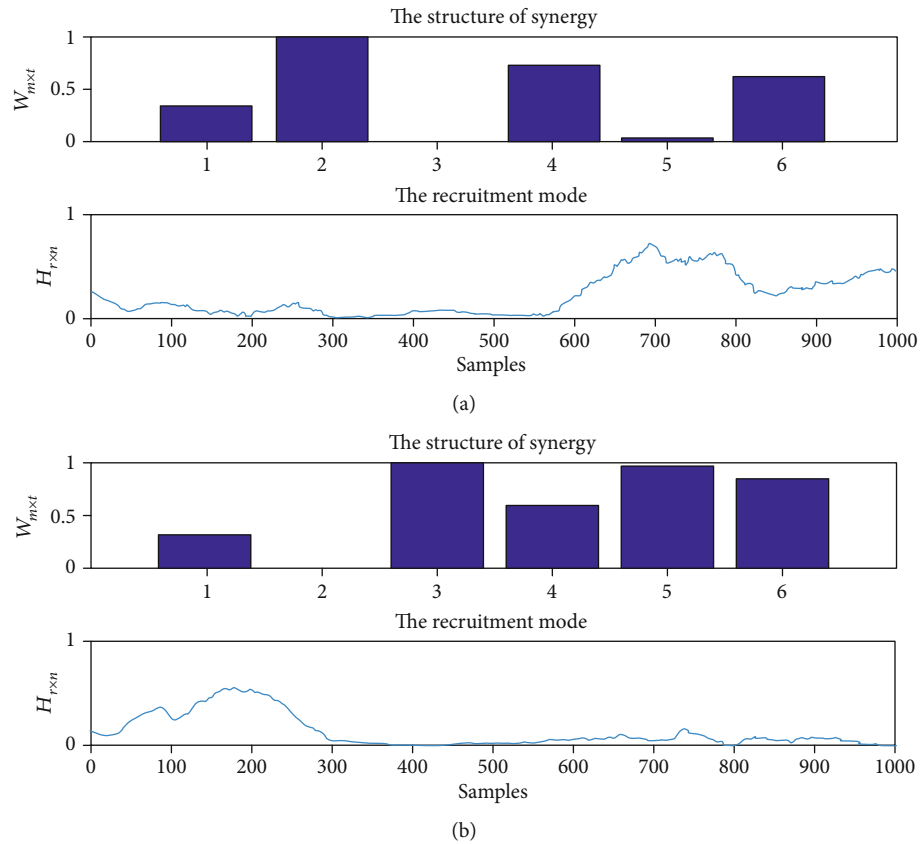
FIGURE 8: The typical results of muscle synergies of upper limbs for stroke patients during the HRI with clockwise circle-drawing movements. (a) The synergy pattern and activation coefficients for the first synergy; (b) the synergy pattern and activation coefficients for the second synergy. The structure of synergy represents the synergy pattern of muscle synergies, and the recruitment mode represents the activation coefficients of muscle synergies.

during the HRI with constrained circle-drawing movement could be considered as a task for upper-limb motor function assessments.

There are still several limitations in this study. Firstly, the sEMG signals are normalized to the peak value for a specific task [27]. However, the maximal isometric voluntary contraction (MVC) may not represent the real maximal activating level of muscles during the complex movements [28]. The MVC measurements in patients are usually affected by their varying degrees of motor deficits. This might bring a larger intersubject variability [29]. Nevertheless. the sEMG variations between different tasks and the same task collected at different recovery stages in the same patients could not be intuitively comparable by this normalization method [28]. In future study, a proper method of sEMG normalization is needed to be considered.

Secondly, the number of extracted muscle synergies has been proposed to reflect the complexity of motor control [16]. As mentioned in Methods, we extracted the number of muscle synergies by using VAF for all participants. A threshold needs to be set by experience. The thresholds may be different between healthy subjects and stroke patients. Therefore, a more objective approach to determine the number of muscle synergy is needed to be further developed.

Thirdly, due to the limited clinical resource, the sample size of stroke patients was only two in this study. The trend of decrease of muscle synergy number was found when the stroke patients were compared with healthy subjects, but there was no statistical evidence due to small sample size. A larger sample size of stroke patients with similar disease stage will be considered in the future study.

Abbreviations

HRI: Human-robot interaction
sEMG: Surface electromyography
NMF: Nonnegative matrix factorization
EULRR: End-effector upper-limb rehabilitation robot
AD: Anterior deltoid
PD: Posterior deltoid
BB: Biceps brachii
TB: Triceps brachii
FCR: Flexor carpi radialis
ECR: Extensor carpi radialis
SENIAM: Surface EMG for noninvasive assessment of muscles
VAF: Variance account for
MVC: Maximal voluntary contraction.

Data Availability

The (Excel) data used to support the findings of this study are available from the corresponding author upon request.

Conflicts of Interest

The authors declare that they have no competing interests.

Authors' Contributions

CW and SZ conceptualized the idea, proposed the experimental design, and participated in data acquisition and analysis and writing of the manuscript at all stages. CS contributed to development of the conceptualized idea, took active part in data acquisition, and revised the manuscript at all stages. JH and ZH participated in data analysis and revised the manuscript at all stages. All authors read and approved the final manuscript. Cheng Wang and Shutao Zhang contributed equally to this work.

References

[1] C. Duret, A. G. Grosmaire, and H. I. Krebs, "Robot-assisted therapy in upper extremity hemiparesis: overview of an evidence-based approach," *Frontiers in Neurology*, vol. 10, p. 412, 2019.

[2] M. L. Aisen, H. I. Krebs, and N. Hogan, "The effect of robot-assisted therapy and rehabilitative training on motor recovery following stroke," *Archives of Neurology*, vol. 54, no. 4, pp. 443–446, 1997.

[3] C. J. Winstein, J. Stein, R. Arena et al., "Guidelines for adult stroke rehabilitation and recovery: a guideline for healthcare professionals from the American Heart Association/American Stroke Association," *Stroke*, vol. 47, no. 6, pp. 98–169, 2016.

[4] N. Nordin, S. Q. Xie, and B. Wünsche, "Assessment of movement quality in robot- assisted upper limb rehabilitation after stroke: a review," *Journal of Neuroengineering and Rehabilitation*, vol. 11, no. 1, p. 137, 2014.

[5] H. I. Krebs, M. Krams, D. K. Agrafiotis et al., "Robotic measurement of arm movements after stroke establishes biomarkers of motor recovery," *Stroke*, vol. 45, no. 1, pp. 200–204, 2014.

[6] T. Krabben, B. I. Molier, A. Houwink, J. S. Rietman, J. H. Buurke, and G. B. Prange, "Circle drawing as evaluative movement task in stroke rehabilitation: an explorative study," *Journal of Neuroengineering and Rehabilitation*, vol. 8, no. 1, p. 15, 2011.

[7] A. Schwarz, C. M. Kanzler, O. Lambercy, A. R. Luft, and J. M. Veerbeek, "Systematic review on kinematic assessments of upper limb movements after stroke," *Stroke*, vol. 50, no. 3, pp. 718–727, 2019.

[8] P. Tropea, V. Monaco, M. Coscia, F. Posteraro, and S. Micera, "Effects of early and intensive neuro-rehabilitative treatment on muscle synergies in acute post-stroke patients: a pilot study," *Journal of Neuroengineering and Rehabilitation*, vol. 10, no. 1, p. 103, 2013.

[9] A. Scano, A. Chiavenna, M. Malosio, L. Molinari Tosatti, and F. Molteni, "Muscle synergies-based characterization and clustering of poststroke patients in reaching movements," *Frontiers in Bioengineering and Biotechnology*, vol. 5, p. 62, 2017.

[10] S. T. Zhang, G. K. Zuo, C. C. Shi et al., "The sEMG characteristics of human upper limb during circle drawing on EULRR system," in *2017 IEEE International Conference on Cybernetics and Intelligent Systems (CIS) and IEEE Conference on Robotics, Automation and Mechatronics (RAM)*, pp. 423–427, Ningbo, Zhejiang, China, 2017.

[11] H. J. Hermens, B. Freriks, C. Disselhorst-Klug, and G. Rau, "Development of recommendations for SEMG sensors and sensor placement procedures," *Journal of Electromyography and Kinesiology*, vol. 10, no. 5, pp. 361–374, 2000.

[12] D. D. Lee and H. S. Seung, "Learning the parts of objects by non-negative matrix factorization," *Nature*, vol. 401, no. 6755, pp. 788–791, 1999.

[13] J. F. Yang and D. Winter, "Electromyographic amplitude normalization methods: improving their sensitivity as diagnostic tools in gait analysis," *Archives of Physical Medicine and Rehabilitation*, vol. 65, no. 9, pp. 517–521, 1984.

[14] M. C. Tresch, V. C. Cheung, and A. d'Avella, "Matrix factorization algorithms for the identification of muscle synergies: evaluation on simulated and experimental data sets," *Journal of Neurophysiology*, vol. 95, no. 4, pp. 2199–2212, 2006.

[15] F. Li, Q. Wang, S. Cao, D. Wu, Q. Wang, and X. Chen, "Lower-limb muscle synergies in children with cerebral palsy," in *2013 6th International IEEE/EMBS Conference on Neural Engineering (NER)*, pp. 1226–1229, San Diego, CA, USA, 2013.

[16] D. J. Clark, L. H. Ting, F. E. Zajac, R. R. Neptune, and S. A. Kautz, "Merging of healthy motor modules predicts reduced locomotor performance and muscle coordination complexity post-stroke," *Journal of Neurophysiology*, vol. 103, no. 2, pp. 844–857, 2010.

[17] G. Torres-Oviedo and L. H. Ting, "Subject-specific muscle synergies in human balance control are consistent across different biomechanical contexts," *Journal of Neurophysiology*, vol. 103, no. 6, pp. 3084–3098, 2010.

[18] E. Chiovetto, B. Berret, I. Delis, S. Panzeri, and T. Pozzo, "Investigating reduction of dimensionality during single-joint elbow movements: a case study on muscle synergies," *Frontiers in Computational Neuroscience*, vol. 7, p. 11, 2013.

[19] V. C. Cheung, A. Turolla, M. Agostini et al., "Muscle synergy patterns as physiological markers of motor cortical damage," *Proceedings of the National Academy of Sciences of the United States of America*, vol. 109, no. 36, pp. 14652–14656, 2012.

[20] V. C. Cheung, A. d'Avella, M. C. Tresch, and E. Bizzi, "Central and sensory contributions to the activation and organization of muscle synergies during natural motor behaviors," *Journal of Neuroscience*, vol. 25, no. 27, pp. 6419–6434, 2005.

[21] G. Torres-Oviedo, J. M. Macpherson, and L. H. Ting, "Muscle synergy organization is robust across a variety of postural perturbations," *Journal of Neurophysiology*, vol. 96, no. 3, pp. 1530–1546, 2006.

[22] A. D'Avella and F. Lacquaniti, "Control of reaching movements by muscle synergy combinations," *The Journal of Neuroscience*, vol. 26, no. 30, pp. 7791–7810, 2016.

[23] W. W. Wang, B. C. Tsai, L. C. Hsu et al., "Guidance-control-based exoskeleton rehabilitation robot for upper limbs: application to circle drawing for physiotherapy and training," *Journal of Medical and Biological Engineering*, vol. 34, no. 3, pp. 284–292, 2014.

[24] G. Kwakkel, B. J. Kollen, and H. I. Krebs, "Effects of robot-assisted therapy on upper limb recovery after stroke: a

systematic review," *Neurorehabilitation and Neural Repair*, vol. 22, no. 2, pp. 111–121, 2008.

[25] D. G. Kamper, A. N. McKenna-Cole, L. E. Kahn, and D. J. Reinkensmeyer, "Alterations in reaching after stroke and their relation to movement direction and impairment severity," *Archives of Physical Medicine and Rehabilitation*, vol. 83, no. 5, pp. 702–707, 2002.

[26] J. P. Dewald, P. S. Pope, J. D. Given, T. S. Buchanan, and W. Z. Rymer, "Abnormal muscle coactivation patterns during isometric torque generation at the elbow and shoulder in hemiparetic subjects," *Brain*, vol. 118, no. 2, pp. 495–510, 1995.

[27] L. M. Knutson, G. L. Soderberg, B. T. Ballantyne, and W. R. Clarke, "A study of various normalization procedures for within day electromyographic data," *Journal of Electromyography and Kinesiology*, vol. 4, no. 1, pp. 47–59, 1994.

[28] A. Burden, "How should we normalize electromyograms obtained from healthy participants? What we have learned from over 25 years of research," *Journal of Electromyography and Kinesiology*, vol. 20, no. 6, pp. 1023–1035, 2010.

[29] G. T. Allison, R. N. Marshall, and K. P. Singer, "EMG signal amplitude normalization technique in stretch-shortening cycle movements," *Journal of Electromyography and Kinesiology*, vol. 3, no. 4, pp. 236–244, 1993.

Research Article

Lower-Limb-Assisting Robotic Exoskeleton Reduces Energy Consumption in Healthy Young Persons during Stair Climbing

Hanseung Woo [ID],[1] **Kyoungchul Kong** [ID],[1,2] **and Dong-wook Rha** [ID] [2,3]

[1]*Department of Mechanical Engineering, Korea Advanced Institute of Science and Technology (KAIST),*
 Daejeon 34141, Republic of Korea
[2]*Angel Robotics, Seoul 04798, Republic of Korea*
[3]*Department and Research Institute of Rehabilitation Medicine, Yonsei University College of Medicine,*
 Seoul 03722, Republic of Korea

Correspondence should be addressed to Kyoungchul Kong; kckong@kaist.ac.kr and Dong-wook Rha; medicus@yonsei.ac.kr

Many robotic exoskeletons for lower limb assistance aid walking by reducing energy costs. However, investigations examining stair-climbing assistance have remained limited, generally evaluating reduced activation of related muscles. This study sought to investigate how climbing assistance by a robotic exoskeleton affects energy consumption. Ten healthy young participants wearing a robotic exoskeleton that assists flexion and extension of hip and knee joints walked up nine flights of stairs twice at a self-selected speed with and without stair-climbing assistance. Metabolic cost was assessed by measuring oxygen consumption, heart rate, and the time to climb each flight of stairs. Net oxygen cost (NOC) and total heart beats (THB) were used as measures of metabolic cost, accounting for different climbing speeds. Stair-climbing assistance reduced NOC and THB by 9.3% ($P < 0.001$) and 6.9% ($P = 0.003$), respectively, without affecting climbing speed. Despite lack of individual optimization, assistive joint torque applied to the hip and knee joints reduced metabolic cost and cardiovascular burden of stair climbing in healthy young males. These results may be used to improve methods for stair ascent assistance.

1. Introduction

Various robotic exoskeletons for lower limb assistance have been developed to aid walking, the most common method of human locomotion. Investigations of walking mechanics have provided the foundation for the development of such robots. Kinematics of lower limb joints have been used to determine the range of motion and the degree of freedom of robotic joints [1], whereas kinetics have been used to determine the required robot joint power [2]. Together, kinematics and kinetics have provided important insights into the development of appropriate walking assistance methods.

The benefits of walking assistance provided by robotic exoskeletons have been evidenced as reduced energy costs. For instance, ankle exoskeletons utilizing pneumatic muscles to assist ankle plantar flexion have been shown to reduce the metabolic cost of walking [3–5]. However, these exoskeletons were not fully mobile, as they were powered by an external air pressure source, with the energy cost advantage observed only on a treadmill at a constant walking speed.

The metabolic cost benefits of the portable autonomous ankle exoskeleton developed by Mooney et al. [6, 7] were similarly verified in a controlled environment. Recent studies demonstrated that walking assistance by a tethered multi-joint soft exosuit significantly reduced metabolic costs [8, 9]. Furthermore, an autonomous version of the soft exosuit reduced the metabolic cost of walking together with a carrying load [10, 11]. In a case study of overground walking assistance with two subjects, the autonomous soft exosuit also reduced the metabolic cost of loaded walking over a 500 m cross-country trail [12].

Although stair climbing is almost as frequent as walking, the biomechanical characteristics of the two types of motion are distinct from each other. Relative to walking, stair climbing, characterized by large joint moment and power, increases joint flexion in the hip, knee, and ankle in the
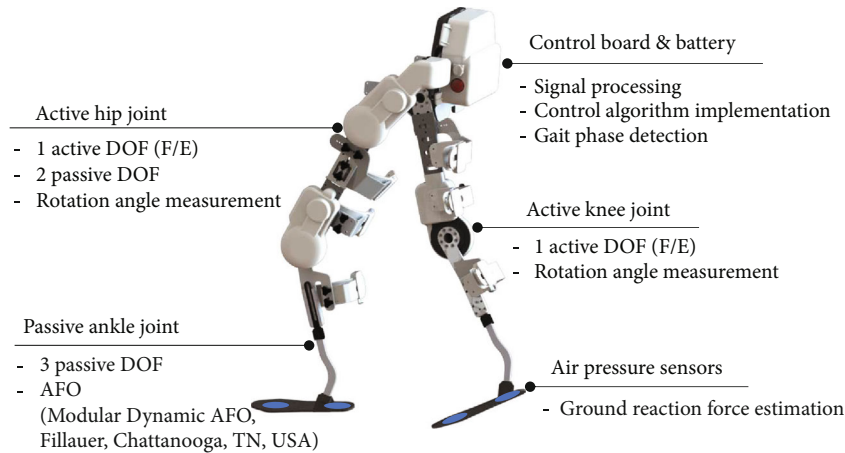
FIGURE 1: A robotic exoskeleton for lower limb assistance. DOF: degree of freedom; AFO: ankle-foot orthosis; F/E: flexion/extension.

sagittal plane. During stair climbing, power generation in the knee joint is dominant relative to power absorption, and the total positive network of the joints is larger than that during walking [13, 14]. Given that stair climbing requires considerable joint torque, positive power, and positive network, assistance provided by a wearable robot is expected to reduce the energetic cost of ascent by providing assistive torque to the wearer's joints.

Previous reports have proposed climbing assistance methods facilitated by robotic exoskeletons. Despite utilizing different exoskeletons, actuators, sensors, and target users, several studies have verified, using electromyography, the effects of stair-climbing assistance on subjects capable of performing voluntary leg motions [15–17]. Yet, to date, the effects of exoskeleton-mediated climbing assistance on energetic costs have not been considered, with a limited number of studies analyzing the metabolic effects of assistance for other related motions. For instance, assistance provided by a knee exoskeleton during step-up-and-down [18] and squatting [19] exercises has been shown to reduce the heart rate and the metabolic equivalent of task [20], respectively. Presently, we sought to investigate the energy consumption effect of stair-climbing assistance provided by a robotic exoskeleton. Specifically, we tested oxygen consumption and heart rate during a nine-flight stair climb in the absence or presence of assistance from an autonomous (i.e., fully mobile) robotic exoskeleton with rigid frames and braces providing assistive torque to the hip and knee joints.

2. Materials and Methods

2.1. Participants. Nondisabled male subjects ($N = 10$, age = 28.3 ± 1.7 years, weight = 68.8 ± 5.5 kg, height = 173.8 ± 5.1 cm) participated in this study. None of the subjects have been diagnosed with musculoskeletal or neurologic disorders affecting walking or stair climbing. Ethical approval was granted by the institutional review board and ethics committee (4-2017-0578).

2.2. Robotic Exoskeleton. The robotic exoskeleton used in this study (Figure 1) consisted of active hip and knee joints and

passive ankle joints. Active joints were powered by electrical motors with a gear ratio of 76 : 1, with assistive torque delivered to the wearer's joints in the sagittal plane. Active joints adopted a series elastic actuation mechanism [21, 22], enabling accurate control of the interaction torque between robot and human joints. Dynamic ankle-foot orthosis was used as the passive ankle joint to support the weight of the exoskeleton and to provide a sufficient degree of freedom in the wearer's ankle joint. Foot pressure under the metatarsal joint and the heel was measured using silicon tubes and air pressure sensors to estimate the ground reaction force [23]. All algorithms required to operate the exoskeleton, such as sensor signal processing and the control algorithm, were implemented using the embedded control board (sbrio 9651, National Instruments, TX, USA) and software (Lab-VIEW 2015, National Instruments, TX, USA). The embedded control board and battery, enclosed in a backpack, enabled the exoskeleton to be fully mobile. The total weight of the robotic exoskeleton was 13 kg.

2.3. Assistance Strategy for a Stair-Climbing Motion. Common robotic joints are actuated by motors and gear reducers to amplify output torque to the desired magnitude. However, such a gear train is associated with large resistive torque. To remove the resistance and allow the wearer to move freely without discomfort, the robotic exoskeleton used a zero-impedance control (ZIC) algorithm [21, 24–26]. As shown in Figure 2, the ZIC application reduced the interaction torque between robotic and human joints such that it lies under 0.87 Nm. Also, it allowed the wearer to move the joint much faster with reduced resistive force.

Following ZIC-mediated removal of resistance, assistive torque can be provided via an assist-as-needed strategy [27, 28], which requires the determination of the timing for the application of the assistive torque. Previous studies [5, 29, 30] have used actuation onset timing, with a predefined assistive force provided at onset timing determined based on the percentages of a gait cycle. Presently, we employed a similar strategy for the stair-climbing assistance.

An investigation by Riener et al. of stair-climbing biomechanics and motor coordination [13] revealed substantial
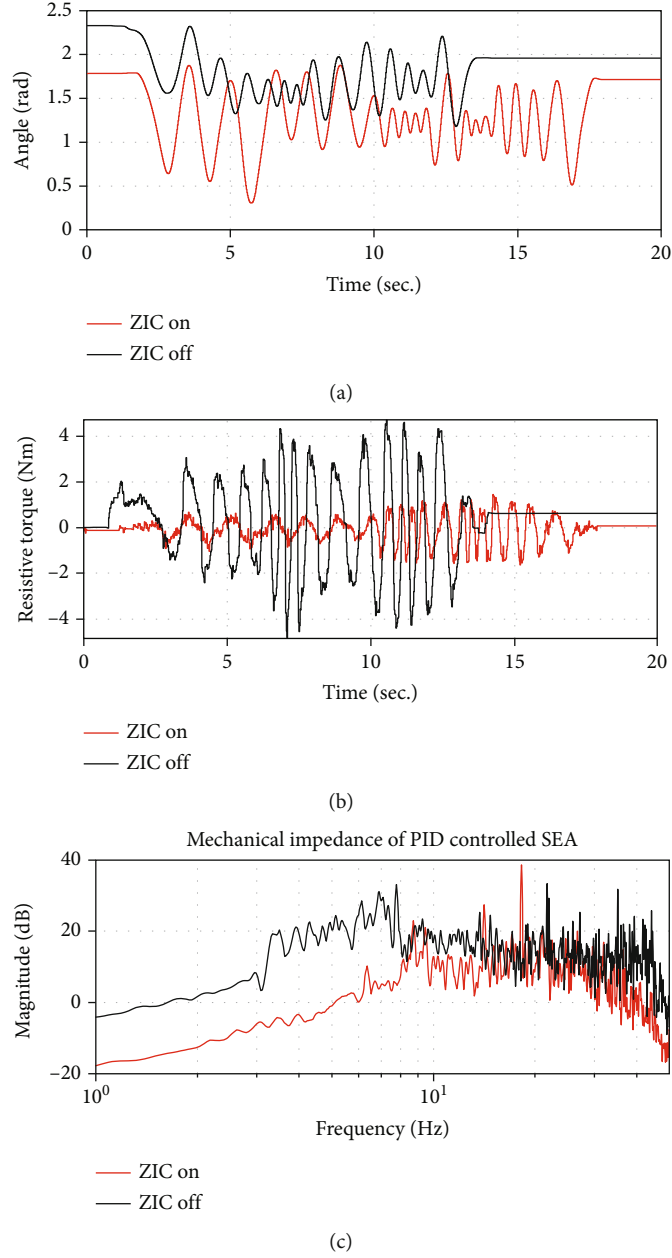
FIGURE 2: Reduced mechanical impedance (resistive force) on the knee joint of the robotic exoskeleton after applying ZIC: (a) an arbitrary motion applied to the joint; (b) a resistive force against motion inputs; (c) a mechanical impedance defined as the magnitude of the ratio of the resistive force to the joint velocity in the frequency domain.

extension torque of the hip and knee joints during the early section of the stance phase. Flexion torques are also observed in both joints during the initial section of the swing phase. The developed assistive joint torque profile for stair climbing emulated the joint torques during the early sections of the stance and swing phases. The assistive torque profile for the hip and knee joints can be simplified and parameterized as

$$\tau_o(t) = \begin{cases} -0.5\left(\tau_p \cos\left(\frac{\pi}{t_p}(t-t_i)\right) - \tau_p\right), & \text{if } t \in [t_i, t_i + 2t_p], \\ 0, & \text{otherwise}, \end{cases}$$

(1)

where t_i, τ_p, and t_p indicate onset time, peak value of the assistive torque, and time to reach, τ_p, respectively. When $\tau_o(t) = 0$, the desired interaction torque is zero, indicating a zero-impedance mode. Positive and negative values of τ_p indicate extension and flexion torque, respectively. To provide assistive torque during the early section of both phases, t_i can be set as the time when each phase is detected by analyzing the ground reaction forces [23]. Determination of onset timing by phase detection, rather than via percentage of gait cycle assessment, allowed the synchronization of assistive torque with the wearer's motion regardless of climbing speed changes. To prevent assistive torque for level-ground

walking during the stair climb, the assistance algorithm assessed the current ground state. The workflow of stair-climbing assistance is shown in Figure 3.

The τ_p and t_p, not optimized for each subject, were set empirically using preliminary experiments (Table 1). The assistive torques defined in the time domain were equally applied to all subjects after initiation of motion. However, their application varied in a subject-specific manner based on stair-climbing speed and stance cycles (Figure 4).

2.4. Experimental Protocol. The subjects were asked to rest for at least 5 min in a sitting position. Subsequently, oxygen consumption and heart rates were measured for 2 min in a standing position using a portable metabolic system (K4b2, COSMED, Rome, Italy) and a heart rate monitor (TICKR X, Wahoo, Atlanta, United States), respectively. Following the establishment of the resting heart rate (±5 beats per min), the subjects climbed nine flights of stairs (total of 195 steps; 20 steps per level through the 7th floor and 25 steps per level from the 7th floor to the 10th floor) twice at a self-selected speed. One trial was carried out without assistance (i.e., zero-impedance mode), with stair-climbing assistance applied for the other trial, and the order of trials was randomized. Subjects rested for at least 10 min between trials. During climbing, oxygen consumption, heart rate, and time to climb each level were measured. A practice period was provided to help subjects adapt to the wearable robot, with a maximum of two practice periods allowed.

2.5. Data Processing. A custom *m*-file (MATLAB, MathWorks, Natick, MA, USA) was used for data processing. Oxygen consumption and heart rate values were smoothed to eliminate measurement noise and outliers using smooth.*m*, with span = 10%, and method = rloess, where span is the length of the moving window as a percentage of the raw data, with the rloess method applying a second-order regression to the raw data from which the outlier is excluded [31]. Net oxygen cost (NOC) was calculated as the difference between the oxygen consumption rate and the average resting oxygen consumption rate divided by the stair-climbing speed [32]. Total heart beats (THB) [33] during the climbing session were calculated by numerical integration of the heart rate. The average climbing speed was calculated by dividing the number of steps by the climbing time. NOC, THB, and average climbing speed of the two climbing trials were compared using a paired *t*-test, with *P* values < 0.05 considered statistically significant. The paired *t*-test was performed using SPSS ver. 24 (SPSS Inc., Chicago, IL, USA).

3. Results and Discussion

3.1. Results. On average, stair-climbing assistance reduced NOC and THB by 9.3% ($P < 0.001$) and 6.9% ($P = 0.003$), respectively (Figure 5). For all subjects, although the average speed per level varied during climbing, no significant between-trial differences were observed (Figure 6).
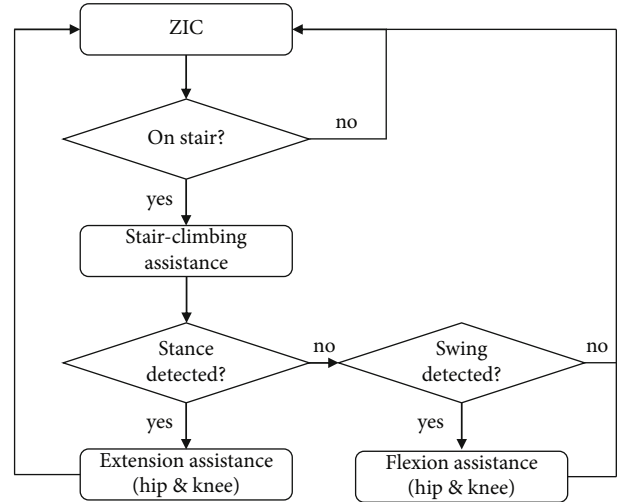
FIGURE 3: Workflow schematic of the stair-climbing assistance provided by the robotic exoskeleton. ZIC: zero-impedance control.

TABLE 1: Defined assistive torque parameters. τ_p: peak value of the assistive torque; t_p: time taken to reach the τ_p.

Joint	Stance phase		Swing phase	
	τ_p	t_p	τ_p	t_p
Hip	-27 Nm	0.25 s	16 Nm	0.2 s
Knee	-29 Nm	0.25 s	12 Nm	0.2 s
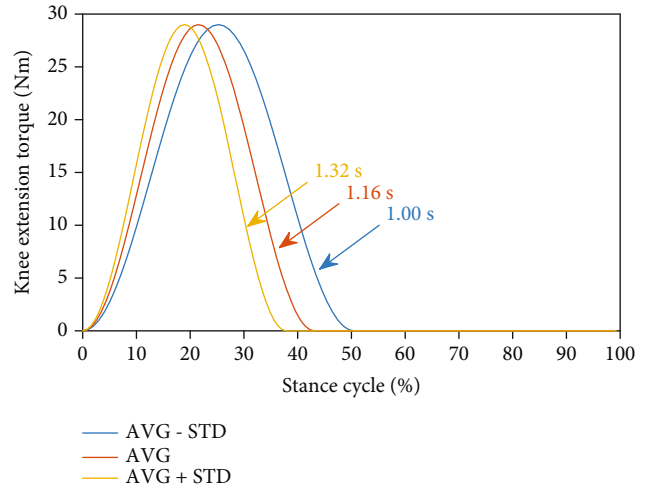
FIGURE 4: Example of knee extension torque for different stance times with the same t_p (0.25 s). AVG and STD indicate the mean and standard deviation of the stance time of the subject, respectively.

4. Discussion

4.1. Stair-Climbing Speed. In contrast to previous studies utilizing treadmills, the present experiments were conducted using nine flights of physical stairs. Despite the lack of a controlled experimental environment with strict regulation of climbing speed and motion analysis, these results more closely reflect real-life circumstances. With the ability to self-select climbing speed, the subjects demonstrated individual and

(a)

(b)
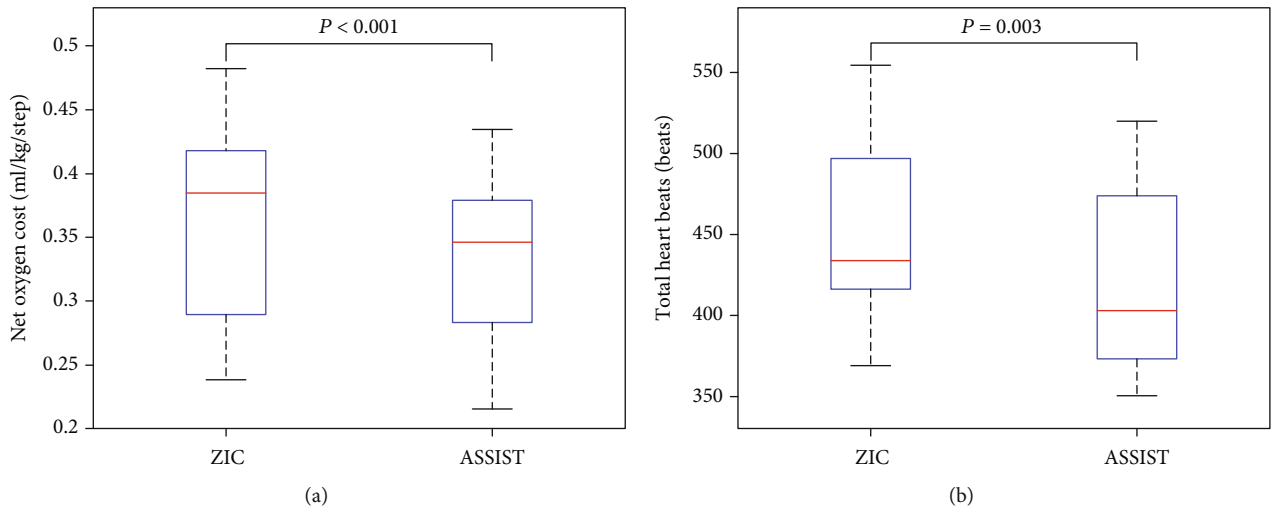
Figure 5: Stair-climbing net oxygen cost (NOC) and total heart beats (THB). NOC (a) and THB (b) were calculated for a 9-level stair climb with (ASSIST) and without climbing assistance (ZIC).

(a)

(b)
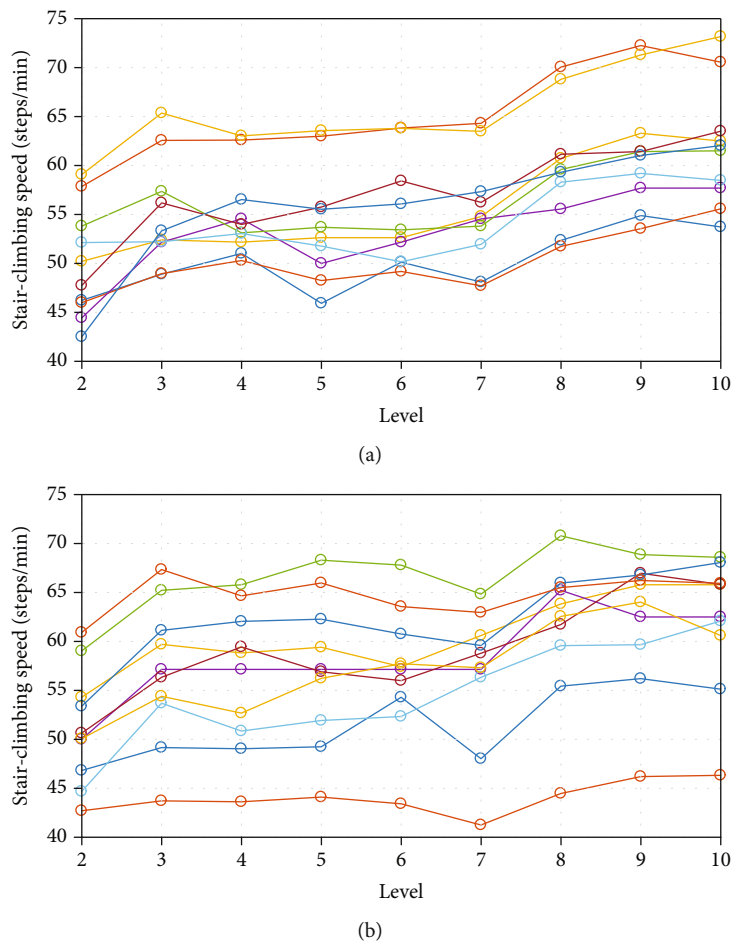
Figure 6: Average climbing speed. Climbing speed was measured under zero-impedance control (a) or climbing assistance (b) conditions.

within-climb differences in ascent speeds. However, the ZIC and assist conditions did not result in significant differences in the average stair-climbing speeds. These results indicated that, under the conditions tested, stair-climbing assistance has no effect on climbing speed.

4.2. NOC Reduction. Multiple studies of exoskeleton assistance [3–11], utilizing a treadmill environment to regulate walking speed, evaluated steady-state values of oxygen consumption and heart rate as indices of metabolic cost. Presently, we also considered the self-selected climbing speed for the assessment of metabolic cost. Plasschaert et al. previously defined NOC as the difference between the average oxygen consumption rate during walking and that during resting divided by the average walking speed [32]. Substituting the average climbing speed (steps/min) into the equation, we found that the metabolic cost decreased by 9.3% in the presence of stair-climbing assistance.

4.3. THB Reduction. In a manner similar to NOC, the heart rate should also be analyzed in a nonsteady state induced by climbing speed changes. Hood et al. defined the THB index as the ratio of THB during the exercise period to the total traveled distance [33]. As the subjects covered the same climbing distance in the present study, unadjusted THB values were considered. In addition to serving as an accurate and convenient estimate of energy expenditure, the heart rate also directly reflects the cardiac burden of a person. Presently, THB decreased by 6.9% following robotic exoskeleton assistance, suggesting that climbing assistance can reduce cardiovascular burden.

4.4. Methodological Issues and Limitations. The present study used a trunk-hip-knee-ankle-foot- (THKAF-) type multi-joint robotic exoskeleton [34]. Exoskeletons of this type have been used to provide full assistance to paraplegic patients to move their legs. Using such exoskeletons on nondisabled wearers requires the exoskeletal joints to have zero impedance, or zero torque [35]. Ankle exoskeletons for walking assistance have provided energetic cost advantages due to negligible device weight and minimal interference in joint function. Multijoint soft exosuits, utilizing special actuation and power transmission mechanisms, have also considerably reduced metabolic costs due to limited weight and minimized resistive force. During stair climbing, the function of the knee joint (i.e., torque, power, and work) supersedes that of other joints [14], with most exoskeletons for stair-climbing assistance previously developed as knee-type devices. Thus, stair-climbing assistance using a THKAF-type exoskeleton was expected to be effective for metabolic cost reduction.

Despite its considerable weight, the THKAF-type exoskeleton was sufficiently portable to perform experiments using a physical stair environment. However, our experiments were limited in their ability to obtain data for biomechanical analyses, including measurements of muscle activity and of human motion in a three-dimensional space. Lack of kinematic and kinetic information, as well as of electromyography data, represents a limitation of this study that hinders direct comparisons with other works. Despite this drawback, this study demonstrated, for the first time, reduction in climbing-associated energy consumption using a THKAF-type exoskeleton.

Presently, equal assistive torque was provided to all subjects, with parameters (Table 1) empirically determined using preliminary studies. However, subject-specific assistive torque parameters may maximize the assistance effect for individual subjects. Recent studies have demonstrated that optimization of individual assistive force profiles can further reduce energy consumption [11, 36]. Thus, subject-specific optimization of the assistive torque provided by the exoskeleton tested here may result in improved climbing assistance effects. However, despite identical assistive torques, the present study demonstrated effective stair-climbing assistance for all subjects.

Multiple studies have compared metabolic costs between robotic assistance and no-robot or unpowered conditions [5, 8, 9, 36, 37]. However, the use of nondisabled subjects proficient in performing the tested physical tasks unassisted can mask the effects of assistance. The assistance effect can only emerge when the assistance overcomes the negative effects on energy consumption of factors such as exoskeleton weight, robot-imposed limitations in joint degree of freedom, and resistive forces of robotic joints [35]. Ding and colleagues [8, 36] used a tethered actuation system to facilitate assistance without increasing the weight load on the subjects. In cases where power sources could not be separated from the robot body, unpowered conditions have been used as controls to identify the assistance effect [5, 37]. However, it is also necessary to guarantee compliance of the robotic joints using specific mechanisms or control algorithms. Presently, as the actuation parts of the exoskeleton could not be separated from the robot body, ZIC was applied to ensure compliance of the robotic joints, with the metabolic cost compared to that under conditions of applied assistance. Thus, the possibility that the exoskeleton increases metabolic costs relative to no-robot conditions represents another limitation of this study. Such limitations, reported in other studies [3, 4], can be addressed by reducing exoskeleton weight, improving wearability, and ensuring greater degree of freedom of leg joints.

5. Conclusions

Stair-climbing assistance provided by an exoskeleton that assists flexion and extension of hip and knee joints reduced the metabolic cost and cardiovascular burden in healthy young males climbing nine floors of stairs.

Data Availability

The data used to support the findings of this study are available from the corresponding author upon request.

Conflicts of Interest

The authors declare that there is no conflict of interest regarding the publication of this paper.

Acknowledgments

References

[1] A. Chu, H. Kazerooni, and A. Zoss, "On the biomimetic design of the berkeley lower extremity exoskeleton (BLEEX)," in *Proceedings of the 2005 IEEE International Conference on Robotics and Automation*, pp. 4345–4352, Barcelona, Spain, 2005.

[2] M. Cenciarini and A. M. Dollar, "Biomechanical considerations in the design of lower limb exoskeletons," in *Proceedings of the IEEE International Conference on Rehabilitation Robotics ICORR*, pp. 297–302, Zurich, Switzerland, 2011.

[3] J. A. Norris, K. P. Granata, M. R. Mitros, E. M. Byrne, and A. P. Marsh, "Effect of augmented plantarflexion power on preferred walking speed and economy in young and older adults," *Gait & Posture*, vol. 25, no. 4, pp. 620–627, 2007.

[4] G. S. Sawicki and D. P. Ferris, "Mechanics and energetics of level walking with powered ankle exoskeletons," *Journal of Experimental Biology*, vol. 211, no. 9, pp. 1402–1413, 2008.

[5] P. Malcolm, W. Derave, S. Galle, and D. De Clercq, "A simple exoskeleton that assists plantarflexion can reduce the metabolic cost of human walking," *Plo S one*, vol. 8, no. 2, article e56137, 2013.

[6] L. M. Mooney, E. J. Rouse, and H. M. Herr, "Autonomous exoskeleton reduces metabolic cost of human walking during load carriage," *Journal of Neuroengineering and Rehabilitation*, vol. 11, no. 1, p. 80, 2014.

[7] L. M. Mooney and H. M. Herr, "Biomechanical walking mechanisms underlying the metabolic reduction caused by an autonomous exoskeleton," *Journal of Neuroengineering and Rehabilitation*, vol. 13, no. 1, p. 4, 2016.

[8] Y. Ding, I. Galiana, A. T. Asbeck et al., "Biomechanical and physiological evaluation of multi-joint assistance with soft exosuits," *IEEE Transactions on Neural Systems and Rehabilitation Engineering*, vol. 25, no. 2, pp. 119–130, 2017.

[9] B. Quinlivan, S. Lee, P. Malcolm et al., "Assistance magnitude versus metabolic cost reductions for a tethered multiarticular soft exosuit," *Science robotics*, vol. 2, no. 2, article eaah4416, 2017.

[10] F. A. Panizzolo, I. Galiana, A. T. Asbeck et al., "A biologically-inspired multi-joint soft exosuit that can reduce the energy cost of loaded walking," *Journal of Neuro Engineering and Rehabilitation*, vol. 13, no. 1, p. 43, 2016.

[11] S. Lee, J. Kim, L. Baker et al., "Autonomous multi-joint soft exosuit with augmentation-power-based control parameter tuning reduces energy cost of loaded walking," *Journal of Neuroengineering and Rehabilitation*, vol. 15, no. 1, p. 66, 2018.

[12] S. Lee, N. Karavas, B. T. Quinlivan et al., "Autonomous multi-joint soft exosuit for assistance with walking overground," in *2018 IEEE International Conference on Robotics and Automation (ICRA)*, pp. 2812–2819, Brisbane, QLD, Australia, 2018.

[13] R. Riener, M. Rabuffetti, and C. Frigo, "Stair ascent and descent at different inclinations," *Gait & Posture*, vol. 15, no. 1, pp. 32–44, 2002.

[14] P. DeVita, J. Helseth, and T. Hortobagyi, "Muscles do more positive than negative work in human locomotion," *Journal of Experimental Biology*, vol. 210, no. 19, pp. 3361–3373, 2007.

[15] C. Fleischer and G. Hommel, "A human–exoskeleton interface utilizing electromyography," *IEEE Transactions on Robotics*, vol. 24, no. 4, pp. 872–882, 2008.

[16] T.-J. Yeh, M.-J. Wu, T.-J. Lu, F.-K. Wu, and C.-R. Huang, "Control of McKibben pneumatic muscles for a power-assist, lower-limb orthosis," *Mechatronics*, vol. 20, no. 6, pp. 686–697, 2010.

[17] D. Sasaki, T. Noritsugu, and M. Takaiwa, "Development of pneumatic lower limb power assist wear driven with wearable air supply system," in *2013 IEEE/RSJ International Conference on Intelligent Robots and Systems*, pp. 4440–4445, Tokyo, Japan, 2013.

[18] T. Nakamura, K. Saito, and K. Kosuge, "Control of wearable walking support system based on human-model and grf," in *Proceedings of the 2005 IEEE International Conference on Robotics and Automation*, pp. 4394–4399, Barcelona, Spain, 2005.

[19] A. Gams, T. Petrič, T. Debevec, and J. Babič, "Effects of robotic knee exoskeleton on human energy expenditure," *IEEE Transactions on Biomedical Engineering*, vol. 60, no. 6, pp. 1636–1644, 2013.

[20] B. E. Ainsworth, W. L. Haskell, S. D. Herrmann et al., "2011 compendium of physical activities: a second update of codes and met values," *Medicine & Science in Sports & Exercise*, vol. 43, no. 8, pp. 1575–1581, 2011.

[21] K. Kong, J. Bae, and M. Tomizuka, "Control of rotary series elastic actuator for ideal force-mode actuation in human–robot interaction applications," *IEEE/ASME Transactions on Mechatronics*, vol. 14, no. 1, pp. 105–118, 2009.

[22] K. Kong, J. Bae, and M. Tomizuka, "A compact rotary series elastic actuator for human assistive systems," *IEEE/ASME Transactions on Mechatronics*, vol. 17, no. 2, pp. 288–297, 2012.

[23] K. Kong and M. Tomizuka, "A gait monitoring system based on air pressure sensors embedded in a shoe," *IEEE/ASME Transactions on Mechatronics*, vol. 14, no. 3, pp. 358–370, 2009.

[24] J. A. Blaya and H. Herr, "Adaptive control of a variable-impedance ankle-foot orthosis to assist drop-foot gait," *IEEE Transactions on Neural Systems and Rehabilitation Engineering*, vol. 12, no. 1, pp. 24–31, 2004.

[25] J. F. Veneman, R. Ekkelenkamp, R. Kruidhof, F. C. van der Helm, and H. van der Kooij, "A series elastic-and Bowden-cable-based actuation system for use as torque actuator in exoskeleton-type robots," *The international journal of robotics research*, vol. 25, no. 3, pp. 261–281, 2006.

[26] S. Kim and J. Bae, "Force-mode control of rotary series elastic actuators in a lower extremity exoskeleton using model-inverse time delay control," *IEEE/ASME Transactions on Mechatronics*, vol. 22, no. 3, pp. 1392–1400, 2017.

[27] S. K. Banala, S. H. Kim, S. K. Agrawal, and J. P. Scholz, "Robot assisted gait training with active leg exoskeleton (alex)," *IEEE Transactions on Neural Systems and Rehabilitation Engineering*, vol. 17, no. 1, pp. 2–8, 2009.

[28] E. H. Van Asseldonk, J. F. Veneman, R. Ekkelenkamp, J. H. Buurke, F. C. Van der Helm, and H. van der Kooij, "The effects on kinematics and muscle activity of walking in a robotic gait trainer during zero-force control," *IEEE Transactions on Neural Systems and Rehabilitation Engineering*, vol. 16, no. 4, pp. 360–370, 2008.

[29] Y. Ding, F. A. Panizzolo, C. Siviy et al., "Effect of timing of hip extension assistance during loaded walking with a soft

exosuit," *Journal of Neuroengineering and Rehabilitation*, vol. 13, no. 1, p. 87, 2016.

[30] S. Galle, P. Malcolm, S. H. Collins, and D. De Clercq, "Reducing the metabolic cost of walking with an ankle exoskeleton: interaction between actuation timing and power," *Journal of Neuroengineering and Rehabilitation*, vol. 14, no. 1, p. 35, 2017.

[31] Mathworks Inc, "Matlab smooth function," Apr. 2018, https://www.mathworks.com/help/curvefit/smooth.html.

[32] F. Plasschaert, K. Jones, and M. Forward, "Energy cost of walking: solving the paradox of steady state in the presence of variable walking speed," *Gait & Posture*, vol. 29, no. 2, pp. 311–316, 2009.

[33] V. L. Hood, M. H. Granat, D. J. Maxwell, and J. P. Hasler, "A new method of using heart rate to represent energy expenditure: the total heart beat index," *Archives of Physical Medicine and Rehabilitation*, vol. 83, no. 9, pp. 1266–1273, 2002.

[34] T. Yan, M. Cempini, C. M. Oddo, and N. Vitiello, "Review of assistive strategies in powered lower-limb orthoses and exoskeletons," *Robotics and Autonomous Systems*, vol. 64, pp. 120–136, 2015.

[35] C. J. Walsh, K. Endo, and H. Herr, "A quasi-passive leg exoskeleton for load-carrying augmentation," *International Journal of Humanoid Robotics*, vol. 4, no. 3, pp. 487–506, 2007.

[36] Y. Ding, M. Kim, S. Kuindersma, and C. J. Walsh, "Human-in-the-loop optimization of hip assistance with a soft exosuit during walking," *Science robotics*, vol. 3, no. 15, article eaar5438, 2018.

[37] S. Galle, P. Malcolm, W. Derave, and D. De Clercq, "Uphill walking with a simple exoskeleton: plantarflexion assistance leads to proximal adaptations," *Gait & Posture*, vol. 41, no. 1, pp. 246–251, 2015.

Research Article

Effect of Muscle Fatigue on Surface Electromyography-Based Hand Grasp Force Estimation

Jinfeng Wang,[1] Muye Pang [ID],[2] Peixuan Yu [ID],[2] Biwei Tang,[2] Kui Xiang,[2] and Zhaojie Ju [ID][3]

[1]*Department of Information, Wuhan Huaxia University of Technology, 430223 Wuhan, China*
[2]*Intelligent System Research Institute, Wuhan University of Technology, 430070 Wuhan, China*
[3]*Intelligent System & Biomedical Robotics Group, University of Portsmouth, PO1 3HE Portsmouth, UK*

Correspondence should be addressed to Muye Pang; pangmuye@whut.edu.cn

Surface electromyography- (sEMG-) based hand grasp force estimation plays an important role with a promising accuracy in a laboratory environment, yet hardly clinically applicable because of physiological changes and other factors. One of the critical factors is the muscle fatigue concomitant with daily activities which degrades the accuracy and reliability of force estimation from sEMG signals. Conventional qualitative measurements of muscle fatigue contribute to an improved force estimation model with limited progress. This paper proposes an easy-to-implement method to evaluate the muscle fatigue quantitatively and demonstrates that the proposed metrics can have a substantial impact on improving the performance of hand grasp force estimation. Specifically, the reduction in the maximal capacity to generate force is used as the metric of muscle fatigue in combination with a back-propagation neural network (BPNN) is adopted to build a sEMG-hand grasp force estimation model. Experiments are conducted in the three cases: (1) pooling training data from all muscle fatigue states with time-domain feature only, (2) employing frequency domain feature for expression of muscle fatigue information based on case 1, and 3) incorporating the quantitative metric of muscle fatigue value as an additional input for estimation model based on case 1. The results show that the degree of muscle fatigue and task intensity can be easily distinguished, and the additional input of muscle fatigue in BPNN greatly improves the performance of hand grasp force estimation, which is reflected by the 6.3797% increase in R^2 (coefficient of determination) value.

1. Introduction

Surface electromyography (sEMG) is the recording of myoelectric signals of muscle fiber contraction captured by electrodes attached on the surface skin. Due to this electrical manifestation, sEMG has the ability to represent the muscle activation level and contains rich information of muscle force. This ability is widely applied in the accurate estimation of human joint moment which holds significant importance for robot control system design. Human hand grasp force estimation is one of the compelling applications among all of these implementations. The manipulability and dexterity of prosthetic hands, human-assisting devices, and telerobots are facilitated by grasp force estimation. Yamanoi et al. used sEMG signals to determine hand posture and estimate grip

force simultaneously for a myoelectric hand [1]. Kim et al. obtained grasp force through upper limb forearm sEMG to control a teleoperation system in real-time [2]. Peternel et al. proposed a muscle fatigue-based method for human-robot collaboration, by which the robot's physical behaviour can be adapted online to human motor fatigue [3]. It should be noticed that the effectiveness and robustness of these applications are depended on the validation of the sEMG-based force estimation which is highly affected by the properties of sEMG signals.

The relationship between sEMG signals and muscle force is mostly extracted by either machine learning-based method or model-based method. Machine learning methods, such as artificial neural network [4] and support vector machines [5], enable the direct mapping from sEMG signals to desired

force estimation. The model-based method takes advantage of the musculoskeletal dynamics and incorporates the human knowledge of physiology and motor functionality in an explicit way [6]. The disadvantages of the model-based method are that a general musculoskeletal system modeling for force estimation is still missing which is attributed to the unknown properties, and the corresponding parameters are inherently difficult to identify. Machine learning-based methods mitigate the gap with a compromised yet acceptable interpretability. Among all the modalities, sEMG together with classic regression models has been mostly investigated. Naeem et al. estimated joint force from EMG signals based on a back-propagation neural network (BPNN) [7]. Yang et al. compared different pattern regression methods to optimize the relationship between sEMG signals and hand grasp force [8]. Zhang et al. used linear discriminant analysis (LDA) to realize pattern recognition and artificial neural networks (ANN) to establish the relationship between sEMG signals and fingertip force in each hand grasp modes [9].

Most current research is confined within the improvement of accuracy and reliability for sEMG-based grasp force estimation through a single optimisation of regression algorithms in a laboratory environment instead of a clinical scenario. And the practical factors in clinical settings such as fatigue, sweating, and electrode shift are normally ignored [10]. As one of the most critical factors, muscle fatigue influences the force estimation to a large extent in sEMG-based applications [11]. In daily activities, muscle fatigue leads to failure of force generation to a required value at a normal muscle activation level [12]. When a muscle becomes fatigued, the amplitude-related features of its sEMG signals are notably affected [13]. A typical example is that the root mean square (RMS) of sEMG increases when muscle fatigue happens. In grasp force estimation, RMS is the main feature adopted for EMG-force regression. As a result, the performance of the pretrained force prediction model deteriorates, which is attributed to the unstable RMS representation of sEMG signals. It has been demonstrated that the variant of amplitude-based representation of sEMG-like multiscale RMS (MRMS) gets almost doubled under fatigue condition in a laboratory environment [14]. It is reasonable to incorporate muscle fatigue in sEMG-based grasp force estimation instead of solely depending on the plausible consistency of sEMG signals.

Frequency domain-based method is mostly explored to estimate muscle fatigue from sEMG signals by the analysis of mean frequency (MNF) or median frequency (MDF) [15]. A general conclusion summarises the decreasing shift of MNF or MDF along with the increase of muscle fatigue [15]. Xie et al. applied MNF derived via Hibert-Huang transform to analyse fatigue sEMG signals [16]. Fernando et al. used the ratio of MNF to average rectified value (ARV) as the index of muscle fatigue and muscle fatigue is detected when MNF/ARV falls below a predetermined baseline [13]. Despite the promising results shown by the transition between nonfatigue and fatigue status, the frequency domain metrics exhibit without a determined trend of shifting during singly-fatigue status [17]. An intuitive difficulty brought by this property is seen in the estimation of muscle fatigue using solely frequency metric-based sEMG signal representation. Thus, a more indicative metric is desired to function robustly during the lasting fatigue. The definition of fatigue as any reduction in the maximal capacity to generate force [12] allows the adoption of the loss of maximal voluntary contraction (MVC) to estimate muscle fatigue, where the degree of muscle fatigue is represented by the variant exerted force which is relatively accurate to be measured by additional tangible sensors.

Muscle fatigue has to be taken into account in order to acquire accurate grasp force from sEMG signals. However, so far nobody has been able to explain the relationship between muscle fatigue and sEMG's time-domain features. Even the conclusions of some studies are completely opposite. In this paper, we propose an algorithm to quantitatively estimate the degree of muscle fatigue and evaluate the results by three distinct methods. The substantial effect of muscle fatigue on the performance of hand grasp force estimation is preliminarily demonstrated with experiments on 10 healthy subjects. As the muscle fatigue detection and grasp force estimation are improved, we believe that current applications such as presented in [1–3] will be benefited from our proposed method.

2. Forearm Muscle Fatigue Evaluation

Based on the fact that muscle force will decline steadily during a sustained maximal contraction as shown in Figure 1, it is straight to adopt MFL as the index for evaluation of muscle fatigue. In this section, the definition of the proposed force-based metric is given with an emphasis on the case of static contraction for application.

2.1. Maximum Force Loss (MFL). The proposed method to estimate muscle fatigue depends on the measurement of maximal voluntary contraction, which is performed by exerting maximum hand grasp force. To acquire reliable contraction measurement, an easy-to-implement protocol is designed in this paper. At the beginning of a measurement session, the maximum force value is exerted by the subjects and recorded as MVC_i. After repetition of predefined types of static contraction, the force value is recorded for multiple trials as MVC_t. The maximum hand grasp force, as shown in Figure 2, will decrease over contraction tasks and reflects the remained muscle force capacity at the end of each trial. The termination of a session is determined by the failure to accommodate the exertion of required force which indicates that the muscle is too fatigued to accomplish contraction tasks. The required force value is recorded as MVC_f. MFL is finally defined as the following:

$$MFL = MVC_i - MVC_t, \quad (1)$$

where MVC_i and MVC_t correspond to the initial and current MVC force.

To eliminate individual differences, the ratio of the variant maximum hand grasp force to the initial value is adopted
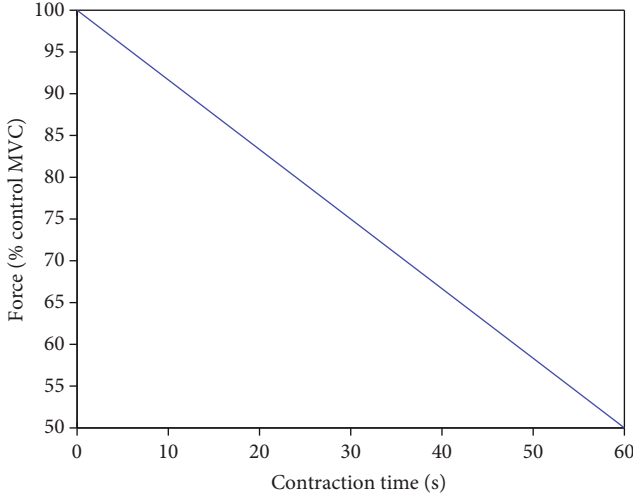
FIGURE 1: MVC changes during a sustained maximal contraction [12].
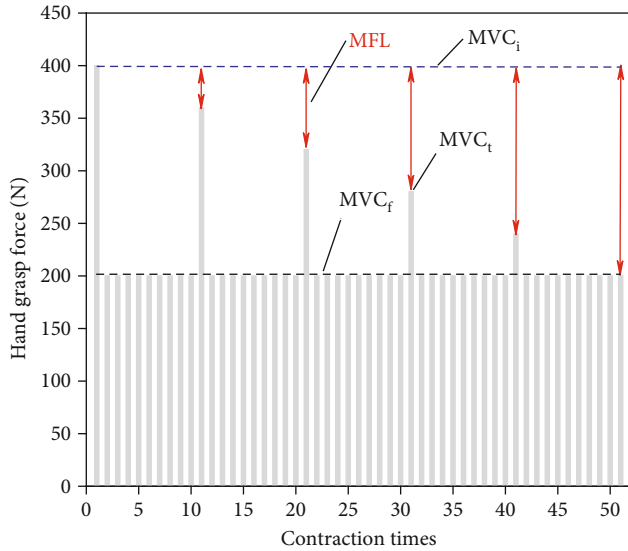
FIGURE 2: The measured maximum hand grasp force during a measurement session.

as the index of the degree of forearm muscle fatigue, defined as

$$MFL = \frac{MVC_i - MVC_t}{MVC_i}. \tag{2}$$

2.2. Case Study of Static Contraction. The definition given in the previous section indicates the importance of required force in forearm muscle fatigue estimation. The greater the required force becomes, the less contraction time to maintain the required force level lasts and the muscle is easier to fall into fatigue state. In a case study where subjects perform static contraction tasks by maintaining the required hand grasp force level as steadily as possible, it is necessary to

incorporate the influence of required force on muscle fatigue and MFL can be further redefined as

$$MFL = \frac{MVC_i - MVC_t}{MVC_i - MVC_f}, \tag{3}$$

where MVC_f corresponds to the MVC force in the exhausted condition. The proposed muscle fatigue metric MFL can vary from 0 to 1 where 0 indicates the nonfatigue condition and 1 indicates the exhausted condition during static contraction tasks. Equation (3) is adopted together with the assumption of static contraction to estimate muscle fatigue in the following sections.

3. Hand Grasp Force Estimation

In this preliminary study, back-propagation neural network (BPNN) is adopted to build sEMG based hand grasp force estimation model.

3.1. Experimental Protocol. Ten subjects (seven males and three females, mass 61.1 ± 3 kg, height 1.70 ± 0.03 m, all right-handed) have been recruited in the experiment study. The subjects gave written informed consent before the experiment, and the study was approved by the ethics committee of Wuhan University of Technology. The experiment is conducted with solely nondominant hands, i.e., the left hands, of our recruited subjects, where muscles are more prone to fatigue during the measurement session [18]. The subjects are asked first to seat in a comfortable position with their forearm rest on the table. The sleeve with sEMG electrodes embedded is worn on the subject's forearm with appropriate fixation to avoid the electrode shifting. A hand-muscle developer is held by the subjects' nondominant hand. A pressure sensor is attached to the hand-muscle developer for the measurement of grasp force. With the forearm muscle initially at rest, the captured sEMG with an amplitude at 0 uV is secured prior to the measurement session. Then, the subject is asked to hold the hand-muscle developer in the nondominant hand, with the chair height subsequently adjusted to form an obtuse angle between the forearm equipped with sensor and the upper arm (shown in Figure 3). The sEMG signals are easily interfered by cable movements or the surface electrodes relative movement caused by sleeve slipping ground the forearm. Thus, the subject is required to maintain his posture as much as possible throughout the session to reduce these artefacts.

There are three sessions for one subject to perform: named 50%, 60%, and 70% session. At the beginning of one session, the subject is instructed by visual hints to conduct a 5-second hand grasps at MVC by exerting maximum hand grasp force with the hand-muscle developer, and the force is recorded as MVC_i. Then, a 10-minute rest is provided. After the break, the subject is asked to perform a hand grasp with a muscle contraction at x% MVC_i ($x = 50, 60, 70$, according to which session is performed) as steadily as possible for 10 seconds. This grasp force is recorded as MVC_f. Then, a 5-second grasp at MVC is performed immediately, without a rest, and the maximum hand grasp force is recorded as MVC_t. After
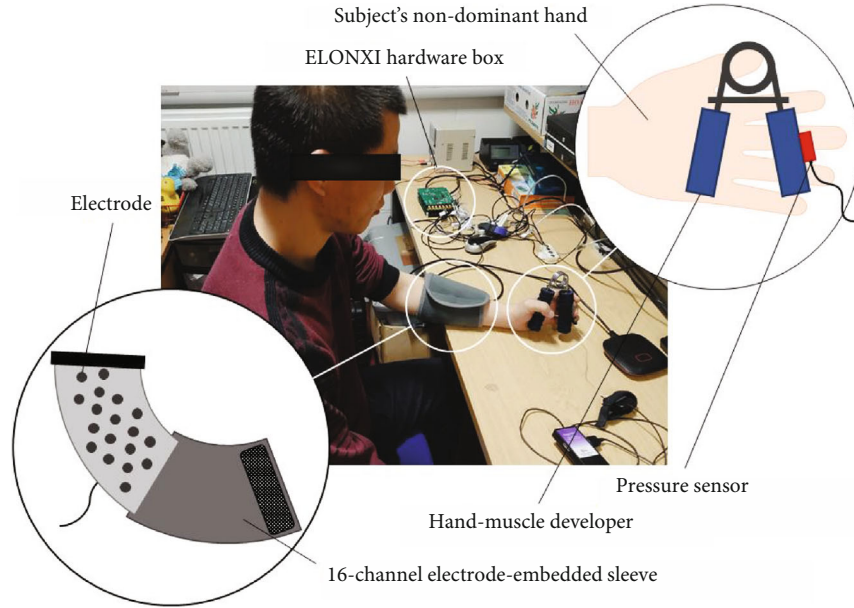
FIGURE 3: Experimental setup.

that, another loop of 10-second $x\%$ MVC_i steady contraction and 5-second MVC contraction is performed and repeated multiple times continuously, without a break until MVC_t falls below MVC_f. Then, one session is finished and a 30 minutes rest is given for the purpose of recovering from the muscle fatigue and preparing for the next session. The subject is provided with visual hints throughout the experiments to ensure their adaption to the force variance. The entire experimental procedure of one session is shown in Figure 4.

3.2. Data Acquisition. In this study, three muscles closely related to hand grasp are selected to record the sEMG signals, which are palmaris longus, flexor carpiulnaris, and extensor digitorum. A 16-channel electrode-embedded sleeve (ELONXI, UK) is used to cover the aforementioned forearm muscles to collect the sEMG signals where palmaris longus, flexor carpiulnaris, and extensor digitorum mainly correspond to 1-channel electrode, 3-channel electrode, and 5-channel electrode, respectively, as shown in Figure 5. The reference electrode is at the subject's wrist. Before wearing the electrode sleeve, the skin is cleaned by alcohol, and a 10-minute-rest is given after the electrode attachment to improve the contact of the electrode with skin to reduce the resistance within [19]. sEMG signals are amplified by a factor of 5000 with linear range 20 Hz to 500 Hz and sampled at 1000 Hz. The FingerTPS system (Pressure Profile Systems, Inc. (PPS), USA), originally utilised for capturing the tactile force on the finger pulp, is used to measure the hand grasp force in the experiment. Since the finger pulp is not the optimum pressure point during hand grasp, a highly sensitive capacitive-based pressure sensor is fixed to the appointed position on hand-muscle developer (shown in Figure 3). The sample frequency is 100 Hz controlled by the PC clock. The sEMG

signals and force measurements are captured and synchronized simultaneously during the experiment.

3.3. Data Processing. The relation between sEMG and force signals is extracted in an offline scheme. Two Sallen-Key filters are employed to band-pass filter raw sEMG signals at a bandwidth between 20 Hz and 500 Hz. In addition, a notch filter with central cut-off frequency at 50 Hz (UK power line frequency) is used to remove the power line interference.

The sEMG signals of each channel are segmented by the overlapped windowing technique [20] with a 300 ms window and 100 ms window shift for feature extraction. In this study, RMS and MNF/ARV [21–23] are selected as sEMG features. Except for sEMG signal processing, the mean value of hand grasp force data is adopted in each analysis window.

3.4. Force Estimation Methods. BPNN is used to learn the association between sEMG signals and hand grasp forces. In order to evaluate the effect of muscle fatigue on hand grasp force exertion, we propose the following three methods and compare them with locally acquired experiment data.

Time-domain feature driving machine learning-based method (TMLM, as shown in Figure 6): train the BPNN with pooled training data from all muscle fatigue status together. The inputs of BPNN are three muscles' sEMG feature RMS, forming the feature vector

$$[RMS_{i\times n}], \tag{4}$$

where i is the channel and n is the number of window shift. And the output is the measured hand grasp force. All the data acquired under three distinct hand grasp force levels are formed as the training/testing data for the BPNN.

Combined feature driving machine learning-based method (CMLM, as shown in Figure 7): train the BPNN with
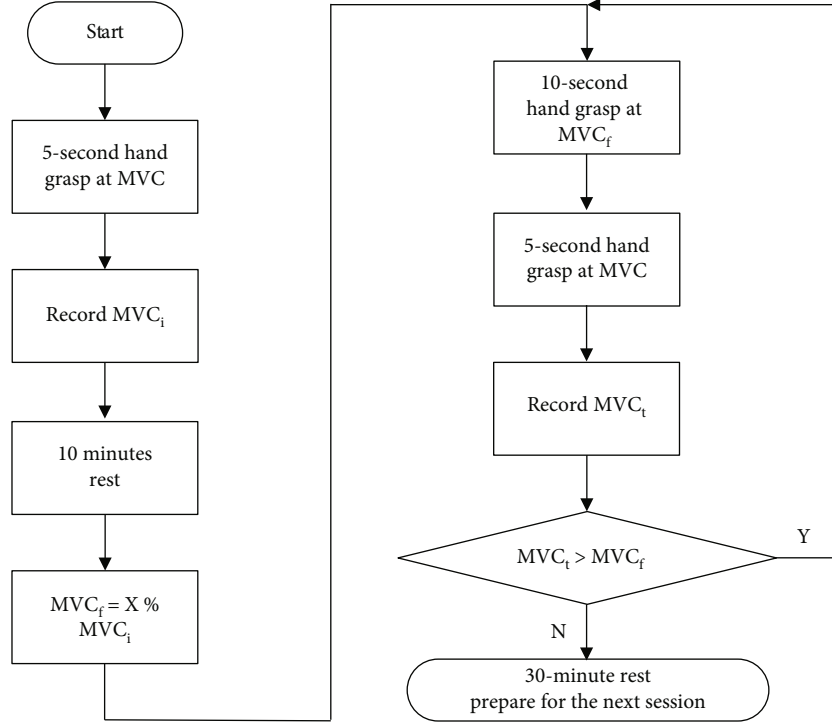
Figure 4: Diagram of the experimental procedure of one session.
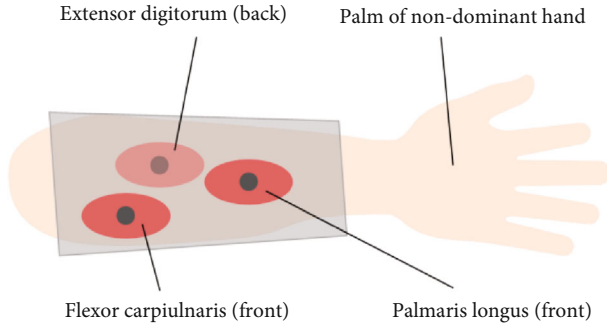
Figure 5: Diagram of the experimental procedure.

combination of time domain and frequency domain features. MNF is often employed for the expression of muscle fatigue information in sEMG-based force estimation. And Japanese researchers further proposed MNF/ARV, which has achieved good results in muscle fatigue detection [13]. So, a combined feature vector is given as

$$\left[(RMS_i)_n, (MNF_i/ARV_i)_n\right]$$
$$R^2 = 1 - \frac{\sum_{k=1}^{N}(F_k - F\wedge_k)^2}{\sum_{k=1}^{N}(F_k - \bar{F}_k)^2}, \tag{5}$$

where i is the channel and n is the number of window shift. F_k denotes the actual hand grasp force, $\widehat{F}_k$ is the predicted hand grasp force, $\bar{F}_k$ is the average of actual hand grasp force, and N is the number of testing data.

This method is identical with the above method in output and selection of training/testing data.

Fatigue feature driving machine learning method (FMLM, as shown in Figure 8): train the BPNN with estimated muscle fatigue value as an additional attribute. An additional input of the degree of muscle fatigue estimated by using (3) in combination with the RMS features is provided to the BPNN and expressed as

$$\left[RMS_{i \times n}, MFL_{i \times n}\right], \tag{6}$$

where i is the channel and n is the number of window shift. The output and selection method of training/testing data remain the same for all methods, as shown in the following three figures.

All methods adopt the BPNN architecture for force estimation, whose performance is dependent on the choice of network structure, training data, and testing data. The network structure is adjusted by setting different number of nodes from 2 to 20 in the hidden layer with the optimal results [24] provided by a three-layer BPNN. And a Log-Sigmoid function is selected as the transfer function in the network.

$$S(x) = \frac{1}{1 + e^{-x}}, \tag{7}$$

where x is the input and e is the exponential function. Moreover, a four-fold cross validation is adopted to avoid random classification of training data and test data from affecting the prediction results, which helps ensure the reliability and stability of the model.
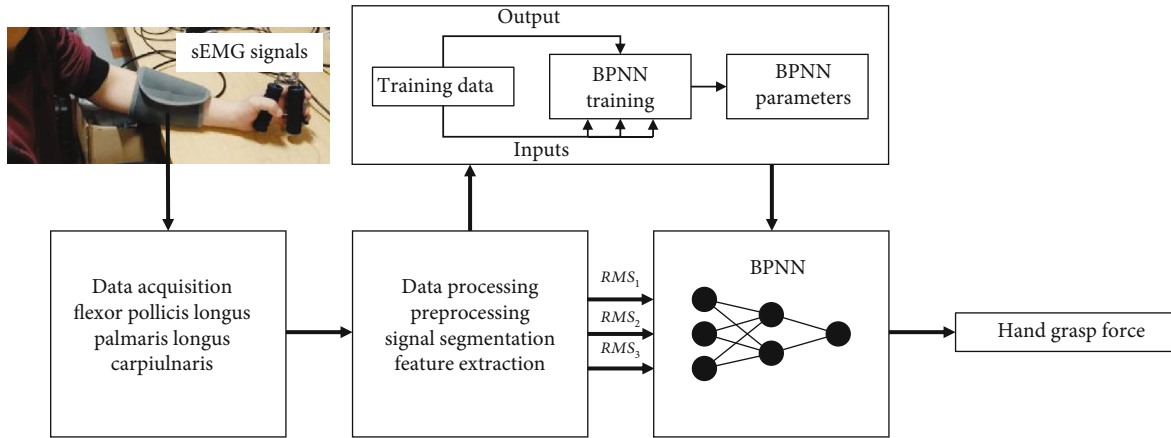
FIGURE 6: Flowchart of grasp force estimation—TMLM.
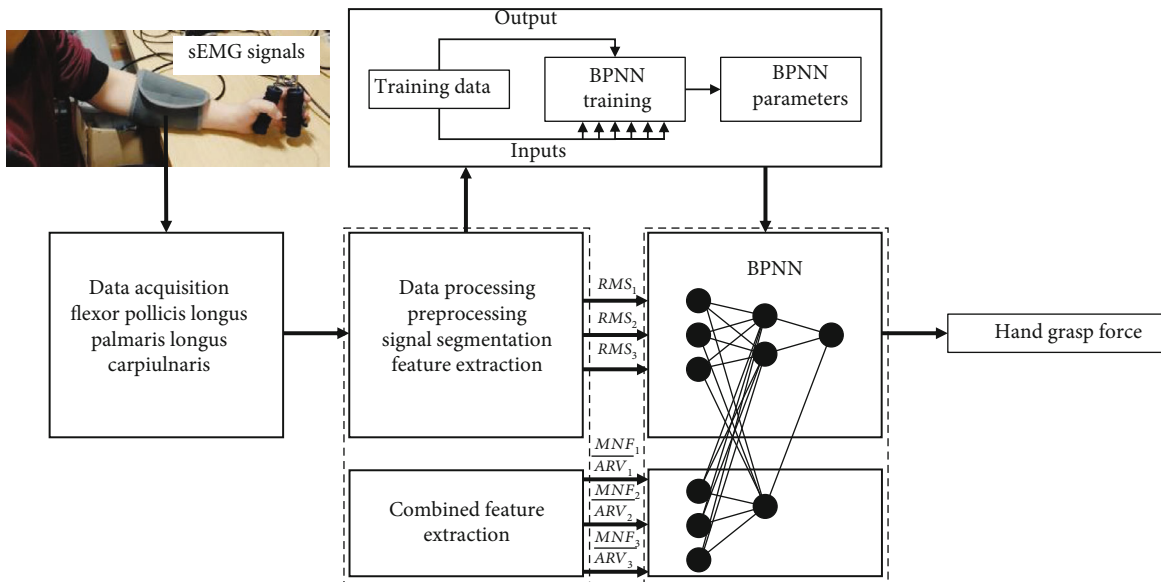
FIGURE 7: Flowchart of grasp force estimation—CMLM.
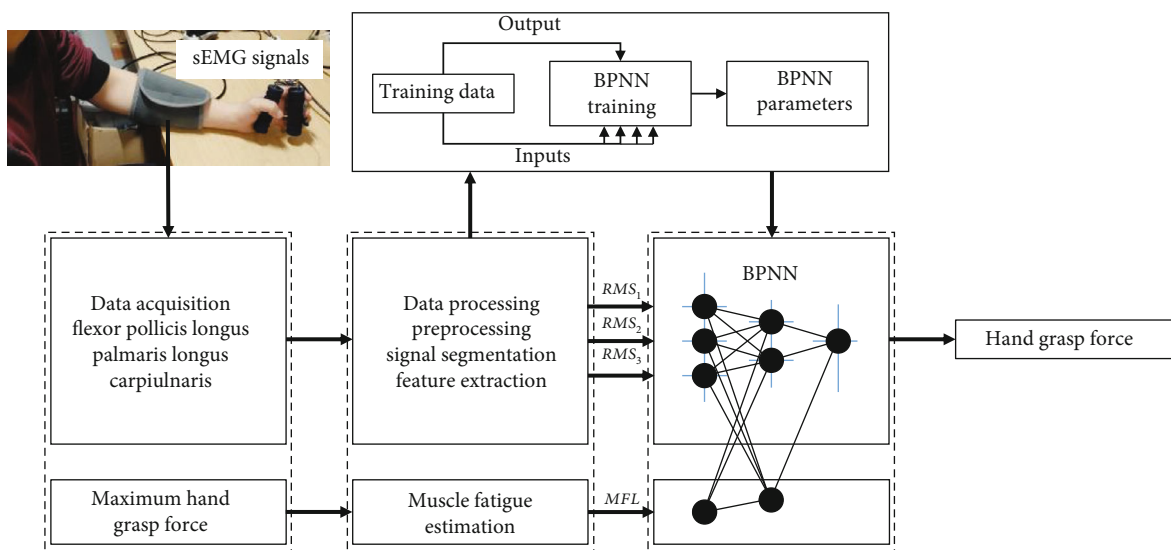
FIGURE 8: Flowchart of grasp force estimation—FMLM.
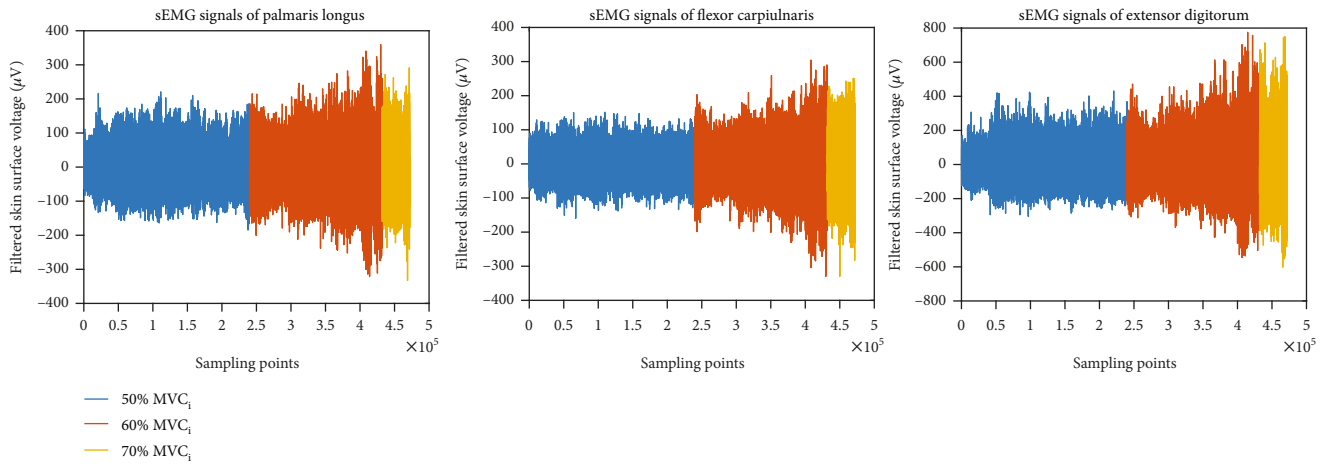
(a)
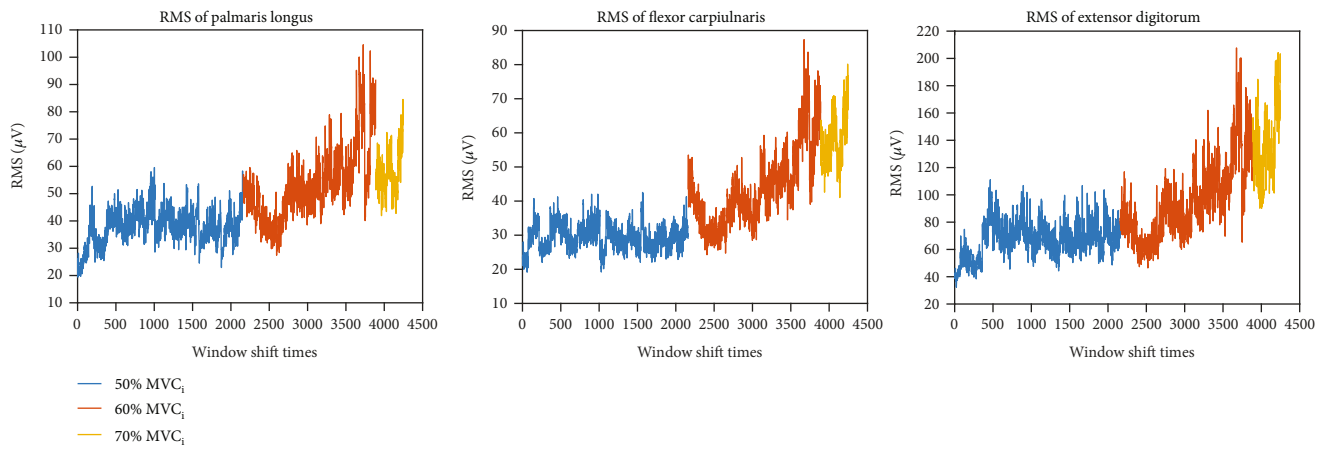
(b)
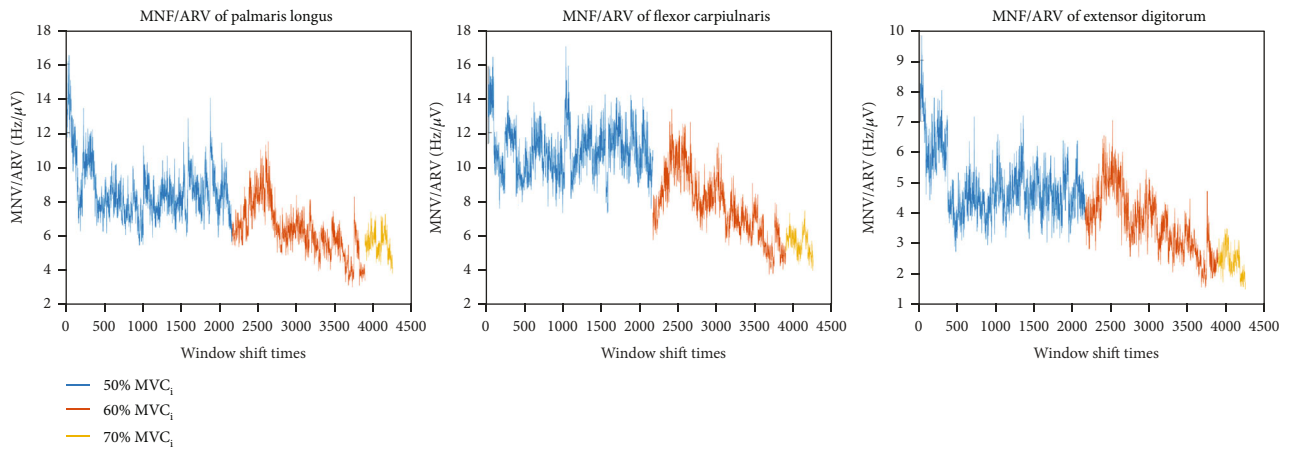
(c)

Figure 9: Continued.

(d)
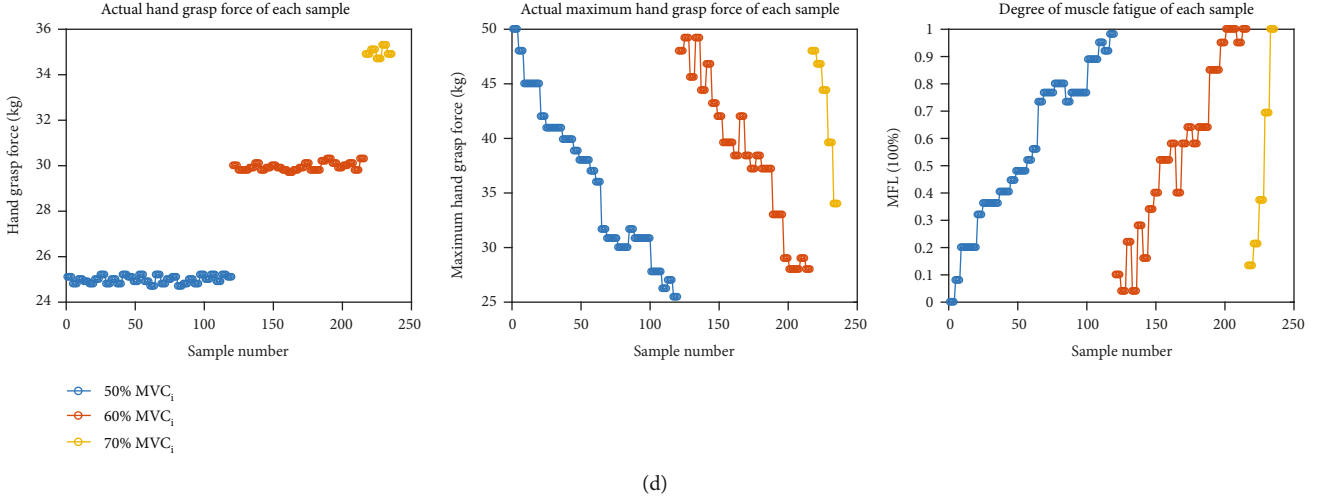
Figure 9: Data of static contraction tasks. (a) sEMG signals of three muscles. (b) RMS of three muscles. (c) MNF/ARV of three muscles (d) actual hand grasp force, maximum hand grasp force, and MFL.
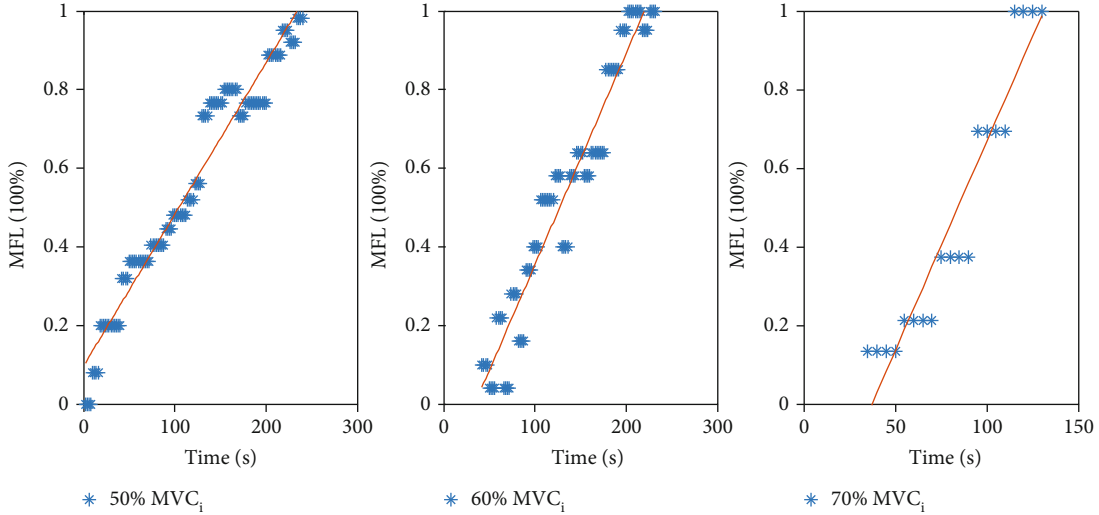
Figure 10: Muscle fatigue estimation results. Solid lines are linear fitting of the estimation.

In this study, R^2 is used to evaluate the estimation performance of three methods, which can be expressed as

$$R^2 = 1 - \frac{\sum_{i=1}^{N}(F_i - F\wedge_i)^2}{\sum_{i=1}^{N}(F_i - \bar{F}_i)^2}. \quad (8)$$

The R^2 can be comprehended as the percentage of the response variable variation that is explained by a linear model [25] and ranges from 0 to 1. In general, the higher the R^2, the better the model fits the data.

T-tests were used to verify differences in TMLM, CMLM, and FMLM between different conditions. Differences among subjects are not considered in this paper, as muscle-level dynamic variation is commonly existed. $p < 0.05$ is considered statistically significant for all tests.

Table 1: Gradient of MFL.

MVC_f	50% MVC_i	60% MVC_i	70% MVC_i
Gradient	0.0077	0.0108	0.0532

4. Results and Discussion

In this paper, an algorithm to quantitatively estimate the degree of muscle fatigue is introduced. And the effect of muscle fatigue on hand grasp force estimation is evaluated by conducting three distinct comparison methods. The experimental results of one subject are shown in Figure 9. They are sEMG signals, RMS, and MNF/ARV of three muscles in different levels of static contraction tasks, actual hand grasp force, maximum hand grasp force, and MFL of each sample in different levels of static contraction tasks. These selected features, seen in Figure 10, can basically reflect the force and muscle fatigue information.

Table 2: R^2 (mean ± sd) of predictions in TMLM.

Number of nodes	2	3	4	5	6
R^2 (mean ± sd)	0.6530 ± 0.0314	0.7037 ± 0.0037	0.9093 ± 0.0205	0.6933 ± 0.0083	0.4682 ± 0.0949
Number of nodes	7	8	9	10	11
R^2 (mean ± sd)	0.8328 ± 0.0095	0.8201 ± 0.0013	0.7978 ± 0.0311	0.7738 ± 0.0183	0.8610 ± 0.0406
Number of nodes	12	13	14	15	16
R^2 (mean ± sd)	0.8259 ± 0.0007	0.7103 ± 0.0074	0.7561 ± 0.0273	0.6653 ± 0.0170	0.6531 ± 0.0713
Number of nodes	17	18	19	20	
R^2 (mean ± sd)	0.7817 ± 0.0211	0.8261 ± 0.0021	0.8156 ± 0.0076	0.8033 ± 0.0145	

Table 3: R^2 (mean ± sd) of predictions in CMLM.

Number of nodes	2	3	4	5	6
R^2 (mean ± sd)	0.7321 ± 0.0599	0.8357 ± 0.0081	0.7897 ± 0.0276	0.9255 ± 0.0063	0.6594 ± 0.1223
Number of nodes	7	8	9	10	11
R^2 (mean ± sd)	0.7623 ± 0.0132	0.6229 ± 0.0818	0.6648 ± 0.0049	0.7149 ± 0.0563	0.7281 ± 0.0218
Number of nodes	12	13	14	15	16
R^2 (mean ± sd)	0.7579 ± 0.0357	0.7932 ± 0.0026	0.5954 ± 0.0214	0.4769 ± 0.1373	0.8362 ± 0.0035
Number of nodes	17	18	19	20	
R^2 (mean ± sd)	0.7074 ± 0.0104	0.6305 ± 0.0201	0.5928 ± 0.0450	0.7207 ± 0.0422	

Table 4: R^2 (mean ± sd) of predictions in FMLM.

Number of nodes	2	3	4	5	6
R^2 (mean ± sd)	0.8158 ± 0.0096	0.8663 ± 0.0220	0.8425 ± 0.0055	0.9193 ± 0.0185	0.8356 ± 0.0149
Number of nodes	7	8	9	10	11
R^2 (mean ± sd)	0.8343 ± 0.0205	0.8795 ± 0.0016	0.8746 ± 0.0127	0.9572 ± 0.0030	0.8842 ± 0.0122
Number of nodes	12	13	14	15	16
R^2 (mean ± sd)	0.8312 ± 0.0474	0.8652 ± 0.0018	0.8892 ± 0.0017	0.7465 ± 0.1342	0.7358 ± 0.0545
Number of nodes	17	18	19	20	
R^2 (mean ± sd)	0.8272 ± 0.0143	0.8100 ± 0.0063	0.7836 ± 0.0054	0.8472 ± 0.0010	

Table 5: Prediction results of three different methods.

Method	TMLM	CMLM	FMLM
Number of nodes	4	5	10
R^2 (mean ± sd)	0.8782 ± 0.0005	0.9065 ± 0.0011	0.9506 ± 0.0009

4.1. Results of Muscle Fatigue Estimation. The experiments last for 300 s, 240 s, and 50 s corresponding to 50% MVC_i (250 N), 60% MVC_i (300 N), and 70% MVC_i (350 N kg) in static contraction tasks, respectively. Figure 10 shows the estimation results of muscle fatigue by the proposed method. Dot arrays of different colors represent the estimation results at different force levels. Through linear fitting, it can be directly seen that MFL grows linearly with the increase of contraction time, which is in accordance with Vøllestad's assumption [12] of muscle fatigue's variety law during a sustained and steady contraction. In addition, the results show that the gradient of time-varying MFL varies at different levels of static contraction. The greater the required force becomes in static contraction, the faster MFL rises, shown in Table 1, which implies that the task intensity can also be distinguished through the proposed metric. The feasibility of the proposed method is recognized in static contraction tasks to estimate muscle fatigue quantitatively.

4.2. Results of Hand Grasp Force Estimation. In order to weaken effect of network structure, initial weights, and bias values on the estimation performance, the neural network is retrained ten times at different numbers of nodes (from 2 to 20) in the hidden layer.

(a)

(b)

(c)
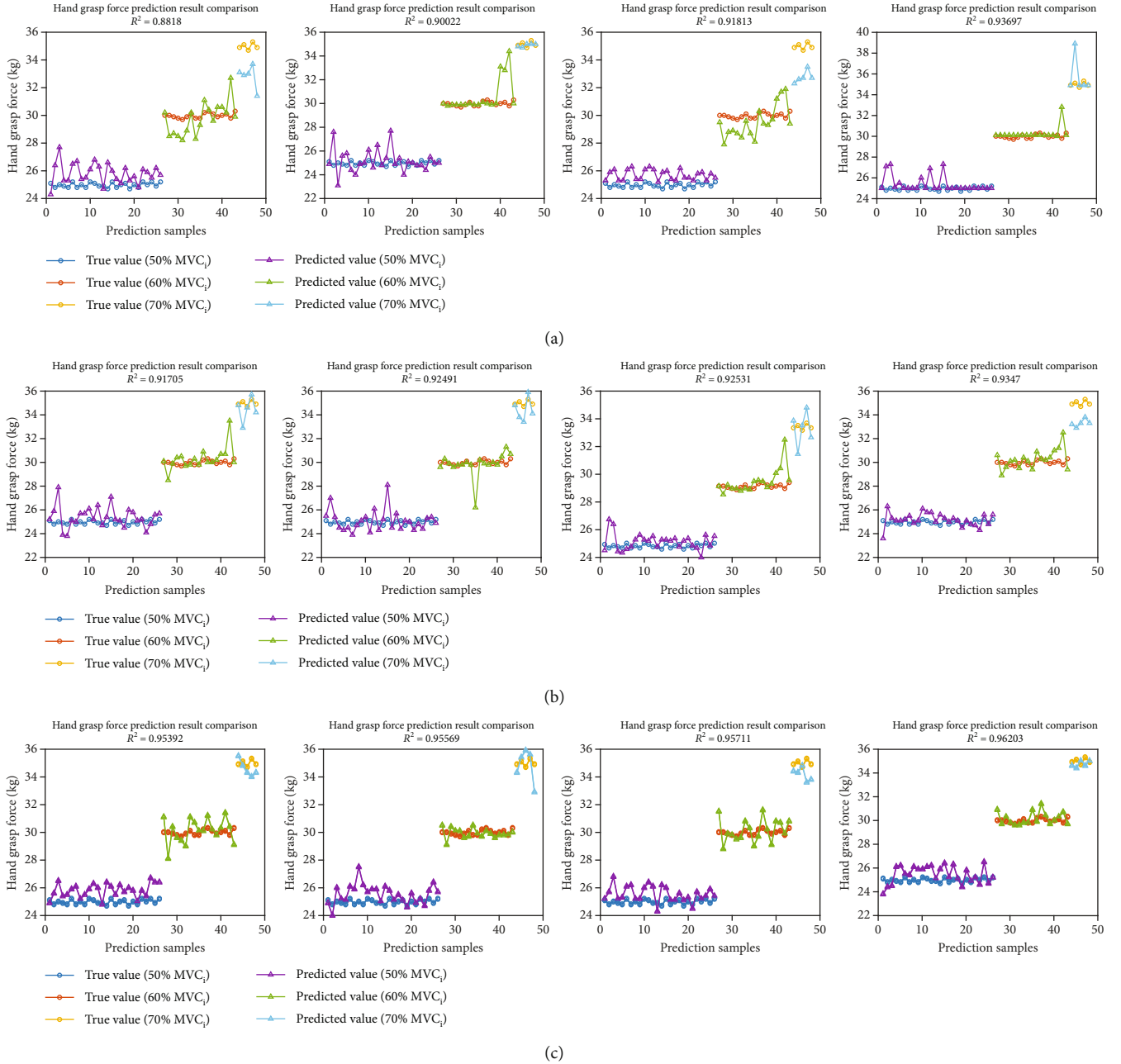
FIGURE 11: Single four-fold cross-validation results of each method (a) TMLM. (b) CMLM. (c) FMLM.

In TMLM, we pool training data from all muscle fatigue states to make the network learn the differences among them alone. Predictions of BPNN are shown in Table 2. When the number of node is 4, the mean R^2 is 0.9093, which is the maximum.

In CMLM, we employ MNF/ARV, one feature proposed by Fernando's team for the expression of muscle fatigue information. Predictions of BPNN are shown in Table 3. We set 5 nodes in the hidden layer, and the mean R^2 of prediction results is 0.9255.

In FMLM, we incorporate the quantitative metric of muscle fatigue value as an additional input to explain the effect of muscle fatigue on hand grasp force estimation. Predictions of

BPNN are shown in Table 4. The network structure of 10 nodes in the hidden layer brings the maximum mean R^2. Its value is 0.9572.

Comparing the best prediction results of three different methods, as shown in Table 5 and Figure 11, it can be indicated that the mean R^2 obtained in TMLM is 0.9093. It just passes the baseline of applicability (0.9000), which implies the estimation performance of the BPNN model in TMLM is not good enough and predicting model need to be readjusted. In CMLM, the mean R^2 is 0.9255. This shows that employing MNF/ARV proposed by Fernando et al. [13] in sEMG-based force estimation under fatigued conditions is indeed feasible. But it is not an obviously

TABLE 6: R^2 (mean ± sd) of predictions of all subjects under three methods.

Method	TMLM	CMLM	FMLM
Subject 1	0.9093 ± 0.0205	0.9255 ± 0.0063	0.9572 ± 0.0030
Subject 2	0.8910 ± 0.0092	0.9210 ± 0.0039	0.9548 ± 0.0009
Subject 3	0.8255 ± 0.0043	0.8517 ± 0.0064	0.8938 ± 0.0189
Subject 4	0.8224 ± 0.0042	0.8464 ± 0.0049	0.8805 ± 0.0028
Subject 5	0.8286 ± 0.0012	0.8571 ± 0.0014	0.9070 ± 0.0190
Subject 6	0.9293 ± 0.0132	0.9411 ± 0.0209	0.9554 ± 0.0182
Subject 7	0.9199 ± 0.0126	0.9262 ± 0.0050	0.9426 ± 0.0181
Subject 8	0.8802 ± 0.0431	0.9359 ± 0.0088	0.9438 ± 0.0088
Subject 9	0.8153 ± 0.0268	0.8526 ± 0.0131	0.8753 ± 0.0267
Subject 10	0.8350 ± 0.0097	0.8620 ± 0.0130	0.8983 ± 0.0121

effective approach. Compared with the result in TMLM, R^2 increases by 1.7816%.

As the main work of this study, the estimated muscle fatigue value is used directly as an additional input in FMLM. The results show mean R^2 can reach to 0.9572, which proves predicting model fits the data very well. It is a great improvement (5.2678%, above 5%, $p < 0.05$) in estimation performance compared with CMLM. It is demonstrated that the additional attribute is an applicable solution to the effect of muscle fatigue on sEMG-based hand grasp force estimation. And MFL proposed in this paper is better than MNF/ARV ($p < 0.05$).

For further explanation, the experimental results of all subjects under different methods are presented as shown in Table 6. Statistics show that the mean R^2 values obtained under the three methods are 0.8656, 0.8919, and 0.9209. Adopting MNF/ARV proposed in [12] for measure muscle fatigue could bring the 3.0383% growth in R^2 in hand grasp force estimation. For comparison, using the MFL proposed in this paper can increase R^2 by 6.3797%.

The experimental results show that FMLM provides the best estimation performance among the three methods.

5. Conclusion

In this paper, we propose an easy-to-implement method to quantitatively estimate muscle fatigue and evaluate the effect of muscle fatigue on hand grasp force estimation. The experiment results demonstrate that the incorporation of muscle fatigue metrics explicitly in the grasp force estimation has a substantial impact on the performance. When estimated muscle fatigue value as an additional input in the machine learning approach, the estimation accuracy improves to a large extent in FMLM. Because the neural network is trained offline and is computationally cheap, the proposed method can be implemented in the current applications, such as in [1–3], as a calibration part to improve the effectiveness and robustness. At the same time, there are still some limitations in this study. During the experiments mentioned above, the degree of the subject's forearm muscle fatigue needs to be estimated at each moment, which requires to intermittently measure the subject's current maximum grasp force. As a result, the force estimation in this work could only be processed offline. So the future work is mainly to address how to estimate muscle fatigue online, that is, how to get MFL online. In fact, the results of this study have provided some potential and guiding ideas for the following work. Under static muscle contraction, the subject's forearm muscle fatigue and muscle contraction time are approximately linear when maintaining a fixed level of hand grasp force. And this linear coefficient seems to have a nonlinear increasing relationship with the target hand grasp force level. Therefore, a nonlinear estimation model of muscle fatigue could be more appropriated in this case, such as

$$MFL = \left(a \times e^{b \times n\%MVC} \right) \times t + c, \qquad (9)$$

where $n\%MVC$ is the target hand grasp force level. t is muscle contraction time. a, b, and c are model parameters.

Data Availability

The EMG and force data used to support the findings of this study are available from the corresponding author upon request.

Conflicts of Interest

The author(s) declare(s) that they have no conflicts of interest.

Acknowledgments

References

[1] Y. Yamanoi, S. Morishita, R. Kato, and H. Yokoi, "Development of myoelectric hand that determines hand posture and estimates grip force simultaneously," *Biomedical Signal Processing and Control*, vol. 38, pp. 312–321, 2017.

[2] M. Kim, J. Lee, and K. Kim, "Tele-operation system with reliable grasping force estimation to compensate for the time-varying sEMG feature," in *2016 IEEE International Conference on Robotics and Automation (ICRA)*, pp. 5561–5567, Stockholm, Sweden, 2016.

[3] L. Peternel, N. Tsagarakis, D. Caldwell, and A. Ajoudani, "Robot adaptation to human physical fatigue in human–robot co-manipulation," *Autonomous Robots*, vol. 42, no. 5, pp. 1011–1021, 2018.

[4] C. Choi, S. Kwon, W. Park, H. D. Lee, and J. Kim, "Real-time pinch force estimation by surface electromyography using an artificial neural network," *Medical Engineering & Physics*, vol. 32, no. 5, pp. 429–436, 2010.

[5] C. Castellini, E. Gruppioni, A. Davalli, and G. Sandini, "Fine detection of grasp force and posture by amputees via surface electromyography," *Journal of Physiology-Paris*, vol. 103, no. 3-5, pp. 255–262, 2009.

[6] A. Erdemir, S. McLean, W. Herzog, and A. J. van den Bogert, "Model-based estimation of muscle forces exerted during movements," *Clinical biomechanics*, vol. 22, no. 2, pp. 131–154, 2007.

[7] U. J. Naeem, C. Xiong, and A. A. Abdullah, "EMG-muscle force estimation model based on back-propagation neural network," in *2012 IEEE International Conference on Virtual Environments Human-Computer Interfaces and Measurement Systems (VECIMS) Proceedings*, pp. 222–227, Tianjin, China, 2012.

[8] D. Yang, J. Zhao, Y. Gu, L. Jiang, and H. Liu, "Estimation of hand grasp force based on forearm surface EMG," in *2009 International Conference on Mechatronics and Automation*, pp. 1795–1799, Changchun, China, 2009.

[9] B. Zhang and S. Zhang, "Pattern-based grasping force estimation from surface electromyography," in *2017 International Conference on Algorithms, Methodology, Models and Applications in Emerging Technologies (ICAMMAET)*, pp. 1–5, Chennai, India, 2017.

[10] N. Jiang, S. Dosen, K.-R. Muller, and D. Farina, "Myoelectric control of artificial limbs—is there a need to change focus? [in the spotlight]," *IEEE Signal Processing Magazine*, vol. 29, no. 5, 2012.

[11] T. D. Lalitharatne, Y. Hayashi, K. Teramoto, and K. Kiguchi, "Compensation of the effects of muscle fatigue on EMG-based control using fuzzy rules based scheme," in *2013 35th Annual International Conference of the IEEE Engineering in Medicine and Biology Society (EMBC)*, pp. 6949–6952, Osaka, Japan, 2013.

[12] N. K. Vøllestad, "Measurement of human muscle fatigue," *Journal of Neuroscience Methods*, vol. 74, no. 2, pp. 219–227, 1997.

[13] J. B. Fernando, M. Yoshioka, and J. Ozawa, "Estimation of muscle fatigue by ratio of mean frequency to average rectified value from surface electromyography," in *2016 38th Annual International Conference of the IEEE Engineering in Medicine and Biology Society (EMBC)*, pp. 5303–5306, Orlando, FL, USA, 2016.

[14] M. Navaneethakrishna and S. Ramakrishnan, "Multiscale feature based analysis of surface EMG signals under fatigue and non-fatigue conditions," in *2014 36th Annual International Conference of the IEEE Engineering in Medicine and Biology Society*, pp. 4627–4630, Chicago, IL, USA, 2014.

[15] Y. Masakado, Y. Noda, K. Hase, A. Kimura, and N. Chino, "Muscle fatigue assessed by frequency analysis of surface electromyographic signals: topographical analysis in the same muscle," *The Japanese Journal of Rehabilitation Medicine*, vol. 31, no. 6, pp. 409–414, 1994.

[16] H. Xie and Z. Wang, "Mean frequency derived via Hilbert-Huang transform with application to fatigue EMG signal analysis," *Computer Methods and Programs in Biomedicine*, vol. 82, no. 2, pp. 114–120, 2006.

[17] T. Öberg, L. Sandsjö, and R. Kadefors, "Subjective and objective evaluation of shoulder muscle fatigue," *Ergonomics*, vol. 37, no. 8, pp. 1323–1333, 1994.

[18] H. Oka, "Estimation of muscle fatigue by using EMG and muscle stiffness," in *Proceedings of 18th Annual International Conference of the IEEE Engineering in Medicine and*

[19] Biology Society*, pp. 1449-1450, Amsterdam, Netherlands, 1996.

[19] C. J. De Luca, "Use of the surface EMG signal for performance evaluation of back muscles," *Muscle & Nerve*, vol. 16, no. 2, pp. 210–216, 1993.

[20] Y. Fang and H. Liu, "Robust sEMG electrodes configuration for pattern recognition based prosthesis control," in *2014 IEEE International Conference on Systems, Man, and Cybernetics (SMC)*, pp. 2210–2215, San Diego, CA, USA, 2014.

[21] N. A. Shrirao, N. P. Reddy, and D. R. Kosuri, "Neural network committees for finger joint angle estimation from surface EMG signals," *Biomedical Engineering Online*, vol. 8, no. 1, p. 2, 2009.

[22] S. Suryanarayanan, N. P. Reddy, and V. Gupta, "Artificial neural networks for estimation of joint angle from EMG signals," in *Proceedings of 17th International Conference of the Engineering in Medicine and Biology Society*, pp. 823-824, Montreal, Quebec, Canada, 1995.

[23] Y. Koike and M. Kawato, "Estimation of dynamic joint torques and trajectory formation from surface electromyography signals using a neural network model," *Biological Cybernetics*, vol. 73, no. 4, pp. 291–300, 1995.

[24] O. Fujita, "Statistical estimation of the number of hidden units for feedforward neural networks," *Neural Networks*, vol. 11, no. 5, pp. 851–859, 1998.

[25] C. Hagquist and M. Stenbeck, "Goodness of fit in regression analysis – R2 and G2 reconsidered," *Quality and Quantity*, vol. 32, no. 3, pp. 229–245, 1998.

Research Article

Animal Experiment of a Novel Neurointerventional Surgical Robotic System with Master-Slave Mode

Keyun Liu,[1] Yuhua Jiang [ID],[2] and Youxiang Li[2]

[1]*Department of Intervention, Beijing Chaoyang Hospital, Capital Medical University, Beijing 100020, China*
[2]*Department of Interventional Neuroradiology, Beijing Neurosurgical Institute and Beijing Tiantan Hospital,*
 Capital Medical University, Beijing 100050, China

Correspondence should be addressed to Yuhua Jiang; jxy_200321@163.com

In order to inspect and improve the system performance of the neuro-interventional surgical robot and its effectiveness and safety in clinical applications, we conducted ten animal experiments using this robotic system. Cerebral angiography was performed on ten experimental animals, and various mechanical performance indicators, operating time, X-ray radiation dosage to the experimental animals and the experimenter, and arterial damage in the experimental animals were recorded when the robotic system completed cerebral angiography. The results show that the robotic system can successfully complete the cerebral angiography surgery, and the mechanical performance is up to standard. The operating time is almost the same as the physician's operating time. And the mean X-ray radiation dosage received by the experimental animals and experimenter was 0.893 Gy and 0.0859 mSv, respectively. There were no complications associated with damage to the vascular endothelium. The robotic system can basically complete the relevant assessment indicators, and its system performance, effectiveness, and safety in clinical applications meet the standards, basically meeting the requirements of clinical applications of neurointerventional surgery.

1. Introduction

Vascular disease is an important cause of human death, involving all types of arteries in the whole body, but the aorta, coronary artery, carotid artery, and cerebral artery are the main sites, so myocardial infarction and cerebral infarction become the main consequences of this vascular disease. In recent years, the incidence of cardiovascular and cerebrovascular diseases is increasing, gradually becoming the disease with the highest incidence, recurrence rate, and mortality [1, 2]. There are various treatment methods for vascular diseases, mainly divided into medical and surgical treatment. Among the various treatment methods, minimally invasive vascular interventional therapy with small trauma, fast recovery, and good healing has played an increasingly important role in the treatment of cardiovascular and cerebrovascular diseases and gradually becomes the best treatment method.

However, there are still bottlenecks that restrict the development of endovascular therapy, such as the difficulty of the operation technique, the risk of surgery caused by the low stability and precision of manual operation, radiation injury, the risk of leucopenia and cell carcinogenesis caused by radiation in the long term [3, 4], the fatigue and chronic injury of interventionalists caused by heavy protective equipment [5, 6], the difficulty in the training of vascular interventionalists, the less primary medical resources, and low level of vascular interventional practice. The vascular interventional robotic system can solve these problems very well. The robotic system can be operated with high precision and stability. It can isolate X-ray operation and avoid radiation. Meanwhile, it can be used for training by surgeons who have no prior experience in interventional surgery. A variety of robotic endovascular treatment systems are now available [7–13]. However, these systems are expensive and complex, with relatively homogeneous product positioning, and all have their own limitations.

Therefore, in collaboration with Beijing Institute of Technology, we have developed a master-slave robotic system for cardiovascular and cerebrovascular interventional

surgery with catheter-guidewire cooperative operation [14–18]. The robot system is divided into two parts: the master end is located outside the operating room, and the slave end is set in the operating room. The control signal is transmitted to the slave end through the doctor's operation at the console of the master end, and the operation is completed by the slave end. There is an accurate force feedback system on the operating handle of the master end, so the operator can accurately feel the change of resistance of the catheter and guidewire from the end, which increases the sense of presence of operation. The slave end device is equipped with a catheter controller and a guidewire controller to enable the catheter and guidewire to operate in concert and has a haptic feedback system. The slave end takes the form of multiple platform connection blocks on the same trajectory, and the platform connection blocks are used to secure a catheter controller or guidewire controller to control the axial movement of the catheter and guidewire on a single trajectory. Since multiple sliders are used to run on the same track, each slider runs at the same distance. The accuracy of catheter pushing and rotation is improved, and damage to the guidewire surface is reduced; all this makes interventional procedures or angiography safer and more maneuverable. Using master-slave operation, it avoids the need for the physician to operate directly under the X-ray, solving a number of problems caused by the physician's prolonged exposure to radiation. The device can also be used for simulation and training in vascular interventional procedures.

The robotic system is capable of performing a variety of vascular interventional procedures. At present, 10 cases of performance self-assessment, partial type testing, and animal testing have been completed. Through the analysis of the experimental process and results, we have further verified the feasibility and safety of the robot for clinical application, and the robot has achieved the same surgical quality as that of manual operation. This report describes the performance and safety of the robotic system in animal studies.

2. Materials and Methods

2.1. Materials

2.1.1. Experimental Animals. In this study, 10 Bama miniature pigs aged 3-4 months, weighing 15-20 kg, were provided by Fulong Tengfei Experimental Animal Base. The breeding conditions and environment met the requirements of animal experiments. The miniature experimental pigs were randomly selected from the same type of experimental pigs.

2.1.2. Experimental Equipment

(1) The robot of endovascular treatment is provided by Beijing Institute of Technology, which mainly includes a master manipulator and a slave robot arm

(2) Routine surgical equipment and vascular interventional surgical equipment and supplies are provided

by Beijing Tiantan Hospital, which mainly include the following equipment:

(a) Puncture needles: arterial puncture needles (TERUMO, Japan)

(b) Arterial sheath: 5 F femoral artery sheath (Cordis Corporation, USA)

(c) Guidewire: 0.035-inch hydrophilic film guidewire (TERUMO, Japan)

(d) Catheter: 5 F single-bend angiographic catheter, Y-valve (Cordis Corporation, USA)

(e) Microcatheter: Exel-14 microcatheters (Boston, USA)

(f) Microguidewire: 0.014-inch Transend platinum microguidewire (Boston, USA)

(g) Laboratory equipment: AXIOM Artis dBA DSA contrast machine, SIEMENS

(h) X-ray radiation dosimeters

2.1.3. Pharmaceutical Reagents

(1) Sodium pentobarbital injection powder (China Pharmaceutical Group Chemical Reagent Company)

(2) Heparin sodium injection (Shanghai Pioneer Pharmaceutical Company)

(3) Injectable thiopental sodium (Shanghai Xinya Pharmaceutical Co., Ltd.)

(4) Injectable penicillin sodium (Shanghai Pioneer Pharmaceutical Company)

(5) Gentamicin sulfate injection (Guangdong Otsuka Pharmaceutical Co., Ltd.)

(6) Sodium lactate ringer injection (Guangdong Otsuka Pharmaceutical Co., Ltd.)

(7) 5% dextrose injection (Shanghai Baxter Medical Supplies Co., Ltd.)

(8) Saline injection (Shanghai Baxter Medical Supplies Co., Ltd.)

(9) Iohexol injection (Shanghai Ansheng Pharmaceutical Co., Ltd.)

(10) 4% paraformaldehyde fixative solution

(11) Disposable aseptic waterproof transparent plastic cover

2.2. Methods

2.2.1. Anesthesia. Randomly selected test pigs should be injected intramuscularly with 3% pentobarbital sodium injection, 2-3 ml at a time for about 20 minutes; the injection volume and time should be changed according to the anesthesia condition.

2.2.2. Fixation. The auricular vein of pigs was selected for intravenous infusion. The experimental animals were fixed on the operating table, electrocardiographic monitoring was performed, and the inguinal area was routinely disinfected and covered with a sterile sheet.

2.2.3. Observation Indicators. (1) Accuracy, effectiveness, and stability indicators

(a) Whether the physician's console is ergonomic and capable of providing an operating platform that is consistent with the physician's habits

(b) The ability of the console to monitor all aspects of catheter and guidewire operation information, catheter and guidewire forces, catheter and guidewire position, and catheter and guidewire contact with blood vessels

(c) Whether the operating table handle is flexible and reliable and can provide force sensory feedback to the operator, making sure the procedure is carried out based on the catheter force sensing information, and the catheter force sensing information is used to determine the status of the procedure

(d) When the gear clamps the guidewire, it has a good fit and will not damage the coating on the guidewire surface

(e) The system must maintain synchronous action with the physician's operation, while also ensuring that the catheter advances in a supple manner

(f) The system, when installed on the operating table, should not interfere with the operation of the equipment around the operating table and has good operability

(g) Under the X-ray line, the system operates the movement of the guidewire catheter in the blood vessels of experimental animals, such as forward and backward movement and rotation and blood vessel superselection, which can accurately and in real time reflect the operation of the master end

(h) The system can deliver the catheter to the designated blood vessel in a precise and timely manner according to the doctor's instructions

(2) Safety index

(a) Ensure that the slave end of the robot is disinfected before each experiment, and the robot equipment can operate normally after disinfection. Meanwhile, the robot is equipped with a disposable sterile transparent plastic cover from the slave end equipment to ensure that each experimental operation is carried out under sterile conditions

(b) The risk of complications from endothelial damage during cerebral angiography with this robotic system is no more than 5% [19]

(c) Cerebral angiography time using the robotic system is not greater than the cerebral angiography time of the neurointerventionalists from different medical centers [20, 21]

(d) Experimenter and experimental animals were exposed to radiation doses no higher than 0.1 mSv and 1 Gy, respectively [22]

2.2.4. Experimental Procedure. (1) The team from Beijing Institute of Technology installed the sterilized robotic system in the catheterization laboratory and fixed the slave end on the operating table, operating the control platform handle to test the system for satisfactory performance. The sterilized robot is equipped with a disposable sterile plastic cover to ensure the whole experiment process is carried out in a sterile environment. Figure 1 shows the performance

(2) The sterilized 5 F single-bend angiographic catheter and 150 cm hydrophilic film guidewire were connected to the system; operating the control platform handle to control the guidewire and catheter for forward, backward, and rotational movements, guidewire and catheter movement performance is good as shown in Figure 2

(3) The experimental Bama small pig was anesthetized and fixed on the operating bed with a bandage, and the skin was prepared at the inguinal region with a diameter of 20 cm. After the inguinal area of the experimental animals was routinely disinfected and sterile treatment towels were laid, 5% lidocaine was applied to the area 3 cm below the groin for local infiltration anesthesia. The skin was cut open, the femoral artery was separated layer by layer, dissociated for about 1 cm, punctured with a puncture needle, and 5 F arterial sheath was placed (Figure 3)

(4) Adjusting the angle of the robotic system arm so that it is consistent with the inclined level of the 5 F arterial sheath, the end of the system catheter running track is approximately 3 cm from the arterial sheath to ensure that the catheter does not fold after entering the arterial sheath, which is located between the arterial sheath and the end of the track. The catheter was connected to high-pressure heparin saline, and the tip of the catheter was placed approximately 5 cm into the arterial sheath (Figure 4)

(5) Adjusting the operating table so that the guidewire and catheter are exposed under the X-ray, the doctor controls the operation handle at the operating table to keep the position of the catheter unchanged. Advancing the guidewire about 10 cm, the guidewire is seen to have entered the right iliac artery under the X-ray, rotating the head of the guidewire to point to the right. Keeping the relative position of the guidewire and catheter unchanged, while advancing the guidewire catheter, the guidewire and catheter enter the aortic arch along the abdominal thoracic aorta. Keeping the catheter position unchanged, the guidewire superselection into the right common carotid artery was controlled. Advancing the catheter along the guidewire, a suitable working position was selected, the guidewire was withdrawn, and cerebral angiography was performed, which shows good angiogram (Figure 5). The procedure is repeated 3 times, with the control handle repeatedly advancing the catheter

FIGURE 1: The manipulator arm of the slave end.

FIGURE 2: The manipulator arm of the slave end holding the guidewire.

FIGURE 3: Prepared experimental Bama small pig.

FIGURE 4: The joint between the manipulator arm of the slave end and the femoral artery sheath.

and guidewire from the femoral artery into the abdominal aorta and then into the aortic arch and the common carotid artery. The robotic system can enter the relevant blood vessels accurately and on time each time to complete the relevant operation process

(a)   (b)

FIGURE 5: (a, b) The images of porcine cerebral angiography, respectively.

(6) The team from Beijing Institute of Technology removed the hydrophilic film guidewire from the robotic arm and attached the sterilized microcatheter and microguidewire to the system. Operating control platform handle to control the guidewire and catheter for forward, backward, and rotary movements, guidewire and catheter movement performance is good

(7) The microcatheter and the microguidewire were inserted into the single-curved angiographic catheter. Operating the handle of the platform to control the forward, backward, and rotating motion of the microguidewire and microcatheter in the single-curved angiography catheter (Figure 6), the motion performance of the microguidewire and the microcatheter was good after entering the single-curved angiographic catheter

(8) The microguidewire, microcatheter, and single-curved angiography catheter were removed, and the experimental animals were sacrificed by bloodletting (Figure 7). Samples of femoral artery, contralateral femoral artery, and bilateral common carotid artery at the puncture site were, respectively, taken for about 1 cm and fixed in 4% paraformaldehyde reagent

(9) Removing the robotic systems, operating rooms were cleaned and disinfected

(10) Paraffin-embedded specimens were cut into 4 to 7 μm thick sections, and three sections were made per specimen, HE-stained, and observed under an optical microscope

2.2.5. Experimental Data Collection. The following information were recorded in detail: name of experimenter, first assistant, second assistant, instrument nurse, technician and anesthesiologist, recorder, date of surgery, start time of surgery, end time of surgery, start time of anesthesia, end time of anesthesia, number of experimental animals, experiment weight of the animal, number of experiments, experimental time, time taken to switch guidewire catheters, experimenter X-ray radiation exposure, and adverse events. Some data on experimental animals are shown in Table 1.

FIGURE 6: The robot system controls the microguidewire and microcatheter movement.

FIGURE 7: Femoral artery pathology specimens from experimental animals.

2.2.6. Pathological Section. The following image shows a pathological section of a more severely damaged arterial wall. HE staining of the femoral artery at the site of femoral artery puncture in the first animal experiment shows a whole layer inflammatory response, endothelial cells, edema, subendothelial tissue, and fibrous hyperplasia. Red blood cells, lymphocytes, leukocytes, and lamellar fibrillar-like changes are seen in the arterial wall, suggesting thrombosis (Figure 8).

In the second animal experiment, HE staining of the artery wall of the right common carotid artery showed inflammatory proliferation of endothelial cells, infiltration of lymphocytes, and tissue cell and fibrinoid changes (Figure 9).

There were no associated complications due to endothelial injury in the ten animal studies, which is less than the risk odds of complications due to endothelial injury during human manipulation for cerebral angiography.

3. Results

We have conducted ten animal experiments using this endovascular therapy robotic system, and the robotic system was able to successfully complete the manipulation of the guidewire and catheter into the common carotid artery for cerebral angiography. We recorded the process and results of each experiment in detail and evaluated the system performance, effectiveness, and safety of the robot system in clinical application. The results are as follows.

(1) The system is capable of accurately and timely realizing the forward, backward, and rotational motion of a single-curved angiographic catheter and 150 cm hydrophilic film guidewire in the vasculature of experimental animals under master operation. The gear with the microguidewire and microcatheter can basically complete the forward and rota-

tion motion in the single-curved angiography catheter. The system can achieve the following indicators:

(a) The maximum distance of catheter pushing is 1.2 m. The accuracy of axial position detection is not less than 0.1 mm, the maximum speed is <5 cm/s, rotation accuracy not less than 5°, maximum speed of rotation < 180°/s, and switching time less than 3 min

(b) The disposable sterile transparent plastic cover ensures that the operating system of the slave end is sterile during the experiment. The time of cleaning and sterilization is less than 1 h

(c) The time of switching catheter and guidewire is less than 3 min

(d) DSA equipment will not affect the robot stability

(e) The robot can control the catheter to enter any branch vessel with an inside diameter of >3 mm and an angle of <90° to the trunk

(2) The slave end system is capable of delivering catheters into designated vessels in experimental animals in a precise and timely manner in accordance with physician instructions

(3) The console handle provides force feedback to the operator, enabling the operation to sense the status of the catheter, guidewire, microcatheter, and microguidewire. Then, according to the feedback sensory information, proceed to the next step

(4) The master end of the robot operating system basically meets the requirements of ergonomics

(5) Ten animal cerebral angiograms were performed using this robotic system without complications related to endothelial damage to the vasculature. The average operation time of 38.8 minutes is almost the same as the time of cerebral angiography operation by the neurointerventionalists from different medical centers. The average time to switch the catheter and guidewire was 2.8 minutes. The average radiation dose of experimental animals and experimenters was 0.893 Gy and 0.0859 mSv, respectively

4. Discussions

With the advancement of minimally invasive interventional equipment and interventional-related technologies, vascular interventional surgery has developed rapidly. However, the accuracy and stability of manual operation cannot meet the requirements of the rapidly developing vascular interventional technology, and interventionalists have long faced the problem of X-ray radiation and the inconvenience of wearing heavy protective clothing which have limited the development of interventional vascular procedures. The vascular intervention robotic system solves these problems well. There are several interventional vascular robotic systems available, but they differ greatly in terms of design philosophy and the real-world problems they solve [23–26]. Therefore, we designed this master-slave vascular interventional robot with catheter-guidewire cooperative operation according to the actual clinical needs. The system improves the accuracy

TABLE 1: Partial experimental data.

Number	Date of operation	Animal body weight	Time of operation takes	Time of switching the guidewire catheter	Experimenter X-ray radiation dose (mSv)	X-ray radiation levels in experimental animals (Gy)	Adverse event
1	2017.06.24	18 kg	45 min	4 min	0.11	1.1	Sputum interferes with breathing, give suctioning treatment
2	2017.07.29	17 kg	40 min	3.5 min	0.1	1	Sudden cardiac arrest and resuscitation
3	2017.10.21	15 kg	40 min	2.5 min	0.085	0.86	None
4	2017.10.21	18 kg	36 min	2.5 min	0.078	0.83	None
5	2018.06.23	17 kg	37 min	2 min	0.079	0.91	None
6	2018.07.28	20 kg	35 min	2.5 min	0.086	0.88	None
7	2018.08.18	19 kg	34 min	2 min	0.084	0.87	None
8	2018.09.23	18 kg	32 min	2 min	0.082	0.85	None
9	2018.10.20	19 kg	30 min	2 min	0.079	0.83	None
10	2018.11.17	18 kg	29 min	2 min	0.076	0.80	None
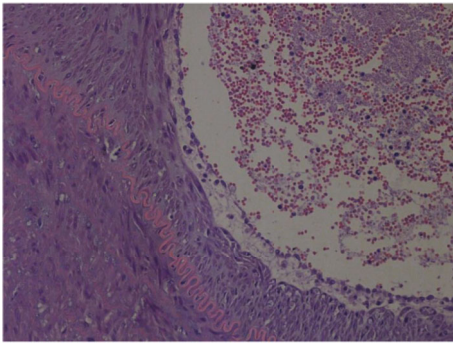
FIGURE 8: Pathological section of the femoral artery in the first experimental animal.
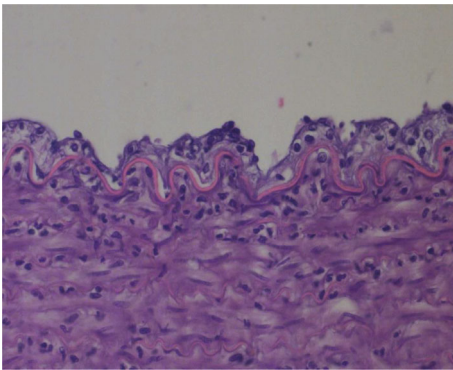
FIGURE 9: Pathological section of the right common carotid artery in the second experimental animal.

and stability of vascular interventions and frees the interventionalist from X-ray radiation.

The robotic vascular interventional surgical system has been repeatedly tested and improved on a human vascular model prior to animal testing. A number of improvements and optimizations have been made to the various performance indicators. Therefore, we conducted animal experiments to further investigate and improve the robotic system. The robotic system was investigated in terms of system performance, as well as validity and safety for clinical applications.

The mechanical specifications of the robot are the basis for all operations, and we must ensure that the mechanical performance of the robot system is not compromised in different environments. Therefore, we used this robotic system to repeatedly test the mechanical properties in the vessels of experimental animals. We ran at least three tests in different vessels in each animal. In 10 animal experiments, the speed and precision of the forward, backward, and rotation of the guidewire and catheter controlled from the slave end were continuously adjustable. Simultaneously, the catheter and guidewire can cooperate with each other and be delivered at the same time, which can precisely and appropriately realize the movement of single-curved angiography catheter and hydrophilic film guidewire in the animal's blood vessels, such as forward, backward, and rotation. Its feasibility, accuracy, and stability are up to standard. Compared with manual operation, its accuracy and stability are better, which meet the requirements of clinical vascular interventional surgery.

The effectiveness and safety of robotic systems for clinical applications are mainly focused on the sterile handling of the system, the integration with the surgical environment, and the absence of harm to the patient.

In vascular interventional surgery, the catheter needs to be continuously injected with saline solution to prevent the blood flow from forming blood clots and causing vascular embolism complications. Therefore, the slave end needs to be waterproofed. At the same time, vascular interventional procedures need to be performed in a sterile environment. So we add a disposable, sterile, waterproof, and transparent membrane to the slave end, which can not only isolate the damage of normal saline to the slave end but also achieve the effect of sterilizing.

When the slave end is fused with the surgical environment, the direction of movement of the guidewire and

catheter clamped by the slave end is not the same as the direction of the arterial sheath where the femoral artery is disposed. Consistently, this problem has always plagued us. After continuous experiments and improvements, we designed a special transparent sleeve that can be connected and fixed to the arterial sheath. At the same time, we added a robot arm angle-dependent adjustment device to the slave end so that the angle of the catheter guidewire entering the arterial sheath is consistent with the angle of the arterial sheath inclination.

The safety of vascular interventional procedures is mainly due to the fact that the interventional device does not cause damage to the vessel wall, which can lead to corresponding complications. After each experiment, the femoral artery, contralateral femoral artery, and bilateral common carotid artery specimens at the puncture site were collected and pathological sections were performed. The damage to the intima of the artery was observed. In the first animal experiment, due to the thin femoral artery in the experimental animals, it was difficult to puncture, and the damage to the wall of the femoral artery was greater, which belonged to human factor interference. None of the remaining animal experiments caused damage to the vascular wall, and none of them caused relevant complications.

There are still deficiencies in our experiments and robotic system. First of all, we have only conducted ten animal experiments, and we are still a long way from the application of robotic systems in the clinic, and we need more animal experiments, including further clinical trials. Secondly, for the safety evaluation of this robotic system, we only performed the evaluation of pathological sections of the vessel wall; there was no long-term observation of the postoperative situation of experimental animals. Finally, the robot system is currently in the stage of experimental development which has not been combined with DSA equipment.

5. Conclusions

The robot of neuro-interventional surgical has been continuously investigated and improved though 10 animal experiments. The robot system can realize the cooperative operation of the guidewire and the catheter and has a force feedback system with good accuracy and stability. And various mechanical performance indexes basically meet the needs of vascular intervention surgery. Meanwhile, the sterilization effect, integration with the operating environment, and safety index of the improved robotic system basically reach the standard.

Data Availability

The data of relevant parameters of the robot system used to support the findings of this study have not been made available because the robot system is in the development stage.

Conflicts of Interest

The authors declare that there are no conflicts of interest.

Authors' Contributions

Keyun Liu and Yuhua Jiang are the co-first authors.

Acknowledgments

References

[1] F. Jokar, H. Yousefi, A. Yousefy, and M. Sadeghi, "Begin again and continue with Life: A Qualitative Study on the Experiences of Cardiac Rehabilitation Patients," *The Journal of Nursing Research*, vol. 25, no. 5, pp. 344–352, 2017.

[2] J. Yong, L. Xiao-Yan, H. Nan, H. Zheng-Jing, and W. Fan, "Epidemiologic characteristics of cerebrovascular disease mortality in China, 2004-2005," *Zhonghua Yu Fang Yi Xue Za Zhi*, vol. 44, no. 4, pp. 293–297, 2010.

[3] Center for Devices and Radiological Health (CDRH), U.S. Food and Drug Administration (FDA), *Initiative to reduce unnecessary radiation exposure from medical imaging*, FDA, Silver Spring, MD, USA, 2010.

[4] K. P. Kim, D. L. Miller, S. Balter et al., "Occupational radiation doses to operators performing cardiac catheterization procedures," *Health Physics*, vol. 94, no. 3, pp. 211–227, 2008.

[5] L. W. Klein, D. L. Miller, S. Balter et al., "Occupational health hazards in the interventional laboratory: time for a safer environment," *Journal of Vascular and Interventional Radiology*, vol. 20, no. 2, pp. 147–152, 2009.

[6] N. L. Hughes, A. Nelson, M. W. Matz, and J. Lloyd, "AORN ergonomic tool 4: solutions for prolonged standing in perioperative settings," *AORN Journal*, vol. 93, no. 6, pp. 767–774, 2011.

[7] C. Pappone, G. Vicedomini, F. Manguso et al., "Robotic magnetic navigation for atrial fibrillation ablation," *Journal of the American College of Cardiology*, vol. 47, no. 7, pp. 1390–1400, 2006.

[8] V. Y. Reddy, P. Neuzil, Z. J. Malchano et al., "View-synchronized robotic image-guided therapy for atrial fibrillation ablation," *Circulation*, vol. 115, no. 21, pp. 2705–2714, 2007.

[9] B. Schmidt, K. R. J. Chun, R. R. Tilz, B. Koektuerk, F. Ouyang, and K. H. Kuck, "Remote navigation systems in electrophysiology," *Europace*, vol. 10, Supplement 3, pp. iii57–iii61, 2008.

[10] P. Kanagaratnam, M. Koa-Wing, D. T. Wallace, A. S. Goldenberg, N. S. Peters, and D. W. Davies, "Experience of robotic catheter ablation in humans using a novel remotely steerable catheter sheath," *Journal of Interventional Cardiac Electrophysiology*, vol. 21, no. 1, pp. 19–26, 2008.

[11] B. Schmidt, R. R. Tilz, K. Neven, K. R. Julian Chun, A. Furnkranz, and F. Ouyang, "Remote robotic navigation and electroanatomical mapping for ablation of atrial fibrillation," *Circulation. Arrhythmia and Electrophysiology*, vol. 2, no. 2, pp. 120–128, 2009.

[12] O. M. Wazni, C. Barrett, D. O. Martin et al., "Experience with the Hansen robotic system for atrial fibrillation ablation-lessons learned and techniques modified: Hansen in the real

world," *Journal of Cardiovascular Electrophysiology*, vol. 20, no. 11, pp. 1193–1196, 2009.

[13] R. Bai, L. U. I. G. I. di Biase, M. Valderrabano et al., "Worldwide experience with the robotic navigation system in catheter ablation of atrial fibrillation: methodology, efficacy and safety," *Journal of Cardiovascular Electrophysiology*, vol. 23, no. 8, pp. 820–826, 2012.

[14] X. Bao, S. Guo, N. Xiao et al., "Operation evaluation in-human of a novel remote-controlled vascular interventional robot," *Biomedical Microdevices*, vol. 20, no. 2, p. 34, 2018.

[15] X. Bao, S. Guo, N. Xiao, Y. Li, C. Yang, and Y. Jiang, "A cooperation of catheters and guidewires-based novel remote-controlled vascular interventional robot," *Biomedical Microdevices*, vol. 20, no. 1, p. 20, 2018.

[16] Y. Zhao, S. Guo, N. Xiao, Y. Wang, Y. Li, and Y. Jiang, "Operating force information on-line acquisition of a novel slave manipulator for vascular interventional surgery," *Biomedical Microdevices*, vol. 20, no. 2, p. 33, 2018.

[17] Y. Wang, S. Guo, N. Xiao, Y. Li, and Y. Jiang, "Online measuring and evaluation of guidewire inserting resistance for robotic interventional surgery systems," *Microsystem Technologies*, vol. 24, no. 8, pp. 3467–3477, 2018.

[18] S. Guo, Y. Wang, N. Xiao, Y. Li, and Y. Jiang, "Study on real-time force feedback for a master-slave interventional surgical robotic system," *Biomedical Microdevices*, vol. 20, no. 2, p. 37, 2018.

[19] T. J. Kaufmann, I. I. I. John Huston, J. N. Mandrekar, C. D. Schleck, K. R. Thielen, and D. F. Kallmes, "Complications of diagnostic cerebral angiography: evaluation of 19 826 consecutive patients1," *Radiology*, vol. 243, no. 3, pp. 812–819, 2007.

[20] M. D. Kwang Wook Jo, M. D. Sung Man Park, M. D. Sang Don Kim, M. D. Seong Rim Kim, M. D. Min Woo Baik, and M. D. Young Woo Kim, "Is transradial cerebral angiography feasible and safe? A single center's experience," *Journal of Korean Neurosurgical Association*, vol. 47, no. 5, pp. 332–337, 2010.

[21] D. J. Hildick-Smith, J. T. Walsh, M. D. Lowe, L. M. Shapiro, and M. C. Petch, "Transradial coronary angiography in patients with contraindications to the femoral approach: an analysis of 500 cases," *Catheterization and Cardiovascular Interventions*, vol. 61, no. 1, pp. 60–66, 2004.

[22] ICRP, "Avoidance of radiation injuries from medical interventinal procedure," *ICRP Publication 85*, vol. 30, no. 2, pp. 7–67, 2000.

[23] M. Schiemann, R. Killmann, M. Kleen, N. Abolmaali, J. Finney, and T. J. Vogl, "Vascular guide wire navigation with a magnetic guidance system: experimental results in a phantom," *Radiology*, vol. 232, no. 2, pp. 475–481, 2004.

[24] W. Saliba, J. E. Cummings, S. Oh et al., "Novel robotic catheter remote control system: feasibility and safety of transseptal puncture and endocardial catheter navigation," *Journal of Cardiovascular Electrophysiology*, vol. 17, no. 10, pp. 1102–1105, 2006.

[25] E. M. Khan, W. Frumkin, G. A. Ng et al., "First experience with a novel robotic remote catheter system: Amigo™ mapping trial," *Journal of Interventional Cardiac Electrophysiology*, vol. 37, no. 2, pp. 121–129, 2013.

[26] M. N. Faddis, W. Blume, J. Finney et al., "Novel, magnetically guided catheter for endocardial mapping and radiofrequency catheter ablation," *Circulation*, vol. 106, no. 23, pp. 2980–2985, 2002.

Research Article

Design of a New Catheter Operating System for the Surgical Robot

Xu Ma [ID],[1] Jinpeng Zhou [ID],[1] Xu Zhang [ID],[2] Yang Qi,[2] and Xiaochen Huang[2]

[1]*Tianjin Key Laboratory for Control Theory & Applications in Complicated Industry Systems, College of Electrical and Electronic Engineering, Tianjin University of Technology, Tianjin, China 300384*
[2]*Tianjin Key Laboratory of High Speed Cutting and Precision Machining, School of Mechanical Engineering, Tianjin University of Technology and Education, Tianjin, China 300222*

Correspondence should be addressed to Xu Ma; maxu2015@aliyun.com and Xu Zhang; 52914262@qq.com

In interventional surgery, the manual operation of the catheter is not accurate. It is necessary to operate the catheter skillfully and effectively to protect the surgeon from radiation injury. The purpose of this paper is to design a new robot catheter operating system, which can help surgeons to complete the operation with high mechanical precision. On the basis of the original mechanical structure—real catheter, the operation information of the main end operator is collected. After the information is collected, the control algorithm of the system is improved, and the BP neural network is combined with the traditional PID controller to adjust the PID control parameters more effectively and intelligently so that the motor can reflect the output of the controller better and faster. The feasibility and superiority of the BP neural network PID controller are verified by simulation experiments.

1. Introduction

Vascular interventional surgery can be used not only for preoperative diagnosis but also for practical surgical treatment, which is expected to get more applications in future medical practice. However, the development of new technology needs a lot of basic technology support. In addition, because the operation is carried out in the patient, the real-time status cannot be directly monitored [1]. Often, a doctor with rich operation experience is required to insert the catheter manually. For example, in interventional surgery, the catheter is inserted through the patient's blood vessel. In this process, any small mistake will hurt the patient and cause vascular damage. According to experience, a mature neurosurgeon can achieve a surgical accuracy of about 2 mm. However, the contact force between blood vessels and catheters in the human body cannot be detected. However, if an X-ray camera is used during the operation, the long-term operation will cause radiation damage to patients. Moreover, although doctors wear protective clothing, it is difficult to protect their

bodies from radiation in the face of X-ray radiation. In order to overcome these problems, we need a better surgical plan and supporting equipment to help and train doctors. The advantages of a robot assistant system are high control precision and remote control. However, compared with the human hand, there is no robot-assisted system that can meet all the technical requirements of vascular interventional therapy.

In this respect, there are many similar application products and research results on the market. One of the popular products is called the da Vinci robot catheter pushing system [2]. The da Vinci system (see Figure 1) provides doctors with more system stability and greater force support during catheter pushing compared with manual tools and can prevent unnecessary radiation exposure to doctors during more precise operations [2].

The Sensei Xi system (see Figure 2) was certified by the FDA and CE, respectively, in 2007 [3]. The system is used for cardiovascular interventional surgery. Doctors can control the remote catheter robot to push the catheter by

Figure 1: The da Vinci system.

Figure 2: Sensei Xi system.

manipulating the force feedback device. The end of the catheter is equipped with a force sensor, which can let doctors feel the force of the catheter on the blood vessel wall so as to control the catheter.

The core function of the robot system is the propulsion and navigation of the catheter, as well as the force feedback and perception during the propulsion of the catheter. Beijing University of Aeronautics and Astronautics and Institute of Automation of the Chinese Academy of Sciences have carried out research on the propulsion mechanism and end force feedback of the conduit, but no product has been formed yet [4].

In this study, according to the technical requirements of vascular interventional surgery, we designed a new robotic
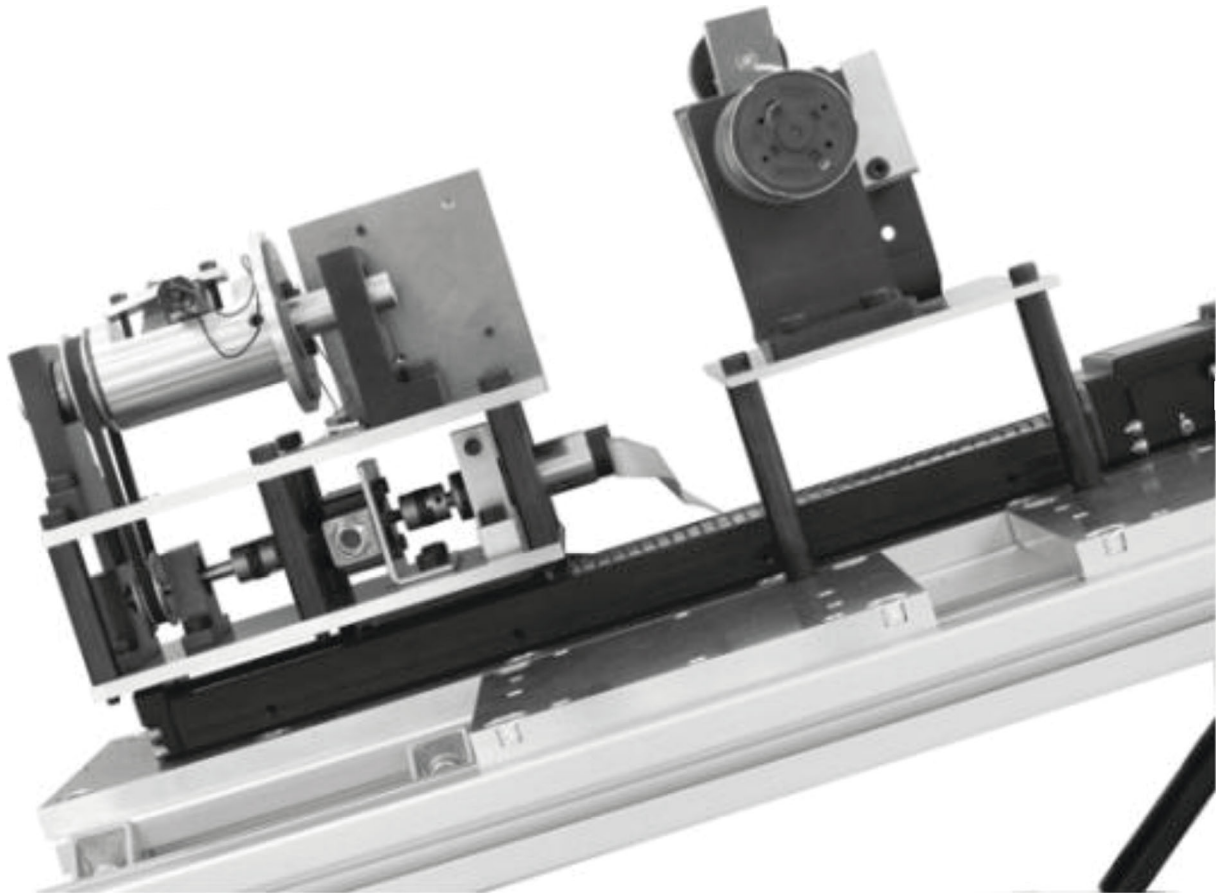
FIGURE 3: Slave end manipulator of the robot conduit control system.
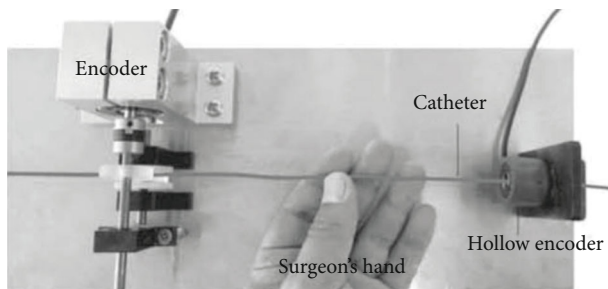
FIGURE 4: Main end manipulator of the robot conduit control system.

conduit control system [5]. Compared with the robot system mentioned above, our system has a slave consisting of a two-degrees-of-freedom conduit operation platform and a rotatable platform. The slave end is shown in Figure 3, which can complete the conduit turning and inserting operation. In addition, a newly developed force feedback measuring mechanism is developed from the slave end to measure the near side thrust generated when inserting the catheter and provide force feedback to the main end. The surgical robot system has a main end manipulator, as shown in Figure 4, which is called the surgeon's console. The console uses a real catheter instead of the mechanical handle of the previous

generation and uses a force sensor (UNCSR, UNIPULSE, Japan; ±nonlinearity 1.0%), torque sensor (OPT-563B, NMB, Japan; ±nonlinearity 0.01%F.S.), DC motor (AM11HS1008-07, MOONS', Japan; step angle accuracy ± 5 %), stepping motor (AR Series, Dongfang Electric Machinery, Japan; step angle 0.0036°), and DSP (Texas Ti, TMS320F28335, America) [6]. The communication determines the position and rotation angle of the conduit operated by the slave and provides force feedback to the console operator [7]. The BP neural network PID control algorithm is used to improve the accuracy and real-time manual control operation in the system.

2. Robot Conduit Operating System

The mechanical structure design of the surgical robot system is divided into two parts: the main end and the slave end. The surgeon's console is the main side of the system, and the catheter operating end is the slave end of the system. The design is to maintain the same displacement, speed, and rotation angle between the real catheter and the end catheter console [8]. As a result, surgeons can operate the system smoothly and easily. DSP is used as the control unit of each doctor console and catheter console. The doctor console and catheter console establish an Internet-based communication, and the schematic diagram of display communication
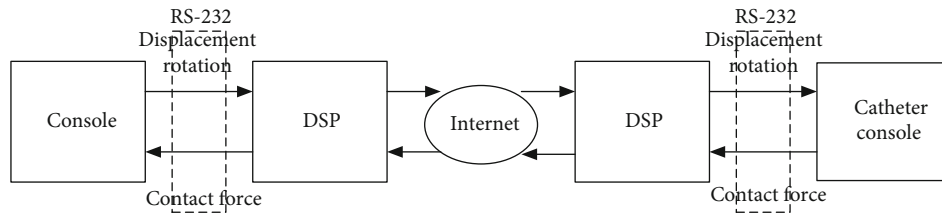
FIGURE 5: Communication diagram.
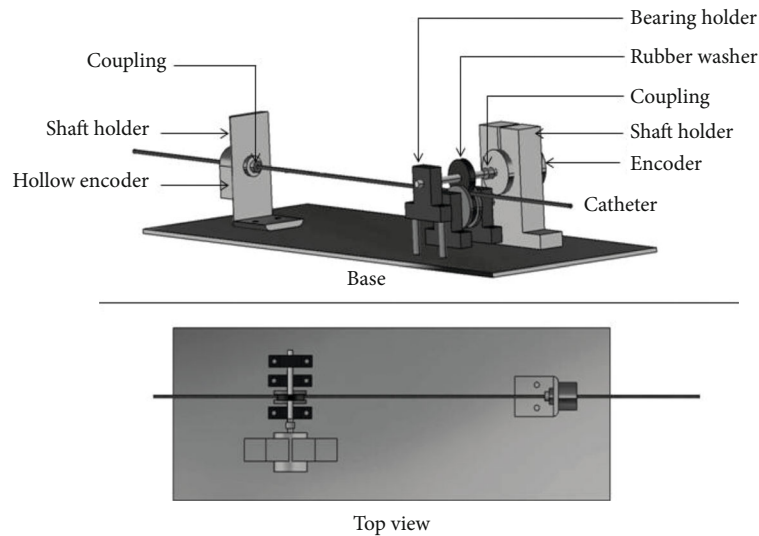
FIGURE 6: Surgeon's console.
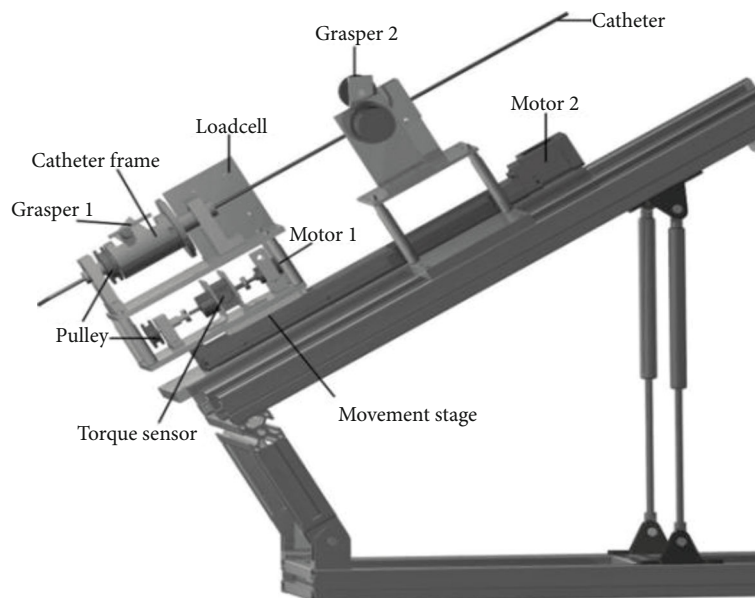
FIGURE 7: Slave end console.

is shown in Figure 5. The console at the main end sends the axial displacement and rotation angle of the operator to the operating end of the real catheter. At the same time, the operating end of the conduit sends the force signal back to the main end console. The serial communication adopts the communication mechanism of DSP and master-slave connection. The baud rate is set to 19200 B/s [9].

2.1. Main End Console. The surgeon's console is shown in Figure 6, called the surgeon's console. The surgeon's console
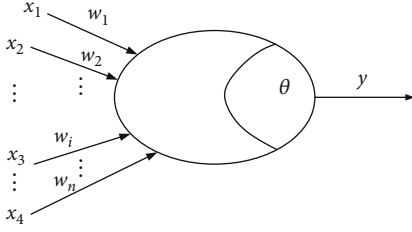
FIGURE 8: Artificial neuron model.

is the main end console, and the whole system is operated by experienced surgeons. The surgeons use the console to perform the operation and use the real catheter to collect the thrust value of the operator and the displacement value and rotation value of the catheter being pushed. The movable part of the operating end of the catheter keeps the same action as the real catheter of the main end. The real conduit is connected to the sensor through a pulley. A DC motor with an encoder is used to generate force-torque feedback, and the motor is fixed on the pulley.

2.2. Slave End Console. Figure 7 shows the slave end console. This part is next to the patient. The conduit is inserted by using this device. This part of the mechanical structure contains two degrees of freedom, one is the frame of axial independent motion, and the other is the rotating motion frame [10]. Two clips are installed in this part of the structure. When the surgeon drives the catheter to move and rotate along the axial direction through the main end console, the catheter is clamped by clamp 1, and the catheter maintains its position. When the conduit is clamped, the conduit driving part can move freely through clamp 2 and insert the conduit.

3. Control Algorithm

3.1. BP Neural Network PID Control Algorithm Introduction. Figure 8 shows a simple model of neuron operation, called the classic "M-P neuron model" [11]. In this model, neurons receive input signals from n other neurons connected by weighting. The total input value received by the neuron will be the threshold value of the neuron. The comparison is then processed by an "activation function" to produce the output of the neuron.

In order to improve the control effect of the traditional PID controller, many intelligent control algorithms are introduced, which are combined with the traditional PID controller to produce good results [12]. As a classical intelligent optimization algorithm, the BP algorithm has the advantages of distributed storage, parallel processing, and self-learning, which makes up for the shortcomings of the traditional PID controller. Therefore, BP and traditional PID control are combined to complement each other and optimize the control effect. The input and output samples are learned by the BP algorithm, and the weight value of the network is adjusted in real time so that the output is optimal. Especially for the servomotor system, the self-learning of the BP neural network comes from three important parameters of the PID

controller, which can effectively solve the problem that PID control parameters of the motor are difficult to adjust and that the whole system control cannot solve.

Figure 9 shows the block diagram of the BP neural network PID controller system. It is an organic combination of the traditional PID controller and BP neural network. The detailed analysis of each part is as follows.

3.1.1. BP Neural Network Part. The BP neural network is the core part of the BP neural network PID system [13]. Its main function is to adjust the weight coefficient of neurons through self-learning and adaptive ability of the BP algorithm, then adjust three parameters of the PID controller, and optimize the performance of the whole control system. The output signal of the input layer in the BP neural network corresponds to K_p, K_i, and K_d of the traditional PID controller. The parameter output is shown in Figure 10.

3.1.2. Traditional PID Part. The BP neural network is only an abstract optimization algorithm, and the actual control of the motor still depends on the traditional PID controller [14]. Therefore, the traditional PID part is an indispensable part of the BP neural network PID system. The specific control of the motor still depends on the closed-loop control of the traditional PID controller, so the speed output of the motor follows the input.

3.2. Algorithm Simulation. Taking the axial motion of the vascular intervention robot as an example, the dynamic analysis is carried out. Its axial movement is driven by Maxon ec32. The motor pushes the clamp of the whole clamping conduit to move back and forth, thus driving the conduit to move together. According to Newton's second law, the dynamic model of the axial motion of the intervention robot is established:

$$f(t) = m\ddot{x}(t) + c\dot{x}(t) + kx(t), \tag{1}$$

where $f(t)$ is the motor driving force, $x(t)$ is the displacement of this motion, $\dot{x}(t)$ is the motion velocity, and $\ddot{x}(t)$ is the motion acceleration, and formula (1) illustrates the relationship between motor drive force and output displacements.

If $x_1(t) = x(t)$ and $x_2(t) = \dot{x}(t)$, then

$$\begin{cases} \dot{x}(t) = AX(t) + Bu(t), \\ y(t) = CX(t), \end{cases} \tag{2}$$

where $X(t) = \begin{bmatrix} x_1(t) \\ x_2(t) \end{bmatrix}$, $A = \begin{bmatrix} 0 & 1 \\ -k/m & -c/m \end{bmatrix}$, $B = \begin{bmatrix} 0 \\ 1/m \end{bmatrix}$, and $C = \begin{bmatrix} 1 & 0 \\ 0 & 0 \end{bmatrix}$.

m is the mass of the overall axial movement of the push platform, c is the overall damping coefficient of the push platform, and k is the overall elastic coefficient of the push platform. From formula (3), it can be concluded that the
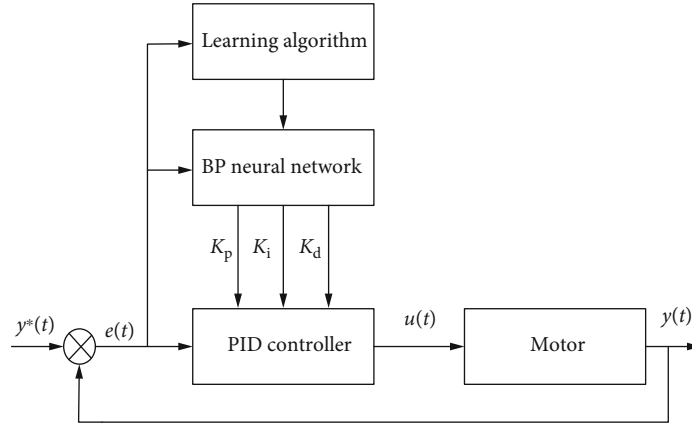
FIGURE 9: BP neural network PID control system.
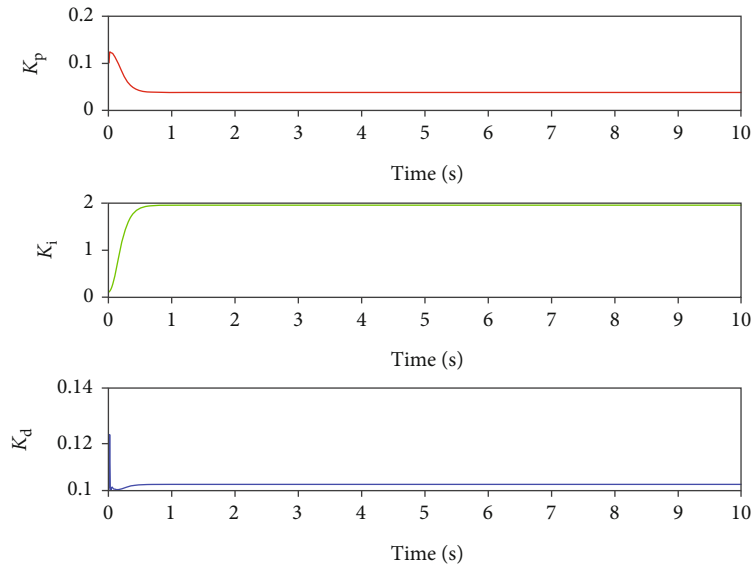
FIGURE 10: Intelligent adjustment output of parameters K_p, K_i, and K_d.

transfer function of the axial movement of the push device is

$$H(s) = \frac{m}{ms^2 + cs + k}. \tag{3}$$

3.3. Simulation Analysis. Taking the axial motion of the interventional robot as an example, the step signal $y = 1$ is used to simulate the expected axial displacement of the main hand catheter during the actual operation of the doctor [15]. Take formula (3), where $m = 1$ kg, $c = 0.05$ N/(m/s), and $k = 1.5$ N/m. After MATLAB simulation, the simulation results shown in Figure 11 are obtained and the results are in BP for comparison control effects.

Figure 11 is the simulation comparison between the BP neural network PID controller and the traditional PID controller. It can be seen from the results that the overshoot of the system is 20% under the traditional PID control and 12% under the BP neural network PID control. Compared with the traditional PID control, the adjustment time and response speed of the BP neural network PID control are

greatly improved. In the actual operation process, doctors need to push the intubation process several times to reach the designated lesion, so reducing the adjustment time is helpful. It can shorten the operation time and improve operational efficiency.

4. Experiment

Before the experiment, the specific parameters of the experiment are specified. The axial displacement stroke of the system mechanism is set as 300 mm, and the axial displacement verification experiment of the whole system is divided into two parts: pushing and withdrawing, which ensures that the axial displacement pushing and withdrawing speed is 30 mm/s. This can ensure that the verification experiment is carried out under the premise of the same push speed and the same time delay so as to ensure the authenticity and reliability of the results.

First of all, we use the traditional PID controller to perform basic experiments during the manual control operation
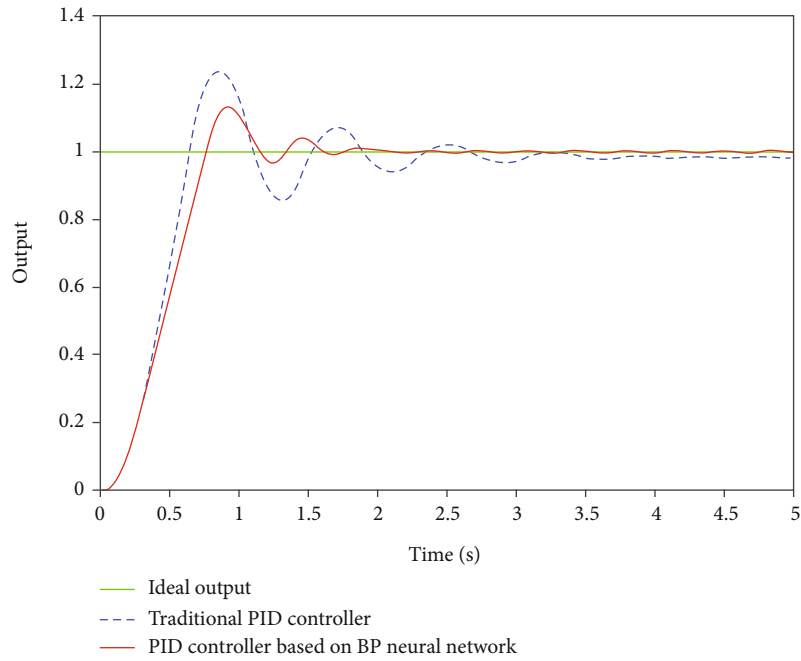
FIGURE 11: Simulation results.
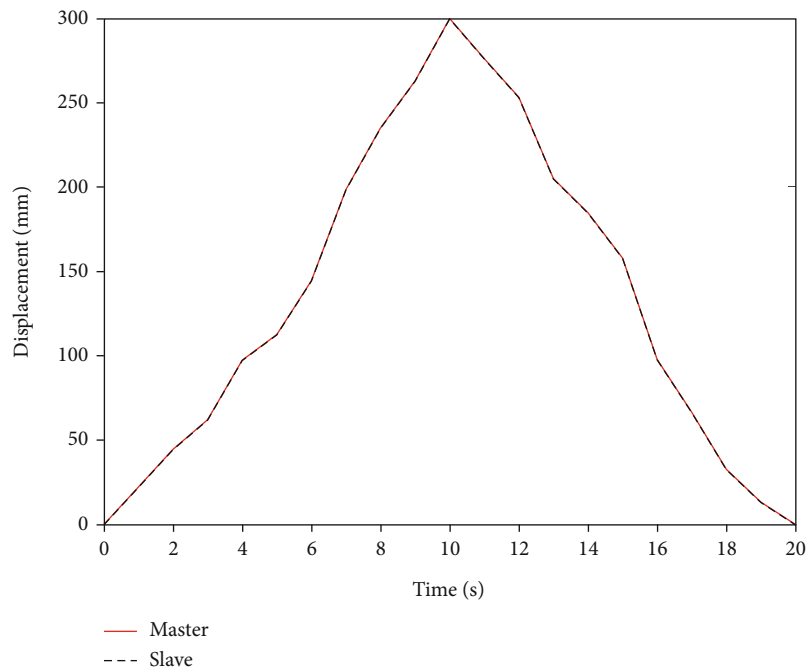
FIGURE 12: Axial displacement of the BP neural network PID controller.

[16]. In this case, performance characteristics can be obtained by experiments. Then, we continue to use the designed BP neural network PID controller to improve the accuracy of manual operation. The experimental results obtained by the BP neural network PID controller are shown in Figure 12, and a smooth displacement response without the overshoot is obtained. These two controller axial displacement errors are shown in Figure 13.

The traditional PID controller has many steady-state errors, and its synchronous tracking performance is worse than the BP neural network PID controller. However, although the performance of the BP neural network PID controller is good, due to the communication delay in manual operation, it will cause some errors. The input signal of the system is the pull value of the main end console. The axial displacement value of the main end console is calculated by
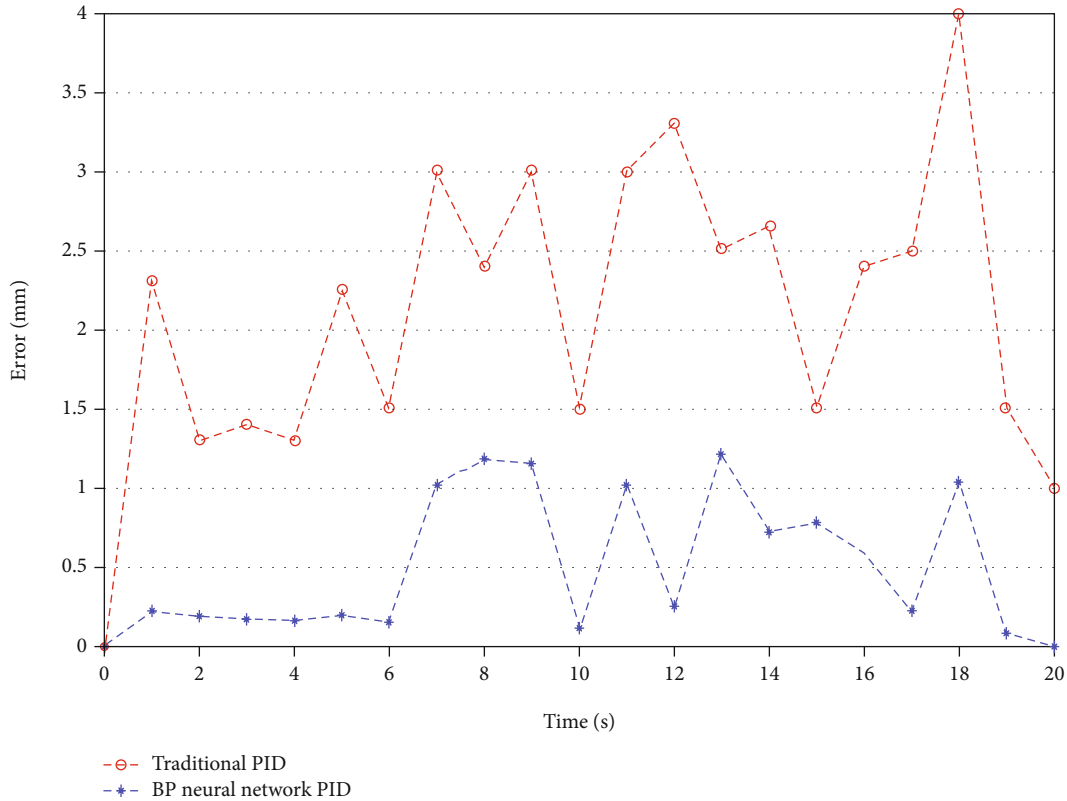
FIGURE 13: Axial displacement errors of the traditional PID controller and BP neural network PID controller.

a mathematical equation, and then these values are converted into the input signal of the stepping motor by the DSP control unit.

Figure 12 shows the axial displacement tracking of the BP neural network PID controller. The new algorithm is suitable not only to reduce the steady-state error and overshoot of the system but also to shorten the rise time and improve the accuracy. Better tracking performance can be achieved. The experimental results show that compared with the traditional PID controller, the overshoot of the new controller is significantly reduced, the axial displacement error is improved, and the tracking speed and accuracy are also significantly improved.

Through the error comparison in Figure 13, we can find that the system under the premise of two different control systems will produce a large error in about 10 s. This is because the stroke of the linear guide rail used in the system is a little small. When the push mechanism is about to reach the end, there will be a large error due to mechanical friction. This is an error in the selection process of mechanical equipment, which will be studied in the future. In order to eliminate this effect, a better linear guide will be selected. In addition, in the whole verification experiment process, the error of push and withdraw also has a certain difference because the motion performance will have a certain change when the motor rotates forward and reverses. In future research, we have to improve the design of the mobile platform, reduce the system error of mechanical equipment, and ensure the reliability of the system.

However, for the modeling of the DC motor, we use a physical method to establish the dynamic model of axial displacement movement, but we need to consider the operation needs under different working conditions, which requires the use of a nonlinear method in modeling and system identification. Most mechanical systems used in the industry consist of motion information such as position and speed. These motion information will show nonlinear behavior in some work areas. For the system with two degrees of freedom (rotation and insertion), when the speed and direction of rotation change, nonlinearity will significantly affect the operation of the system. Therefore, we should pay attention to the nonlinear modeling and parameter identification of system dynamics in the future.

5. Conclusions

In this paper, a new catheter operating system of the surgical robot is proposed, and a new mechanical structure of force feedback is designed to measure the near-end force during the operation. Surgeons can also sense the force feedback of the system to avoid misoperation [17]. Secondly, the BP neural network PID controller is designed to improve the motion accuracy of the axial displacement in the process of teleoperation. Compared with the traditional PID control method, the BP neural network PID controller has better control quality.

In the manual control process, the maximum error of the BP neural network PID axial tracking is less than 1.5 mm,

and the average error is only 0.48 mm, which basically meets the experimental requirements. Although there are some errors in the axial motion due to the time delay of communication, it can also be used in practical operation. The experimental results show that the BP neural network algorithm is applicable and easy to understand [18].

In the future research work, we will redesign the dynamic model of the catheter operating system of the surgical robot to improve the control accuracy of the system, and through the introduction of the optical fiber sensor and magnetic sensor to form a new collision force acquisition unit, we can obtain the accurate information of the internal force (contact force and friction force) and displacement between the surgical catheter and the blood vessel [19].

Data Availability

The experiment data used to support the findings of this study are available from the corresponding authors upon request.

Conflicts of Interest

The authors declare that they have no conflicts of interest.

Acknowledgments

References

[1] L. Fang, "Research on DC motor intelligent control algorithm," *Applied Mechanics and Materials*, vol. 462-463, pp. 775–781, 2013.

[2] W. G. Phillips and T. Thieme, "da Vinci surgical robot," *Popular Science*, 2002.

[3] H. H. Lee, J. C. Na, Y. E. Yoon, K. H. Rha, and W. K. Han, "Robot-assisted laparoendoscopic single-site upper urinary tract surgery with da Vinci Xi surgical system: initial experience," *Investigative and Clinical Urology*, vol. 61, no. 3, pp. 323–329, 2020.

[4] N. Aoide, "Hansen, Sensei," *Sensei robotic catheter system*, 2012.

[5] Y. Wang, S. Guo, B. Gao, W. Peng, and G. Li, "Study on motion following with feedback force disturbance in interventional surgical robot system," in *2016 IEEE International Conference on Mechatronics and Automation*, Harbin, China, 2016.

[6] C. Ji, Z. G. Hou, and X. L. Xie, "An image-based guidewire navigation method for robot-assisted intravascular interventions," in *2011 Annual International Conference of the IEEE Engineering in Medicine and Biology Society*, pp. 6680–6685, Boston, MA, USA, 2011.

[7] X. Ma, S. Guo, and N. Xiao, "Development of a novel robotic catheter manipulating system with fuzzy PID control," *International Conference on Manipulation*, 2013.

[8] S. Miyachi, Y. Nagano, T. Hironaka et al., "Novel operation support robot with sensory-motor feedback system for neuroendovascular intervention," *World Neurosurgery*, vol. 127, pp. e617–e623, 2019.

[9] L. L. Buchan, M. S. Black, M. A. Cancilla et al., "Making safe surgery affordable: design of a surgical drill cover system for scale," *Journal of Orthopaedic Trauma*, vol. 29, Suppl 10, pp. S29–S32, 2015.

[10] J. Guo, C. Meng, S. Guo, Q. Fu, Q. Zhan, and L. Qi, "Design and evaluation of a novel slave manipulator for the vascular interventional robotic system," in *2019 IEEE International Conference on Mechatronics and Automation (ICMA)*, Tianjin, China, China, 2019.

[11] V. Srinivasan, T. Lazaro, P. Cooper et al., "P-014 applications of a novel microangioscope for neuroendovascular intervention," in *SNIS 16th Annual Meeting*, Miami, U.S.A., 2019.

[12] H. J. Cha, B. J. Yi, and J. Y. Won, "An assembly-type master–slave catheter and guidewire driving system for vascular intervention," *Proceedings of the Institution of Mechanical Engineers, Part H: Journal of Engineering in Medicine*, vol. 231, no. 1, pp. 69–79, 2017.

[13] G. Peng, C. Yang, W. He, and C. L. P. Chen, "Force sensorless admittance control with neural learning for robots with actuator saturation," *IEEE Transactions on Industrial Electronics*, vol. 67, no. 4, pp. 3138–3148, 2020.

[14] M. A. Tavallaei, D. Gelman, M. K. Lavdas et al., "Design, development and evaluation of a compact telerobotic catheter navigation system," *International Journal of Medical Robotics & Computer Assisted Surgery*, vol. 12, no. 3, pp. 442–452, 2016.

[15] X. Ma, S. Guo, N. Xiao, S. Yoshida, and T. Tamiya, "Evaluating performance of a novel developed robotic catheter manipulating system," *Journal of Micro-Bio Robotics*, vol. 8, no. 3-4, pp. 133–143, 2013.

[16] D. Liu, G. Shen, S. Qiao, and N. Wu, "A real time multi-angle adjustable phased high intensity focused ultrasound system," *Cognitive Systems Research*, vol. 52, pp. 610–614, 2018.

[17] L. Zhang, S. Guo, H. Yu et al., "Design and performance evaluation of collision protection-based safety operation for a haptic robot-assisted catheter operating system," *Biomedical Microdevices*, vol. 20, no. 2, p. 22, 2018.

[18] L. S. Medina, E. Alvarado, E. Pacheco et al., "Minimally invasive MR imaging-guided stereotactic laser thermal ablation in neurosurgical cases of pediatric lesional epilepsy: a didactic step-by-step practical approach," *Neurographics*, vol. 6, no. 6, pp. 390–399, 2016.

[19] R. Kumar, B. D. Hoffman, G. M. Prisco et al., *Multi-user medical robotic system for collaboration or training in minimally invasive surgical procedures*, 2016.

Research Article

Exoskeleton Follow-Up Control Based on Parameter Optimization of Predictive Algorithm

Shijia Zha [iD],[1] **Tianyi Li** [iD],[1] **Lidan Cheng** [iD],[1] **Jihua Gu,**[1] **Wei Wei** [iD],[1] **Xichuan Lin,**[2] **and Shaofei Gu** [iD][3]

[1]*College of Optoelectronics Science and Engineering, Soochow University, Suzhou Jiangsu Province, 215000, China*
[2]*Micro-Nano Automation Institute, Jiangsu Industrial Technology Research Institute, Suzhou, Jiangsu Province 215131, China*
[3]*Shanghai Huangpu District Fire Rescue Detachment, Shanghai 200001, China*

Correspondence should be addressed to Wei Wei; weiwei0728@suda.edu.cn

Received 28 May 2020; Revised 15 October 2020; Accepted 8 January 2021; Published 21 January 2021

Academic Editor: Jose Merodio

The prediction of sensor data can help the exoskeleton control system to get the human motion intention and target position in advance, so as to reduce the human-machine interaction force. In this paper, an improved method for the prediction algorithm of exoskeleton sensor data is proposed. Through an algorithm simulation test and two-link simulation experiment, the algorithm improves the prediction accuracy by $14.23 \pm 0.5\%$, and the sensor data is smooth. Input the predicted signal into the two-link model, and use the calculated torque method to verify the prediction accuracy data and smoothness. The simulation results showed that the algorithm can predict the joint angle of the human body and can be used for the follow-up control of the swinging legs of the exoskeleton.

1. Introduction

The exoskeleton is a wearable device that combines human intelligence and mechanical power, widely appearing in the fields of assistance, rehabilitation training, and disability assistance. In recent years, with the continuous development of drive technology and sensor technology, more and more exoskeletons have appeared in the market [1]. Exoskeletons are often designed to perform specific functions such as walking, weight-bearing, lumbar support, and spinal support. In order to assist the specific movements of the human body, a very critical point for the exoskeleton is to realize the recognition of the human motion intention.

1.1. Introduction to Exoskeleton Classification. There are many ways to classify active exoskeletons. One classification way is based on the methods of the exoskeleton acquiring the intention of human motion, which can be roughly divided into four categories: The first is preprogrammed. The gait of the exoskeleton system is designed, so the wearer can only intervene in limited ways with devices such as but-

tons or HMI (Human Machine Interface). However, only relying on some external devices to obtain the motion intention of the human body limits the use scope of the exoskeleton, which makes this kind of exoskeleton often appear in the rehabilitation and correction equipment with fixed gait [2]. The second is the use of EEG (electroencephalogram) signals to identify the intention of human movement. Such systems are susceptible to interference from the external environment and are not suitable for the wearer to perform multibrain tasks [3]. The third method uses the surface EMG (electromyography) signals of the human body to capture the movement intention of the human body. Obtaining surface EMG signals is usually done by attaching electrodes on the skin of the human body, which is also vulnerable to the environment. Sweat on the surface of the skin often affects the accuracy of the signals [4], and long-term wear is easy to cause the surface electrode to fall off; some teams have developed exoskeletons (e.g., HAL) that recognize the body's intentions based on electromyographic signals. The fourth way is to collect human body motion mechanics information to identify human body motion intentions. Such systems have installed

a large number of kinematics and dynamics sensing devices on the exoskeleton and human body to obtain the interaction information of the human body and the motion intention of the human body. Many lower limb exoskeletons, such as WEAR [5], MEBOTX-EXO [6], and HUALEX [7], use kinematic information to capture the human body's intention and kinetic information to control the motion of the exoskeleton. This type of exoskeleton has the characteristics of easy to put on and take off, and the system sensor signal is stable, which makes it become the main research direction of exoskeleton. However, the kinematic sensor requires the human body to drive the exoskeleton movement, inevitably causing the delay of motion intention perception and control.

Since the exoskeleton involved in this paper is the fourth method to obtain the human movement intention and the sensor data is collected by the sensor network, it takes some time until the control signal is generated. The actuators (typically motors or hydraulic) cause time delay, too [8]. Meanwhile, the motion signal of the human body is behind the motion intention of the human body. Therefore, it is necessary to solve the time delay in the fourth exoskeleton system.

1.2. Introduction to Prediction Algorithm. In the exoskeleton control strategies, only relying on the sensor data detected by the sensors of the system and giving the exoskeleton drive structure motion instruction will cause the exoskeleton and the human body a position deviation. The position deviation is the main source of human-machine interaction. An appropriate prediction algorithm needs to be added to help the control strategies judge the wearer's motion intention and the possible motion position at the next moment according to the current and historical motion sensing data, so as to give the system appropriate control commands. Due to the significant difference in the delay between the exoskeleton and the wearer due to different wearing methods and the tightness of the binding, some prediction methods can only predict the one step size, such as Kalman prediction [9], need to continuously iterate the Kalman gain coefficient according to the measured value, and cannot deal with the longer step size prediction. Similar problems also exist in the prediction methods based on the ARMA model, such as LMS linear prediction [10] and RLS linear prediction [11, 12]. When the prediction step size becomes longer, the accuracy of the prediction will decrease significantly [13]. Moreover, LMS linear prediction and RLS linear prediction require more historical data and a large amount of computation, and the prediction curve is not smooth, which makes it difficult to implement such prediction algorithm in an embedded system.

Yang [13] et al. compared the performance of LMS and Takens prediction algorithms in the prediction of human gait data. The results showed that Takens is more stable, accurate, and suitable than LMS, but it did not solve the zero dead time problem of the prediction algorithm. So, Duan et al. [14] use the combination of the Takens prediction algorithm and Newton-based-method to solve the problem of the zero dead time of the prediction algorithm but did not make progress in solving the parameter tuning process.

In this work, we have made improvements to the prediction algorithm for exoskeleton, so that the parameters of the prediction algorithm can be optimally determined. Applying it to exoskeleton gait prediction can accurately predict the joint angle of the exoskeleton, making joints motor reach the aim position in advance.

The reminder of this paper is organized as follows:

In Section 2.1, we introduce the IMU-based pose capture system. In Section 2.2, we briefly introduce the Takens prediction algorithm. In Section 2.3, we introduce the process of the PSO-Takens algorithm. Section 2.4 is mainly about the simulation of the control of the prediction algorithm in the two-link model.

In Section 3, the experimental results are analyzed. We mainly discussed the performance of the improved prediction algorithm and the original prediction algorithm in exoskeleton gait data prediction.

In Section 4, we conclude the paper.

2. Materials and Methods

2.1. Motion Capture System. The process of human lower limb movement has the characteristics of high autonomy, complex information, diverse movements, and multiple degrees of freedom. Biomechanical simulation and experimental studies have shown that the motion consumption power in the sagittal plane of the human body is the largest relative to the frontal plane and horizontal plane [15], so the three-dimensional walking motion of human hip joint often can be simplified to a single plane motion in the sagittal plane. The corresponding position sensor used in the exoskeleton is usually placed in a position parallel to the sagittal plane of the human body, which describes the motion angle of the sagittal plane of the lower limb joints of the human body. With the development of inertial measurement units, more and more IMUs (inertial measurement units) were used as examples of kinematic sensors, beginning to appear in the motion capture system. Compared with the method of collecting joint angles using an absolute encoder, IMU has an advantage of flexible installation and cheap price, and its measurement accuracy can reach 0.1°, which can meet the needs of the human motion capture system.

In order to collect human gait information and verify the accuracy of the prediction algorithm, we designed a flexible motion capture system for human sagittal plane motion based on IMUs. The system will automatically capture the sagittal plane motion data of the human body at 50 Hz sampling frequency and transmit the motion data through CAN (Controller Area Network) (Figure 1(a)) to the data collection and processing module. As shown in Figure 1(b), the system mainly collected the pitch angle data of the back, thigh, shank, and the pressure sensor data of the heel. The system also includes power module, data collection and processing module, and data transmission module. Figure 1(c) shows the actual mechanical structure of the exoskeleton system, a hinged structure is adopted between the thigh and shank, and this structure can support the exoskeleton system and reduce the load on the body while standing upright, but it also leads to the inability to directly measure the motion angle of the human knee joint through the angle sensor.
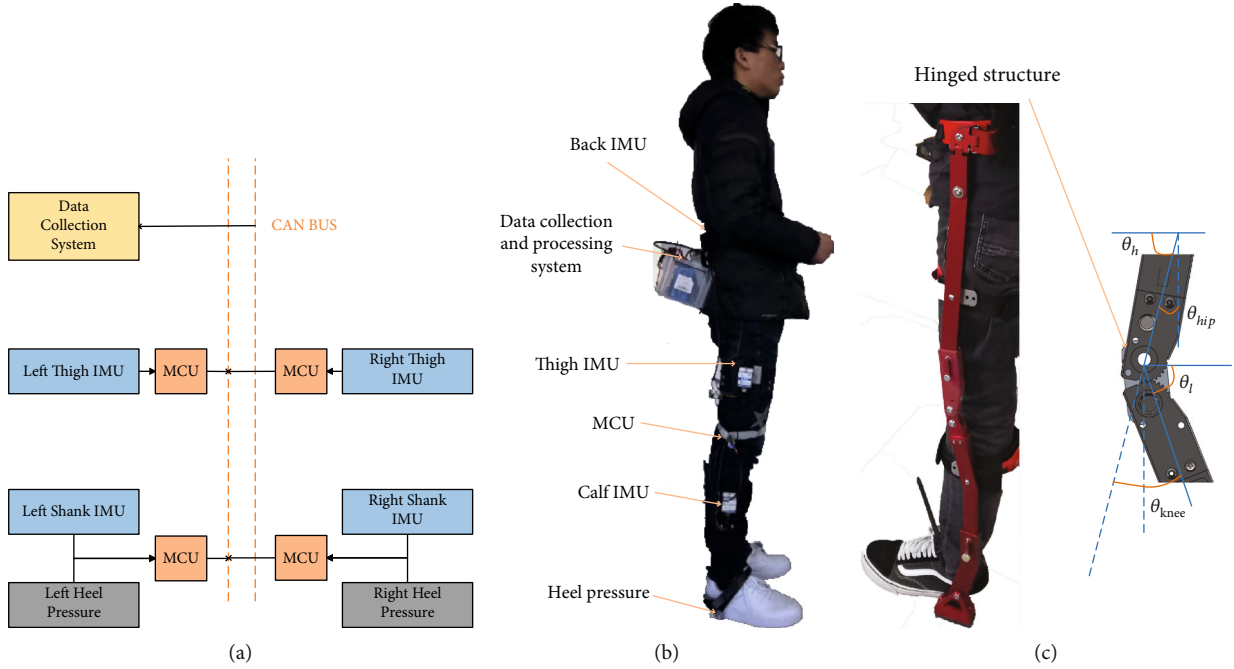
FIGURE 1: Motion capture system and exoskeleton structure. (a) Nets of the motion capture system. (b) Motion capture system. (c) Mechanical structure of the exoskeleton.

Therefore, IMUs were placed on the thighs, shanks, and back to calculate the angle of the human joints.

The formula for calculating the angle of the hip and knee joints is as follows:

$$\theta_{\text{hip}} = \frac{\pi}{2} - \theta_h,$$
$$\theta_{\text{knee}} = \pi - \theta_h - \theta_l. \tag{1}$$

θ_h, θ_l represents the pitch angle of thigh and shank, respectively; due to the mirror relationship between the left and right legs, the calculated angle values are opposite, and there is a phase difference between the hip joints and knee joints.

2.2. Takens Prediction Algorithm. The continuous walking of the human body is periodic and nonlinear. The left and right leg sensor data are only different in phases and directions. Therefore, the algorithms used in the prediction of the joint angle are the same; the prediction algorithms discussed in this section are nonlinear time series Takens prediction algorithm of the lower limb hip and knee joint data.

The Takens algorithm for nonlinear time series forecasting is based on the Takens embedding theorem, which is also called the weighted zero-order local prediction method. This method is closely related to Takens' reconstruction theorem. It is essentially a nonlinear time series analysis method, which requires historical data of the system to obtain the best performance. The main idea is to find several historical data vectors that are the most similar to the current reconstruction delay vector by traversing the sensor data for a period of time, and the historical data vector is normalized and weighted according to the similarity with the current sampling data. The prediction data at a specific time is deter-

mined through function fitting or search. The predicted data of each vector are multiplied by their respective weights to obtain the final predicted value at the determined moment. The algorithm implementation steps are as follows:

(1) According to the Takens embedding theorem, for a given time series $y(t)$, select the appropriate sampling interval Δt and embedding dimension n, and collect and store n data; the adjacent data differ in time Δt; constitute the reconstruction delay vector $D(t)$. The time series $y(t)$ can be any type of sensor data in the motion capture system, such as angle, angular velocity, or heel pressure data. The contents of $D(t)$ is

$$D(t) = [y(t), y(t - \Delta t), y(t - 2\Delta t), y(t - 3\Delta t) \cdots y(t - (n-1)\Delta t)] \tag{2}$$

(2) Calculate the similarity between the current reconstruction delay vector $D(t)$ obtained by sampling at the current time and the historical reconstruction delay vector $D_i(t)$ obtained from all previous observations; the methods for calculating similarity in reconstruction delay vectors are usually Euclidean distance, Pearson's correlation coefficient, Manhattan distance, and hash distance. The Euclidean distance has the following expression in this algorithm:

$$\delta(i) = \sqrt{\sum_{k=1}^{n} (y(t - (k-1)\Delta t) - y_i(t - (k-1)\Delta t))^2} \quad (1 \leq i \leq N). \tag{3}$$
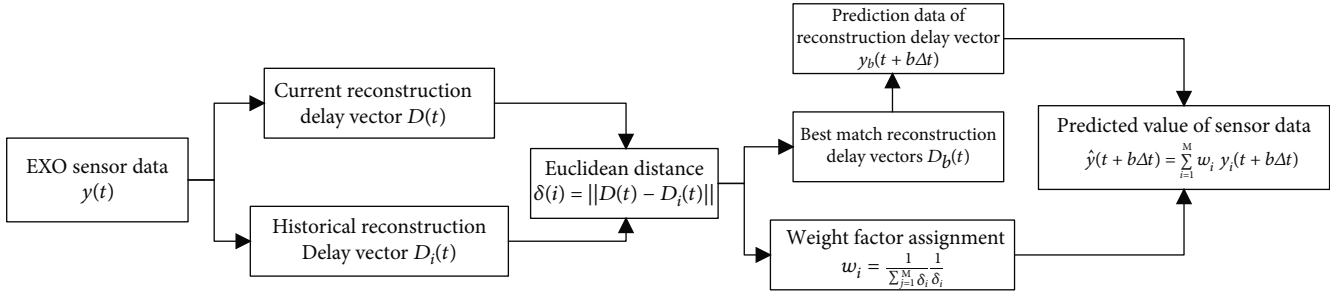
FIGURE 2: Flow chart of the Takens algorithm.

In formula (3), the value of i represents the position of the currently traversed vector, N is the reconstruction delay vector length. The smaller the Euclidean distance is, the more similar the two reconstruction delay vectors are, and the more accurate when the historical reconstruction delay vector is used to predict the data of the subsequent period of time. While Pearson's correlation coefficient or Manhattan distance is used as a similarity calculation, the expression becomes

$$\delta(i) = \frac{\sum_{k=1}^{n}(y(t-(k-1)\Delta t - \bar{y})(y_i(t-(k-1)\Delta t - \overline{y_i})))}{\sqrt{\sum_{k=1}^{n}(y(t-(k-1)\Delta t - \bar{y})^2}\sqrt{\sum_{k=1}^{n}(y_i(t-(k-1)\Delta t - \overline{y_i}))^2}} \quad (1 \leq i \leq N),$$

$$\delta(i) = \sum_{k=1}^{n}|y(t-(k-1)\Delta t) - y_i(t-(k-1)\Delta t)| \quad (1 \leq i \leq N). \tag{4}$$

In formula (4), $\bar{y}$ is the average value of the reconstructed delay vector, Pearson's correlation coefficient and Manhattan distance can also be used as a similarity calculation function, and the difference is only the amount of calculation. Among the three calculation methods, Manhattan has the smallest amount of calculation and Pearson's correlation coefficient is the largest

(3) From the observed historical reconstruction delay vector $D_i(t)$, the best matching M sets of reconstruction delay vectors $\{D_1(t), \cdots, D_M(t)\}$ are selected according to the similarity with the reconstruction delay vector $D(t)$ at the current moment. The corresponding Euclidean distances are $\{\delta(1), \cdots, \delta(M)\}$. The predicted value $\{y_1(t+b\Delta t), \cdots, y_M(t+b\Delta t)\}$ of each group of reconstruction delay vectors is determined by searching, $T = b\Delta t$ is the predicted duration. The weighting factor formula of each best matching amount in the final prediction amount calculation formula is as follows:

$$w_i = \frac{1}{\sum_{j=1}^{M}\delta_i}\frac{1}{\delta_i} \quad (1 \leq j \leq M) \tag{5}$$

(4) According to the predicted values and weight factors of each historical reconstruction delay vector group, the estimated predicted values at time $b\Delta t$ after the current moment $y(t)$ are calculated as follows:

$$\hat{y}(t+b\Delta t) = \sum_{i=1}^{M} w_i y_i(t+b\Delta t) \tag{6}$$

The flow chart of the algorithm is shown in Figure 2.

The Takens algorithm is to make predictions on the sensor data for a period of time by searching historical sensor data, which means that the prediction algorithm is to find the most similar data out of the current motion situation from the historical vectors. The sensor data of the human walking motion detected on the sagittal plane has obvious periodicity, so the Takens algorithm has a well performance in predicting such signals. Among multiple optimal reconstruction delay vectors, the algorithm can dynamically adjust the weight factor through the Euclidean distance, which can adjust the proportion of the optimal reconstruction delay vector in the final prediction data.

2.3. PSO-Takens Prediction Algorithm Design. Although the Takens algorithm cannot predict that all motion sensor data are completely correct, some papers also give an optimization method based on this algorithm [14], which makes the Takens algorithm used in embedded systems become possible. Whitney's topological embedding theorem shows that the phase space of the original system can be reconstructed by any value of the delay time of the single variable time series in the case of noiseless and infinitely long time series. In fact, the measured time series is of limited length and is inevitably polluted by noise. Therefore, arbitrary delay time cannot reconstruct the phase space of the system; the key to reconstruct the phase space using the measured time series is how to select these reconstruction parameters. However, the Takens embedding theorem does not indicate how to select these parameters. This problem has become an important issue in nonlinear time series analysis.

Duan et al. have found that inappropriate historical vector dimension and embedding dimension will cause irrelevant data to enter the reconstruction delay vector, resulting in lower prediction accuracy [14]. While inappropriate prediction duration and optimal matching number will cause data jitter and affect the smoothness of the predicted data. Fortunately, the predicted duration, which is also called delay time, is a constant we want to compensate. It is mainly caused by inertial sensors and inherent defects of the system, and the duration can be measured by wearing exoskeletons. The delay time is expressed as the angle difference between the human body and the exoskeleton.

In order to evaluate the algorithm performance and adjust the parameters of the algorithm, the following two formulas were introduced which are aimed at judging the pros and cons of the prediction effect:

2.3.1. Prediction Accuracy Rate (PR).

$$e_k(t) = y(t) - \widehat{y}(t \mid t - b\Delta t),$$

$$\text{RMS}(e_k) = \sqrt{\frac{1}{n} \sum_{t=2}^{n} e_k(t)^2}. \tag{7}$$

$e_k(t)$ records the error between the predicted value and the actual value at each sampling point, and $\text{RMS}(e_k)$ (Root Mean Square error) characterizes the degree of deviation of the overall predicted value from the actual value. The greater the $\text{RMS}(e_k)$ is, the greater the deviation of the predicted data from sensor data and the worse the predicted performance. By normalizing the $\text{RMS}(e_k)$, the prediction accuracy rate (PR) is defined as

$$\text{PR}(y(t), e_k(t)) = 1 - \frac{\text{RMS}(e_k(t))}{\text{RMS}(y(t))} \times 100\%. \tag{8}$$

2.3.2. Smooth Factor (SF).

$$\text{SF}(\widehat{y}(t)) = \frac{1}{t_{\text{end}}(\max{(\widehat{y}(t))} - \min{(\widehat{y}(t))})} \int_0^{t_{\text{end}}} |f(t) - \widehat{y}(t)|. \tag{9}$$

In formula (9), t_{end} is the duration of the algorithm, and a 5 Hz low-pass filter is used to filter $y(t)$ to obtain $f(t)$. The parameter smooth factor (SF) indicates whether the data is smooth or not. In the course of human gait walking, the predicted sensor data is smooth and stable to match the actual walking data. Therefore, the smaller the SF is, the closer the predicted sensor data is to the sensor data measured by the actual gait walking. Since the data actually collected in the algorithm is discrete, when calculating the SF, formula (12) is usually discretized to the following formula:

$$\text{SF}(\widehat{y}(t)) = \frac{1}{N(\max{(\widehat{y}(t))} - \min{(\widehat{y}(t))})} \sum_{i=0}^{N} |f(i) - \widehat{y}(i)|. \tag{10}$$

The parameters affecting the prediction effect of the Takens algorithm are as follows: (i) the predicted duration (T), (ii) historical reconstruction delay vector length (P), (iii) optimal matching reconstruction vector number (M), and (iv) embedding dimension (N).

We introduced PSO (Particle Swarm Optimization) on the basis of Takens prediction algorithms, which is a swarm intelligence optimization algorithm in addition to an ant colony algorithm and a genetic algorithm in the field of computer intelligence. It originated from the study of bird predation behavior, and the basic idea is to solve and cooperate with individuals in the group to achieve the search for the optimal solution in a complex space [16]. Compared with other intelligent adjustment algorithms [17–18], such as derivative-based or derivative-based (or gradient-based) (e.g., backpropagation (BP), Levenberg-Marquardt (LM), Kalman filter, least square methods, and sliding-mode learn-

ing algorithm), hybrid learning methods, it belongs to the derivative-free method and does not need to update complex parameter equations, making it more suitable for nonlinear output situations. Meanwhile, it has the advantages of strong global search ability and easy implementation and has strong convergence and robustness in the process of solving. In the PSO algorithm, each particle represents a potential solution, and the velocity of the particle represents the direction and distance of each potential solution, which can be used to seek the optimal value in the multidimensional space.

The PSO-Takens algorithm flow chart is shown in Figure 3.

Step 1. Initialize a swarm of particles (population size m), including the random position and velocity, and limit the upper and lower limits of the particle's velocity and position. The optimized parameters in the Takens algorithm are as follows: historical vector dimension P, optimal matching number M, and embedding dimension N; therefore, the population of particles is $\{x1, x2, x3 \cdots Xm\}$, and the position of the i-th particle is $\{XP_i, XM_i, XN_i\}$, The velocity of the i-th particle is $\{VP_i, VN_i, VM_i\}$.

Step 2. Use the evaluation function to calculate the fitness of each particle.

Step 3. For each particle, comparing its fitness with the optimal value $p$best, it has passed through. If the current value is better than $p$best, the $p$best will be set to the current value, and the position of $p$best is set as the current position in the n-dimensional space.

Step 4. For each particle, comparing its fitness value with the best position $g$best, all particles passed through. If the current value is better, the current position will be regarded as the best position $g$best.

Step 5. After updating the local and global optimal values of the current iteration, the particle adjusts its velocity and position through the following formulas.

$$V_{i+1} = V_i + c_1 \times r\text{and}() \times (p\text{best}_i - x_i) + c_2 \times r\text{and}() \times (g\text{best}_i - x_i),$$

$$x_{i+1} = x_i + V_{i+1}. \tag{11}$$

When the inertia factor is added, the velocity expression becomes

$$V_{i+1} = \omega V_i + c_1 \times r\text{and}() \times (p\text{best}_i - x_i) + c_2 \times r\text{and}() \times (g\text{best}_i - x_i). \tag{12}$$

Step 6. If the condition to terminate the iteration is not reached, go to Step2, until the iteration termination condition is met.

According to the specific issue, the iteration termination condition is generally to reach the maximum iteration number Gk or the optimal value of the evaluation function to
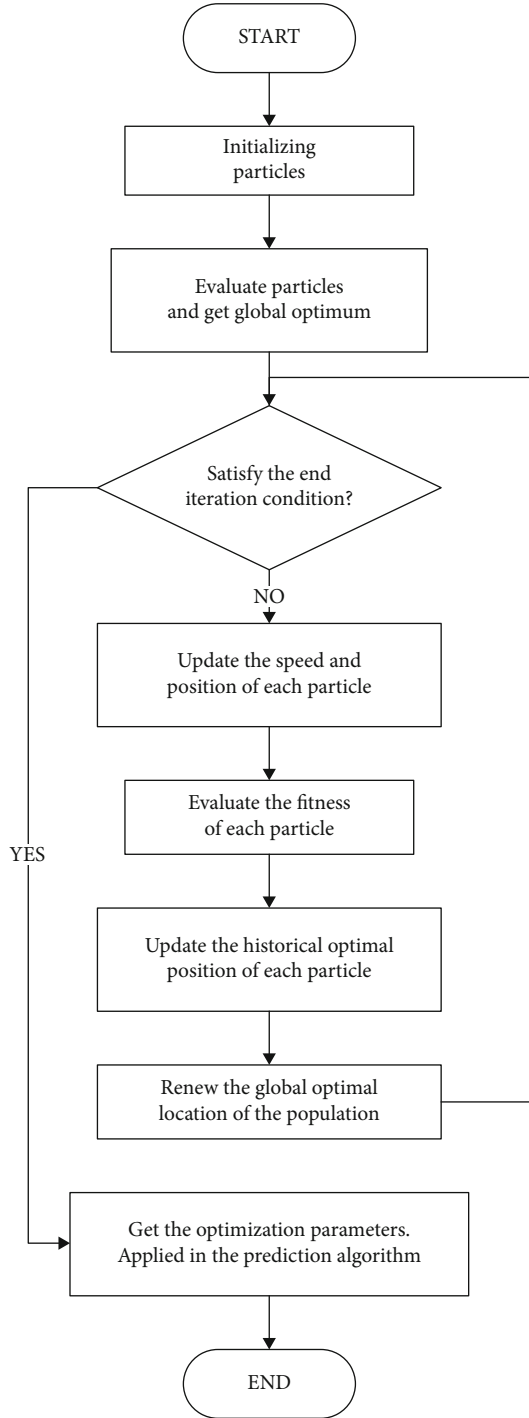
Figure 3: Flow chart of the PSO-Takens algorithm.

Figure 4: Lower extremity exoskeleton leg's simplified second link kinetic model.

In formula (15), w_1 and w_2 are constants (0.5), which means that we believe that the accuracy of data is as important as the smooth factor in the human lower limb prediction algorithm. The goal of the PSO-Takens prediction algorithm is to adjust the complex parameter tuning problem of the Takens algorithm in gait prediction, so as to achieve the optimal prediction effect.

2.4. Follow-Up Control Design

2.4.1. Dynamic Model of Swing Leg. The movement of the lower limbs of the human body can be regarded as a combination of swing phase and support phase. Usually, the swing phase accounts for 60% of the gait cycle and the support phase accounts for 40% [19]. For the swinging phase, the swinging legs of the human body can be regarded as an inverted two-link with uniform mass distribution. During the support phase, the leg and the upper body of the human body can be regarded as three links fixed at the bottom. This division method can simplify the complexity of torque calculation in inverse dynamics, making it easy to implement on embedded systems.

The lower limb-assisted exoskeleton single leg model is shown in Figure 4. L_0 and L_1 are the length of thigh and shank, and the ankle joint is omitted.

Assuming that the mass distribution of the exoskeleton lower limb members is uniform, the centroid coordinates $G_i(x_i, z_i)$ of the exoskeleton thigh and shank are as follows:

$$\begin{cases} x_0 = a_0 \sin q_{0,} \\ z_0 = -a_0 \cos q_{0,} \end{cases} \tag{14}$$

$$\begin{cases} x_1 = L_0 \sin q_0 + a_1 \sin q_{1,} \\ z_1 = -(L_0 \cos q_0 + a_1 \cos q_1). \end{cases} \tag{15}$$

The kinetic energy of the two connecting rods of lower limb swing is the sum of the rotational kinetic energy and

meet the established threshold. The condition for the algorithm to stop iteration is as follows: the number of iterations over 50, or the fitness calculated by the evaluation function over 100. The fitness (Y_{ef}) evaluation function expression is follows:

$$Y_{\mathrm{ef}} = w_1 \times \frac{1}{\mathrm{SF}} + w_2 \times \mathrm{PR}. \tag{13}$$
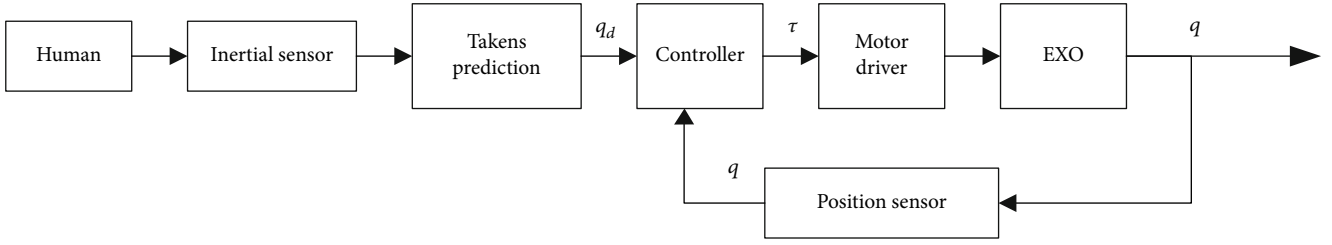
FIGURE 5: Follow-up control strategy block diagram of the exoskeleton.
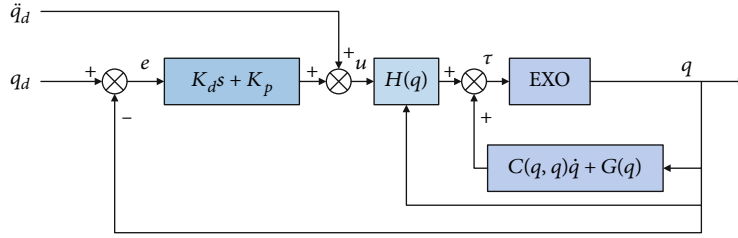
FIGURE 6: Control block diagram of calculate torque method.

(a)

(b)
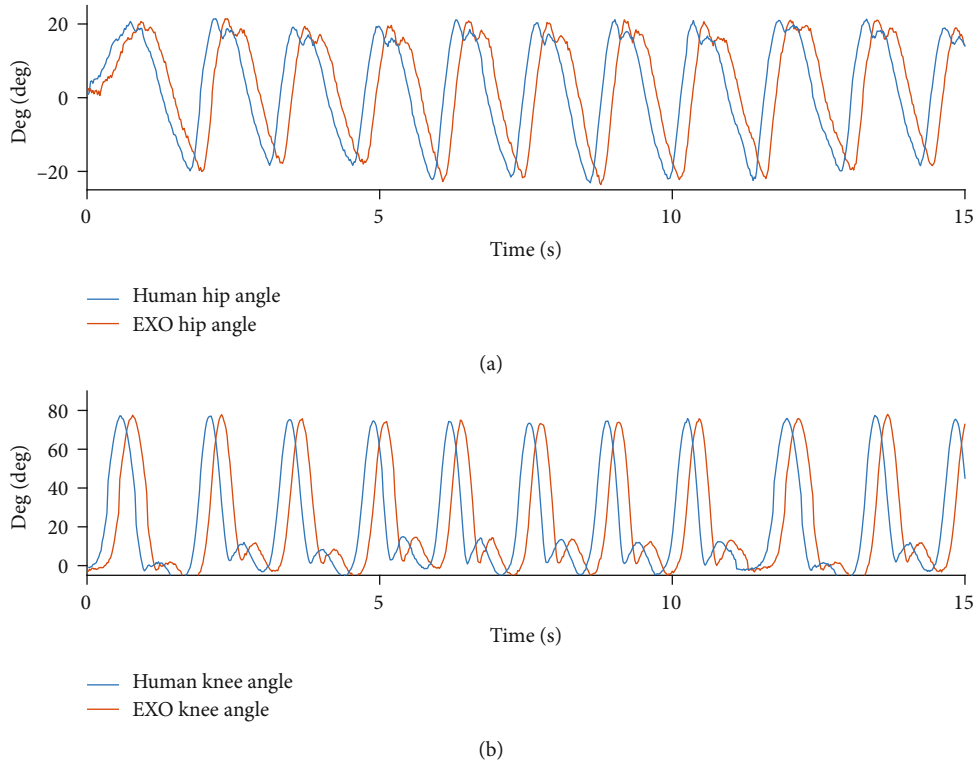
FIGURE 7: Joint angle deviation between human and exoskeleton.

kinetic energy of the connecting rod, which can be expressed as follows:

$$E = \frac{1}{2}\left(\sum_{i=0}^{1} I_i \ddot{q}_i + m_i\left(\dot{z}_i^2 + \dot{x}_i^2\right)\right). \tag{16}$$

In formula (16), I_i is the moment of inertia when the exoskeleton is the i-th lower extremity connecting rod rotating

around the sagittal plane of the joint. The expression is $I_i = (1/3)m_i L_i^2$, and $\ddot{q}_i$ is the angular acceleration of the joint. $\dot{z}_i$ and $\dot{x}_i$ are the velocities of the linkage in the x and z directions, and the total potential energy of the lower limb linkage is as follows:

$$P = \sum_{i=0}^{1} m_i g z_i. \tag{17}$$
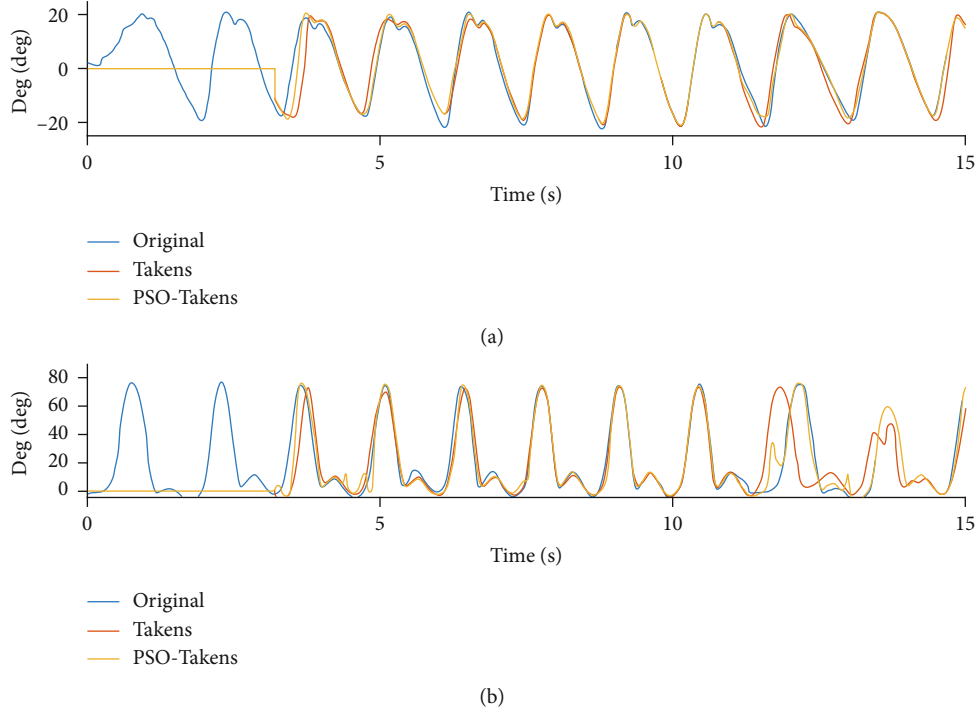
FIGURE 8: Comparison of Takens and PSO-Takens in prediction of nonstandard gait data. (a) Comparison of hip joint prediction angle. (b) Comparison of knee joint prediction angle.

By defining the Lagrangian function $L = E - P$ and the Lagrangian formula, the expression of the joint torque in the two-link can be expressed as

$$H(q)\ddot{q}_i + C(q, \dot{q})\dot{q} + G(q) = \tau_i. \tag{18}$$

In formula (18), τ_i is the joint torque between the links, $H(q)$ is the inertia matrix, $C(q, \dot{q})$ is the friction matrix, and $G(q)$ is the gravity vector. The expressions of the matrix $H(q)$, $C(q, \dot{q})$, and the gravity vector $G(q)$ are as follows:

$$H(q) = \begin{bmatrix} \frac{7}{12} m_0 l_0^2 + m_1 l_1^2 & m_1 l_0 l_1 \cos (q_0 + q_1) \\ 0 & \frac{7}{12} m_1 l_1^2 \end{bmatrix},$$

$$C(q, \dot{q}) = \begin{bmatrix} 0 & -m_1 l_0 l_1 \sin (q_0 + q_1) \\ -m_1 l_0 l_1 \sin (q_0 + q_1) & 0 \end{bmatrix},$$

$$G(q) = \begin{bmatrix} \frac{1}{2} m_0 g l_0 \sin q_0 + m_1 g l_0 \sin q_0 \\ \frac{1}{2} m_1 g l_1 \sin q_1 \end{bmatrix}. \tag{19}$$

2.4.2. Follow-Up Control Strategy. After obtaining the inverse dynamics model of the joint, we use the prediction angle obtained by the prediction algorithm to do Simulink simulation of the two-link model in MATLAB. The follow-up control strategy block diagram is shown in Figure 5.

TABLE 1: Parameter changes of hip joint prediction algorithm under nonstandard gait data.

#	T	P	M	L	PR	SF	Fitness
Takens	10	80	10	300	73.23%	0.2226	38.86
PSO-Takens	10	26	7	644	87.74%	0.2196	46.14

TABLE 2: Parameter changes of knee joint prediction algorithm under nonstandard gait data.

#	T	P	M	L	PR	SF	Fitness
Takens	10	80	10	300	71.80%	0.2317	38.05
PSO-Takens	10	48	12	536	85.75%	0.2388	44.97

The input of the control system is the angle of the human joint q_d and the angle sensor placed on the exoskeleton q, and the joint torque is as the output of the controller and outputted by the motor driver. It is not necessary and convenient to install an angle sensor on the lower limbs of the human body. Since the angle deviation between the exoskeleton and the human body is usually a constant value, this means we can predict the angle of the human body through the position sensor of the exoskeleton, instead of placing the inertial sensor outside the human body, which is the role of the predict algorithm played in follow-up control strategy.

For the angle data predicted by an algorithm, we used the calculated torque method for systematic control, aiming at making the lower extremity two-link of the exoskeleton follow the changing joint curve predicted by the algorithm. Compared with PD control and PD control with gravity compensation terms, the calculated torque method changes

(a)

(b)
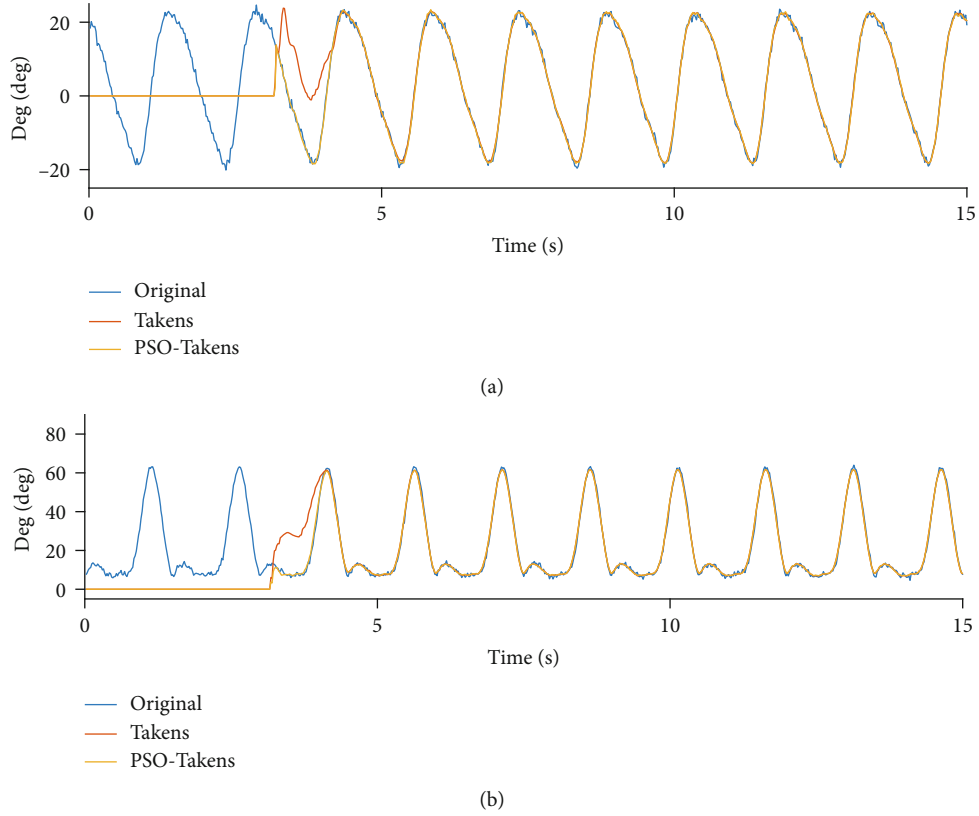
FIGURE 9: Comparison of Takens and PSO-Takens in prediction of standard gait data. (a) Comparison of hip joint prediction angle. (b) Comparison of knee joint prediction angle.

the lower extremity joints of the exoskeleton into a linear time-invariant system that is easier to control due to the introduction of nonlinear compensation. Huo [20] proved the stability of the control method. Based on the inverse dynamics equation, the system can follow the target position well. The control block diagram of this method is shown in Figure 6.

The torque expression calculated by the system control output to the hip and knee joints is as follows:

$$\tau = H(q)\left(\ddot{q} + K_d \dot{e} + K_p e\right) + C(q, \dot{q})\dot{q} + G(q). \tag{20}$$

In formula (20), the parameters $H(q)$, $C(q, \dot{q})$, and $G(q)$ are the matrixes of inverse dynamics in the two-link model; K_d and K_p are diagonal matrices, which are proportional and differential terms for the tracking error e.

3. Results and Discussion

3.1. Experimental Results

3.1.1. Prediction Algorithm Experiment Result. Figure 7 represents the sensor data of the motion angle data of the joints in the continuous walking movement. Compared with the sensor data of the wearing exoskeleton, we found that the angle detected from the exoskeleton and the actual motion angle detected from the human body are generally delayed by 200 ms, about 10 sampling cycles. Therefore, in a prediction algorithm, the sensor data at 200 ms after the current sampling point will be predicted based on EXO historical

TABLE 3: Parameter changes of hip joint prediction algorithm under standard gait data.

#	T	P	M	L	PR	SF	Fitness
Takens	10	120	10	900	77.52%	0.2133	41.10
PSO-Takens	10	69	3	767	88.19%	0.2091	46.48

TABLE 4: Parameter changes of knee joint prediction algorithm under standard gait data.

#	T	P	M	L	PR	SF	Fitness
Takens	10	120	15	900	87.14%	0.2063	45.99
PSO-Takens	10	77	15	1296	95.50%	0.2051	50.18

data. The angle sensor data obtained by three participants (65 ± 5 kg, 170 ± 5 cm) continuously walking at a speed of 3.6 km/h on a treadmill was recorded and predicted. None of the participants reported healthy problems in the previous three months.

From the analysis of the accuracy of the prediction angle data shown in Figure 8 and Tables 1 and 2, for both joints, the PSO-Takens has increased the accuracy of the prediction nearly $14.23 \pm 0.5\%$ ($n = 3$, two-sided paired t-test, $p = 0 < 0.05$), while the smoothing factor is almost unchanged. Due to the fact that the algorithm needs to store historical data, the algorithm will not immediately predict when the algorithm starts to execute. The area where the predicted value is 0 is the dead zone.

(a)

(b)

(c)

(d)
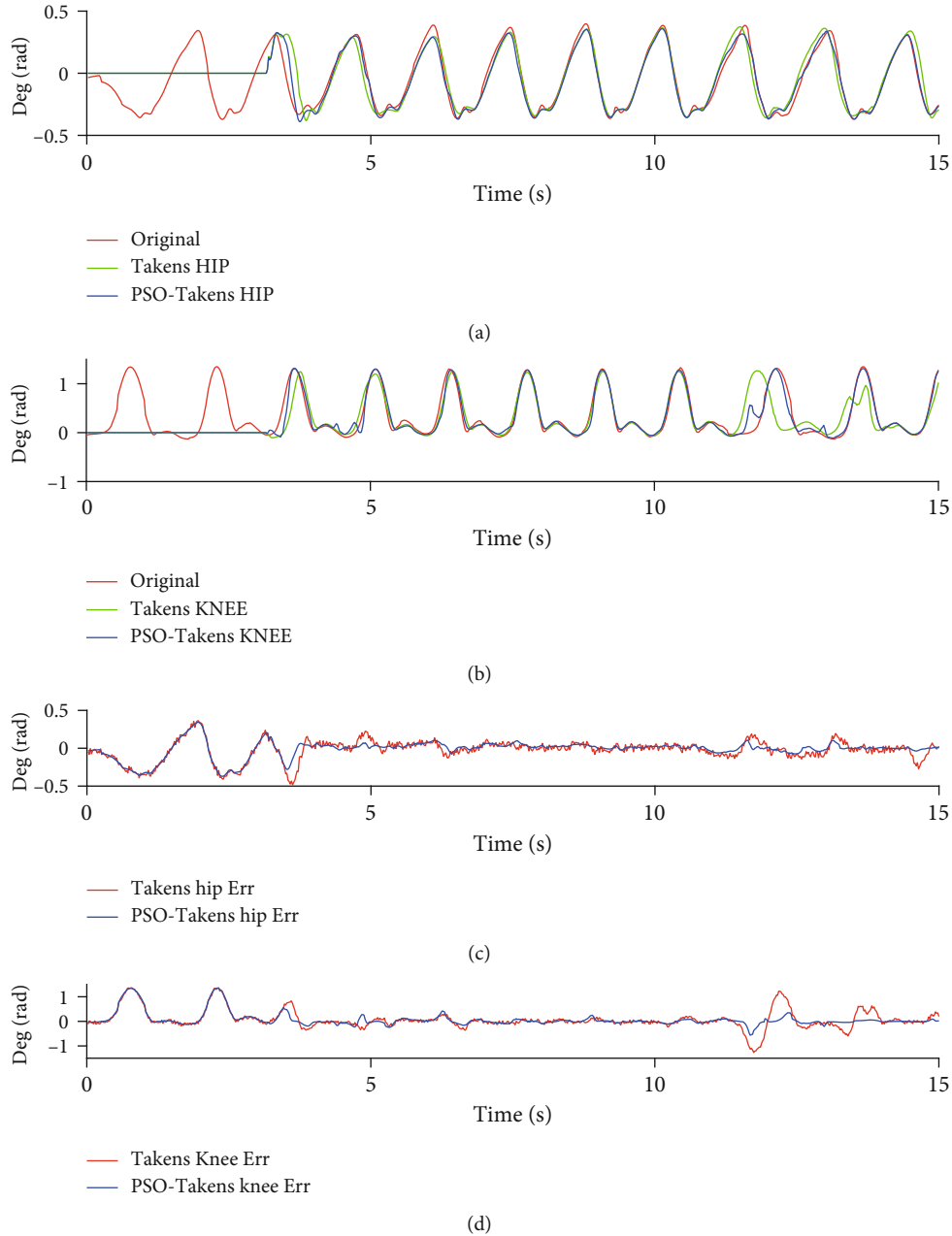
Figure 10: System joint angular output (a). System hip joint angle output (b). System knee joint angle output (c). Hip joint follow control angle error (d). Knee joint follows control angle error.

Figure 9 and Tables 3 and 4 show the performance of the two prediction algorithms under the standard and fixed frequency of the joint angle (data from [21]). The prediction accuracy in Tables 3 and 4 shows that the accuracy of the prediction is improved (hip joint from 77.85% to 88.19%, knee joint from 87.14% to 95.50%), while the smooth factor remains almost unchanged. Therefore, after the PSO-Takens algorithm is executed, for the movement data of the lower limbs, the prediction algorithm with optimized parameters becomes accurate and stable.

3.2. Prediction Algorithm Experiment Result. Since the current pose and the motion-sensing data of the previous period can only reflect the current motion state, to achieve better performance, the exoskeleton system needs to predict the posture data of the following period of time. After processing and analyzing the predicted pose data, the motion intention was judged in advance. By predicting the motion angle of the human body and introducing it into the control of the exoskeleton, the human-machine coordinated motion process of the exoskeleton can be more flexible and smoother.

In order to compare the performance of prediction algorithms and algorithm optimization in simulation, the joint data during motion and the predicted joint data were imported into the two-link model simulation system for a comparative experiment, and the evaluation method of the

(a)

(b)

(c)

(d)
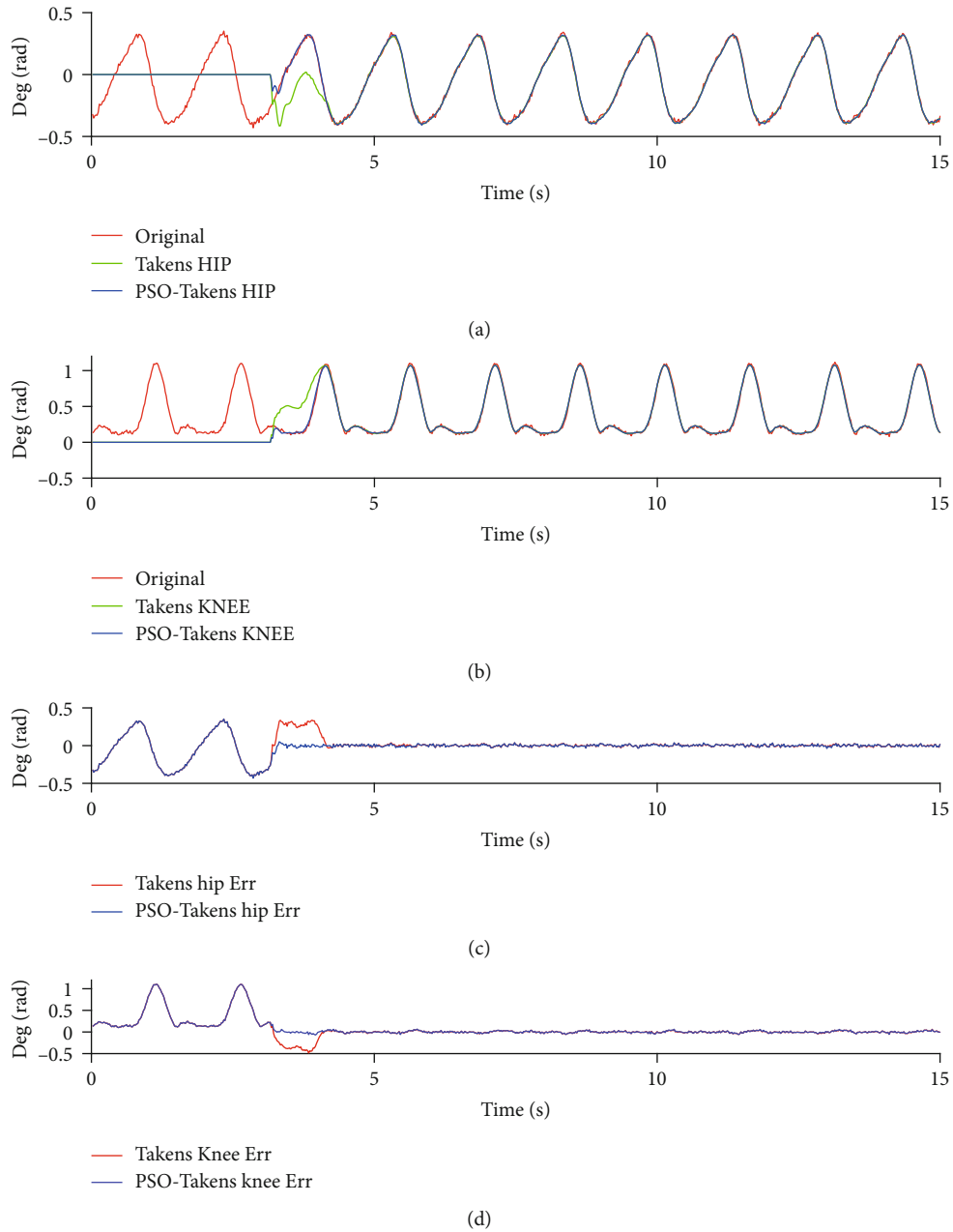
FIGURE 11: System joint angle output for standard gait data input (a). Hip joint angle output (b). Knee joint angle output (c). Hip joint follow control angle error (d). Knee joint follows control angle error.

algorithm mentioned in the second section was used to evaluate the performance of the algorithm. The experimental results are shown in Figure 10.

It can be found that the predicted data lags behind the sensor data of human motion when the system's lower limb joints are controlled to follow the human body at the beginning. Over time, the torque control algorithm with gravity compensation can control the two links to the angle predicted by the two prediction algorithms. When the state or frequency of the motion changes, the prediction error occurs, but the PSO-Takens algorithm shows a better antidisturbance ability, and the maximum error during movement is also better than the original algorithm.

It can be found from Figure 10, in the case of control the movement of the exoskeleton following the lower limbs of the human body without using prediction algorithm, due to the large deviation of the angle, a large interaction force of human-computer interaction force may occur. If the method of prediction is adopted in the control loop of the exoskeleton, the movement of the exoskeleton will be at an angle different from the actual movement of the human body at the initial stage. With the increase of time, the two links of the lower limbs of the exoskeleton gradually follow the movement of the human body and maintain a high consistency with the movement of the human body. It is undeniable that there is still a deviation between the exoskeleton and the

human body. According to formula (8), the accuracy of the prediction using the Takens method for hip joint and knee joint is 65.10% and 66.71%, while the PSO-Takens has increased to 82.13% and 83.03%. When the gait becomes stable, the error of Takens algorithms ranges from -0.13 rad to 0.18 rad (hip) and from -0.17 rad to 0.11 rad (knee). While the error of PSO-Takens ranges from -0.04 rad to 0.07 rad (hip) and from -0.05 rad to 0.09 rad (knee).

For standard gait data with a fixed frequency, inappropriate parameters of the Takens algorithm will have obvious errors at the beginning of the prediction, while the PSO-Takens algorithm will not have this problem. Figure 11 shows that the error of Takens algorithms ranges from -0.14 rad to 0.10 rad (hip) and from -0.12 rad to 0.09 rad (knee), the error of PSO-Takens algorithms ranges from -0.05 rad to 0.06 rad (hip) and from -0.03 rad to 0.04 rad (knee). According to formula (8), the Takens algorithm prediction accuracy rates of the hip and knee joints are calculated as 72.10% and 83.73%, and the PSO-Takens algorithm prediction accuracy rates are 86.07% and 94.01%, which also shows the PSO-Takens algorithm performs better in predicting such data.

4. Discussion

In the case of ignoring the elasticity coefficient and inertia coefficient, the human-computer interaction model can be simplified; in this situation, Racine [22] proposed the interaction force can be calculated as follows:

$$F_e = K(q_h - q_e). \tag{21}$$

In formula (24), F_e is the human-machine interaction force and q_h, q_e represent the human joint angle and EXO joint angle detected by a sensor, while K equals K_0/L_0 (Nm/rad·m), L_0 indicates the distance between the measurement point and the joint rotation center, and K_0 is a constant that varies from the system. Formula (24) means that if there is no angle deviation between the human body and the exoskeleton, it can be considered that the exoskeleton will not hinder the movement of the human body in the walking state of the human body, and the human-machine interaction force will close to 0.

The difficulty of the exoskeleton system controller is how to control the system to move to the target posture of the human body at the next moment. Relying on the installation of an inertial sensor on the exoskeleton has hysteresis and cannot judge the posture of the human body at the subsequent moment. This paper is devoted to the realization of human body motion prediction angle algorithm and introduces it to the control system. The simulation experiment results show that, for the angle prediction of exoskeleton, the PSO-Takens algorithm has the function of improving algorithm parameters. Whether it is linear prediction based on ARMA model LMS, RLS, or DMP [23], the algorithm parameters need to be optimized according to different systems. The PSO-Takens algorithm can deal with periodic during gait walking data, and when the body's movement law changes, such as from walking to jumping or stopping, the

accuracy of the prediction algorithm will be reduced, which is the point that the prediction algorithm needs to be improved in the future study.

5. Conclusions

In this paper, a human motion capture system is designed to acquire human walking joint data, and a method for optimizing parameters of Takens nonlinear prediction algorithm is proposed. Compared with the original Takens prediction algorithm, the prediction angle obtained by the improved prediction PSO-Takens algorithm is more closely related to the actual motion angle data of the human body, with a smaller error rate and smooth features. When the predicted sensor data from the PSO-Takens algorithm were applied to the joint angle prediction algorithm of the lower extremity exoskeleton, it can improve the accuracy of prediction and enhance the adaptability of the exoskeleton and human body.

Data Availability

The EXO and predicted sensor data based on different algorithms used to support the findings of this study are available from the corresponding author upon request.

Conflicts of Interest

The authors declare that there is no conflict of interests regarding the publication of this paper.

Acknowledgments

References

[1] J. Wesslén, "Exoskeleton exploration: research, development, and applicability of industrial exoskeletons in the automotive industry, [M.S. thesis]," *Master's Thesis, School of Engineering in Jönköping*, Jönköping, Sweden, 2018.

[2] A. Esquenazi, M. Talaty, A. Packel, and M. Saulino, "The ReWalk powered exoskeleton to restore ambulatory function to individuals with thoracic-level motor-complete spinal cord injury," *American Journal of Physical Medicine & Rehabilitation*, vol. 91, no. 11, pp. 911–921, 2012.

[3] D. P. Yang, L. Jiang, J. D. Zhao, and H. Liu, "Prosthetic hand control based on intelligent control of EEG," *Journal of Jilin University*, vol. 38, no. 5, pp. 1225–1230, 2008.

[4] Y. H. Yin, Y. J. Fan, and L. D. Xu, "EMG and EPP-integrated human machine interface between the paralyzed and rehabilitation exoskeleton," *IEEE Transactions on Information Technology in Biomedicine*, vol. 16, no. 4, pp. 542–549, 2012.

[5] A. M. Dollar and H. Herr, "Lower extremity exoskeletons and active orthoses: challenges and state-of-the-art," *Transactionson Robotics*, vol. 24, no. 1, pp. 144–158, 2008.

[6] W. Wei, S. Zha, Y. Xia, J. Gu, and X. Lin, "A hip active assisted exoskeleton that assists the semi-squat lifting," *Applied Sciences*, vol. 10, no. 7, p. 2424, 2020.

[7] R. Huang, H. Cheng, H. Guo, Q. Chen, and X. Lin, "Hierarchical interactive learning for a human-powered augmentation lower exoskeleton," in *IEEE International Conference on Robotics and Automation (ICRA)*, pp. 257–263, Stockholm, 2016.

[8] P. Zhou, Y. Yang, L. Ma, and Y. Shu, "Human gait awareness system design of exoskeleton robot," *Sensor and Microsystem*, 2016.

[9] Z. Cao, X. Ye, Y. C. Wang, L. J. Cheng, and H. S. Zhu, "Study of swing leg follow-up control of exoskeleton based on Kalman prediction," in Science Technology and Engineering, 2016.

[10] F. Ernst, A. Schlaefer, S. Dieterich, and A. Schweikard, "A fast lane approach to LMS prediction of respiratory motion signals," *Biomedical Signal Processing and Control*, vol. 3, no. 4, pp. 291–299, 2008.

[11] P. R. Diniz, *Adaptive flitering: algorithms and practical implementation second edition*, Kluwer Academic Publisher Norwell, 2004.

[12] G. V. Moustakides, "Study of the transient phase of the forgetting factor RLS," *IEEE Transactions on Signal Processing*, vol. 45, no. 10, pp. 2468–2476, 1997.

[13] Y. Yang, P. Zhou, L. Ma et al., "Gait recognition and trajectory prediction of lower limb load exoskeleton," in *2016 35th Chinese Control Conference (CCC)*, Chengdu, China, July 2016.

[14] P. Duan, S. Li, Z. Duan, and Y. Chen, "Bio-inspired real-time prediction of human locomotion for exoskeletal robot control," *Applied Sciences*, vol. 7, no. 11, p. 1130, 2017.

[15] T. Hayashi, H. Kawamoto, and Y. Sankai, "Control method of robot suit HAL working as operator's muscle using biological and dynamical information," in *2005 IEEE/RSJ International Conference on Intelligent Robots and Systems*, Edmonton, Alta., Canada, August 2005.

[16] J. Kennedy and R. Eberhart, "Particle swarm optimization," in *Proceedings of ICNN'95 - International Conference on Neural Networks*, pp. 1942–1948, Perth, WA, Australia, 1995.

[17] K. Gao, Z. Cao, Z. C. Le Zhang, Y. Han, and Q. Pan, "A review on swarm intelligence and evolutionary algorithms for solving flexible job shop scheduling problems," *IEEE/CAA Journal of Automatica Sinica*, vol. 6, no. 4, pp. 875–887, 2019.

[18] J. Wang and T. Kumbasar, "Parameter optimization of interval type-2 fuzzy neural networks based on PSO and BBBC methods," *Acta Automatica Sinica*, vol. 6, no. 1, pp. 247–257, 2019.

[19] A. D. Grant, "Gait Analysis: Normal and Pathological Function," *Jama*, vol. 304, no. 8, p. 907, 2010.

[20] W. Huo, *Robot Dynamics and Control*, Higher Education Press, Beijing, 2005.

[21] Y. L. Han and X. S. Wang, "Research on the biomechanics of human walking lower limbs," *Science China: Technical Sciences*, vol. 41, no. 5, pp. 592–601, 2011.

[22] J. L. C. Racine, *Control of a lower extremity exoskeleton for human performance amplification*, University of California, Berkeley, 2003.

[23] A. J. Ijspeert, J. Nakanishi, H. Hoffmann, P. Pastor, and S. Schaal, "Dynamical movement primitives: learning attractor models for motor behaviors," *Neural computation*, vol. 25, no. 2, pp. 328–373, 2013.

Research Article

Development of a Robotic Catheter Manipulation System Based on BP Neural Network PID Controller

Xu Ma [iD],[1] Jinpeng Zhou [iD],[1] Xu Zhang [iD],[2] and Qi Zhou [iD][2]

[1]*Tianjin Key Laboratory for Control Theory & Applications in Complicated Industry Systems, College of Electrical and Electronic Engineering, Tianjin University of Technology, Tianjin, China 300384*
[2]*Tianjin Key Laboratory of High Speed Cutting and Precision Machining, School of Mechanical Engineering, Tianjin University of Technology and Education, Tianjin, China 300222*

Correspondence should be addressed to Xu Ma; maxu2015@aliyun.com and Xu Zhang; 52914262@qq.com

In the process of artificial interventional therapy, the operation of artificial catheter is not accurate, which will bring strong radiation damage to surgeons. The purpose of this study is to develop a catheter operating system of surgical robot to assist doctors in remote operation and avoid the influence of radiation. BP neural network plays an important role in the flexibility and rapidity of control. According to the actual output of the system, the control parameters of the controller are constantly adjusted to achieve better output effect. This paper introduces the practical application of BP neural network PID controller in the remote operation of the system and compares with the traditional PID controller. The results show that the new control algorithm is feasible and effective. The results show that the synchronization performance of BP neural network PID controller is better than that of traditional PID controller.

1. Introduction

Vascular interventional surgery in medicine, whether from the diagnosis or the actual operation, has been welcomed by the society. However, as a new way of operation, it needs surgeons with high skill to intubate in vivo. In addition, the interventional operation is carried out in the patient's body, and the specific process cannot be directly observed by the doctor. During the operation, any incorrect operation may cause damage to the patient. According to the data survey, a surgeon with rich clinical experience can achieve an operation accuracy of about 2 mm in the interventional operation. However, the contact force between the blood vessels in the patient's body and the surgical catheter cannot be perceived by the doctor [1]. In addition, X-ray camera is needed for angiography during the operation, and long-term radiation will cause harm to patients. Although doctors wear protective clothing, it is difficult to protect their hands and faces from X-ray radiation. In order to solve these problems effectively, we need better medical equipment to assist doctors [2]. The robot system has the advantages

of high control accuracy and remote control. Therefore, in this paper, according to the needs of interventional surgery, combined with the robot system, the master-slave operating system of interventional surgery robot which can assist doctors in interventional surgery is designed [3].

There are a large number of products and research reports in the field of surgical robots [4]. One of the most popular commercial products is the Sensei robotic catheter system designed and developed by Hansen, which is mainly to help doctors push the catheter. Compared with the manual push, the Sensei robot catheter system can make the push process more stable and rapid, and the operation accuracy is higher. The remote control method can reduce the original radiation impact of doctors. Another commercial product is amigo, which is mainly designed to solve the problem that the sheath of the surgical catheter has multiple degrees of freedom and the force detection at the end of the catheter is difficult. The robotic catheter system has an additional mechanical sheath to guide the surgical catheter [5]. The pushing process of the surgical catheter is controlled by the console at the host end.

In 2010, Magnetecs Company got the design inspiration from the treatment of atrial fibrillation and designed a system that can use magnetic field to guide, control, and image the surgical catheter in British. The system consists of four permanent magnets placed around the table, and the top of the designed surgical catheter is equipped with magnets. The catheter moves in the magnetic field under the control of the console at the main end. With the popularity of surgical robots, stereotactic companies have also developed a magnetic navigation system: Stereotactic Niobe. The system can generate controllable magnetic field by two permanent magnets on both sides of the operating table, reduce the number of permanent magnets, and make the navigation of magnetic guide wire more convenient and accurate in percutaneous coronary intervention (PCI). In other universities, Ma and others developed a catheter navigation system that can be operated remotely [6]. The system allows the main end operator to use the real surgical catheter instead of the handle to control the movement of the surgical catheter in the patient's body. This progress can make the doctor's original surgical experience applied to the actual operation. However, the system is lack of force feedback, which operational safety cannot be guaranteed. In order to simulate the use of doctors' hands, Bao et al. proposed a special linear step structure in Nagoya University. Based on the above products and academic research, the main problem lies in the security of system operation [8]. During the operation, it is an important step to monitor the force information of the catheter inserted into the blood vessel to ensure the safety of the operation. However, in these systems, there is a lack of effective measurement of conduit stress [8].

In this paper, according to the operation needs of vascular interventional surgery, a new robot operation system of surgical catheter is designed and constructed. Compared with the abovementioned surgical robot system, the system is also divided into two parts: one is the main end of the robot catheter manipulating system, as shown in Figure 1(a), which is mainly used to collect the axial displacement and radial rotation movement of the operator, consisting of pressure sensor, torque sensor, stepping motor, and controller. The other is the slave end of the robot catheter manipulating system, which is mainly used for the insertion and twisting operation of the conduit is shown in Figure 1(b). In addition, aiming at the safety of force detection, the research team designed a new force feedback detection device, which can detect the change of contact force between the catheter and the vessel wall during the insertion of the surgical catheter from the end of the system [9], and timely provide force feedback to the main end of the system to ensure the safety of the operation [10].

2. Robotic Catheter Manipulation System

In this paper, the main mode of master-slave operation is adopted. The main end of the system is the surgeon's console, and the slave end of the system is the surgical catheter console. Setting the mobile platform of the main end doctor console and the slave end catheter console to maintain the same displacement, speed and rotation angle will make the operation more stable and convenient [11]. At the same time,

the same digital signal processor (Ti, TMS320F28335) is used as the control unit of the master doctor console and the slave catheter console [12]. The main end and the slave end of the surgical robot system establish a communication network through the Internet, and the communication diagram is shown in Figure 2. The console at the main end of the system transmits the axial displacement and radial rotation motion information of the mechanical handle to the catheter console at the slave end to perform specific operation. Set the baud rate of the communication serial port between the master and slave of the system to 19200 B/s [13].

2.1. The Surgeon's Console. The doctor's console at the main end of the system is shown in Figure 1(a). Two independent sensors are used to measure the axial and radial movement of the mechanical handle. The switch on the left mechanical handle is used to control the two graspers on the console of the slave end conduit of the system to help realize the insertion process of the slave end conduit. The mechanical handle on the right is used to collect the specific actions of the surgeon, including the axial movement and the radial movement. The moving part of the slave end conduit console maintains the same amount of movement as the right mechanical handle of the main end console. The mechanical handle on the right side of the main end is supported by the mechanical bearing and connected with the load cell through the coupling; the pulley are fixed on the mechanical handle for the convenience of force transmission.

The measurement process of the axial movement of the mechanical handle is as follows. When the doctor pulls or pushes the right mechanical handle, the load cell measures the pull/push force. According to the thrust value, the corresponding displacement of the mobile platform is calculated, that is, the mechanical handle can follow the synchronous movement of the surgeon's hand. By adjusting the moving speed of the mobile platform, the force feedback of the system can be realized. The displacement and speed information of the system's main end console is sent to the system's slave end console, and then, the slave end catheter console and the main end doctor console are set to keep synchronous motion. When the doctor turns the mechanical handle, the mechanical encoder installed under the main end moving platform will drive the encoder, then measure the actual angle, and transmit the measured value to the slave end catheter console for synchronous movement. In this way, the implementation process of the master side operation in the slave side is realized.

2.2. The Surgical Catheter Console. Figure 1(b) shows the conduit console at the slave end of the system. The device is placed next to the patient. The catheter console can assist doctors to push the catheter. It has two degrees of freedom: axial displacement and radial rotation. Two clips are placed in the pushing guide, and the switch of the clips is controlled by the button on the left mechanical handle of the main end. When the surgical catheter is clamped by the grasper 1 and the jacket together, the movement of the main end doctor to the mechanical handle can be realized, and the synchronous movement of the slave end surgical catheter along the

(a) The main end

(b) The slave end
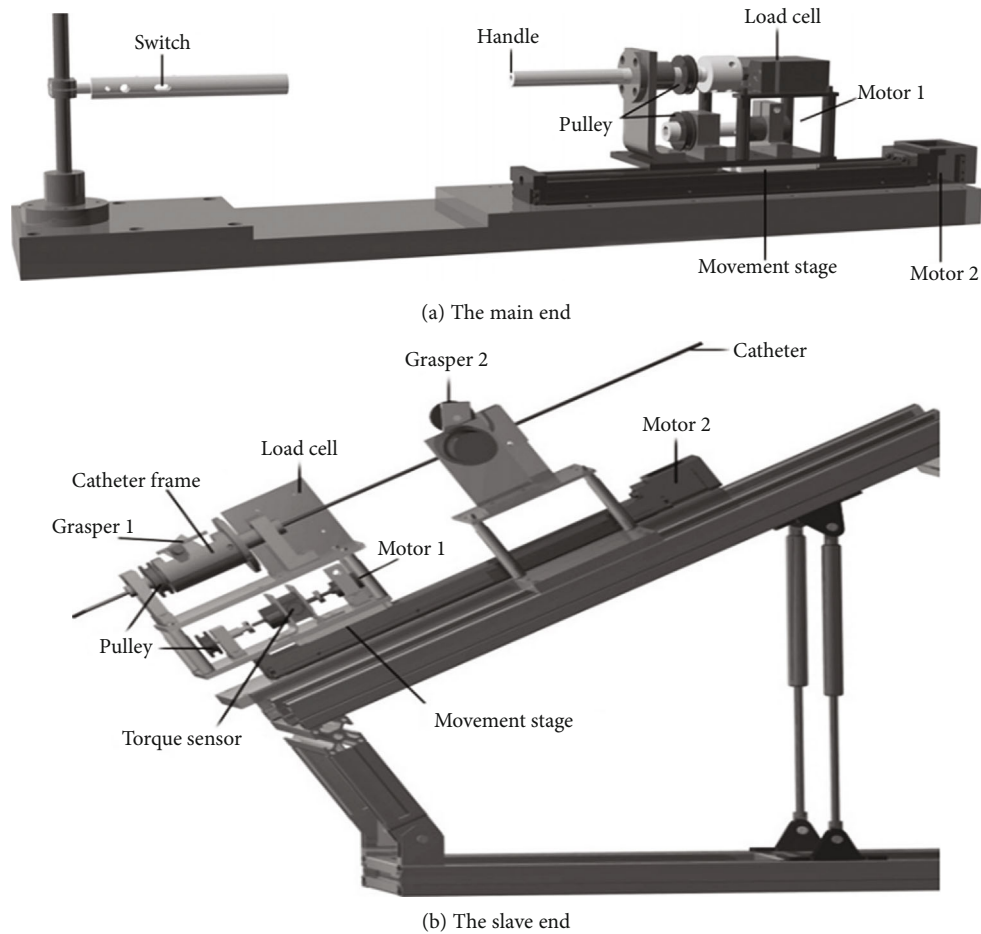
Figure 1: The robotic catheter manipulating system.
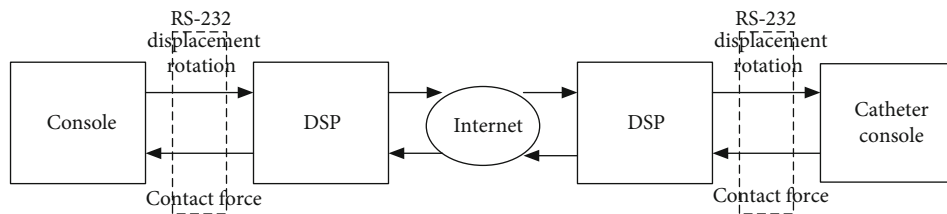
Figure 2: The communication diagram.

axial and radial directions can be driven [14]. When the surgical catheter is clamped by the grasper 2, the catheter maintains its position, and then, the catheter driving part at the end can move freely to prepare for the next push. The pushing action of the catheter from the end of the operation is shown in Figure 3.

In order to achieve the axial movement of the conduit, all the driving components are fixed on the mobile platform (the flat plate under the motor 1). The mobile platform is driven by a stepping motor (motor 2) to achieve axial movement. The radial movement of the conduit needs to be realized by the DC motor (motor 1), which is realized by the jacket connected by two pulleys. When the surgical catheter is fixed by the grasper 1, the surgical catheter is driven by the motor 1 to rotate.

The robot system uses the torque sensor installed at the slave end of the system to measure the actual rotation information of the catheter during the operation. The torque data will be sent to the surgeon's console at the main end, and the actual torque will be fed back to the surgeon. The specific working process is that the torque sensor is connected with the motor 1 and the pulley on a common shaft. In the process of pushing conduit, the resistance of conduit rotation can be transmitted to the torque sensor through the coupling pulley, and then, the actual resistance value can be measured by the torque sensor.

In order to measure the axial resistance of the catheter during pushing, a new force measuring mechanism is designed, which is shown in Figure 4 [15]. Use the load cell fixed on the mobile platform to measure the resistance value.
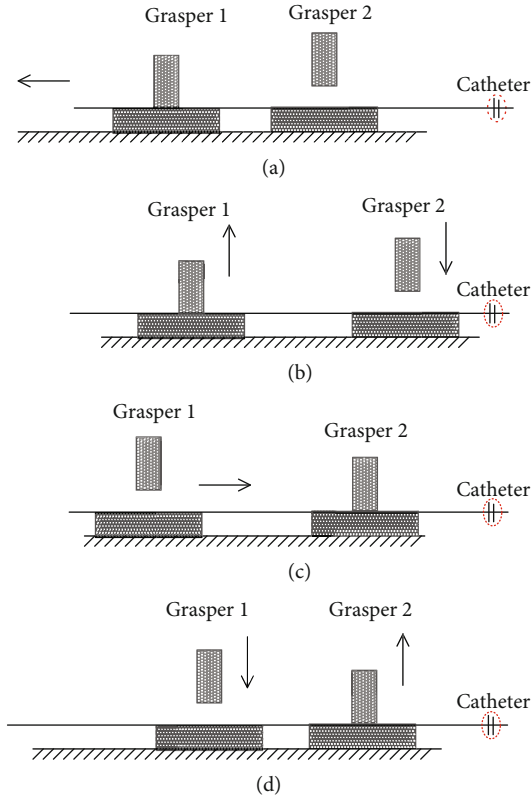
Figure 3: Pushing action.

The measured resistance value is sent to the main end of the system. Combined with the push/pull value of the doctor to the mechanical pusher, the system force feedback is realized.

2.3. Control of the System. At the slave end of the system, each motor is coupled to the coder. The speed and angle of rotation of these motors can be measured. Therefore, it is necessary to design control algorithms to improve the operation accuracy and motion performance of surgical robot system in remote operation. At the main end of the system, the mechanical handle should be able to move smoothly with the surgeon's hand. This means that the output displacement/speed of the stepper motor should be the same as or similar to the input displacement/speed of the surgeon's hand. The speed and displacement of the stepping motor can be measured by an encoder coupled to the motor 2 in Figure 1(b). Therefore, it is necessary to determine the axial and radial dynamic models of the surgical robot system and establish the relationship between the input force of the main end and the displacement output of the stepper motor. In terms of synchronous tracking performance, a PID controller based on BP neural network is adopted to improve the accuracy of axial displacement during remote operation [16].

3. BP Neural Network

Due to the high requirements for the positioning of surgical catheter in interventional surgery, it is difficult to accurately establish the control model of interventional surgery robot system due to the influence of nonlinear factors such as blood flow and vascular wall in human blood vessels, which has the risk of vascular damage. Based on the analysis of the related motion control algorithm, combined with the technical requirements of catheter propulsion accuracy and collision force in interventional surgery, a PID controller based on BP neural network is designed. Through MATLAB simulation, the control accuracy of the designed controller is verified.

3.1. Neural Network Theory. Figure 5 shows a simple artificial neuron model, the "M–P neuron" model. In this neuron model, each neuron receives input signals from other n neurons. After entering the neuron, these input signals will be weighted and then transmitted to the next step [17]. In the process of transmission, the weighted signal value is compared with the threshold set by neurons. If not, the neurons are not activated if they are not transferred down [18].

The model consists of multiple inputs x_i, $i = 1, 2, \cdots, n$ and a single output y. The expression for y is as follows:

$$y = f\left(\sum_{i=1}^{n} w_{ji} x_i - \theta_j\right), \tag{1}$$

where θ_j is the threshold, w_{ji} is the connection weight (w_{ji} is positive in the excited state; w_{ji} is negative in the suppressed state), n is the number of input signals, and $f()$ is the activation function.

3.2. The Definition and Characteristics of BP Neural Network. BP neural network is a kind of feedforward multilayer network, including input layer, implicit layer, and output layer [19]. The neurons in the same layer of BP neural network are not connected with each other, and the neurons in the upper and lower layers are connected [20].

Figure 6 shows the network structure of simple BP neural network. It consists of input layer, hidden layer, and output layer. The connection weights of the j-th neuron in the input layer and the i-th neuron in the hidden layer are w_{ij}, and the weight between the i-th neuron in the hidden layer and the l-th neuron in the output layer is w_{li}. The input value of the i-th neuron in the hidden layer is $\text{net}_i^{(2)} = \sum_{j=1}^{m} w_{ij}^{(2)} o_j^{(1)}$. The input value of the l-th neuron in the output layer is $\text{net}_l^{(3)} = \sum_{i=1}^{q} w_{li}^{(3)} o_i^{(2)}$. Finally, the output value of the whole neural network is obtained after the weighted sum calculation [21].

BP neural network has the following characteristics in information processing [22]:

(1) Distributed storage. The weights of neurons in each layer of BP neural network represent the information of the whole network. Therefore, all information is distributed and stored through the network, and its fault tolerance is relatively high

(2) Parallel processing of information. All neurons in the BP neural network are relatively independent. The neurons in the same layer are simultaneously processed by signal processing, and the whole network has better real-time performance
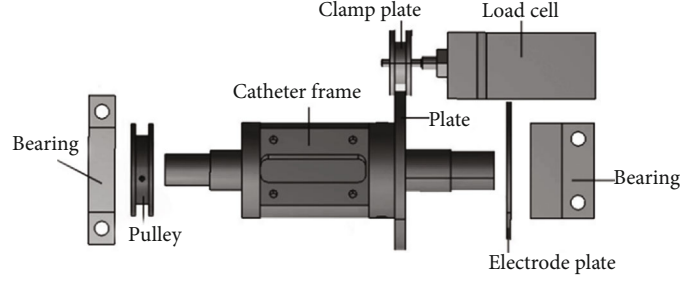
Figure 4: Axial force measurement mechanism.
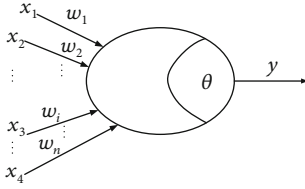
Figure 5: The model of artificial neuron.

(3) Adapt ability. The connection strength of the BP neural network increases with use, which increases the sensitivity of each neuron

3.3. Self-Learning of BP Neural Network. The BP neural algorithm proposed in this paper is based on gradient descent that is to adjust the parameters in the direction of negative gradient of the expected target. The details are as follows: three layer network structures, such as m neurons in the input layer, q neurons in the hidden layer, and r neurons in the output layer.

3.3.1. Information Forward Propagation. The output of the j-th node of the input layer is as follows:

$$o_j^{(1)} = x(j), j = 1, 2, \cdots, m. \tag{2}$$

Then, the output of the input layer is weighed and summed; it is the input of the i-th neuron of the hidden layer.

$$net_i^{(2)} = \sum_{j=1}^{m} w_{ij}^{(2)} o_j^{(1)}, i = 1, 2, \cdots, q. \tag{3}$$

After activating the function operation, the hidden layer output is as follows:

$$o_i^{(2)} = f\left(net_i^{(2)}\right), i = 1, 2, \cdots, q. \tag{4}$$

The superscripts (1), (2), and (3) represent the input layer, the hidden layer, and the output layer, respectively. $W_{ij}^{(2)}$ is the weight of the input layer to the hidden layer, and $f()$ is the hidden layer activation function.

The output of the hidden layer is the input of the l-th neuron of the output layer after the weight summation calculation.

$$net_l^{(3)} = \sum_{i=1}^{q} w_{li}^{(3)} o_i^{(2)}, l = 1, 2, \cdots, r. \tag{5}$$

The output of the output layer is as follows:

$$y_l = o_l^{(3)} = g\left(net_l^{(3)}\right), l = 1, 2, \cdots, r, \tag{6}$$

where $w_{li}^{(3)}$ is the weight of the hidden layer to the output layer; g is the output layer excitation function.

3.3.2. Error Backpropagation [23]. If there is a large error between the actual output value and the initial set value in BP neural network, the closed-loop regulation will feed the error back to the initial end of the system for regulation. At the same time of system output, the output value of the system gradually approaches to the initial set value by continuously adjusting the weight of each network in the system. The adjustment block diagram is shown in Figure 7.

In this paper, the mean square error of BP network is selected as the standard function of evaluation, and the weight of each layer network in the system is adjusted. The mean square error is defined as follows:

$$E = \frac{1}{r}\sum_{l=1}^{r} e_l^2 = \frac{1}{r}\sum_{l=1}^{r} \left(y_l^* - y_l\right)^2, \tag{7}$$

where y_l^* is the given value of the l-th output node; y_l is the actual value of the l-th output node.

Let k be the number of iterations; then, the implicit layer to output layer weight correction formula is as follows:

$$w_{li}^{(3)}(k+1) = w_{li}^{(3)}(k) + \Delta w_{li}^{(3)} = w_{li}^{(3)}(k) - \eta \frac{\partial E(k)}{\partial w_{li}^{(3)}(k)}, \tag{8}$$

where η is a constant, indicating the learning rate, $l = 1, 2, \cdots, r, i = 1, 2, \cdots, q.$

The total error surface's gradient vector replace the output value y_l into Equation (8). Then we can adjust the hidden layer's connection weight to the output layer. Similarly, the
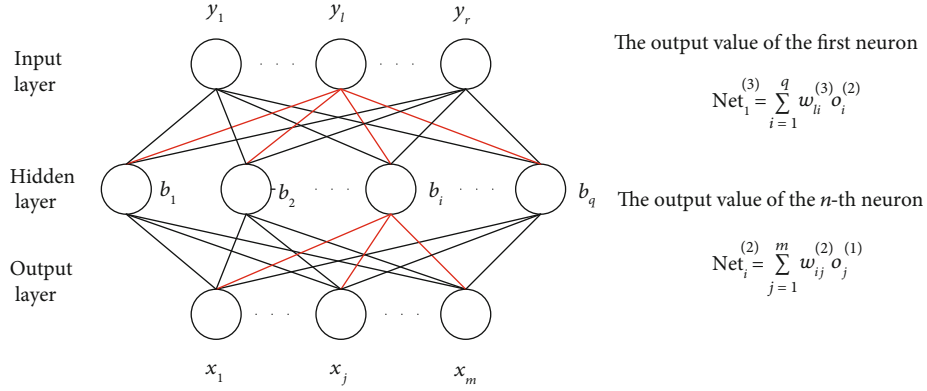
Figure 6: The formation of BP neural network.

The output value of the first neuron

$$\mathrm{Net}_1^{(3)} = \sum_{i=1}^{q} w_{li}^{(3)} o_i^{(2)}$$

The output value of the n-th neuron

$$\mathrm{Net}_i^{(2)} = \sum_{j=1}^{m} w_{ij}^{(2)} o_j^{(1)}$$
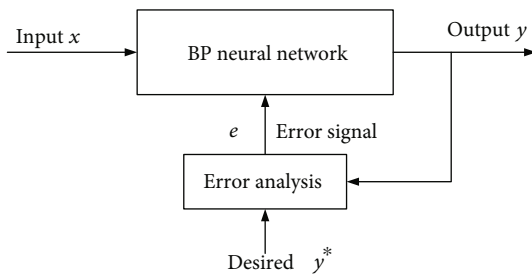
Figure 7: The adjustment process of BP neural network.
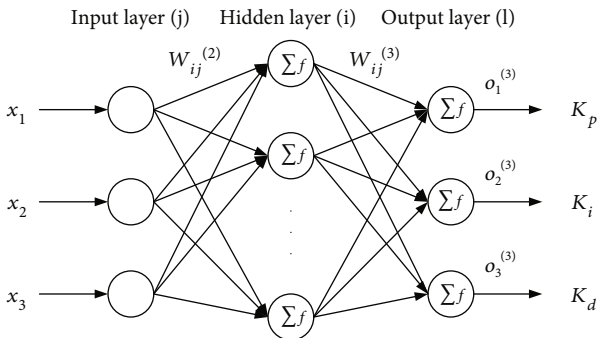
Figure 8: The diagram of BP neural network structure.

connection weight from input layer to hidden layer can be adjusted to gradually reduce the error of the whole system, so that the system can meet the expected requirements.

Figure 8 shows the network topology of BP neural network PID controller. The input signal of the system enters the BP neural network through the network input layer. After weighted processing, it is compared with the neuron threshold and then enters the excitation function as the output of the input layer, that is, the input of the hidden layer. After processing, the output signal of the hidden layer is obtained. After entering the output layer for processing, the final output value of the system is obtained. The actual output value is compared with the expected value, and then, the error signal is fed back from the output layer to the hidden layer twice and then transmitted back to the input layer. In the whole feedback regulation process, the connection weights

of each layer of neurons are modified by the error gradient descent algorithm, so that the actual output of the input signal can be corrected after entering the neural network again, so as to achieve the purpose of self-tuning of PID control parameters and finally achieve the good response of the whole system.

The topological structure of BP neural network proposed in this paper consists of three input nodes, six implicit nodes, and three output nodes. The input signal is the motion state and system error of the motor system, and the output signal is the three parameters of PID.

3.3.3. Network Information Forward Propagation Calculation.

$$\text{Select three inputs as } \begin{cases} o_2^{(1)} = e(k), \\ o_2^{(1)} = e(k-1), \\ o_3^{(1)} = 1. \end{cases} \tag{9}$$

The input and output of the hidden layer are as follows:

$$\mathrm{net}_i^{(2)}(k) = \sum_{j=0}^{m} w_{ij}^{(2)} o_j^{(1)}, \tag{10}$$

$$o_i^{(2)}(k) = f\left(\mathrm{net}_i^{(2)}(k)\right), i = 1, 2, \cdots, \tag{11}$$

$$\begin{cases} o_i^{(2)}(k) = f\left(\mathrm{net}_i^{(2)}(k)\right) \\ o_6^{(2)}(k) = 1 \end{cases}, i = 1, 2, \cdots, \tag{12}$$

where j denotes the number of the input layer node; i denotes the number of the hidden layer; superscripts (1), (2), and (3) decibels represent the input, implicit, and output layers, respectively; $w_{ij}^{(2)}$ is the input layer; j is the weight value of the i-th hidden layer's node.

The excitation function $f(x)$ is a hyperbolic tangent function:

$$f(x) = \tanh(x) = \frac{e^x - e^{-x}}{e^x + e^{-x}}. \tag{13}$$

3.3.4. Network Error Backpropagation Calculation. The gradient descent algorithm is used to adjust the weight coefficient value, and the performance index function is selected as follows:

$$E = \frac{1}{2} e^x(k). \tag{14}$$

Let the error function E adjust in the direction of the fastest change to reduce, that is, adjust the network connection weight coefficient according to the negative gradient direction of the error function E, so that the error converges gradually. There is

$$\Delta w_{li}^{(3)}(k) = -\eta \frac{\partial E(k)}{\partial w_{li}^{(3)}}. \tag{15}$$

In order to speed up the error correction and reduce the probability of the system falling into the local minimum, the momentum factor is added. There is

$$\Delta w_{li}^{(3)}(k) = -\eta \frac{\partial E(k)}{\partial w_{li}^{(3)}} + \alpha \Delta w_{li}^{(3)}(k-1), \tag{16}$$

where η is the learning rate and α is the momentum factor.

According to the gradient descent method,

$$\frac{\partial E(k)}{\partial w_{li}^{(3)}} = \frac{\partial E(k)}{\partial y(k)} \cdot \frac{\partial y(k)}{\partial u(k)} \cdot \frac{\partial u(k)}{\partial o_l^{(3)}(k)} \cdot \frac{\partial o_l^{(3)}(k)}{\partial \mathrm{net}_l^{(3)}(k)} \cdot \frac{\partial \mathrm{net}_l^{(3)}(k)}{\partial w_{li}^{(3)}}. \tag{17}$$

In Equation (17), the variable $\partial y(k)/\partial u(k)$ is unknown, but $u(k)$, $y(k)$, and the relative change amount can be obtained, so

$$\frac{\partial y(k)}{\partial u(k)} = \frac{y(k) - y(k-1)}{u(k) - u(k-1)}. \tag{18}$$

Since $u(k) = u(k-1) + o_1^{(3)}(e(k) - e(k-1)) + o_2^{(3)}e(k) + o_3^{(3)}(e(k) - 2e(k-1) + e(k-2))$, so

$$\begin{cases} \dfrac{\partial u(k)}{\partial o_1^{(3)}(k)} = e(k) - e(k-1), \\[2mm] \dfrac{\partial u(k)}{\partial o_2^{(3)}(k)} = e(k), \\[2mm] \dfrac{\partial u(k)}{\partial o_3^{(3)}(k)} = e(k) - 2e(k-1) + e(k-2). \end{cases} \tag{19}$$

3.4. The Structure of BP Neural Network PID Controller. In order to improve the control system of traditional PID controller, other intelligent optimization algorithms are combined with traditional PID controller to achieve better control effect. Among them, BP neural network algorithm as a classic intelligent optimization algorithm has the characteristics of distributed storage, parallel processing, and adaption, which makes up for the shortcomings of traditional PID controller. Therefore, the combination of BP neural network algorithm and traditional PID control can achieve the purpose of optimizing the control effect. Through the adaptive characteristics of BP algorithm, combined with input and output samples, the BP neural network model is trained, and the connection weights in the network are constantly adjusted to make the output meet the expected requirements and reduce the system error. This combined optimization control method, especially for the servo motor control system, can effectively solve the design problems that the motor PID control parameters are difficult to adjust and the overall control of the system cannot achieve the desired effect.

Figure 9 shows the system diagram of BP neural network PID controller. It is an organic combination of traditional PID controller and BP neural network. The specific contents of each part are as follows:

3.4.1. BP Neural Network Part. BP neural network is an important part of BP neural network PID system. The main function is to modify the connection weight of each layer of neural network according to the actual input and output through the self-learning characteristics of BP algorithm, so as to achieve the purpose of adjusting the output, that is to adjust the control parameters of PID controller in real time and optimize the performance of the whole control system. The output signal of input layer in BP neural network corresponds to three control parameters K_p, K_i, and K_d in traditional PID controller. The adjustment process of control parameters is shown in Figure 10.

3.4.2. Traditional PID Part. BP neural network is only an abstract optimization algorithm, and the actual control of the motor still depends on the traditional PID controller. Therefore, the traditional PID part is an indispensable part of the BP neural network PID system. The specific control of the motor is still dependent on the closed-loop control of the traditional PID controller, so that the motor's speed output follows the input.

3.5. BP Neural Network PID Controller. Taking the axial motion of the surgical robot designed in this paper as an example, the dynamic analysis is carried out. Its axial movement is driven by Maxon EC32 motor. The motor drives the system to move back and forth from the whole clamping catheter platform at the end, so as to realize the purpose of pushing the surgical catheter. According to Newton's second law of physics, after simplifying the reference factors of the system, the dynamic model of the axial motion of the surgical robot is established as follows:

$$f(t) = m\ddot{x}(t) + c\dot{x}(t) + kx(t), \tag{20}$$

where $f(t)$ is the motor driving force, $x(t)$ is the displacement of this motion, $\dot{x}(t)$ is the motion velocity, $\ddot{x}(t)$ is the motion acceleration, and Equation (20) illustrates the relationship of motor drive force and output displacements.
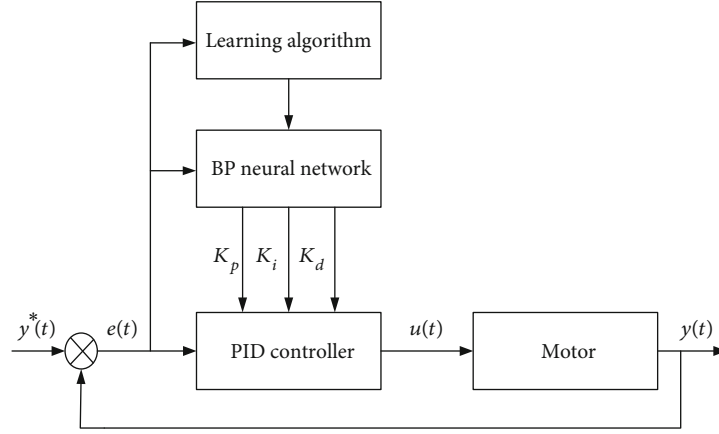
FIGURE 9: The control system of BP neural network PID controller.
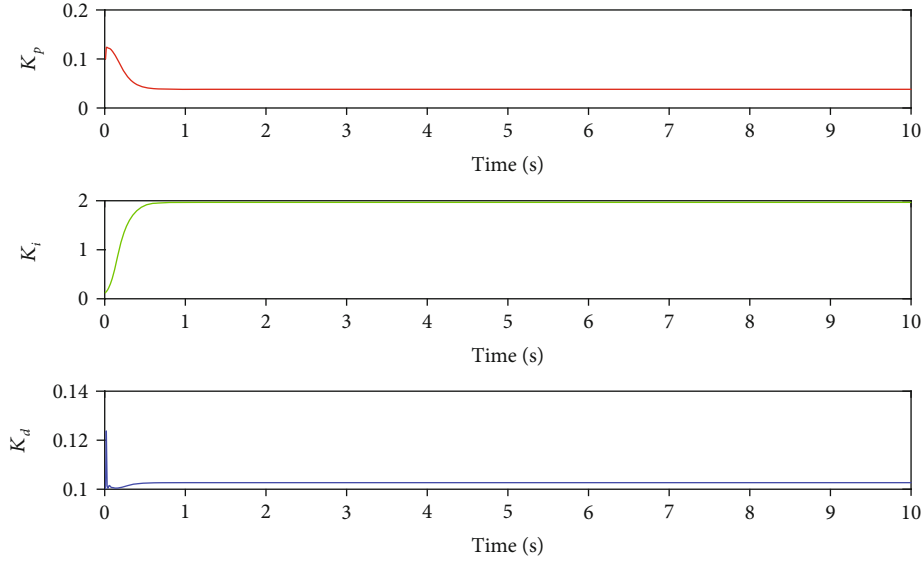
FIGURE 10: Intelligent adjustment output of parameters K_p, K_i, and K_d.

If $x_1(t) = x(t)$ and $x_2(t) = \dot{x}(t)$, then,

$$
\begin{cases}
\dot{x}(t) = AX(t) + Bu(t), \\
y(t) = CX(t),
\end{cases}
\tag{21}
$$

where $X(t) = \begin{bmatrix} x_1(t) \\ x_2(t) \end{bmatrix}$, $A = \begin{bmatrix} 0 & 1 \\ -k/m & -c/m \end{bmatrix}$, $B = \begin{bmatrix} 0 \\ 1/m \end{bmatrix}$,

and $C = \begin{bmatrix} 1 & 0 \\ 0 & 0 \end{bmatrix}$.

That m is the mass of the overall axial movement of the push platform, c is the overall damping coefficient of the push platform, and k is the overall elastic coefficient of the push platform. From Equation (22), it can be concluded that the transfer function of the axial movement of the push device is as follows:

$$
H(s) = \frac{m}{ms^2 + cs + k}.
\tag{22}
$$

3.6. Simulation Analysis. Taking the axial motion of the interventional robot as an example, the step signal $y = 1$ is used to simulate the axial expected displacement of the main hand catheter during the actual operation of the doctor. Take Equation (22) as $m = 1\,\text{kg}$, $c = 0.05\,\text{N}/(\text{m/s})$, and $k = 1.5\,\text{N/m}$. After MATLAB simulation, the simulation results shown in Figure 11 are obtained and the results are in BP for comparison control effects.

Figure 11 shows the simulation comparison between BP neural network PID control and traditional PID control. By comparing the simulation results, it can be found that the overshoot of the traditional PID control system is 22%, while that of the newly designed BP neural network PID control system is only 12%. Compared with the traditional PID control system, the adjustment time and precision of BP neural network PID control system have been greatly improved. In
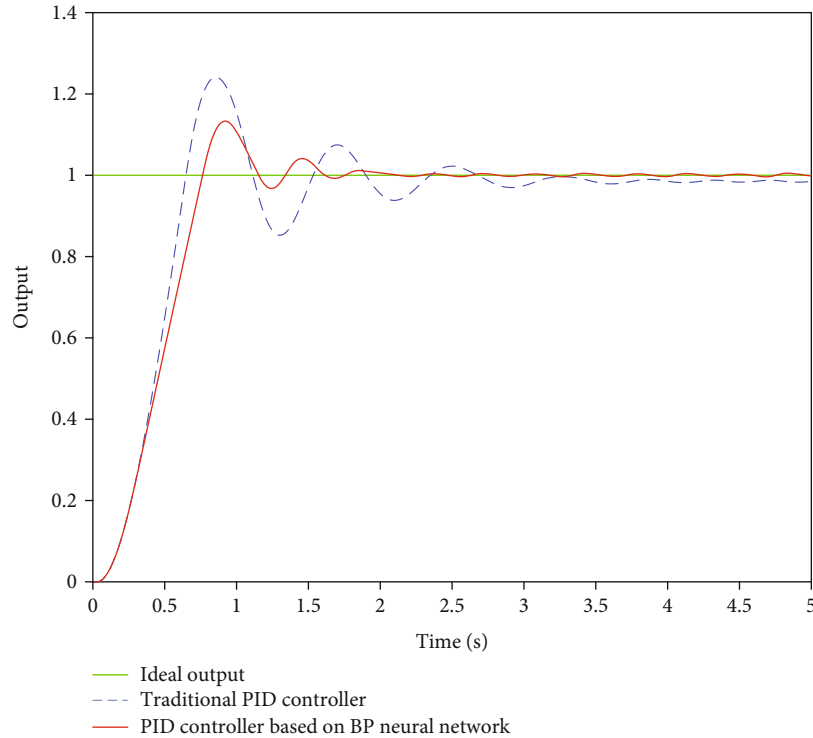
Figure 11: Simulation results.

the actual operation process, the pushing process of the surgical catheter needs several times to push and pull the catheter to reach the designated lesion. Shortening the pushing time of the catheter is helpful to improve the efficiency of intubation and the success rate of operation.

4. Experiments

4.1. Experimental Setup. The simulation experiment is made up of the RCMS which is composed of the main terminal (surgeon console) and the slave terminal (surgical catheter console) by remote operation and connected by network communication. The operation catheter was driven by step motor and DC motor for axial and radial movement. Therefore, in the process of using, it is helpful to monitor the motion state of stepping motor and DC motor for practical application and control. The BP neural network with double input and single output structure is used as the adjusting module of the control parameters in the PID controller. The displacement error $(e(k))$ and the change of displacement error $(ce(k))$ are regarded as two inputs of the controller. The realization process of the new controller is as follows: monitoring the current output value of step motor or DC motor; calculating the movement error and error change speed through the current value; inputting the error into BP neural network; and adjusting it through self-learning characteristics. Then, the adjusted K_p, K_i, and K_d are transmitted to PID controller to adjust the output signal $u(t)$ of the whole system.

4.2. Experimental Results. First of all, we use the traditional PID controller to carry out the basic remote operation experiment. Then, the new designed BP neural network
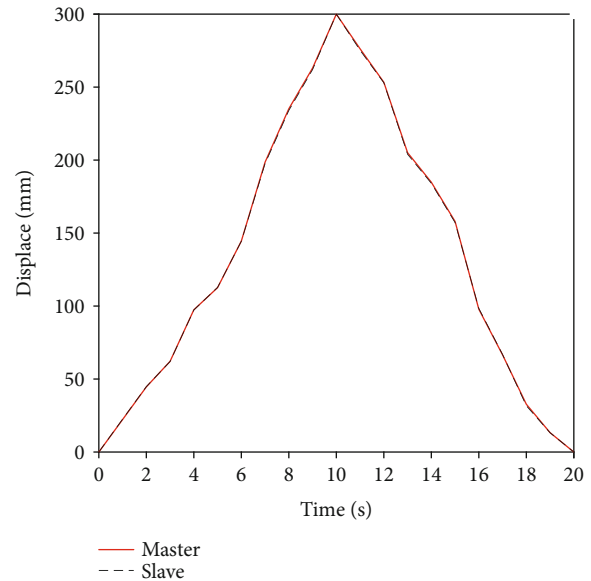
Figure 12: Axial displacement of PID controller.

PID controller is used to carry out the same remote operation experiment. The experimental results of traditional PID axial displacement are shown in Figure 12, and the error of traditional PID axial displacement is shown in Figure 13. Figure 14 shows that BP neural network PID controller obtains smooth response without overshoot, and its axial displacement error curve is shown in Figure 15.

The steady-state error of traditional PID controller is large, and the synchronous tracking performance is far
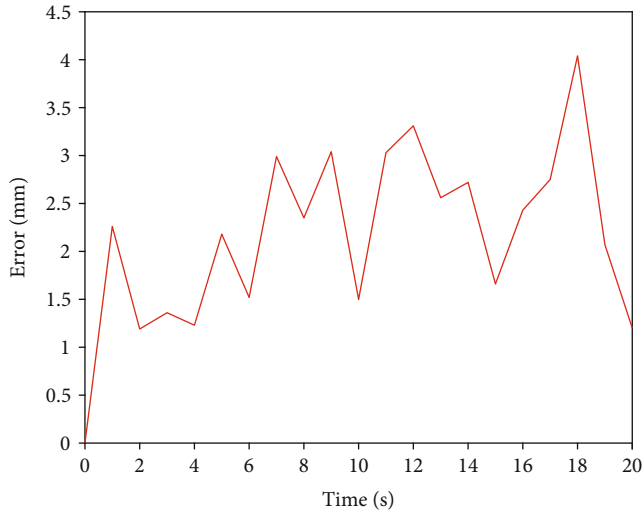
FIGURE 13: Axial displacement error of PID controller.

Master
Slave
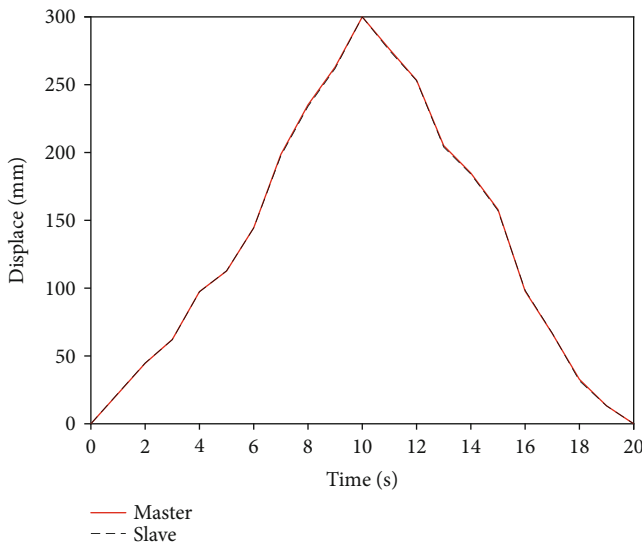
FIGURE 14: Axial displacement of BP neural network PID controller.
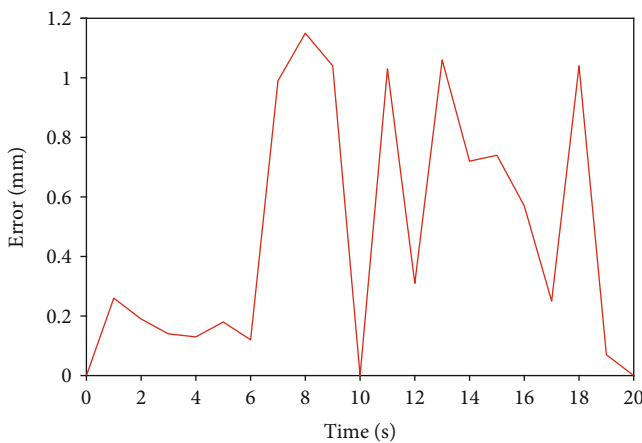
FIGURE 15: Axial displacement error of BP neural network PID controller.

inferior to that of BP neural network PID controller. However, although the BP neural network PID controller has good effect, it also has some errors. These errors are due to time delays in remote operations. This is also a key technical issue to be considered in future research.

Of course, for the axial motion of the system, we only use a simple physical method to establish the system dynamics model, without considering the higher requirements of the system in different working environments or other nonlinear factors. For a system with two degrees of freedom (radial rotation and axial displacement), when the displacement velocity or rotation direction changes, the system operation will be affected by nonlinear factors. Therefore, for the system, the nonlinear dynamic factors should be added to the known model in order to enhance the anti-interference ability of the control system and achieve better control effect.

5. Conclusions and Future Work

The system is based on the catheter robot operating system (RCMS), including a mechanical system with high precision and remote operation to assist surgeons in vascular intervention. The system takes digital signal processor (DSP) as the control unit, and has high measurement accuracy and processing speed in the main terminal console and the slave terminal console. Load cell and torque sensor are used to obtain the motion information of force and rotation angle. A new controller, BP neural network PID controller, is designed, which can improve the axial and rotary motion accuracy of the system in remote operation. Simulation results show that the proposed BP neural network PID controller has good dynamic response quality. When BP neural network PID controller is used for remote control, the synchronous tracking error of axial displacement is less than 1.5 mm. Although there are some errors in radial rotation and axial displacement due to time delay, the system can also meet the actual requirements of minimally invasive surgery. In conclusion, BP neural network PID control algorithm can improve the control performance of the system.

In the future research work, we will add the dynamic model of radial rotation in the operation system of surgical catheter robot, and increase the nonlinear influence factors. Combined with the established dynamic model of axial displacement, we will improve the control accuracy and anti-interference ability of the system in remote control [24]. In addition, more advanced sensors are used to measure the force (contact force and friction force) and displacement information in the system. And for the perfect system, real animal experiments were carried out to verify the reliability and safety of the system and ensure the feasibility of operation.

Data Availability

The article data used to support the findings of this study are available from the submitting author upon request.

Conflicts of Interest

The authors declare that they have no conflicts of interest.

Acknowledgments

References

[1] L. Fang, "Research on DC motor intelligent control algorithm," *Applied Mechanics and Materials*, vol. 462-463, pp. 775–781, 2013.

[2] Y. Wang, S. Guo, Y. Zhao, J. Cui, and Y. Ma, "A CNNs-based of force and torque identification model for vascular interventional surgery robot," in *2019 IEEE International Conference on Mechatronics and Automation (ICMA)*, Tianjin, China, China, 2019.

[3] W. Peng, N. Xiao, S. Guo, and Y. Wang, "A novel force feedback interventional surgery robotic system," in *IEEE International Conference on Mechatronics & Automation*, Beijing, China, 2015.

[4] J. Guo, S. Guo, N. Xiao et al., "Feasibility study for a novel robotic catheter system," in *International Conference on Mechatronics & Automation*, Beijing, China, 2011.

[5] Y. Lai, X. Wang, K. Zhou, J. Su, and G. Che, "The feasibility and safety of no placement of urinary catheter following lung cancer surgery: a retrospective cohort study with 2,495 cases," *Journal of Investigative Surgery*, vol. 5, pp. 1–8, 2019.

[6] X. Ma, S. Guo, N. Xiao, S. Yoshida, and T. Tamiya, "Development of a novel robotic catheter manipulating system," in *International Conference on Manipulation*, Shaanxi, China, 2013.

[7] X. Bao, S. Guo, N. Xiao, Y. Li, and L. Shi, "Compensatory force measurement and multimodal force feedback for remote-controlled vascular interventional robot," *Biomedical Microdevices*, vol. 20, no. 3, pp. 74.1–74.11, 2018.

[8] C. Laura, B. Barbara, and M. Emanuela, "CathROB: a highly compact and versatile remote catheter navigation system," *Applied Bionics and Biomechanics*, vol. 2017, 13 pages, 2017.

[9] H. J. Cha, B. J. Yi, and J. Y. Won, "An assembly-type master–slave catheter and guidewire driving system for vascular intervention," *Proceedings of the Institution of Mechanical Engineers, Part H: Journal of Engineering in Medicine*, vol. 231, no. 1, pp. 69–79, 2016.

[10] G. Peng, C. Yang, W. He, and C. P. Chen, "Force sensorless admittance control with neural learning for robots with actuator saturation," *IEEE Transactions on Industrial Electronics*, vol. 67, no. 4, pp. 3138–3148, 2019.

[11] C. Chen, X. Li, N. Zhang et al., "Different Nuss procedures and risk management for pectus excavatum after surgery for congenital heart disease," *Journal of Pediatric Surgery*, vol. 53, no. 10, pp. 1964–1969, 2018.

[12] M. A. Tavallaei, D. Gelman, M. K. Lavdas et al., "Design, development and evaluation of a compact telerobotic catheter navigation system," *International Journal of Medical Robotics & Computer Assisted Surgery*, vol. 12, no. 3, pp. 442–452, 2016.

[13] T. Gaspar, C. Piorkowski, M. Gutberlet, and G. Hindricks, "Three-dimensional real-time MRI-guided intracardiac catheter navigation," *European Heart Journal*, vol. 35, no. 9, 2014.

[14] N. Xiao, P. Guo, and S. Guo, "Push force feedback for a kind of robotic catheter navigation system," in *IEEE International Conference on Information & Automation*, Lijiang, China, 2015.

[15] X. Ma, S. Guo, N. Xiao, S. Yoshida, and T. Tamiya, "Evaluating performance of a novel developed robotic catheter manipulating system," *Journal of Micro Nano Mechatronics*, vol. 8, no. 3-4, pp. 133–143, 2013.

[16] C. Tercero, S. Ikeda, T. Uchiyama et al., "Autonomous catheter insertion system using magnetic motion capture sensor for endovascular surgery," *International Journal of Medical Robotics and Computer Assisted Surgery*, vol. 3, no. 1, pp. 52–58, 2007.

[17] B. Gao, S. Guo, and K. Hu, "Diagnosis and treatment of navigation technology based on the multi-modality image fusion for angioneoplasm," in *2014 IEEE International Conference on Mechatronics and Automation*, Tianjin, China, 2014.

[18] D. Liu, G. Shen, S. Qiao, and N. Wu, "A real time multi-angle adjustable phased high intensity focused ultrasound system," *Cognitive Systems Research*, vol. 52, pp. 610–614, 2018.

[19] L. Zhang, S. Guo, H. Yu et al., "Design and performance evaluation of collision protection-based safety operation for a haptic robot-assisted catheter operating system," *Biomedical Microdevices*, vol. 20, no. 2, p. 22, 2018.

[20] R. Saeidpourazar and N. Jalili, "Towards fused vision and force robust feedback control of nanorobotic-based manipulation and grasping," *Mechatronics*, vol. 18, no. 10, pp. 566–577, 2008.

[21] C. Zhi, *Analysis of peripheral surgical robot perception and path planning technology*, Electronic Test, 2019.

[22] J. Gonzalez-Martinez, S. Vadera, J. Mullin et al., "Robot-assisted stereotactic laser ablation in medically intractable epilepsy: operative technique," *Operative Neurosurgery*, vol. 10, no. 2, pp. 167–173, 2014.

[23] X. Ma, S. Guo, N. Xiao et al., "Development of a novel robotic catheter manipulating system with fuzzy PID control," *International Journal of Intelligent Mechatronics and Robotics*, vol. 2, no. 2, pp. 58–77, 2012.

[24] F. Li and J. Fei, "Gesture recognition algorithm based on image information fusion in virtual reality," *Personal and Ubiquitous Computing*, vol. 23, no. 3-4, pp. 487–497, 2019.

Research Article

Multichannel Saliency Detection Based on Visual Bionics

Lidan Cheng [ID], Tianyi Li [ID], Shijia Zha [ID], Wei Wei [ID], and Jihua Gu

College of Optoelectronics Science and Engineering, Soochow University, Suzhou Jiangsu Province 215000, China

Correspondence should be addressed to Wei Wei; weiwei0728@suda.edu.cn

Inspired by the visual properties of the human eyes, the depth information of visual attention is integrated into the saliency detection to effectively solve problems such as low accuracy and poor stability under similar or complex background interference. Firstly, the improved SLIC algorithm was used to segment and cluster the RGBD image. Secondly, the depth saliency of the image region was obtained according to the anisotropic center-surround difference method. Then, the global feature saliency of RGB image was calculated according to the colour perception rule of human vision. The obtained multichannel saliency maps were weighted and fused based on information entropy to highlighting the target area and get the final detection results. The proposed method works within a complexity of O(N), and the experimental results show that our algorithm based on visual bionics effectively suppress the interference of similar or complex background and has high accuracy and stability.

1. Introduction

Saliency detection is an important research content in computer vision, which refers to the process of simulating human visual attention mechanism to accurately and quickly detect the most interesting regions in images. Borji et al. defined that saliency visually described the prominent target or area in the scene relative to its neighbouring area [1]. The human visual attention mechanism prioritizes a few significant areas or objectives, while ignoring or discarding others that are not, which can allocate computing resources selectively and greatly improve the efficiency of visual information processing. Therefore, the saliency computing model based on visual attention mechanism has been widely studied. When processing the input image or video, the computer can judge the importance of its visual information by detecting the saliency area. It has been widely applied in object detection and identification [2], image retrieval [3], video quality assessment [4], video compression [5], image cropping [6], and other fields.

The RGB image saliency detection model based on visual attention mechanism uses low-level feature contrast to calculate saliency [7, 8]. Typical of them are global feature comparison calculation model [9], local feature comparison

calculation model [10], and combination of global and local feature comparison model [11]. In order to improve the accuracy of detection, the saliency detection model was proposed based on prior knowledge [12]. Typical of them are position prior [13], background prior [14, 15], colour prior [16], shape prior [17], and boundary prior [18, 19].

However, most 2D image saliency detection models based on human visual attention mechanism ignore the fact that human visual attention mechanism is based on 3D scene. It shows that depth provides extra important information of saliency detection for RGB image. Desingh et al. discussed 3D saliency detection methods based on depth appearance, depth-induced blur, and centre-bias [20]. Niu et al. conducted depth saliency detection based on parallax contrast and professional knowledge in vertical photography [21]. Further, Ju et al. proposed a depth saliency detection model based on depth image anisotropic center-surround difference [22]. Ren et al. [23], respectively, proposed the saliency detection of RGB-D images against a complex background by combining the prior knowledge of depth, indicating the validity of depth information in 3D saliency detection. However, there are two challenges in the process of saliency detection of RGB-D images. The first is how to calculate the saliency of depth images under similar or
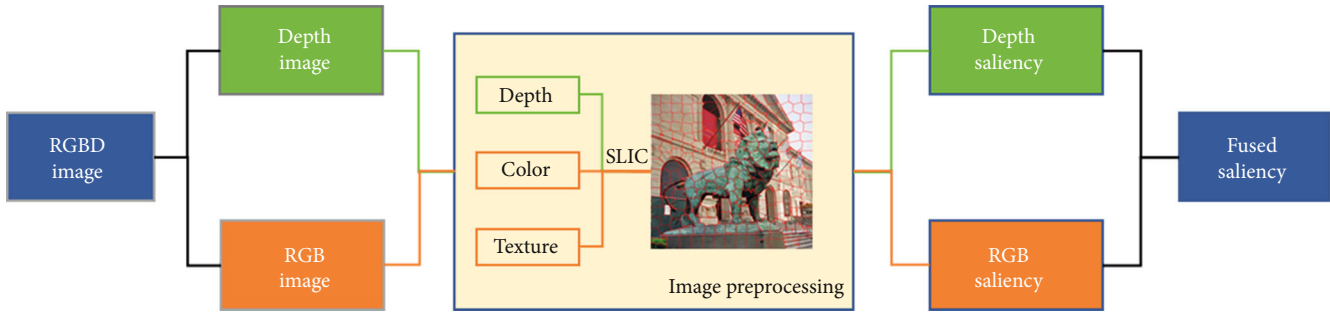
Figure 1: Our framework of saliency detection.

Scanline
Minimum depth
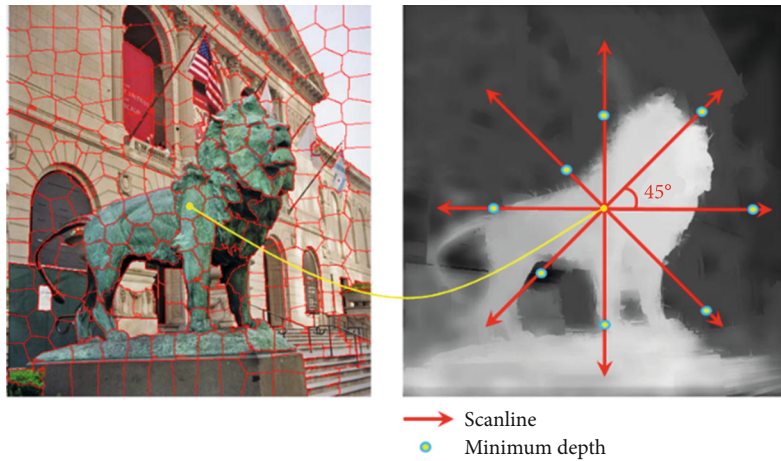
Figure 2: Example of the ACSD operator in a region.

complex background interference, and the second is how to combine the saliency map of depth image and RGB image to obtain the final result with a good performance. In this paper, we proposed a multichannel saliency detection method based on RGBD images, which has the following contributions:

(1) On the basis of SLIC algorithm, colour, texture, and depth information are used to measure the distance of superpixel segmentation

(2) Based on the perception rule of human vision, we introduced the depth information and global information of RGB image as two feature channels for saliency computing

(3) The weighted features of depth saliency and colour saliency were fused by information entropy, and experiment shows that the algorithm has a good performance in case of background interference

2. Saliency Detection

The algorithm framework of this paper is shown in Figure 1. Combining the depth map with the RGB map to carry out image preprocessing and colour, texture, and depth information are introduced as the basis of superpixel segmentation. Then, the colour and depth information were calculated as

two feature channels of saliency map. As is shown in Figure 2, the depth saliency was obtained by the anisotropic center-surround difference (ACSD) method, and the global saliency of RGB image was calculated by global contrast method based on HSV space. Finally, information entropy is used to calculate the weights of two channels, respectively, and get the final fused saliency map.

3. Image Preprocessing

The human visual observation system takes the image region as the basic unit, and the saliency detection based on the region conforms to the visual characteristics of the human eyes. As a construction method of pixel region, superpixel technology has been widely used in computer vision field. Superpixel can quickly segment the image into subregions with certain semantics, which is conducive to the extraction of local features and the expression of structural information [24]. SLIC algorithm has obtained a good balance in the two aspects of edge fitting degree and compactness, which has an excellent comprehensive performance. When the SLIC is used to segment the left image, the obtained boundary is not accurate because of ignoring the mutual constraint relationship between the 2D and depth information. Therefore, colour, texture, and depth information are used to measure the distance of superpixel segmentation in this paper.

Converting the left image to the CIE Lab colour space and dividing the image into k superpixels. Here, each pixel has a unique identifier i. Extract the follow 7 d characteristics of each superpixel region as measurement property. It can be expressed:

$$S_{p\text{-}i} = \{l_i, a_i, b_i, C_{\text{con}i}, C_{\text{cor}i}, E_i, d_i\}\ i = 1, 2, 3, \cdots, k, \quad (1)$$

where l_i, a_i, and b_i are the mean value of L, a, and b colour components of each superpixel region; $C_{\text{con}i}$, $C_{\text{cor}i}$, and E_i are the mean value of contrast, cross-correlation, and energy mean of gray level cooccurrence matrix of each superpixel region; and d_i is the depth value of each superpixel region. Then, we can describe the adjacent superpixel pair as $S_{p\text{-}ij}$:

$$S_{p\text{-}ij} = \left\{ \left(S_{p\text{-}i}, S_{p\text{-}j} \right) \right\}\ i \in [1, k], j \in [1, k], i \neq j, \quad (2)$$

where $S_{p\text{-}ij}$ superpixel pair with i and j as identifier, k is the number of superpixels of the image, and $S_{p\text{-}i}$ and $S_{p\text{-}j}$ are the 7 d characteristics of the adjacent superpixel pair. The number of adjacent superpixel pairs in each image is determined by SLIC superpixel segmentation.

Using colour, texture, and depth features to calculate the difference between all adjacent superpixel pairs $S_{p\text{-}ij}$. d_{lab}, d_{glcm}, and d_{depth} are defined to describe the measurement of colour, texture and depth characters:

$$d_{lab} = \sqrt{\left(l_i - l_j\right)^2 + \left(a_i - a_j\right)^2 + \left(b_i - b_j\right)^2},$$

$$d_{glcm} = \sqrt{\left(C_{\text{con}i} - C_{\text{con}j}\right)^2 + \left(C_{\text{cor}i} - C_{\text{cor}j}\right)^2 + \left(E_i - E_j\right)^2},$$

$$d_{\text{depth}} = \sqrt{\left(d_i - d_j\right)^2}. \quad (3)$$

Then, the distance measurement of superpixel segmentation D_{ij} is

$$D_{ij} = \omega_1 \bullet \sqrt{\frac{\varepsilon + d_{lab}^2}{3}} + \omega_2 \bullet \sqrt{\frac{\varepsilon + d_{glcm}^2}{3}} + \omega_3 \bullet \sqrt{\varepsilon + d_{\text{depth}}^2}, \quad (4)$$

where $\varepsilon = 10^{-4}$. It is used to ensure the validity of the value. ω_1, ω_2, are ω_3 are the weight of colour, texture, and depth.

In the image, the greater the discreteness of a feature data set is, it means that the more influence this feature has on the image. Mean variance can effectively represent the degree of difference between data. Therefore, the global mean variance of colour, texture, and depth is used as the weight values of the three features ω_1, ω_2, and ω_3.

If the difference between adjacent superpixels is less than a certain threshold th_1, the adjacent superpixel pair will be merged.

$$\text{th}_1 = \sqrt{\frac{\omega_1 \bullet \left(\bar{l} + \bar{a} + \bar{b}\right)}{3}} + \sqrt{\frac{\omega_2 \bullet \left(\overline{C_{\text{con}}} + \overline{C_{\text{cor}}} + \bar{E}\right)}{3}} + \sqrt{\omega_3 \bullet \bar{d}}, \quad (5)$$

where $\bar{l}$, $\bar{a}$, and $\bar{b}$ are the mean value of L, a, and b colour components of the image; $\overline{C_{\text{con}}}$, $\overline{C_{\text{cor}}}$, and $\bar{E}$ are the mean value of contrast, cross-correlation, and energy mean of gray level cooccurrence matrix of the image; and $\bar{d}$ is the depth value of the image.

Finding all similar adjacent superpixel pairs and taking the upper left superpixel of the image as the starting point of clustering. The output after clustering contains n regions R_i, $1 \leq i \leq n$.

4. Depth Saliency Map

For each superpixel, the anisotropic center-surround difference (ACSD) value is calculated, and the value of center superpixel is assigned to each pixel within the region R_i. Performing an anisotropic scan along multiple directions, in each scanline, assuming the pixel with the minimum depth value as background and calculate the difference between the center pixel and background. L is the maximum scan length for each scanline. The typical value of L is a third of the diagonal length.

The anisotropic center-surround difference (ACSD) is summed over eight scanning directions 0°, 45°, 90°, 135°, 180°, 225°, 270°, and 315°. The mathematical description of anisotropic center-surround difference (ACSD) measure is

$$S_d^m(x, y) = d(x, y) - \min\left(d^m\right), n \in [1, L],$$

$$S_d(x, y) = \sum_{m=1}^{8} S_d^m, \quad (6)$$

where S_{depth}^m indicates the ACSD value of pixel (x, y) along the scanline m. $d(x, y)$ is the depth value of pixel (x, y). n is the index of the pixels along the scan path m. $\min\left(d^m\right)$ is the minimum depth value along the scanline m. $S_d(x, y)$ is the ACSD value of pixel (x, y) which sums the center-surround difference values in eight directions.

5. Global Saliency Map of RGB Image

Colour histogram is used to regularize the colour of the image to level 128 in order to reduce the computational complexity and save the storage space. On the other hand, the descending dimension algorithm for HSV colour space is proposed. With the decrease of saturation, any colour in HSV space can be described by the change of gray level. The intensity value determines the specific gray level of the conversion [25]. When the colour saturation is close to zero, all pixels look similar regardless of hue. With the increase of saturation, the pixels are distinguished by hue value.

Compared with colour saturation, human vision is more sensitive to hue and intensity. The pixels with lower
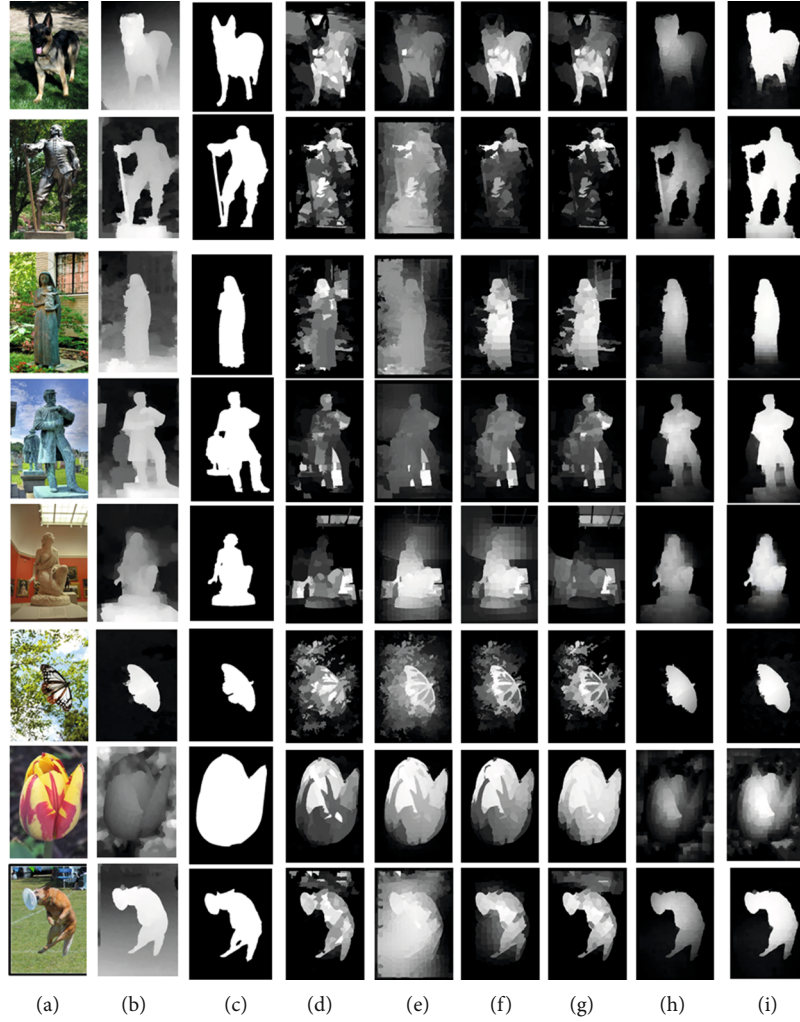
FIGURE 3: Saliency comparisons of different methods in terms of NJU400 dataset: (a) RGB image; (b) depth image; (c) ground truth; (d) GS; (e) MC; (f) MR; (g) WCTR; (h) ACSD; (i) MSD.

colour saturation can be approximately represented by intensity level, while the pixels with higher colour saturation can be approximately represented by hue. Saturation value is used to determine whether each pixel can be represented by hue or intensity value, which is more consistent with the law of human visual perception. Saturation threshold th_2 is

$$\text{th}_2 = 1 - \frac{0.8\,I_v(x,y)}{255},\tag{7}$$

where $I_v(x,y)$ represents the V component value of a pixel. When the saturation value $I_s(x,y)$ is greater than th_2, the pixel point is represented by the hue value $I_v(x, y)$; when the saturation value is less than th_2, the pixel point is represented by the intensity value $I_h(x,y)$. The saliency of each pixel is

$$S_c(x,y) = \begin{cases} \left|\bar{I} - I_v(x,y)\right| I_s(x,y) \le \text{th}_2 \\ \left|\bar{I} - I_h(x,y)\right| I_s(x,y) > \text{th}_2 \end{cases} \forall(x,y) \in R_i,\tag{8}$$

where $I_s(x,y)$ is the saturation value of the pixel, $I_h(x,y)$ is the hue value of the pixel, $I_v(x,y)$ is the intensity value of the pixel, and $\bar{I}$ is the mean value of all pixels.

6. Fusion of Saliency Map

When synthesizing the colour saliency map and the depth saliency map, the information entropy is used to calculate the weights of the channels.

The information entropy of colour saliency is

$$H_c(R) = -\sum_{i=1}^{n} p_c(R_i) \log\left(p_c(R_i)\right),\tag{9}$$

where $p_c(R_i)$ is the ratio of the sum of R_i colour saliency values to the whole image.

The information entropy of depth saliency is

$$H_d(R) = -\sum_{i=1}^{n} p_d(R_i) \log\left(p_d(R_i)\right),\tag{10}$$
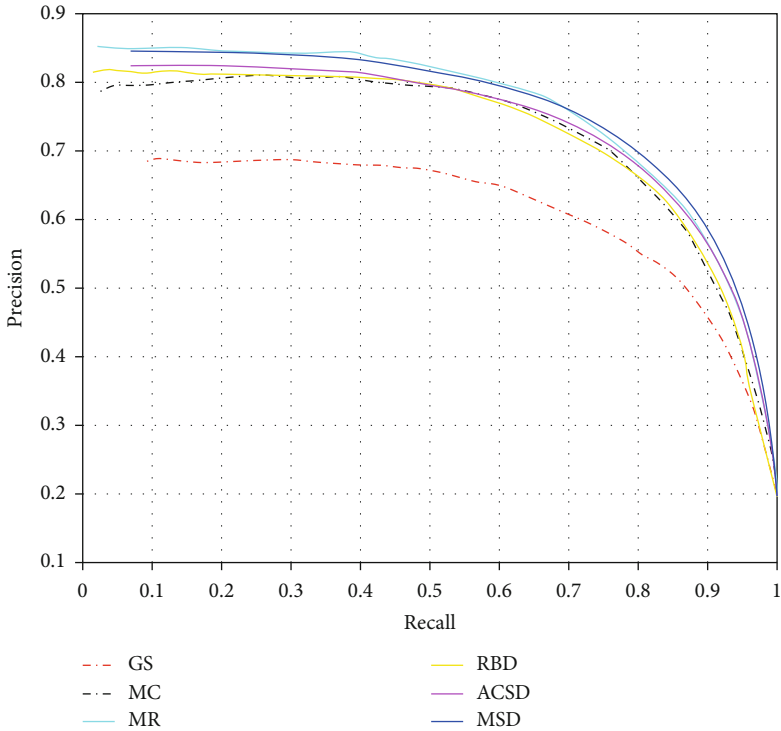
(a)
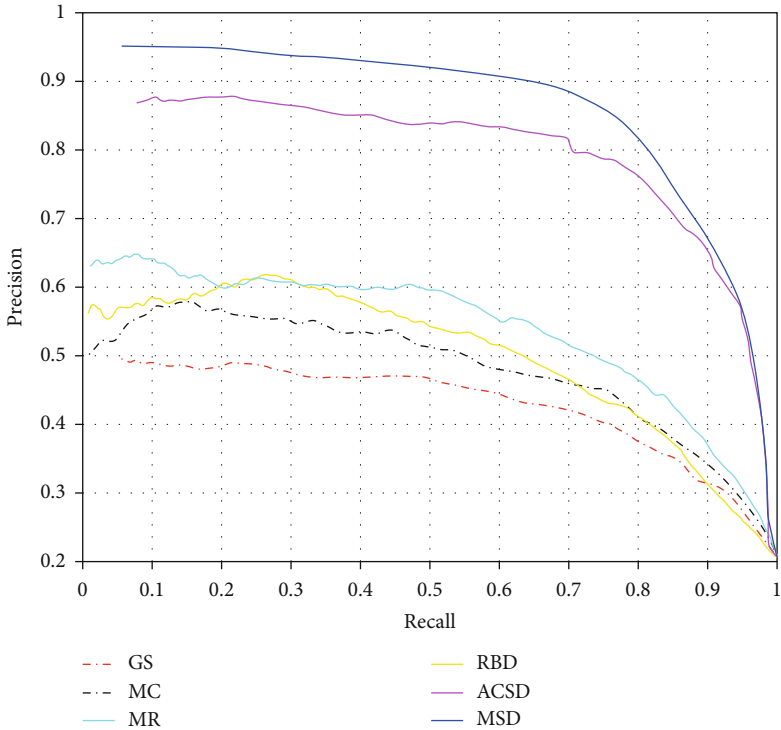
(b)

Figure 4: Continued.

(c)
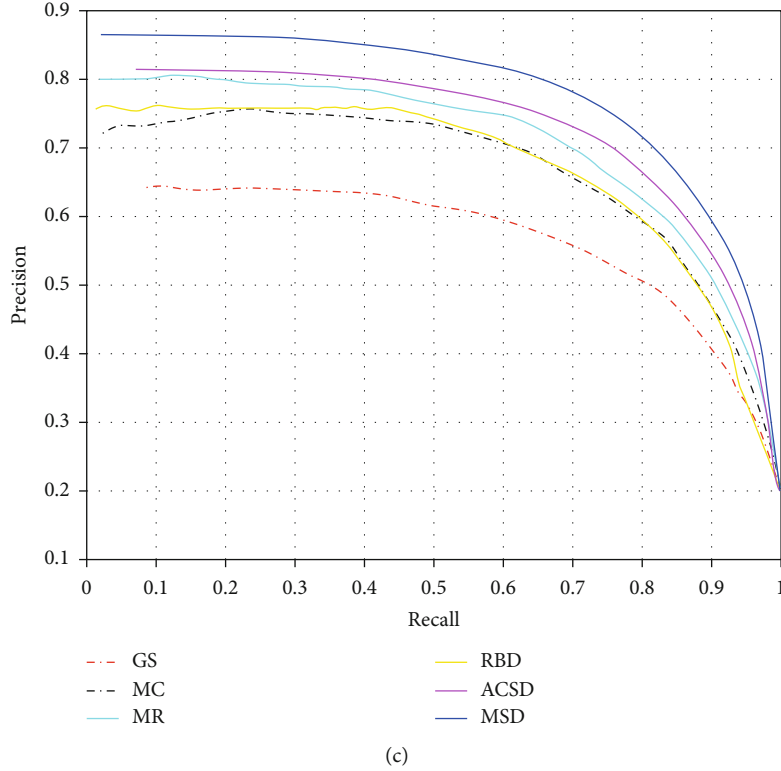
FIGURE 4: The precision-recall curves of different algorithms: (a) the precision-recall curves on the N group; (b) the precision-recall curves on the S/C group; (c) the precision-recall curves on full datasets.

where $p_d(R_i)$ is the ratio of the sum of R_i depth saliency values of to the whole image.

The saliency map $S_{\mathrm{fuse}}(x, y)$ was obtained by fusing the two channels:

$$
\begin{aligned}
S_{\mathrm{fuse}}(x, y) = & \frac{H_c(R)}{H_c(R) + H_d(R)} S_c(x, y) \\
& + \frac{H_d(R)}{H_c(R) + H_d(R)} S_d(x, y) \forall (x, y) \in R_i.
\end{aligned}
\tag{11}
$$

7. Experimental Comparison

We show a few saliency maps generated by different algorithms in Figure 3.

The precision-recall curve is evaluated from two aspects: precision and recall. Precision refers to the ratio between the number of correct saliency pixels and the whole number of saliency pixels, which is used as the y-axis. Recall refers to the ratio of the number of correct saliency pixels to the number of true pixels, which is used as the x-axis.

The algorithms are tested on NJU400 datasets. Two test sets are divided from NJU400 according to the complexity and the similarity of the background. Four volunteers are invited to divide the raw datasets into the normal group (N group) and the similar/complex background group (S/C group). At last, 92 high quality and consistently labelled images are selected into the S/C group, and the rest are divided into the N group. The precision-recall curves of

TABLE 1: The performance of different algorithms tested on three groups.

Group	Algorithms	Precision
N group	GS	0.68
	MC	0.79
	MR	0.85
	RBD	0.81
	ACSD	0.84
	MSD	0.82
S/C group	GS	0.49
	MC	0.50
	MR	0.63
	RBD	0.56
	ACSD	0.87
	MSD	0.95
Full datasets	GS	0.64
	MC	0.72
	MR	0.80
	RBD	0.76
	ACSD	0.81
	MSD	0.86

different algorithms tested on the N group, S/C group, and full datasets are given in Figure 4. The performance of different algorithms tested on three groups is given in Table 1.

The proposed method works within a complexity of O(N), and the evaluation on the results of these saliency detection algorithms in the S/C group shows that our algorithm has a better performance than other algorithms. In full datasets, it also performs well. By selecting the salient subset for further processing, the complexity of higher visual analysis can be reduced significantly. Many applications benefit from saliency analysis such as object segmentation, image classification, and image/video retargeting.

8. Conclusions

A new framework based on visual bionics for saliency detection under similar or complex background interference is proposed in this paper: First, we combine the depth map with the RGB map, and colour, texture, and depth information are introduced as the basis of superpixel segmentation. Second, the colour and depth information were calculated as two feature channels of saliency map. Finally, information entropy is used to calculate the weights of two channels, respectively, and get the final fused saliency map. The proposed method works within a complexity of O(N), and the experimental results show that our saliency detection framework greatly reduces the error detection under similar and complex background and improves the overall saliency detection performance.

Data Availability

The NJU400 datasets used to support the findings of this study are included within the article.

Conflicts of Interest

The authors declare that there is no conflict of interests regarding the publication of this paper.

References

[1] A. Borji and L. Itti, "State-of-the-art in visual attention modeling," *IEEE Transactions on Pattern Analysis and Machine Intelligence*, vol. 35, no. 1, pp. 185–207, 2013.

[2] W. Wang, J. Shen, L. Shao, and F. Porikli, "Correspondence driven saliency transfer," *IEEE Transactions on Image Processing*, vol. 25, no. 11, pp. 5025–5034, 2016.

[3] M. W. Jian, J. Y. Dong, and J. Ma, "Image retrieval using wavelet-based salient regions," *The Imaging Science Journal*, vol. 59, no. 4, pp. 219–231, 2013.

[4] F. Xin, D. Yang, and Z. Ling, "Saliency variation-based quality assessment for packet-loss-impaired videos," *Acta Automatica Sinica*, vol. 37, no. 11, pp. 1322–1331, 2011.

[5] R. Gupta and S. Chaudhury, "A scheme for attentional video compression," in *Proceedings of the 4th International Conference on Pattern Recognition and Machine Intelligence*, pp. 458–465, IEEE, Moscow, Russia, 2011.

[6] Chenlei Guo and Liming Zhang, "A novel multiresolution spatiotemporal saliency detection model and its applications in image and video compression," *IEEE Transactions on Image Processing*, vol. 19, no. 1, pp. 185–198, 2010.

[7] L. Itti, C. Koch, and E. Niebur, "A model of saliency-based visual attention for rapid scene analysis," *IEEE Transactions on Pattern Analysis and Machine Intelligence*, vol. 20, no. 11, pp. 1254–1259, 1998.

[8] Z.-P. Hu and M. Peng-Quan, "Graph presentation random walk salient object detection algorithm based on global isolation and local homogeneity," *Acta Automatica Sinica*, vol. 37, no. 10, pp. 1279–1284, 2011.

[9] M. M. Cheng, N. J. Mitra, X. L. Huang, P. H. S. Torr, and S. M. Hu, "Global contrast based salient region detection," *IEEE Transactions on Pattern Analysis and Machine Intelligence*, vol. 37, no. 3, pp. 569–582, 2015.

[10] T. Yong, L. Yang, and D. Liang-Liang, "Image cell-based saliency detection via colour contrast and distribution," *Acta Automatica Sinica*, vol. 39, no. 10, pp. 1632–1641, 2013.

[11] Y.-C. Guo, H.-J. Yuan, and P. Wu, "Image saliency detection based on local and regional features," *Acta Automatica Sinica*, vol. 39, no. 8, pp. 1214–1224, 2013.

[12] W. Xu and T. Zhen-Min, "Exploiting hierarchical prior estimation for salient object detection," *Acta Automatica Sinica*, vol. 41, no. 4, pp. 799–812, 2015.

[13] T. Liu, Z. Yuan, J. Sun et al., "Learning to detect a salient object," *IEEE Transactions on Pattern Analysis and Machine Intelligence*, vol. 33, no. 2, pp. 353–367, 2011.

[14] Y. Wei, F. Wen, W. Zhu, and J. Sun, "Geodesic saliency using background priors," in *Computer Vision – ECCV 2012*, pp. 29–42, Springer, Berlin, Heidelberg, 2012.

[15] W. Zhu, S. Liang, Y. Wei, and J. Sun, "Saliency optimization from robust background detection," in *Proceedings of the IEEE conference on computer vision and pattern recognition*, Columbus, Ohio, USA, 2014.

[16] X. H. Shen and Y. Wu, "A unified approach to salient object detection via low rank matrix recovery," in *Proceedings of 2012 IEEE Conference on Computer Vision and Pattern Recognition*, pp. 853–860, Providence, RI, USA, 2012.

[17] H. Z. Jiang, J. D. Wang, Z. J. Yuan, T. Liu, N. N. Zheng, and S. P. Li, "Automatic salient object segmentation based on context and shape prior," in *Proceedings of 2011 British Machine Vision Conference*, pp. 110.1–11110, Dundee, UK, 2011, BMVA Press.

[18] C. Yang, L. H. Zhang, H. C. Lu, X. Ruan, and M. H. Yang, "Saliency detection via graph-based manifold ranking," in *Proceedings of 2013 IEEE Conference on Computer Vision and Pattern Recognition*, pp. 3166–3173, Portland, OR, USA, 2013.

[19] B. Jiang, L. Zhang, and H. Lu, "Saliency detection via absorbing markov chain," in *Proceedings of the IEEE international conference on computer vision*, Sydney, Australia, 2013.

[20] K. Desingh, K. M. Krishna, D. Rajan, and C. V. Jawahar, "Depth really matters: improving visual salient region detection with depth," in *Proceedings of 2013 British Machine Vision Conference*, pp. 98.1–9898, Bristol, England, 2013, BMVA Press.

[21] Y. Z. Niu, Y. J. Geng, X. Q. Li, and F. Liu, "Leveraging stereopsis for saliency analysis," in *Proceedings of 2012 IEEE Conference on Computer Vision and Pattern Recognition*, pp. 454–461, Providence, RI, USA: IEEE, 2012.

[22] R. Ju, L. Ge, W. J. Geng, T. W. Ren, and G. S. Wu, "Depth saliency based on anisotropic center-surround difference," in *Proceedings of 2014 IEEE International Conference on Image Processing*, pp. 1115–1119, Pairs, France: IEEE, 2014.

[23] J. Q. Ren, X. J. Gong, L. Yu, W. H. Zhou, and M. Y. Yang, "Exploiting global priors for RGB-D saliency detection," in *Proceedings of 2015 IEEE Conference on Computer Vision and Pattern Recognition Workshops*, pp. 25–32, Boston, MA, USA: IEEE, 2015.

[24] R. Achanta, A. Shaji, K. Smith, A. Lucchi, P. Fua, and S. Süsstrunk, *SLIC superpixels*, EPFL, Switzerland, 2010.

[25] S. Sural, G. Qian, and S. Pramanik, "Segmentation and histogram generation using the HSV colour space for image retrieval," in *Proceedings. International Conference on Image Processing*, pp. 589–592, Rochester, NY, USA, September 2002.

Research Article

The Effect Analysis of Carrier Gas Flow Rate on the Rapid Gas Chromatographic Separation System

Xu Zhang ,[1] **Sixiang Zhang,**[2] **Wei Zhou,**[2] **and Yang Qi**[1]

[1]*Tianjin Key Laboratory of High Speed Cutting and Precision Machining, School of Mechanical Engineering, Tianjin University of Technology and Education, Tianjin, China 300222*
[2]*School of Mechanical Engineering, Hebei University of Technology, Tianjin, China 300100*

Correspondence should be addressed to Xu Zhang; 52914262@qq.com

Odor pollution did not only disturb the human normal life but also aroused the attention of environmental researchers and environmental protection departments. Therefore, the research on odor detecting method and instrument is important to theory and application. On this basis, the self-developed microfluidic chip capillary column is used in our odor detecting system. In this paper, lead the chip column into the chromatography separation system, with its small size, high efficiency, easy integration, and other characteristics to replace the original traditional column. The chip column was used in many gas experiments for several typical VOCs. At different carrier gas flow rates, the baseline value, toluene response, and toluene and methyl sulfide mixed gas separation were compared to verify the experiment to determine the optimal carrier gas flow rate in accordance with its response and separation degree. Under the premise of ensuring column efficiency as high as possible, it is determined that the optimal carrier gas flow rate is 6 ml/min. This paper shows the most proper carrier gas flow rate of our odor detecting system with the self-developed microfluidic chip capillary column.

1. Introduction

In recent years, industrial and agricultural processes and household waste have emitted a large amount of volatile organic compounds (VOCs), causing a series of atmospheric pollution problems. VOCs cause harm to the human respiratory system, digestive system, and endocrine system. Common psychological and emotional injuries include irritability, dizziness, nausea, and vomiting. Environmental pollution has attracted the attention of all countries in the world. The environmental protection monitoring department not only wants to know where the pollution source is but also wants to know the type and concentration of pollutants. At present, the gas detection method at home and abroad is mainly gas chromatography. Chromatography technology is a general term for the separation of complex samples and is an important method for modern separation

detection and analysis [1]. The traditional gas separation and detection equipment has a large volume and mass, the operation process is complex and time-consuming, the analysis speed is slow, and the separation gas mixture uses a longer column, resulting in a long analysis cycle. The research group developed and manufactured a chip-type column for this purpose. It has features such as small sample size, high detection efficiency, low use cost, portability, ease of integration with other technical equipment, and good compatibility [2]. The gas chromatography separation and detection system involved in this article uses Beijing Minnick's ten-way valve as the sample injection system, the chip-type column as the separation system, and the PID (Photoionization Detector) as the detection system. According to the rate theory, the carrier gas flow rate affects the column. Selecting the optimal carrier gas flow rate is of great significance for the evaluation of the instrument's performance and detection accuracy.

2. Experimental Part

2.1. Separation Principle of the Chip Column. The chip column uses the principle of separation by gas chromatography. In gas chromatography, the sample gas to be analyzed is rapidly carried by the carrier gas into the column. The column contains a solid or liquid stationary phase. The polarity, boiling point, or the physical and chemical properties of the adsorbed sample are different. As a result, the components are constantly distributed or adsorbed/desorbed between the stationary phase and fluidity, resulting in different rates of the components flowing out of the column, so that the retention time of the components in the column is different, in chronological order flow out of the column and into the end of the detector for detection [3].

2.2. Processing of the Chip Column. The chip column utilizes the fine sandblasting jet process to etch the surface of the borosilicate glass and adopts an anodic bonding processing method to process a Pyrex type borosilicate glass material chip with a size of $115 \, mm \times 60 \, mm \times 6 \, mm$ as shown in Figure 1. The channel is designed as an S-channel with a circular cross section, which has the advantage of ensuring that the gas molecules of the components travel the same path inside and outside the chip column channel with the same column volume [4]. The channel has an inner diameter of $400 \, \mu m$ and a length of 5.8 m. In order to achieve the separation of VOCs, three kinds of fixing solutions, 100% dimethylpolysiloxane, 14% cyanopropylphenyl-86% dimethylpolysiloxane, and polyethylene glycol, were, respectively, applied. The pipe connection method of the chip is connected by means of a clamp fixture and is connected by a PTFE pipe with a threaded connection, and the connection head is connected by a conical pressure ring and can withstand a temperature of 300°C.

3. Chromatographic Rate Theory

3.1. Several Parameters for Evaluating Column Performance. The theoretical plate number N and the theoretical plate height H are the two main indicators reflecting the column performance of the column [5]. The calculation formula of N is

$$N = 5.54 \left(\frac{t_R}{W_{1/2}} \right)^2 = 16 \left(\frac{t_R}{W_b} \right)^2, \tag{1}$$

where t_R is the retention time, which refers to the time from the start of sampling until the sample passes the column to produce the highest peak; W_b is the width of the bottom of the peak, which refers to the tangent line at the inflection point of the chromatographic peak outflow curve. The distance between the base of the peak or the base line intersecting two points, $W_{1/2}$, is the half width of the peak, which refers to the distance between the line parallel to the base of the peak at the midpoint of the peak height and the point of intersection on both sides of the peak [6].
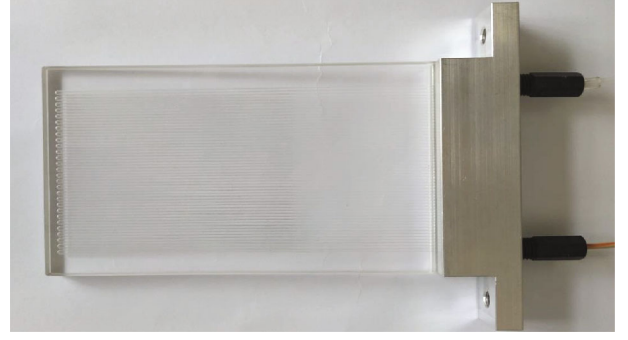
FIGURE 1: The self-developed microfluidic chip capillary column.

H's formula is

$$H = \frac{L}{N}, \tag{2}$$

where L is the length of the column.

It can be seen that the narrowing of the chromatographic peaks and the height of the trays will increase the column efficiency. N and H are the main indicators that describe the performance of a column.

The degree of separation of components—the degree of separation [7] is calculated as

$$R = \frac{2(t_{R2} - t_{R1})}{Y_1 + Y_2}, \tag{3}$$

where Y_1, Y_2 is the peak width of the peak.

The size of R can quantitatively reflect the degree of separation between components. When the chromatographic peak shape is asymmetrical or there is a slight overlap between adjacent two peaks, it is difficult to measure the peak width at the bottom. Instead, half width can be used instead. At this time, the resolution R can be expressed as

$$R = \frac{1.18(t_{R2} - t_{R1})}{Y_{1/2(1)} + Y_{1/2(2)}}, \tag{4}$$

where $Y_{1/2(1)}$, $Y_{1/2(2)}$ is the peak width at the half height of the peak.

3.2. Rate Theory. The column efficiency is the highest when the column and the sample are at a certain flow rate [8], and the relationship of H-u is

$$H = A + \frac{B}{u} + Cu, \tag{5}$$

where H is the tray height, u is the carrier gas velocity, and A, B, and C are three constants, where A is the eddy diffusion term, B is the molecular diffusion coefficient, and C is the mass transfer resistance factor. Equation (5) is a simplified version of the Van Deemter equation. According to equation (5), the height H of the tray measured at different flow rates is plotted against the flow rate u to obtain the H-u
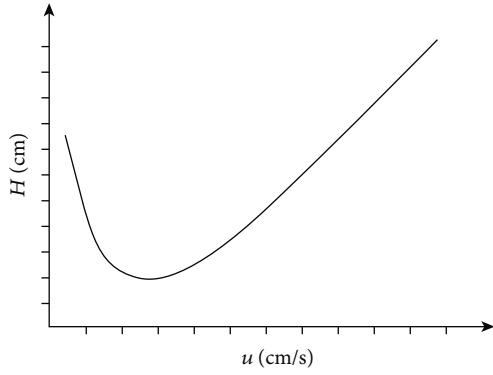
FIGURE 2: Relation curve between plate height and the carrier gas line speed.

curve, as shown in Figure 2. At the lowest point of the H-u curve, the height of the theoretical plate H is the smallest, and the efficiency of the column is the highest. The flow rate corresponding to this point is the best flow rate u_{best}. H_{min} and u_{best} can be differentiated by equation (5). Seek, that is,

$$\frac{dH}{du} = -\frac{B}{u^2} + C = 0, \tag{6}$$

$$u_{best} = \sqrt{\frac{B}{C}}. \tag{7}$$

Bring formula (6) into formula (5):

$$H_{min} = A + 2\sqrt{BC}. \tag{8}$$

In actual work, try to shorten the analysis time without significantly affecting the efficiency of the column. The flow rate is usually slightly higher than the optimal flow rate.

The relationship of the constant terms A, B, and C is brought into equation (5).

$$H = 2\lambda d_p + \frac{2\gamma D_g}{\mu} + \left[\frac{0.01k^2}{(1+k)^2} \cdot \frac{d_p^2}{D_g} + \frac{2}{3} \cdot \frac{k}{(1+k)^2} \cdot \frac{d_f^2}{D_1}\right]\mu. \tag{9}$$

According to equation (9), the column packing uniformity, carrier particle size, carrier gas type, carrier gas flow rate, column temperature, and liquid film thickness of the stationary phase have effects on column efficiency and peak expansion.

4. Experiments and Data

4.1. Experimental Device and Conditions. In order to understand the effect of carrier gas flow on separation of mixtures, the self-developed odor detecting online system is introduced in these experiments. The system is shown in Figure 3.

There are six units in the system, including the gas channel unit, injection unit, separating unit, detecting unit, controlling unit, and data processing unit. This system has

FIGURE 3: Self-developed odor detecting online system.

passed the stability testing, systematic linearity testing, and sensitivity testing. The testing experiments show that the baseline fluctuation value is less than 2.3 mV; the linearity of the system for xylene, ethanol, and butane is 99.98%, 99.99%, and 99.98%, respectively. The sensitivity was 1 ppm, 0.8 ppm, and 0.6 ppm, respectively [9]. We will not elaborate the testing experiments of our self-developed odor detecting online system.

The following experiment is done under the normal operating conditions. The normal operating conditions are as follows: (1) 99.999% nitrogen (N_2) was used as carrier gas; (2) the lab environmental temperature is at 25°C; (3) the pressure in the laboratory is 0.101 MPa.

4.2. Effect of Carrier Gas Flow on Baseline Value. Baseline refers to the signal curve produced by the detector when only nitrogen passes through the column and detector under normal operating conditions. The ideal stable baseline should be a horizontal straight line. The peak height is the vertical distance between the highest point of the chromatographic peak and the bottom of the peak and the vertical distance between the highest point of the chromatographic peak and the baseline. In gas chromatography, the peak height is one of the commonly used quantitative parameters. From the theory of velocity, the flow affects the height of the theoretical plate, thus affecting the size of the baseline value. By changing the flow rate before the column, the voltage value of the PID is monitored with a voltmeter. After the baseline is stabilized, the corresponding baseline value is obtained. We used 99.999% nitrogen (N_2) as carrier gas in this experiment. The carrier gas flow rate changed from 0 ml/min to 9 ml/min at 25°C in the lab. The effect of carrier gas flow on baseline values is shown in Figure 4. It shows that the baseline value was low while the carrier gas flow speeded up.

4.3. Effect of Carrier Gas Flow Rate on Toluene Response. From the rate theory, the flow rate of the carrier gas has an opposite effect on the mass transfer resistance term and the vertical diffusion term. If the carrier gas velocity u increases, the longitudinal diffusion term decreases so that the column
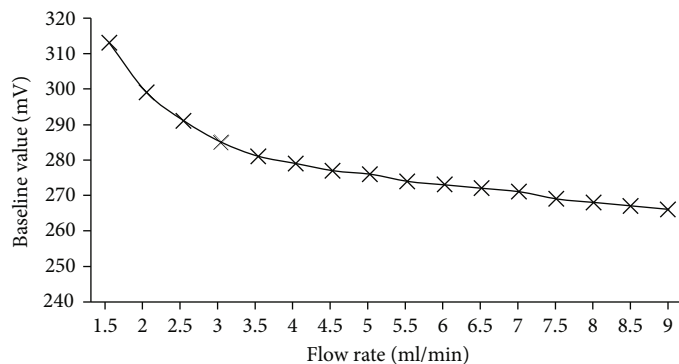
Figure 4: Effect of carrier gas flow rate on the baseline value.
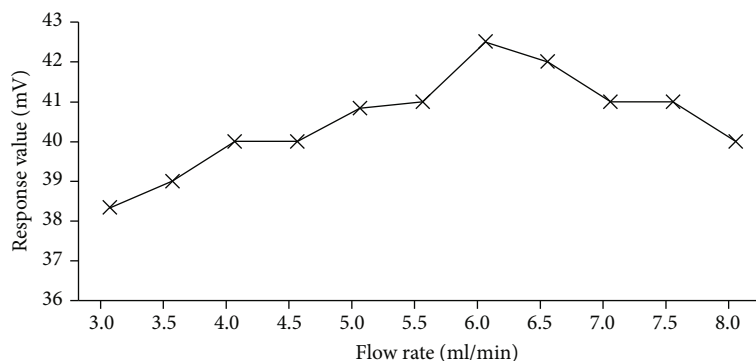
Figure 5: Effect of carrier gas flow rate on 200 ppb toluene response value.

Table 1: Dimethyl sulfide and toluene separation results in different carrier gas flow rates.

Flow rate (ml/min)	Substance category	Retention time (s)	Peak width	Separation degree
2	Dimethyl sulfide	78	26	2.79
	Toluene	176	44	
2.5	Dimethyl sulfide	65	37	2.13
	Toluene	146	39	
3	Dimethyl sulfide	55	46	1.66
	Toluene	127	41	
3.5	Dimethyl sulfide	47	46	1.51
	Toluene	107	34	
4	Dimethyl sulfide	44	33	1.68
	Toluene	96	29	
4.5	Dimethyl sulfide	37	33	1.53
	Toluene	85	29	
5	Dimethyl sulfide	34	26	1.68
	Toluene	76	24	
5.5	Dimethyl sulfide	28	20	1.63
	Toluene	61	21	
6	Dimethyl sulfide	26	26	1.50
	Toluene	60	20	
6.5	Dimethyl sulfide	24	20	1.74
	Toluene	57	18	
7	Dimethyl sulfide	23	23	1.58
	Toluene	54	16	

efficiency increases, but at the same time, the mass transfer resistance term increases, which in turn reduces the column efficiency. The flow rate of the carrier gas influences the height of the tray, so there is an optimum flow rate so that the column efficiency is the highest. In this experiment, the sample gas was sampled using 200 ppb toluene standard gas prepared by DaLian Date and the carrier gas used was 99.999% nitrogen (N_2). By changing the flow rate of the carrier gas before the column, the corresponding response value of the 200 ppb toluene standard gas is shown in Figure 5. It shows that toluene response value had a peak value at about 6 ml/min.

4.4. Effect of Carrier Gas Flow on Separation of Mixtures. A gas generator was used to prepare dimethyl sulfide and toluene gas mixture. The gas mixture was separated and detected by the gas chromatographic separation and detection system developed by our group [10, 11]. In this experiment, 99.999% nitrogen (N_2) was used as the carrier gas. The temperature of the chip column is 85°C, select the S48 300/HMT type mass flow controller manufactured, and control the flow rate at 2~7 ml/min, and each flow rate is carried out. Two repeated injection tests were performed to determine the retention time and peak width of the mixture, and the mean value was calculated. Separation of the mixture is mainly achieved by using the separation of the system; the relative physical and chemical properties such as the boiling point, polarity, and adsorption and desorption of each component are fixed [12]. After separation and detection of dimethyl sulfide and toluene mixture, data processing was performed using the software of the upper computer to calculate the retention time and peak width of dimethyl sulfide and toluene at different flow rates, and the separation was calculated according to equation (3). The specific data results are shown in Table 1.

From Table 1, the flow rate is between 2 and 7 ml/min, the separation degree of methyl sulfide and toluene is $R > 1.5$, and the two peaks are completely separated. The higher the degree of separation, the more accurate detection results could be [13]. When the flow rate is low, as the flow rate increases, the peak width of the peak narrows, the retention time becomes shorter, the number of theoretical plates becomes larger, and the column efficiency of the chip column increases [14].

5. Conclusions

During the rate theory, the flow rate of the carrier gas affects the column and column efficiency. Using the developed chip-type column at different carrier gas flow rates, experiments were carried out to examine the effect of carrier gas flow rate on the baseline value, 200 ppb toluene response, and mixture separation. The flow rate was between 2 and 7 ml/min, and the baseline value gradually decreased. The response value of 200 ppb toluene reached maximum at a flow rate of about 6 ml/min. The separation of dimethyl sulfide and toluene was not less than 1.5. Both were completely separated. Based on comprehensive column efficiency, gas response value, high separation of mixed gas, short analysis cycle, and other

factors, the optimal carrier gas flow rate for the chip column is 6 ml/min.

Data Availability

The data used to support the findings of this study are included within the article.

Conflicts of Interest

All the authors of this manuscript declare no competing financial interest.

Acknowledgments

References

[1] J. Pfahler, J. Harley, H. Bau, and J. Zemel, "Liquid transport in micro and submicron channels," *Proceedings of SPIE*, vol. 1167, no. 89, pp. 159–169, 1992.

[2] M. Yu, Z. Hongmei, Z. Hua, and Q. Dewen, "Research progress and application of microfluidic chip technology," *Plant Protection*, vol. 4, pp. 1–8, 2014.

[3] S. Dongping, *Modern instrument analysis and experimental techniques (volume 1)*, Science Press, Beijing, 2015.

[4] L. Yang, Z. Sixiang, L. Shanshan, Z. Xu, Y. Xinying, and H. Xiaowei, "Development of the micro gas chromatography columns for malodorous gas detection," *Micronanoelectronic Technology*, vol. 7, pp. 447–450, 2014.

[5] L. Huwei, *Gas chromatography method and its application*, Chemical Industry Press, Beijing, 2007.

[6] Q. Meiling, *Gas chromatographic analysis and application*, vol. 43, Science Press, Beijing, 2012.

[7] H. Jintu, "Inquiry upon the separating rate of chromatography," *Journal of Xinyang Teachers College (Natural Science Edition)*, vol. 4, pp. 351–353, 1990.

[8] M. Zhu and P. Hu, *Instrumental analysis*, Higher Education Press, Beijing, fourth edition, 2008.

[9] X. Zhang, L. Liu, Y. Xu, J. Li, F. Wang, and S. Zhang, "Odor gas online detection system and experiments research," *Journal of Hebei University of Technology*, vol. 3, pp. 38–43, 2015.

[10] X. Yang, *The development and experimental research of odorous gases detecting system*, Hebei University of Technology, Tianjin, 2015.

[11] F. Wang, "The research on data processing and calibration of odorous detection system," Hebei University of Technology, Tianjin, 2016.

[12] S. P. Cram and R. S. Juvet, "Gas chromatography," *Analytical Chemistry*, vol. 44, no. 5, pp. 213–241, 2002.

[13] Y. Haiming and S. Meihua, "Influence of resolution on quantitative analysis by gas chromatography," *Pollution Control Technology*, vol. 6, pp. 49-50, 2006.

[14] R. Nasreddine, V. Person, C. A. Serra, and S. le Calvé, "Development of a novel portable miniaturized GC for near real-time low level detection of BTEX," *Sensors & Actuators B Chemical*, vol. 224, pp. 159–169, 2016.

Research Article

Kinetic Gait Changes after Robotic Exoskeleton Training in Adolescents and Young Adults with Acquired Brain Injury

Kiran K. Karunakaran [ID],[1,2,3] **Naphtaly Ehrenberg** [ID],[1,3] **JenFu Cheng** [ID],[2,3]
Katherine Bentley,[2,3] **and Karen J. Nolan** [ID][1,2,3]

[1]*Center for Mobility and Rehabilitation Engineering Research, Kessler Foundation, West Orange, New Jersey 07052, USA*
[2]*Physical Medicine and Rehabilitation, Rutgers New Jersey Medical School, Newark, New Jersey 07103, USA*
[3]*Research Department, Children's Specialized Hospital, New Brunswick, New Jersey 08901, USA*

Correspondence should be addressed to Kiran K. Karunakaran; kkarunakaran@kesslerfoundation.org

Background. Acquired brain injury (ABI) is one of the leading causes of motor deficits in children and adults and often results in motor control and balance impairments. Motor deficits include abnormal loading and unloading, increased double support time, decreased walking speed, control, and coordination. These deficits lead to diminished functional ambulation and reduced quality of life. Robotic exoskeletons (RE) for motor rehabilitation can provide the user with consistent, symmetrical, goal-directed repetition of movement, as well as balance and stability. *Purpose.* The goal of this preliminary prospective before and after study is to evaluate the therapeutic effect of RE training on the loading/unloading and spatial-temporal characteristics in adolescents and young adults with chronic ABI. *Method.* Seven participants diagnosed with ABI between the ages of 14 and 27 years participated in the study. All participants received twelve 45 minute sessions of RE gait training. The bilateral loading (linearity of loading and rate of loading), speed, step length, swing time, stance time, and total time were collected using Zeno™ walkway (ProtoKinetics, Havertown, PA, USA) before and after RE training. *Results.* Results from the study showed improved step length, speed, and an overall progression towards healthy bilateral loading, with linearity of loading showing a significant therapeutic effect ($p < 0.05$). *Conclusion.* These preliminary results suggest that high dose, repetitive, consistent gait training using RE has the potential to induce recovery of function in adolescents and young adults diagnosed with ABI.

1. Introduction

Acquired brain injury (ABI) is a leading cause of hemiparesis resulting in gait and balance deficits in adolescents and young adults [1–3]. These deficits result in abnormal loading and unloading, increased double support time, and decreased walking speed, control, and coordination, leading to impairment in functional ambulation and associated activities of daily living [2–5]. Recovery involves rehabilitation through high dose physical therapy [6]. It is based on the theory that the human brain is capable of self-reorganization, or plasticity, through continuous, consistent, repeated practice aimed at restoring function and independence [7–9]. Conventional therapy alone may not be able to provide enough consistent mass practice and repetition to facilitate the neuroplasticity

needed for a functional recovery [10]. Consequently, after motor rehabilitation individuals with ABI can experience variable recovery with residual gait deviations. As a result of these residual motor and balance deficits, individuals diagnosed with ABI may develop compensatory mechanisms such as abnormal or asymmetrical loading and unloading characteristics and prolonged weight transfer, in order to achieve ambulation [4, 11].

Ground reaction force (GRF) parameters, e.g., peak values, linearity, and rates of loading/unloading, symmetry coefficients, and force integrals, are used for assessment of pathological gait and evaluation of therapeutic efficacy [12–14]. The analysis of vertical forces during gait provides information on weight bearing and balance, and these force or pressure patterns in the paretic leg are known to be

TABLE 1: Subject demographics.

Subject	Condition	Affected side	Gender	Age	Height (m)	Weight (Kg)	Years since injury
1	TBI	Left	Male	23	1.83	90.00	1
2	Stroke	Left	Female	23	1.60	54.00	.9
3	Anoxic	Left	Female	17	1.63	54.00	2
4	Stroke	Left	Male	16	1.83	67.50	.5
5	TBI	Left	Male	22	1.78	63.50	3
6	TBI	Left	Female	27	1.63	62.60	5
7	TBI	Right	Male	14	1.65	49.44	0.5
Mean ± SD				20.29 ± 4.68	1.71 ± 0.10	63.01 ± 13.51	1.84 ± 1.66
1	HC	n/a	Male	26	1.57	77.11	n/a

correlated with walking speed and motor recovery in stroke patients [15, 16]. Therefore, improvements in vertical pressure profiles might demonstrate improvement in gait and overall functional ambulation.

In a healthy gait cycle, the loading response is bilaterally symmetrical [17]. It has three distinct phases, starting with a peak force during the initial loading phase, followed by a midstance phase where there is a decrease in loading, and ending with another peak force during the terminal unloading phase [17]. Thus, the loading response resembles a bimodal M shape [17]. The transfer of weight during the initial loading phase allows for the efficient transfer of momentum from one leg to the other and the uninterrupted use of the kinetic energy that is created by swing limb activity [18]. The rate of loading determines the speed of gait [15]. Research has shown that smooth linear loading helps conserve momentum and shifts the body's weight to the next phase of the gait cycle while maintaining speed [14, 17, 19]. If weight transfer is delayed or loading is nonlinear, it will result in a loss of energy and hence less efficient gait, leading to decreased speed and necessitating the use of other compensatory gait mechanisms. Limb loading is often inefficient in individuals with ABI because the affected limb has a difficult time accepting weight, resulting in a nonlinear loading and decreased momentum. Consequently, a targeted goal during gait rehabilitation in ABI is to improve loading profiles in order to facilitate healthier movement patterns.

Lower extremity robotic exoskeletons (REs) are currently being used in rehabilitation to restore gait functionality. REs have the potential to provide the user with high dose, consistent, symmetrical bilateral loading [9, 20–26] profiles during gait. It can provide an increased number of steps (increased dosing) in a consistent and controlled training environment, which is ideal for inducing neuroplasticity [20, 27]. This is essential for chronic ABI patients who need high dose, consistent therapy to induce cortical reorganization for functional recovery. This study utilized an RE to provide intensive gait training to adolescents and young adults diagnosed with an ABI, with the goal of evaluating the efficacy of high repetition robotic training on loading/unloading profiles. The objective of this preliminary prospective study was to evaluate the therapeutic effect of RE on their loading/unloading characteristics. This paper also provides details

of the RE gait training environment for reference, to help understand the therapeutic effects.

2. Materials and Methods

This is a preliminary prospective before and after study which is to evaluate the therapeutic effect of RE training on the loading/unloading and spatial-temporal characteristics in adolescents and young adults with chronic ABI.

2.1. Participants. Twelve participants with ABI were recruited for this study. Kinetic and temporal-spatial data for baseline and follow-up visits were only available from nine participants. Further, two participants were excluded from the analysis as they were diagnosed with bilateral deficits. Therefore, seven participants diagnosed with ABI and hemiparesis and a single healthy control (HC) were included for this analysis (Table 1). The inclusion criteria for ABI participants in this investigation included (1) diagnosed with an acquired brain injury (anoxic, stroke, or TBI); (2) between the ages of 13 and 28; (3) able to walk with or without an assistive device; (4) no additional orthopedic, neuromuscular, or severe neurological pathologies (unrelated to their ABI) that would interfere with their ability to walk; (5) able to stand upright for 30 minutes with assistance; and (6) able to physically fit into the RE (weight ≤ 100 kg, height ≤ 1.88 m, hip width 0.36 m-0.46 m). The inclusion criteria for the HC were no orthopedic, neuromuscular, or severe neurological pathologies that would interfere with gait and balance. All procedures performed in this investigation were approved by the Human Subjects Institutional Review Board at Kessler Foundation, and informed consent was obtained prior to study participation.

2.2. Robotic Exoskeleton Gait Training. Robotic gait training in bilateral assistance mode was administered as an outpatient rehabilitation gait intervention at the Kessler Foundation using a commercially available robotic exoskeleton (Figure 1, EksoGT, Ekso Bionics, Inc., Richmond, CA, USA) for 45 minutes per day for 12 days over a period of 4 weeks. A licensed physical therapist administered all RE gait training sessions and adjusted the assistance provided by the robot to the individual participant's therapy progression. A member of the study team was present at all times during

Figure 1: Robotic gait training with a participant with ABI administered by a trained physical therapist.

the RE gait training sessions to assist the physical therapist and ensure participant safety. The healthy control participant was not given RE training as part of the investigation.

The RE provided overground gait rehabilitation under the guidance of a licensed physical therapist. The RE's upper section is attached to the user's upper body, with a backpack style shoulder harness and torso brace and also houses the battery pack, while the lower sections are affixed to the legs with upper thigh straps, shin guards, and secure foot bindings. The RE has two active degrees of freedom at the hip and the knee, respectively, and a passively sprung ankle joint with adjustable stiffness in the sagittal plane. The RE provides assistive torques to the hip and knee joints to perform the predefined gait trajectory and provides variable assistance as required by the participants bilaterally. The actuated range of motion at the hip is -20° to 135°, and the actuated range for the knee is 0° to 120° [28]. All steps were initiated by the participant. In order to trigger a step, the subject performed a

lateral weight shift to a predetermined distance from midline to initiate advancement of the back (preswing) leg.

2.3. Data Collection Procedures. The participants with ABI participated in two data collection sessions (baseline and follow-up after 12 sessions of outpatient RE training), and data was collected while walking with (training environment) and without the RE. The participants with ABI did not utilize any orthotic devices or dorsiflexion wrap during data collection. The reference HC participated in one data collection session, and data was collected while walking without the RE.

During each data collection session, temporal, spatial, and loading data was collected using a Zeno™ walkway (ProtoKinetics, Havertown, PA, USA) at 120 Hz. The participant performed up to 6 walking trials (approximately six 10 meter walks) at a self-selected pace per condition (with and without RE) and wore shoes for all walking assessments. Participants were allowed to rest or take breaks at any time during testing to minimize the effects of fatigue. A member of the study

TABLE 2: Outcome measures.

Outcome measure	Description	Statistical analysis
Total vertical pressure (TVP)	TVP during the stance phase of each gait cycle was computed, and an average TVP for all gait cycles was calculated for both the legs without and with RE that was computed for each subject and for the HC. The TVP was normalized to 100% of stance in each condition for comparison. The stance phase was further divided into initial double support (IDS) and terminal double support (TDS) phases based on heel strike and toe off. The IDS pressure was computed as the pressure between ipsilateral heel strikes to contralateral toe off. The TDS pressure was computed as the pressure between contralateral heel strikes to ipsilateral toe off. Mean and standard deviation TVP for all participants with ABI was computed.	
Linearity of loading (goodness of fit)	A best fit line was computed for the average IDS loading phase for each session for each subject. A goodness of the fit was computed to assess the error between the fitted line and the average loading during IDS for each subject in each session. The goodness of fit was used to assess the smooth linearity of loading. R-square (R^2) was computed to assess the square of the correlation between average loading during IDS and the best fit line. A higher R^2 value signifies a closer fit to the best fit line or increased linearity.	Kolmogorov- Smirnov Z test ($p < 0.05$) of normality showed that the data were not normal. Wilcoxson signed rank test was used to determine the therapeutic effect (baseline to follow-up without RE) on goodness of fit.
Rate of linear loading (slope of initial loading)	The slope of the average IDS loading phase was computed for each subject. Slope indicates the rate of linear loading. Increased slope in the IDS phase indicates an increased moment during the first rocker.	Kolmogorov- Smirnov Z test ($p > 0.05$) of normality showed that the data were normal. A paired sample t-test was performed to determine the therapeutic effect (baseline to follow-up without RE) on the slope of initial loading.
Walking speed	The average walking speed was computed for each subject as the linear distance with respect to time to complete a gait cycle.	Kolmogorov- Smirnov Z test ($p > .05$) of normality showed that the data were normal. A paired sample t-test was performed to determine the therapeutic effect (baseline to follow-up without RE) on walking speed.
Step length	The average step length for each gait cycle was computed as the forward linear displacement between foot contact of the ipsilateral leg to foot contact of the contralateral leg during each gait cycle. Average step length was computed for each subject.	Kolmogorov- Smirnov Z test ($p > .05$) of normality showed that the data were normal. A paired sample t-test was performed to determine the therapeutic effect (baseline to follow-up without RE) on step length.
Temporal measures	Total time was computed as the time between foot contact of one leg to the subsequent foot contact of the same leg. The average total time was computed for each gait cycle. Further, average swing time for each subject during each condition was computed as the time between the foot off the floor of one leg to foot contact of the same leg during the gait cycle. Average stance time for each subject during each condition was computed as the time between the foot contact of one leg to toe off the same leg during the gait cycle.	Kolmogorov- Smirnov Z test ($p < .05$) of normality showed that the data were not normal. Wilcoxson signed rank test was used to the therapeutic effect (baseline to follow-up without RE) on total time, swing time, and stance time.

team was present with the participants at all times during the walking trials.

During the baseline and follow-up gait assessments in the RE, torque was provided bilaterally as needed at the hip and knee to complete the gait.

2.4. Data Analysis. PKMAS (ProtoKinetics Havertown, PA, USA) and MATLAB (MathWorks, Natick, MA, USA) were used for data analysis. The data were preprocessed using the PKMAS software, and temporal, spatial, and normal-ized pressure data were exported. Custom MATLAB algo-rithms were used to analyze the gait trajectories for each session with and without the RE. The exported data were further divided into gait cycles, with a gait cycle being defined as the period from ground contact of one foot to the subsequent ground contact of the same foot. Data for up to 15 gait cycles per condition and per session were available for each subject and were used for data analysis. Selected outcome measures and statistical analyses are pre-sented in Table 2.
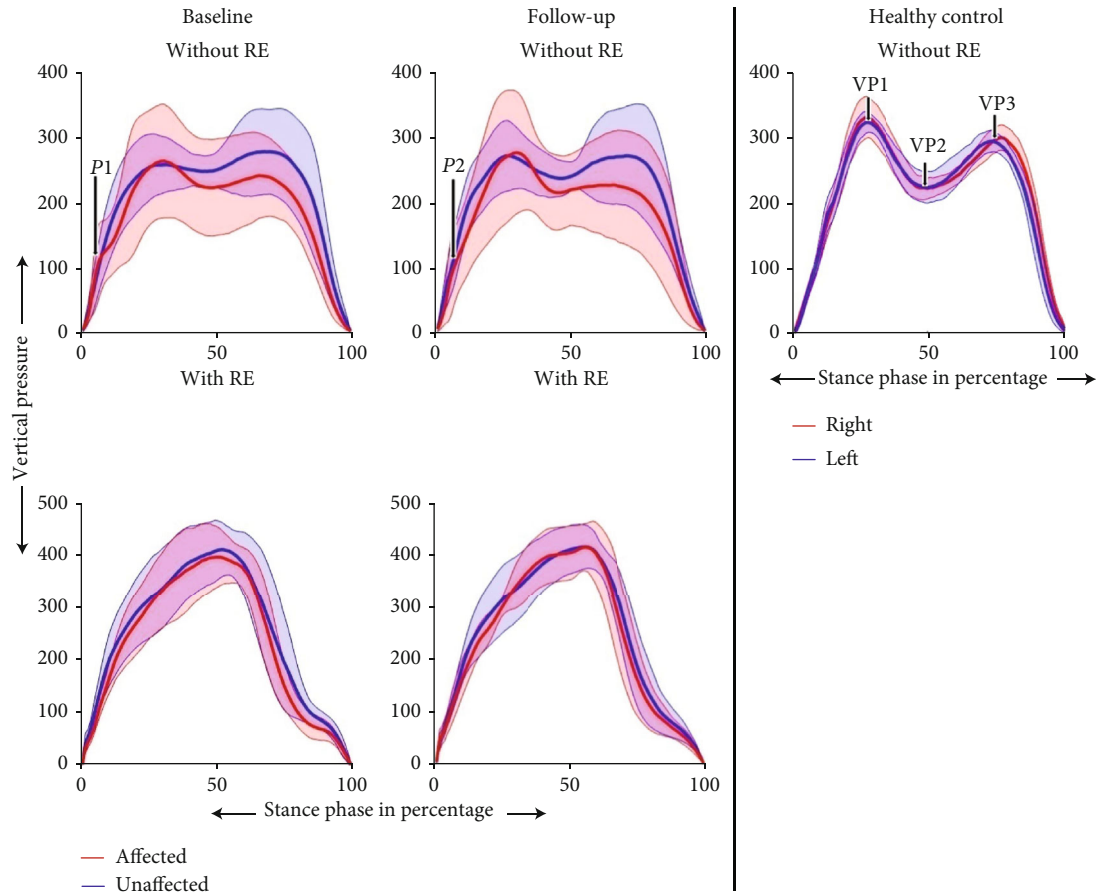
FIGURE 2: Mean ± standard deviation of the TVP of the affected and unaffected leg of individuals with ABI during walking with and without an RE at baseline and follow-up and one reference HC. Data is normalized to 100% of the stance phase.

3. Results

3.1. Total Vertical Pressure (TVP). Figure 2 shows the average TVP of all participants with ABI at baseline and at follow-up for both the affected and the unaffected sides with and without RE and one reference HC. The reference HC's TVP profile demonstrated linear loading and unloading, a symmetrical loading pattern during stance bilaterally, and a minimal deviation from the mean across gait cycles. For participants with ABI walking without RE at baseline, the TVP demonstrated a perturbation during loading for the IDS phase (Figure 2-P1and Figure 3-P3) and increased loading on the unaffected side. At follow-up, the perturbation during loading for IDS decreased (Figure 2-P2 and Figure 3-P3), and there was increased loading on the affected limb during midstance. There was increased variation in the TVP on the affected side compared to the unaffected side for individuals with ABI, demonstrated by the standard deviations.

In the RE training environment, the TVP profile showed linear loading during IDS, but did not show the distinctive peaks as observed in the HC's data (Figure 2-VP1 and Figure 2-VP3) in both the affected and unaffected sides at both baseline and follow-up. Furthermore, a bilaterally symmetrical loading profile was observed in the RE training environment and for the HC as compared to without RE. The

deviation from the mean across gait cycles for participants with ABI was smaller in the RE training environment compared to without the RE at both baseline and follow-up.

3.2. Rate of Linear Loading (Slope of Initial Loading). There was an increase in the average slope from baseline to follow-up while walking without the RE (Table 3). A paired sample t-test for average slope did not show a significant therapeutic effect between baseline and follow-up, though the effect size ($p = 0.136$, Cohen's d effect size was 0.59) was high (Table 3). The average slope was higher in the training environment (with the RE) both at baseline and at follow-up compared to without the RE. The RE training environment was similar to HC (Table 3).

3.3. Linearity of Loading (Goodness of Fit). There was an increase in average R^2 from baseline to follow-up while walking without the RE (Table 3). The Wilcoxson signed rank test for R^2 showed a significant therapeutic effect between baseline and follow-up, and the effect size ($p = 0.018$, Cohen's d effect size was 0.6334) was high. The R^2 of loading was higher in the training environment (with the RE) at baseline and about the same at follow-up compared to without the RE. The RE training environment was similar to the HC (Table 3).
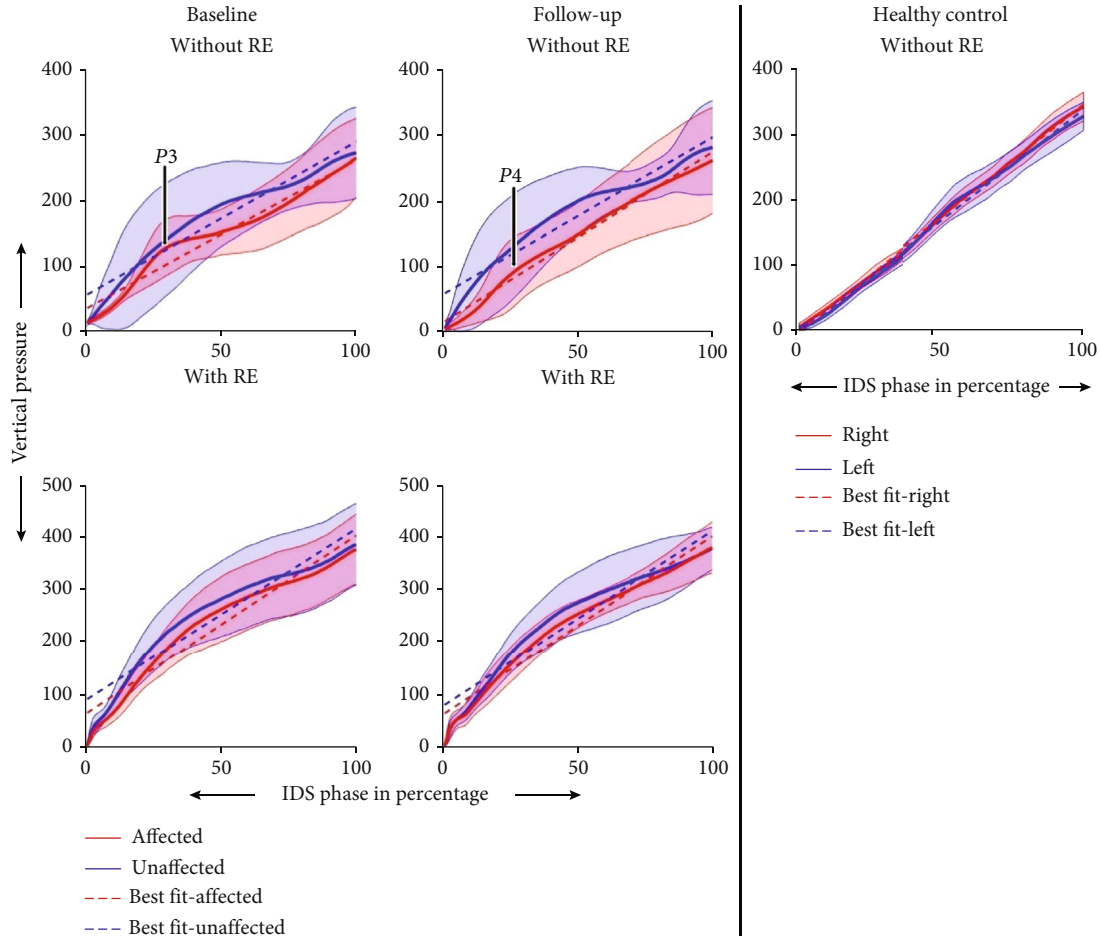
FIGURE 3: Mean ± standard deviation of the initial loading phase of the right and left leg of subjects with ABI while walking with and without the RE at baseline and at follow-up and a reference HC. The dotted lines are the best fit lines for the loading profile.

TABLE 3: Mean ± standard error of initial double support (IDS) loading characteristics on the affected side of all participants with ABI and IDS loading characteristics on the left side of one HC.

Metric	Baseline-without RE	Follow-up-without RE	Baseline-with RE	Follow-up-with RE	HC
Slope	2.33 ± 0.28	2.60 ± 0.36	3.44 ± 0.29	3.43 ± 0.24	3.46
Goodness of fit	0.889 ± 0.05	0.934 ± 0.04	0.927 ± 0.02	0.923 ± 0.02	0.99

3.4. Step Length. Step length without the RE showed an increase in both the unaffected and affected sides at follow-up compared to baseline in subjects 2,3,5,6, and 7, while it showed a decrease in subject 1 and no change on the unaffected side and an increase on the affected side in subject 4 (Figures 2(a) and 2(b)). A paired sample *t*-test did not show a significant therapeutic effect between baseline and follow-up, though the effect size ($p = .075$, Cohen's *d* effect size was 0.81) was high. The average step length was lower in the training environment (with the RE) compared to without the RE at baseline and follow-up. The average step length of the HC data was higher than ABI without RE.

3.5. Walking Speed. Walking speed without the RE increased from baseline to follow-up for subjects 2,4,5,6, and 7, while subject 1 decreased their speed, and subject 3 showed no

change (Figure 2(c)). A paired sample *t*-test did not show a significant therapeutic effect between baseline and follow-up, though the effect size ($p = 0.083$, Cohen's *d* effect size was 0.80) was high. The average walking speed was lower in the training environment (with the RE) compared to without the RE at baseline and follow-up. The average speed of the HC data was higher than ABI without RE.

3.6. Temporal Characteristics. Average total time, stance time, and total double support time decreased from baseline to follow-up (Table 4), but did not show a significant therapeutic effect ($p_{\text{totaltime}} = 0.612$, $p_{\text{stance time}} = 0.398$, $p_{\text{total double support time}} = 0.237$). The average total time, stance time, and total double support time were higher in the training environment (with the RE) compared to without the RE at baseline and at follow-up. Average total time, stance time,

TABLE 4: Mean ± standard error of temporal characteristics.

	Metric	Baseline-without RE	Follow-up-without RE	Baseline-with RE	Follow-up-with RE	HC
Affected	Total time	2.18 ± 0.69	1.98 ± 0.50	3.78 ± 0.17	3.35 ± 0.09	1.24
	Stance time	1.66 ± 0.62	1.46 ± 0.45	3.12 ± 0.15	2.69 ± 0.10	0.80
	Swing time	0.52 ± 0.07	0.52 ± 0.06	0.66 ± 0.05	0.66 ± 0.06	0.44
	Total double support	1.25 ± 0.62	1.05 ± .045	2.40 ± 0.17	2.04 ± 0.10	0.36
Unaffected	Total time	2.15 ± 0.66	1.95 ± 0.48	3.77 ± 0.16	3.33 ± 0.10	1.27
	Stance time	1.74 ± 0.66	1.55 ± 0.47	3.05 ± 0.17	2.69 ± 0.10	0.85
	Swing time	0.41 ± 0.04	0.40 ± 0.04	0.72 ± 0.11	0.64 ± 0.02	0.43
	Total double support	0.73 ± 0.49	0.44 ± 0.21	1.19 ± 0.10	1.01 ± 0.05	0.23

and total double support time of the HC data were lower than ABI without RE.

Swing time did not change ($p = 0.866$) from baseline to follow-up (Table 4). The average swing time was higher in the training environment (with the RE) compared to without the RE at baseline and follow-up. Average swing time of the HC data was lower than ABI without RE.

4. Discussion

Moderate to severe ABIs may result in gait and balance deficits such as reduced speed, step length, and abnormal loading and unloading characteristics during walking. Current research is focused on reducing these deficits with the use of REs and understanding the therapeutic effects of REs in the chronic stages of recovery. Recovery may be gradual during the chronic stages and may take place over the course of several years. In this study, the efficacy of RE usage for 12 sessions on the recovery of gait in adolescents and young adults with chronic ABI was investigated using kinetic and temporal-spatial outcomes, such as loading, unloading, speed, step length, and gait cycle timing. Following the use of the RE, an increase in linearity of loading during IDS with an associated increase in speed, step length, and decrease in stance phase time was observed.

During a healthy gait cycle, the loading/unloading response is bilaterally symmetrical, as is observed in Figure 2. It has three distinct phases. The role of the first phase is the weight acceptance which includes initial contact (heel strike) and the initial loading response. This is the initial double support phase of the gait cycle and starts with heel strike and continues until the contralateral foot is in swing [17]. The second phase supports the upper body on a single limb, and it is comprised of midstance and terminal stance (single support phase). The third phase includes preswing and the terminal unloading phase [17]. Distinct peaks and a valley are observed in the loading profile during these phases, with a peak force (Figure 2-VP1) at the end of the initial loading, followed by a midstance and terminal phase where there is a decrease in loading (Figure 2-VP2) and ending with another peak force (Figure 2-VP3) before terminal unloading [29]. In addition, bilaterally symmetrical loading profiles are present. These attributes are observed in the reference HC gait. In contrast, the individuals with ABI had a perturbation

during initial loading (Figure 2-P1, Figure 3-P3) on the affected side during baseline, which indicates a nonlinear initial loading response. Linear loading directly contributes to the momentum during gait [30]. Therefore, any nonlinearity would result in decreased momentum and slower load transfer during gait, leading to a disruption in forward progression. ABI patients with hemiplegia often present with reduced hip flexion, dorsiflexion, and plantarflexion during the initial loading phase due to muscle paresis [11, 31]. This results in the tibia not rolling forward over the calcanium, which is observed as non-linearity, to complete the transfer of the body weight from the contralateral limb [11]. In this study, linearity of loading was quantified using goodness of fit, which showed that the individuals with ABI had a statistically significant improvement in the linearity of their loading responses at follow-up compared to baseline (Figure 2-P2, Figure 3-P4, and Table 3). This may indicate that the participants have healthier foot strike, and initial loading response with improved momentum, at follow-up compared to baseline. The slope of the initial loading response showed an increase at follow-up compared to baseline (Table 3). Although the difference was not significant, it had a high Cohen's d effect size at follow-up compared to baseline, indicating that the participants had improved their rate of loading, once again, demonstrating preserved forward momentum. Thus, at follow-up, TVP showed an increase in smooth linearity and rate of loading similar to healthy individuals [17]. Research has shown that improved linearity and slope during loading result in improved gait pattern, resulting in improved functional ambulation and quality of life [14]. Also, improvements in initial loading may reduce breaking forces [32], leading to a more efficient gait. Though the participant's overall loading profiles showed improvements from baseline to follow-up, they still preferentially loaded their unaffected side.

The loading profile with the RE showed a smooth linear loading (Figure 3), but without any distinctive peaks. A passive ankle in the RE (which provides a midfoot or flat foot landing) or lower speed may have resulted in the absence of two distinctive peaks. Changes in walking speed may improve this profile and need to be investigated further. In addition, a bilaterally symmetrical profile with lower variability was observed at both baseline and follow-up while walking with the RE compared to walking without the RE,
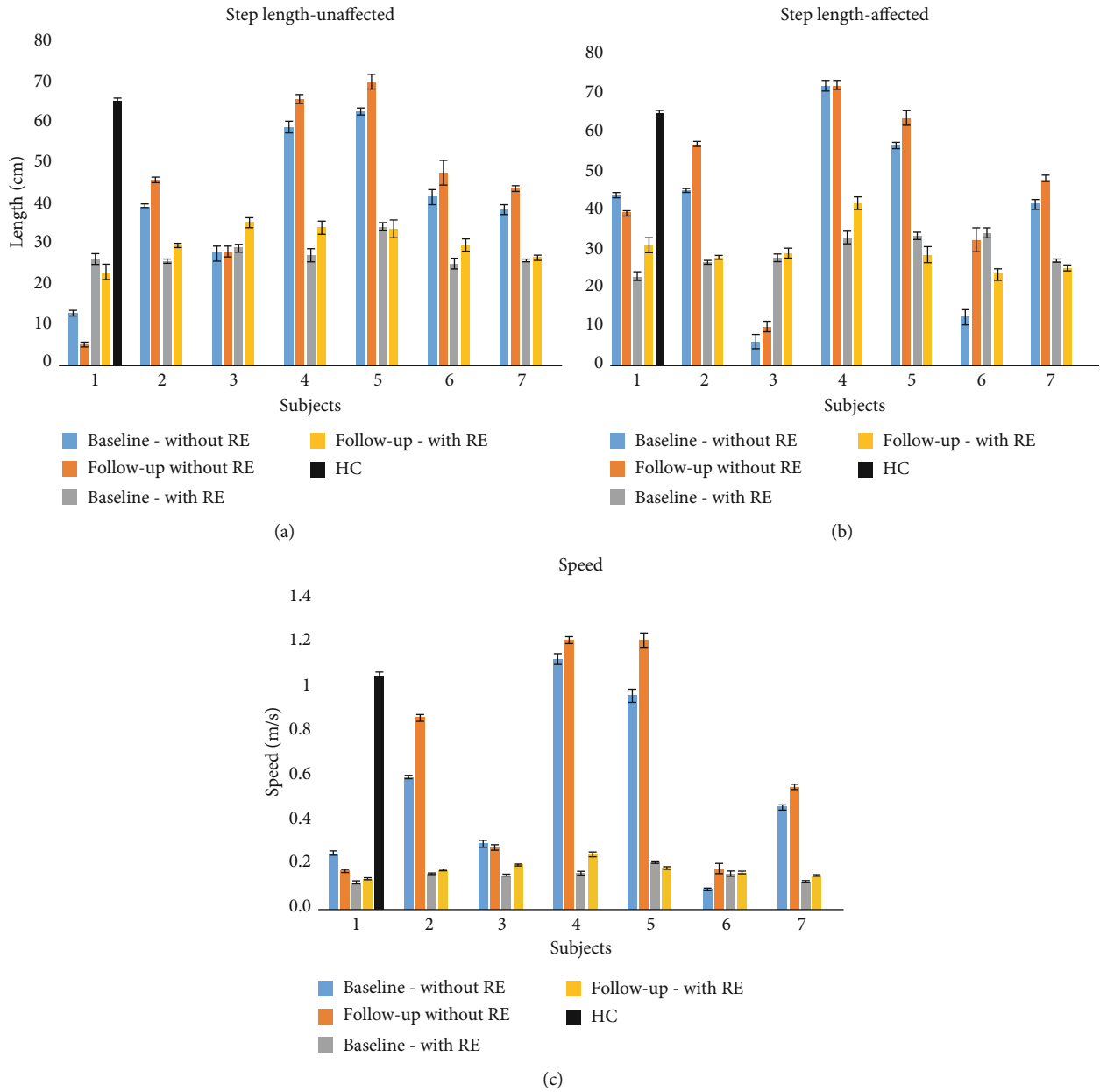
FIGURE 4: Mean ± standard error of the step length with and without the RE on the (a) affected side, (b) unaffected side, and (c) walking speed.

indicating that the RE provides a consistent training environment throughout therapy. Thus, the improvements in the smoothness and linearity of loading could be attributed to the RE training. Our results are in accordance with previous research which showed that with the use of overground RE, there was an increased bilateral limb loading symmetry that closely resembled able-bodied gait [33, 34].

In addition, after 12 sessions of RE gait training, there was a slight increase in the step length and an increase in walking speed (Figure 4(a)). There was no change in swing time and a decrease in stance time. These results suggest that the increased step length (Figure 4(a)) and improved TVP profile may have contributed to the increased walking speed (Figure 2(a)). They are significant since most of the participants in this study were walking below the community

ambulation speed (1 m/s) [35]. An increase in speed could improve their community ambulation and by extension, their activities of daily life. Previous research on overground gait training with RE has shown the ability of RE to improve balance and functional ambulation in patients with ABI [36, 37]. Overground REs require active participation, where patients initiate each step and are responsible for maintaining trunk and balance [21, 37]. Active participation in combination with RE's ability to provide quality gait and increased dose training promotes improved brain plasticity and connectivity remodulation, as compared to conventional gait training [21, 38, 39].

This is one of the first studies to show the feasibility of using RE for gait training in adolescents and young adults with ABI. The results from this preliminary study show a

therapeutic effect of RE on the loading/unloading characteristics and a consequent impact on functional ambulation. Although these results are promising, the limitations of this investigation are the limited sample size, number of training sessions, and absence of control group. The data from this study indicates some promising results for therapeutic effects of an RE device for ABI gait rehabilitation that should continue to be explored with a larger sample.

5. Conclusion

The results from this investigation suggest that improvement in functional and neuromechanical outcomes after 4 weeks of RE gait training can be achieved in adolescents and young adults with chronic ABI. This study suggests that there could be potential long-term effects of improved loading and unloading, increased step length, and increased speed due to RE gait training. While the current results are promising, future studies with a larger sample would be required to further understand the efficacy of the RE in adolescents and young adults to confirm any training effect conclusively.

Data Availability

The data is currently unavailable due to Kessler Foundation IRB restrictions.

Conflicts of Interest

The authors have no conflict of interest.

Acknowledgments

References

[1] R. A. Newton, "Balance abilities in individuals with moderate and severe traumatic brain injury," *Brain Injury*, vol. 9, no. 5, pp. 445–451, 2009.

[2] G. Williams, M. E. Morris, A. Schache, and P. R. McCrory, "Incidence of Gait Abnormalities after Traumatic Brain Injury," *Archives of physical medicine and rehabilitation*, vol. 90, no. 4, pp. 587–593, 2009.

[3] K. M. Michael, J. K. Allen, and R. F. MacKo, "Reduced Ambulatory Activity after Stroke: The Role of Balance, Gait, and Cardiovascular Fitness," *Archives of physical medicine and rehabilitation*, vol. 86, no. 8, pp. 1552–1556, 2005.

[4] M. A. Kemu, "Kinetics and kinematics of loading response in stroke patients (a review article)," *Annals of King Edward Medical University*, vol. 14, no. 4, 2008.

[5] M. G. Benedetti, V. Agostini, M. Knaflitz, V. Gasparroni, M. Boschi, and R. Piperno, "Self-Reported Gait Unsteadiness in Mildly Impaired Neurological Patients: An Objective Assessment through Statistical Gait Analysis," *Journal of neuroengineering and rehabilitation*, vol. 9, no. 1, p. 64, 2012.

[6] N. N. Byl, E. A. Pitsch, and G. M. Abrams, "Functional outcomes can vary by dose: learning-based sensorimotor training for patients stable poststroke," *Neurorehabilitation and Neural Repair*, vol. 22, no. 5, pp. 494–504, 2008.

[7] J. D. Schaechter, "Motor rehabilitation and brain plasticity after hemiparetic stroke," *Progress in Neurobiology*, vol. 73, no. 1, pp. 61–72, 2004.

[8] M. Pekna, M. Pekny, and M. Nilsson, "Modulation of neural plasticity as a basis for stroke rehabilitation," *Stroke*, vol. 43, no. 10, pp. 2819–2828, 2012.

[9] S. Lennon, D. Baxter, and A. Ashburn, "Physiotherapy Based on the Bobath Concept in Stroke Rehabilitation: A Survey within the UK," *Disability and Rehabilitation*, vol. 23, no. 6, pp. 254–262, 2001.

[10] D. R. Louie and J. J. Eng, "Powered robotic exoskeletons in post-stroke rehabilitation of gait: a scoping review," *Journal of Neuro Engineering and Rehabilitation*, vol. 13, no. 1, 2016.

[11] D. A. Winter, *Biomechanics and Motor Control of Human Gait: Normal, Elderly, and Pathological*, Waterloo Biomechanics, Canada, 2009.

[12] M. T. Jahnke, S. Hesse, C. Schreiner, and K. H. Mauritz, "Dependences of Ground Reaction Force Parameters on Habitual Walking Speed in Hemiparetic Subjects," *Gait Posture*, vol. 3, no. 1, pp. 3–12, 1995.

[13] K. Karunakaran, N. Ehrenberg, J. Cheng, and K. J. Nolan, "Effects of Robotic Exoskeleton Gait Training on an Adolescent with Brain Injury," in *IEEE 41h Annual International Conference on Engineering in Medicine and Biology Society (EMBC)*, pp. 4445–4448, Berlin, Germany, Germany, 2019.

[14] K. J. Nolan and M. Yarossi, "Weight Transfer Analysis in Adults with Hemiplegia Using Ankle Foot Orthosis," *Prosthetics and orthotics international*, vol. 35, no. 1, pp. 45–53, 2017.

[15] C. Chen, P. W. Hong, C. Chen et al., "Ground Reaction Force Patterns in Stroke Patients with Various Degrees of Motor Recovery Determined by Plantar Dynamic Analysis," *Chang Gung medical journal*, vol. 30, no. 1, 2007.

[16] A. M. Wong, Y. C. Pei, W. H. Hong, C. Y. Chung, Y. C. Lau, and C. P. Chen, "Foot Contact Pattern Analysis in Hemiplegic Stroke Patients: An Implication for Neurologic Status Determination," *Archives of physical medicine and rehabilitation*, vol. 85, no. 10, pp. 1625–1630, 2004.

[17] J. Perry and J. Burnfield, "GAIT Normal and Pathological Function," *Journal of Sports Science and Medicine*, vol. 9, no. 2, p. 353, 2010.

[18] H. J. Dananberg, "Functional Hallux Limitus and its Relationship to Gait Efficiency," *Journal of the American Podiatric Medical Association*, vol. 76, no. 11, pp. 648–652, 1986.

[19] P. A. Goldie, T. A. Matyas, O. M. Evans, M. Galea, and T. M. Bach, "Maximum Voluntary Weight-Bearing by the Affected and Unaffected Legs in Standing Following Stroke," *Clinical Biomechanics*, vol. 11, no. 6, pp. 333–342, 1996.

[20] A. Esquenazi, M. Talaty, and A. Jayaraman, "Powered exoskeletons for walking assistance in persons with central nervous system injuries: a narrative review," *PM&R*, vol. 9, no. 1, pp. 46–62, 2017.

[21] F. Molteni, G. Gasperini, G. Cannaviello, and E. Guanziroli, "Exoskeleton and end-effector robots for upper and lower limbs rehabilitation: narrative review," *PM&R*, vol. 10, 9 Suppl 2, pp. S174–S188, 2018.

[22] H. Igo Krebs, N. Hogan, M. L. Aisen, and B. T. Volpe, "Robot-aided neurorehabilitation," *IEEE Transactions on Rehabilitation Engineering*, vol. 6, no. 1, pp. 75–87, 1998.

[23] A. M. Dollar and H. Herr, "Lower extremity exoskeletons and active orthoses: challenges and state-of-the-art," *IEEE Transactions on Robotics*, vol. 24, no. 1, pp. 144–158, 2008.

[24] K. Anam and A. A. Al-Jumaily, "Active exoskeleton control systems: state of the art," *Procedia Engineering*, vol. 41, pp. 988–994, 2012.

[25] L. Dipietro, M. Ferraro, J. J. Palazzolo, H. I. Krebs, B. T. Volpe, and N. Hogan, "Customized interactive robotic treatment for stroke: EMG-triggered therapy," *IEEE Transactions on Neural Systems and Rehabilitation Engineering*, vol. 13, no. 3, pp. 325–334, 2005.

[26] A. Jayaraman, S. Burt, and W. Z. Rymer, "Use of lower-limb robotics to enhance practice and participation in individuals with neurological conditions," in *Pediatric Physical Therapy*, vol. 29, pp. S48–S56, 2017.

[27] D. J. Reinkensmeyer, J. L. Emken, and S. C. Cramer, "Robotics, Motor Learning, and Neurologic Recovery," *Annual review of biomedical engineering*, vol. 6, no. 1, pp. 497–525, 2004.

[28] U S F & D Administration, *Ekso User Manual*, 2020, https://www.accessdata.fda.gov/cdrh_docs/pdf20/K200574.pdf.

[29] S. Winiarski and A. Rutkowska-Kucharska, "Estimated Ground Reaction Force in Normal and Pathological Gait," *Acta of Bioengineering & Biomechanics*, vol. 11, no. 1, 2009.

[30] D. A. Winter, *Biomechanics and Motor Control of Human Movement*, John Wiley & Sons., Hoboken, New Jersey, 2009.

[31] K. Fujita, H. Hori, and Y. Kobayashi, "Contribution of Muscle Activity at Different Gait Phases for Improving Walking Performance in Chronic Stroke Patients with Hemiparesis," *Journal of physical therapy science*, vol. 30, no. 11, pp. 1381–1385, 2018.

[32] T. S. Keller, A. M. Weisberger, J. L. Ray, S. S. Hasan, R. G. Shiavi, and D. M. Spengler, "Relationship between Vertical Ground Reaction Force and Speed during Walking, Slow Jogging, and Running," *Clinical biomechanics*, vol. 11, no. 5, pp. 253–259, 1996.

[33] S. R. Husain, A. Ramanujam, K. Momeni, and G. F. Forrest, "Effects of exoskeleton training intervention on net loading force in chronic spinal cord injury," in *Proceedings of the Annual International Conference of the IEEE Engineering in Medicine and Biology Society*, Honolulu, HI, USA, 2018.

[34] A. Ramanujam, A. Spungen, P. Asselin et al., "Training response to longitudinal powered exoskeleton training for SCI," in *Biosystems and Biorobotics*, 2017.

[35] N. M. Salbach, K. O'Brien, D. Brooks et al., "Speed and distance requirements for community ambulation: a systematic review," *Archives of Physical Medicine and Rehabilitation*, vol. 95, no. 1, pp. 117–128.e11, 2014.

[36] A. Rojek, A. Mika, Ł. Oleksy, A. Stolarczyk, and R. Kielnar, "Effects of Exoskeleton Gait Training on Balance, Load Distribution, and Functional Status in Stroke: A Randomized Controlled Trial," *Frontiers in Neurology*, vol. 10, 2020.

[37] F. Molteni, G. Gasperini, M. Gaffuri et al., "Wearable Robotic Exoskeleton for Overground Gait Training in Sub-Acute and Chronic Hemiparetic Stroke Patients: Preliminary Results," *European journal of physical and rehabilitation medicine*, vol. 53, 2017.

[38] R. S. Calabrò, A. Naro, M. Russo et al., "Shaping Neuroplasticity by Using Powered Exoskeletons in Patients with Stroke: A Randomized Clinical Trial," *Journal of neuroengineering and rehabilitation*, vol. 15, no. 1, p. 35, 2018.

[39] G. J. Androwis, R. Pilkar, A. Ramanujam, and K. J. Nolan, "Electromyography Assessment during Gait in a Robotic Exoskeleton for Acute Stroke," *Frontiers in neurology*, vol. 9, 2018.

Research Article

Development and Performance Verification of a Motorized Prosthetic Leg for Stair Walking

Kiwon Park [ID],[1] **Hyoung-Jong Ahn,**[2] **Kwang-Hee Lee,**[2] **and Chul-Hee Lee** [ID][2]

[1]*Department of Mechatronics Engineering, Incheon National University, Incheon 22012, Republic of Korea*
[2]*Department of Mechanical Engineering, Inha University, Incheon 22212, Republic of Korea*

Correspondence should be addressed to Chul-Hee Lee; chulhee@inha.ac.kr

The present study emphasized on the optimal design of a motorized prosthetic leg and evaluation of its performance for stair walking. Developed prosthetic leg includes two degrees of freedom on the knee and ankle joint designed using a virtual product development process for better stair walking. The DC motor system was introduced to imitate gait motion in the knee joint, and a spring system was applied at the ankle joint to create torque and flexion angle. To design better motorized prosthetic leg, unnecessary mass was eliminated via a topology optimization process under a complex walking condition in a boundary considered condition and aluminum alloy for lower limb and plastic nylon through 3D printing foot which were used. The structural safety of a developed prosthetic leg was validated via finite element analysis under a variety of walking conditions. In conclusion, the motorized prosthetic leg was optimally designed while maintaining structural safety under boundary conditions based on the human walking data, and its knee motions were synchronized with normal human gait via a PD controller. The results from this study about powered transfemoral prosthesis might help amputees in their rehabilitation process. Furthermore, this research can be applied to the area of biped robots that try to mimic human motion.

1. Introduction

A prosthetic leg is a basic rehabilitation device that helps rehabilitation of limb amputees, and the number of lower-limb amputees was estimated at approximately 7 million worldwide [1]. The development of prosthetic legs for lower-limb amputees is becoming an important issue. The above-knee amputees and particularly the lower-limb amputees' face increased difficulties in natural walking when compared with lower-knee amputees. This is because of the absence of the knee joints that are mainly responsible (50% of the importance) for the walking mechanism. The development of prosthetic leg that can create the natural knee motion is required for above-knee amputees.

The prosthetic leg can be classified as passive, variable-damping, or powered [2–4]. Prosthetic legs were traditionally classified as passive or variable-damping due to limitations of power generation and battery life. Passive and variable-damping types do not result in a natural motion in keeping with user intentions. Hence, the powered type is considered to replace the passive and variable-damping types. Powered prosthetic legs are enabled by advances in computers, robotics, and battery technology [5]. Powered prosthetic legs can be classified based on their method of torque generation as three linkage types or direct-drive types. Conventional three linkage types are an easy way to convert the linear motion to the rotating motion at the knee joint. However, a longer linkage is required to generate a large angle at the knee joint due to kinematics and leads to issues with the dimensions. Additionally, the center of mass shifts when the translation linkage shortens. The direct-drive type directly transfers the rotational motion of the motor to the joint. However, it requires an additional device to amplify the torque, which can increase the size and weight of the prosthesis.

There have been different kinds of studies about the development of powered prosthetic leg. Some researcher used electrohydraulic actuator for making the knee motion [6]. Due to advances in motor and battery technology, the

motor is introduced as an actuator of a prosthetic leg. Three linkage type powered prosthetic leg was developed using a motor and ball screw system [7, 8]. As motors become more compact and are enable to produce high torque, direct-drive type prostheses have been developed. DC motor was used for the drive system [9–11] or a harmonic drive and belt pulley system to amplify the torque applied to the knee joint [12]. Studies were performed on the kinematic structure design of an active prosthetic leg with a motor system [13, 14]. The extant research examined control mechanisms of knee and ankle joints to mimic a natural human gait [15, 16]. However, most previous studies focused on the kinematic walking mechanism or control for the level walking. Only a few studies carried out for control mechanisms under stair walking condition [9].

Most of the study of the powered prosthetic leg focused on overground walking, but for the disabled to move freely, a prosthetics capable of overcoming various obstacles should be developed. Typical walking obstacles include ramps and stairs, of which obstacles requiring greater power are stairs. In order to climb the stairs, it should be considered for various dynamic loads and requires more power than when walking on the overground. Therefore, it is inevitably required to be lightweight and an optimum structure that is as stable as possible under limited weight conditions. Existing studies focus on control to overcome the staircase, and research on optimizing the structure itself is insufficient. The purpose of this study was to perform the optimization of a motorized prosthesis capable of walking on stairs.

Several major factors influence the behavior of a prosthetic leg and include the alignment, mechanical properties, length, and the weight of the components of a prosthetic leg [17]. Although the weight of the prosthesis is one of the important factors for performance, researches to improve the structure of the prosthesis are rarely carried out. In order to overcome obstacles such as stair, it is necessary to study the optimization of the structure of prosthetic legs. Recently, studies about a prosthetic leg for walking stairs have been actively carried out, but little research has been implemented to design optimal structures for stair walking.

This study focuses on the development of a powered transfemoral prosthetic leg that can imitate the human walking motion and is optimized for stair walking. A structural design with two degrees of freedom at the knee and ankle joint was proposed. The power system of the knee joint is most important because the knee joint plays a major role (exceeding 50%) in the walking mechanism. In order to produce a higher torque for a stair walking, a larger motor and gear set should be applied, and the prosthetic leg must be relatively heavy due to their weight. The prosthetic leg structure was optimized with topology optimization to reduce its weight. Additionally, the ankle joint consists of a spring system to obtain a driving force to shift the body. The structure of the prosthetic leg was optimally designed with topology optimization to minimize weight while maintaining the safety of the structure. FE analysis was performed to verify the safety of the structure, and unlocked prosthetic leg test was carried out for testing the controller.

2. Design of the Motorized Prosthetic Leg System

2.1. Design Torque-Generating System. A transfemoral prosthetic leg is a rehabilitation apparatus for above-knee amputees. Thus, it is necessary for a prosthetic leg to implement the functions of the knee and ankle joints. Furthermore, it is necessary for a powered prosthetic leg to imitate the motion of each joint and to also possess dimensions similar to the body size to ensure user comfort. In this study, the walking mechanism and lower-limb structure were analyzed to determine the dimensions and performance of a prosthetic leg. A target user included a 28-year-old male with a body size involving a height of 176.6 cm and weight of 82 kg.

A previous study indicated that the specific weight of the shank and foot should correspond to 5.99% of the total body mass [18]. Therefore, the weight of the prosthetic leg should be less than 4.912 kg, which is set as the user's body weight. The length of the lower knee leg is measured for design. Figure 1 shows portions of the lower knee leg segment in which the shank possesses a length of 37.3 cm from the knee to the ankle, and the foot is of the length of 6.5 cm. Based on a previous study, the highest knee torque of human gait occurs during stair descent, and the normalized value at that point is approximately 1.3 Nm/kg [19]. Given a user weight of approximately 82 kg, the knee joint of a prosthetic leg can produce a torque of up to approximately 106.6 Nm for functions similar to the human knee. Similarly, the highest plantarflexion moments of human gait occur during level walking, and the maximum normalized value was approximately 1.55 Nm/kg [19]. That is, the ankle joint could support a torque of 127.1 Nm.

The core of the prosthesis that can climb stairs should be light, creating a torque that is strong enough to support the human weight. When selecting torque, safety factor was considered excessively. Since the weight difference due to the reducer was not large compared to other parts, safety was prioritized over weight reduction of the motor within the range that satisfies the weight requirement.

Two types of torque generating systems exist at the knee joint, namely, the three linkage type and the direct-drive type. Conventional linkage types can easily convert linear motion to rotation motion, but the size cannot be reduced due to the geometry limitations. In this study, a BLDC (brushless DC) motor was used because the three linkage-type mechanism involves performance and weight limitations due to the dimensions of the linkage structure [20]. The concept model is shown in Figure 2. EC 45 BLDC motor made by Maxon (136211) was selected as the knee joint motor, given a maximum power production capacity of 250 W. The torque constant and nominal current of the motor corresponded to 0.0328 Nm/A and 10.2 A, respectively. If the maximum current was assumed as the nominal current, then the maximum torque of the motor corresponded to 0.3346 Nm. Therefore, a reduction gear with a gear ratio of 318.5 : 1 was used to achieve the maximum required torque of 106.6 Nm for the knee joint.

During stair walking, the specific aim was to control the joint angle along the reference motion. It was important to
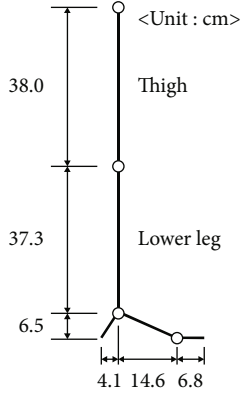
FIGURE 1: Dimensions of the lower knee leg.

check motion stability, not to control in 0.1 degree units like a precision mechanical system. To confirm the feasibility of operation of the entire lightweight prosthetic system (3D printing structure), the experiment was conducted to see if the designed motorized prosthesis can properly follow the reference motion. It has been confirmed that the error of the angle and delay was shown at the degree level.

The spring system was introduced to create the required torque without the addition of a motor and electric devices at the ankle joint. The plate spring was used for the ankle joint because it was advantageous in terms of space applications. Additionally, FE analysis was used to determine the spring coefficient. The maximum required torque corresponded to 127.1 Nm, and the knee flexion angle at that point was approximately 15°. The geometrical relationship indicated that the displacement of the spring δ is based on the following equation: $\delta = d \sin \theta$, in which $\theta = 15°$ and $d = 35$ mm. That is, the value of δ was approximately 9 mm. The thickness of the plate spring was determined by comparing the result of the FE analysis and the theoretical displacement δ at which they coincided. Figure 3 shows the proper thickness of the plate spring calculated by FE analysis. The property of the spring was assumed as SAE1045, which is typically used for spring. This material possessed a density (ρ) of 7,700 kg/m^3, elastic modulus (E) of 207 GPa, Poisson's ratio (ν) of 0.266, and a yield stress of 1515 MPa. Finally, the proper thickness of the spring was determined, and the value corresponded to 0.5 mm.

The design specifications are summarized in Table 1. The design of the active transfemoral prosthetic leg utilizes the BLDC motor designed for the knee joint. A motor with planetary gear and helical bevel gear actuated the knee joint. The spring system generated torque for the driving force from the ground at the ankle joint. The knee joint was capable of 100° of flexion at the knee. Additionally, the ankle was capable of 25° of plantarflexion and 15° of dorsiflexion at the ankle.

2.2. Design Process and Topology Optimization. First, the specifications of the knee joint were defined to satisfy the reported boundary conditions for walking on stairs based on a previous study [19]. The major components, such as the motor and torque amplifier, were then determined. This

was followed by designing a model and improving the model by topology optimization to reduce weight.

Topology optimization involves a mathematical method to obtain the optimal distribution of material for given design conditions including boundary conditions. The topology optimization problem was formulated in 1988 using a homogenization method [21]. Homogenization and solid isotropic material with penalization (SIMP) are widely used methods to solve optimization problems. These methods allow discrete design variables with intermediate density values ranging from 0 to 1. Specifically, SIMP is an extension of the homogenization method that has gained popularity in structural optimization because of its conceptual simplicity and ease of implementation [22].

Design variables, constraints, and an objective function are required to define an optimization problem. The problem for minimizing mass can be expressed as follows [23]:

Minimize: mass.

$$\text{Subject to } F(\sigma(x)) \le 0, \qquad \forall x \in \Omega. \tag{1}$$

The material failure function F depends on the stress field $\sigma(x)$ and strain field $\varepsilon(x)$, which are defined with respect to an original domain Ω. The failure function is defined with the von-Mises criterion, which is normally used as a failure criterion. The failure function F is expressed as follows:

$$F(\sigma) = \frac{\sigma_v}{\sigma_e} - 1, \tag{2}$$

where σ_e denotes the equivalent stress, which is usually regarded as the yield stress of the material, and σ_v denotes the effective von Mises stress that is computed as follows:

$$\begin{aligned} \sigma_v{}^2 = \frac{1}{2} &\left[(\sigma_{11} - \sigma_{22})^2 + (\sigma_{22} - \sigma_{33})^2 + (\sigma_{33} - \sigma_{11})^2 \right] \\ &+ 3 \left(\sigma_{12}{}^2 + \sigma_{23}{}^2 + \sigma_{31}{}^2 \right). \end{aligned} \tag{3}$$

The density approach was used for topology optimization. The standard format of a linear static topology optimization problem is expressed as follows:

$$\begin{aligned} \text{Minimize}: m &= \sum_{i=1}^{N.E.} \rho_i \Omega_i \\ \text{Subject to } &F(\sigma_i) \le 0 \\ \sum_{i=1}^{N.E} &\rho_i V_i \le V_0 \\ 0 < &\rho_{\min} \le \rho_i \le 1 \end{aligned} \tag{4}$$

The number of elements in the design domain is denoted by N.E., and Ω represents the region occupied by a finite element. Furthermore, V_O denotes the volume of the design space, and it denotes the index of the elements. The design variable corresponds to the bulk material density, which can be expressed using relative material density and material properties of each element in the SIMP method. The
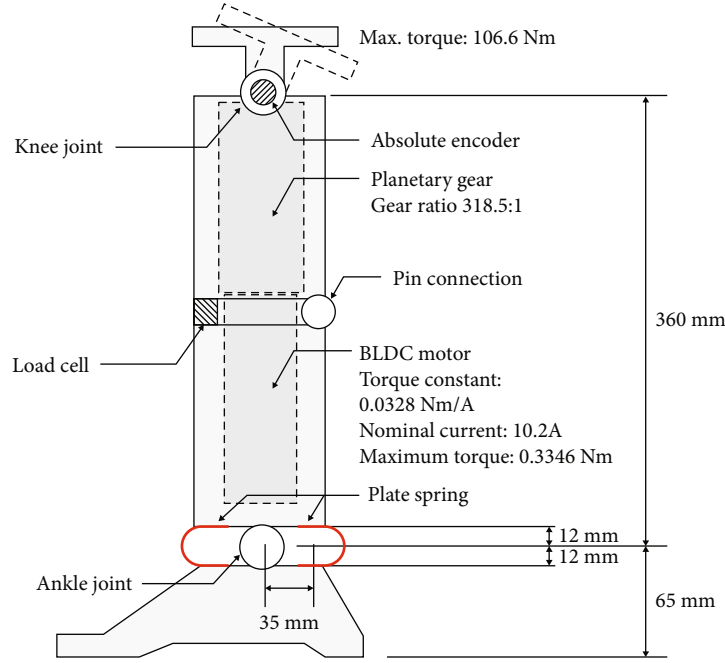
Figure 2: Concept modeling of a powered transfemoral prosthetic leg.
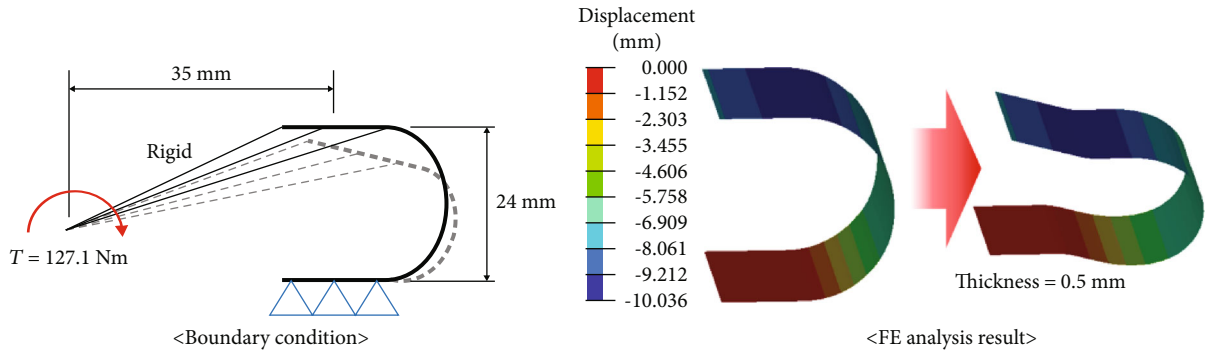
Figure 3: FE analysis to obtain the proper thickness of the plate spring at the ankle joint.

Table 1: Design objectives considering body dimensions.

Specification	Value
Knee range of motion	0° to 100°
Ankle range of motion	−25° to 15°
Maximum knee torque	106.6 nm
Maximum ankle torque	127.1 nm
Peak knee power	250 W
Height (below knee)	438 mm
Maximum total weight	4.912 kg

elasticity tensor (E) includes the following relationship:

$$E(\rho) = \rho^n E_0, \qquad (5)$$

where n denotes a penalization factor, and ρ denotes the density ($0 \leq n$, $0 \leq \rho \leq 1$) [20, 24].

The optimization process and particularly topology optimization converge during the process of developing an active transfemoral prosthetic leg.

The objective of optimization involved determining the optimized structure while ensuring structural safety under working conditions. There are three design optimization methods, namely, shape optimization, size optimization, and topology optimization. Shape optimization involves determining the optimum shape by adjusting the positions of each node on the outer surface of the structure under boundary conditions. Size optimization involves a process of determining the properties of structural elements such as shell thickness, beam cross-sectional properties, spring stiffness, and mass. Finally, topology optimization involves finding an optimized structure by utilizing internal strain energy density distributions and removing any portion that does not contribute to the structural strength. These optimization processes were applied to design the structure of an active transfemoral prosthetic leg.

1205.4 N 1205.4 N 1205.4 N

120.54 N 160.72 N 127.1 Nm

(a) Heel strike (b) Toe off (c) Mid-stance
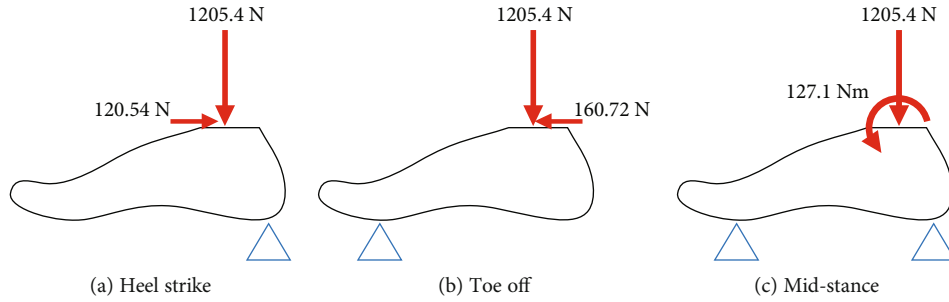
Figure 4: Boundary conditions for foot optimization.

Additionally, NX 9.0 was used for 3D CAD modeling. Shape optimization was implemented by Optistruct Solver of Altair Hyperworks, and Inspire of SolidThinking was used as the solver for topology optimization. The optimization process commenced with the definition of the design space. It was necessary to maximize the design space while minimizing the space for other components and interference caused by the rotating motion of joints. The nondesign space, such as connections to bearings and bolts, in which optimization is not performed, was defined. The FE model was introduced for optimization, and properties of the material and the boundary conditions including external load were applied. The design parameters for optimization were set and included design variables, objective function, constraints, and the minimum or maximum size of the structure. Following the preprocessing, an optimization process was performed to determine the optimal structure while satisfying the constraints. This was followed by performing optimization with iterations until the performances satisfied the objective function. After the optimization process, the optimized shape was designed given the optimization results. Finally, the optimized model was verified by FE analysis.

2.3. Structural Design of Artificial Foot. A prosthetic foot includes malleability to accommodate variation in the physical terrain in conjunction with rigidity to enable transmission of the body weight with adequate stability [25]. Therefore, plastic nylon was used to develop the artificial foot because it possesses sufficient flexibility to absorb shocks while supporting the body weight. It is necessary for the artificial leg to look similar to a human foot because several amputees desire to be perceived as normal. Therefore, it is important that the shape of the artificial foot is similar to that of a human foot and for the size to not exceed real foot size.

A few conditions involving the peak ground reactant force were considered to design the foot structure. According to the previous study [19], the peak ground reaction force appeared during stair descent walking with a magnitude that corresponded to 1.5 times the body weight of a human. The maximum ankle moment corresponded to 1.55 Nm/kg and occurred at the end of the stance phase and was also considered as a boundary condition. Additionally, the anterior/posterior ground reaction force was also considered as a boundary condition. Two notable points occurred at 20% and 85% of the stance phase of level walking. One of the points involved the heel-strike phase in which the magnitude

(a) Design space (b) Topology optimization

(d) Manufacturing (c) 3D modeling
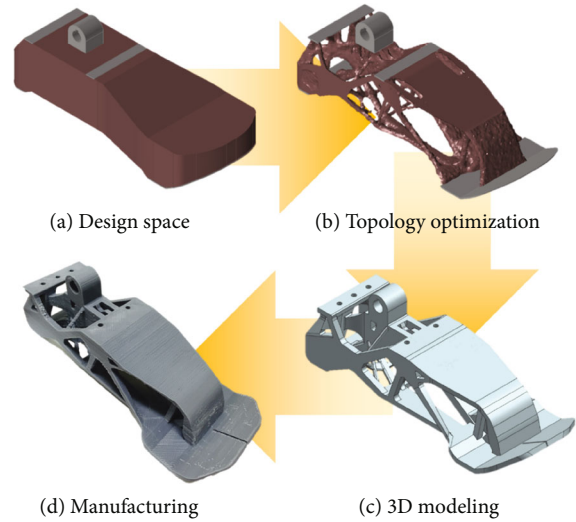
Figure 5: Optimization process for the foot structure.

corresponded to 0.15 times the body weight, and the other point involved the toe-off phase in which the magnitude corresponded to 0.2 times the body weight. The peak values at these points were considered as a boundary condition. The medial/lateral ground reaction force is relatively small and is therefore negligible. The boundary conditions for optimization were determined considering the abovementioned walking characteristics and are shown in Figure 4. There are three load cases for the boundary condition, and optimization was performed by simultaneously applying all three cases as each case was considered independent. The load was imposed on the ankle joint, and fixed boundary conditions were applied to the ball of the foot and heel that were directly in contact with the ground. The foot material corresponded to plastic nylon, which possessed flexibility and robustness. The material had a density (ρ) of 1,230 kg/m^3, an elastic modulus (E) of 2.91 GPa, a Poisson's ratio (ν) of 0.41, and an yield stress of 75 MPa.

Following the definition of the boundary condition and materials, topology optimization was performed to design the optimal shape of the structure. Figure 5(a) shows the maximum designable space, which was maximized while avoiding the space for other components and interference caused by the rotating motion of the ankle joint. The nondesign space where optimization was not performed was defined at the contact surface and joint. The design space
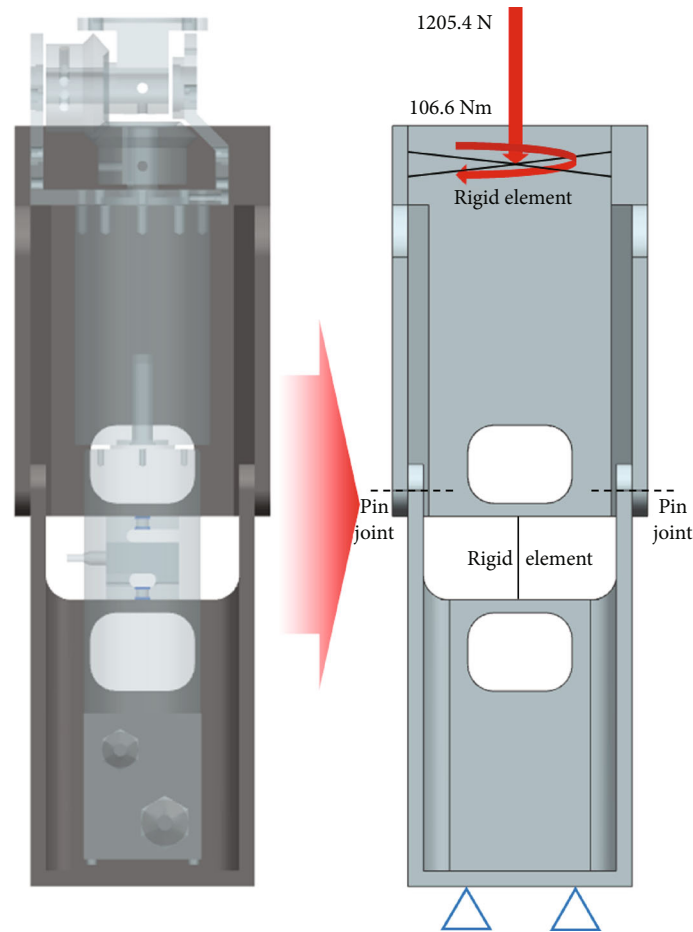
FIGURE 6: Boundary conditions for lower-limb optimization.

was used for topology optimization using boundary conditions, as shown in Figure 4 and applying a material corresponding to plastic nylon. Figure 5(b) shows the topology optimization results. The unnecessary mass was eliminated while maintaining the robustness under the boundary condition. However, it was too complicated to directly manufacture the shape by machining, and thus, 3D printing was used to realize the model. 3D printing is advantageous as it can create complicated shapes. Therefore, the result of optimization can be applied in a very similar manner by using 3D printing. Figure 5(c) shows the optimized model that was designed based on the topology optimization results and manufacturing method. Finally, the optimized foot was manufactured by a 3D printer and is shown in Figure 5(d).

2.4. Structural Design of the Lower Limb. It is necessary for the lower-limb structure of a prosthetic leg to sustain the body weight of the user and bear an approximate torque of 106.6 Nm for the same function as the human knee when a user's weight corresponds to 82 kg. The body weight is assumed as the maximum ground reaction force, which corresponds to 1205.4 N. A previous study [26] indicated that the resultant ground reaction forces were directed towards the center of gravity. Therefore, the resultant force of the ground reaction forces was assumed to be in the same direc-

tion as the shin. Additionally, the torque imposed on the knee joint was supported by the structure of the lower limb and the gear system. Constraints were applied at the end of the bottom of the prosthetic leg, which was connected to an adapter and was assumed as a fixed joint. The boundary condition for optimization was determined considering the abovementioned load conditions and is shown in Figure 6.

It is necessary for the material of the lower-limb structure to exhibit robustness for safety and ensuring weight lightness with respect to user comfort. Thus, 7075 aluminum alloy was used as the design material for the lower-limb structure. This material is usually used for prostheses and is lighter than steel alloy. This material includes a density (ρ) of 2,800 kg/m^3, an elastic modulus (E) of 75 GPa, a Poisson's ratio (v) of 0.33, and a yield stress of 95 MPa.

Similar to the structural design, the optimization process was implemented to design the optimal structure by considering boundary conditions. Figure 7(a) shows the maximum designable space for the lower-limb structure. It was necessary for the maximum designable space to not exceed the dimensions of a human leg and to avoid interferences with other components such as motors and gearbox. The bearings and bolts defined the nondesign space in which optimization was not performed. The design space was used for topology optimization using boundary conditions based on Figure 8

(a) Design space (b) Topology optimization (c) Shape optimization (d) 3D modeling
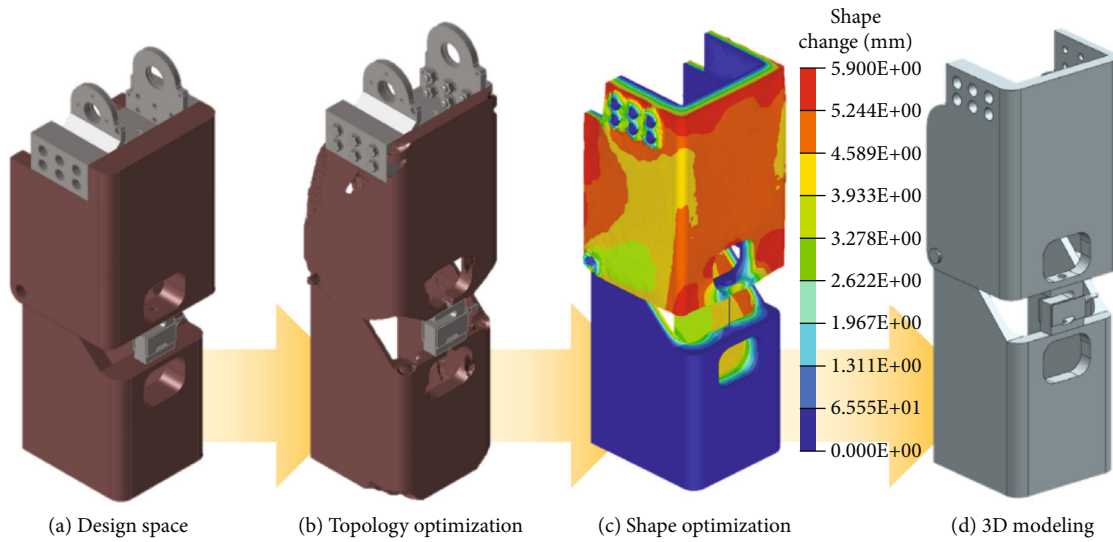
Figure 7: Optimization process for lower-limb optimization.
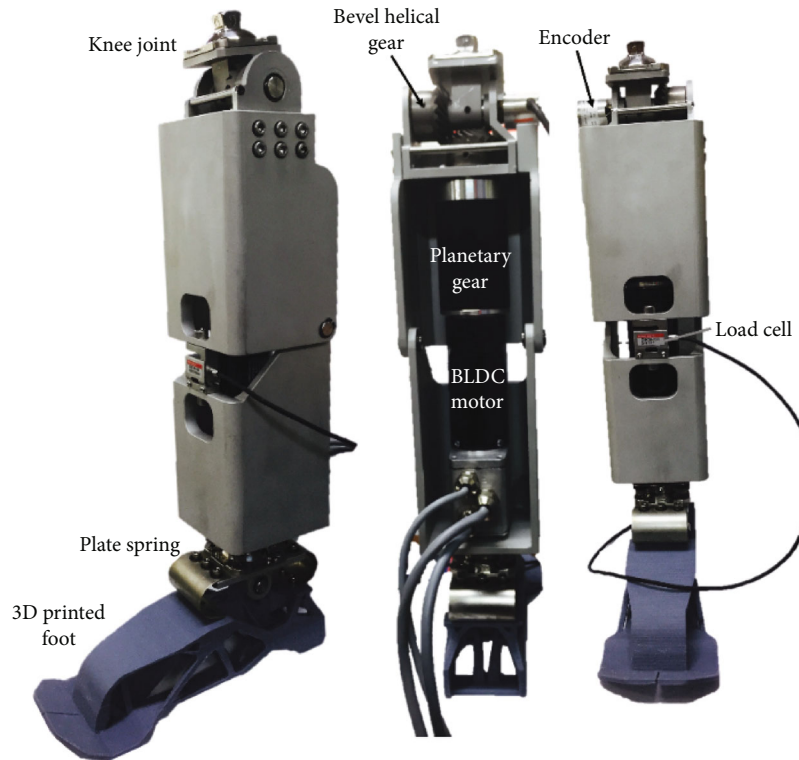
Figure 8: Developed active prosthetic leg system.

and an aluminum alloy. Figure 7(b) shows the topology optimization results. In this phase, geometrical symmetry was considered for the balance of the prosthesis. The result indicated that the shape of the structure did not significantly differ from that of the previous model despite changes in the thickness and edge. Following the topology optimization, shape optimization was implemented to obtain a better model by determining the thickness as shown in Figure 7(c). The degree of freedom of nodes placed on the outer face of the upper structure and the inner face of the

lower structure were considered as a design variable. The constraints and external force were the same as the boundary conditions for topology optimization. The objective function involved minimizing the mass. The contour showed the displacement of the shape change versus the original model. The results indicated that it was necessary to reduce the thickness to approximately 6 mm. The optimal thickness of the structure was determined based on the results. Finally, the advanced shape of the lower-limb structure was obtained while maintaining robustness under boundary conditions.

Figures 7(d) and 8(d) show 3D modeling and the model manufactured by machining, respectively.

2.5. Design of the PD Controller. An important point in the development of active transfemoral prosthetic leg involves implementing the motion of natural gait using a power source. It is important to analyze human gait to determine the walking phase and to implement the motion of the affected side that is similar to that of the normal side. In this study, a walking phase was identified through a mechanical sensor for knee joint control, and the PD controller based on the knee angle position was applied to actively cope with various walking environments.

An encoder was used to collect the walking motion data of the knee joint to analyze the walking behavior. The measuring system is shown in Figure 9. The gait data of each walking situation were collected by walking around stairs and flat ground. The data were measured five times for each case. The noise was removed by filtering, and the standard gait data was determined by averaging. The data of a level and the stair walking are shown in Figure 10, and this was used as a trajectory to implement the walking motion.

The swing motion was implemented by entering the motion to track on the motor for tracking obtained from Figure 10. The dynamic relationship of the walking system is as follows [23]:

$$\tau = k\left(\theta - \theta_{eq}\right) + b\dot{\theta}, \tag{6}$$

where τ denotes the torque of the knee and ankle joint, and k and b denote the linear stiffness and damping coefficient, respectively. Additionally, θ denotes the angle of the knee joint, and θ_{eq} denotes the equilibrium angle during the transition between phases. A position-based PD controller was constructed to control the active prosthetic leg and applied to the developed prosthesis. Based on previous studies, the parameters were tuned using a combination of feedback from the user and from visual inspection of the joint angle, torque, and power data [27].

In the PD controller, a control loop feedback mechanism that is commonly used in industrial control systems is used for control. The control system is shown in Figure 11. The PD controller is used to mitigate the stability and overshoot problems that arise when a proportional controller is used at a high gain by adding a term proportional to the time derivative of the error signal. The value of the damping can be adjusted to achieve a critically damped response.

The decomposition of the joint behavior into passive segments requires division of the gait cycle into modes or "finite states" [8]. The walking phase was distinguished by the load cell and the encoder signal. A finite state machine was constructed as shown in Figure 12 to further divide the walking step into four steps. The finite state machine of the prosthetic leg was based on previous studies [9, 27, 28].

Phase 1 constitutes the stance phase. If the knee was extended over a certain angle in swing flexion, then the phase switched to the stance phase. The sole had contact with the ground, and the load was applied to the knee joint. If the heel

Figure 9: Measuring system of the knee motion.
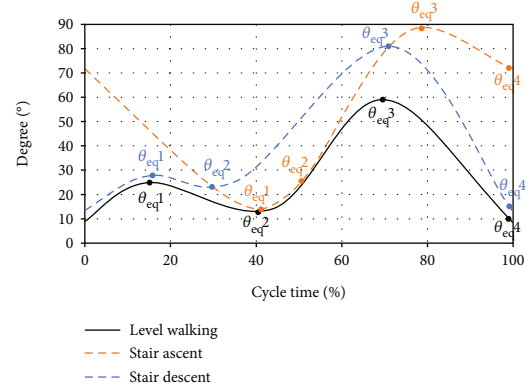
Figure 10: Measuring result of the knee motion.

strike or forefoot strike was detected through the load cell attached to the middle of the structure, then the walking phase was changed from the prelanding phase to the stance phase.

Phase 2 constitutes the preswing phase. This phase immediately preceded the detachment of the sole from the ground, and the load on the knee moved to the opposite leg. The heel fell from the ground while the knee bent over a certain angle, and this was followed by changing the walking phase into the preswing phase.

Phase 3 constitutes the swing flexion phase. When the sole was completely separated from the ground, the load on the knee was completely free because the load was supported by another side leg. When the load cell confirmed that the foot was completely separated from the ground, the walking phase changed from the preswing phase to the swing flexion phase.

Phase 4 constitutes the swing extension phase. The knee joint began to naturally expand. If the direction of the angular velocity of the knee joint was reversed in the swing flexion phase, then the walking phase changed into the swing extension phase.
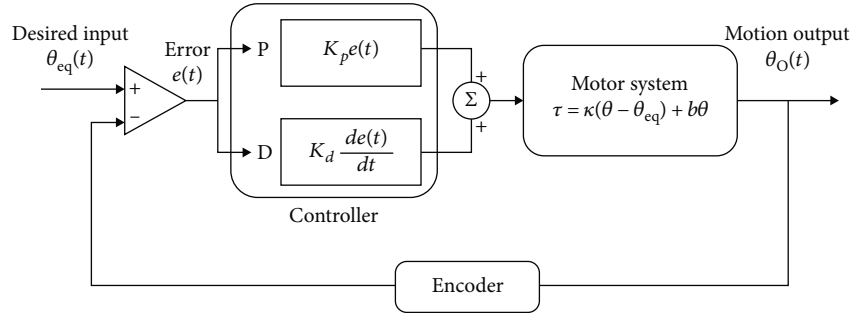
FIGURE 11: PD controller for the knee motion control.
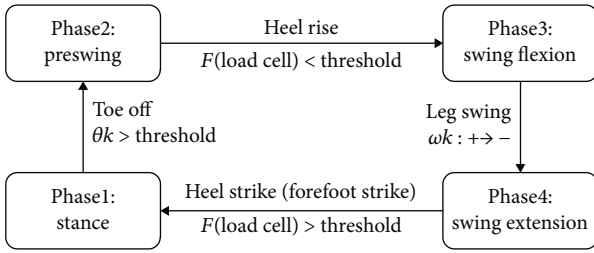
FIGURE 12: Finite state machine.

An experimental method was used to perform coefficient adjustment of the controller to optimize the walking performance of the active prosthesis system.

3. Validation of the Developed Prosthetic Leg

3.1. Artificial Foot Structure Analysis. It is necessary for the artificial foot to support body weight while walking. Therefore, FE analysis was performed to validate its structural safety. The abovementioned boundary condition was applied. FE analysis was performed for each of the boundary conditions. Figure 13 shows the 3D mesh and boundary conditions for the analysis. The quality of the mesh was important for obtaining an accurate result. A tetra mesh was used due to its advantages in meshing a complex solid shape. The outer surfaces and geometrical corners involved compact meshes for accurate analysis. The number of elements corresponded to 141,898, and the number of nodes corresponded to 38,047. The model included three load cases consisting of heel strike, toe off, and mid-stance. The external loads and moment of each load case acted on the center of the ankle joint, and constraints were applied to the ball of the foot and heel. All the materials were modeled as linearly elastic, isotropic, and homogenous. Figure 14 shows the results of the FE analysis of the foot structure. Table 2 summarizes the peak stresses of each phase. The highest von Mises stresses appeared in the heel strike phase, which was located at the lower surface of the heel. The maximum stress obtained in the results was compared with the tensile strength of the materials used to check the stability with respect to the applied load. The maximum stress corresponded to 65.51 MPa, which was lower than the yield strength of the material (75 MPa).

3.2. Lower-Limb Structure Analysis. In order to verify the safety of the structure, FE analysis was performed under a boundary condition similar to that shown in Figure 6. Figure 15(a) shows the 3D mesh for the analysis. A tetra mesh was used owing to its advantages in meshing a complex solid shape. The number of elements corresponded to 365,724, and the number of nodes corresponded to 84,988.

The body weight was applied to the nodes located at the center of the bearing holes that supported the knee shaft. The twelve bolt connections between the support and bevel gearbox were considered as rigid link components based on the assumption that the bolts were nearly rigid bodies with little deformation. Fixed constraints were applied to the bolt hole located at the bottom of the leg that was bolted with a pyramid adaptor. All the materials were modeled as linearly elastic, isotropic, and homogenous.

The results of the FE analysis of the lower-limb structure are shown in Figure 15(b). The maximum stress was exhibited in the area near the bolt hole. The value was 80.71 MPa lower than 95 MPa, which corresponded to the yield strength of the 7075 aluminum alloy. This implied that the structure was safe under the load condition. Furthermore, the bolt holes were simplified to a rigid element, and it displayed a characteristic indicating a stress that exceeded the real stress because the rigid element acted as a load point. Therefore, it was expected that the actual stress at the point was lower than 80.71 MPa.

3.3. Unlocked Prosthetic Leg Test. An experimental setup for the unlocked prosthetic leg test was introduced to create the motion of the knee joint. The experimental setup is shown in Figure 16, and it was designed to ensure that the prosthetic leg could move freely. The coefficient adjustment of the controller to optimize the walking performance of the active prosthesis system was performed through an experimental method. Given the reference walking data and user feedback, the value that could mimic the walking motion in the most natural manner possible was selected as the coefficient value. Tables 3, 4, and 5 show the coefficient of the controller for level walking, stair ascent, and descent, respectively. The controller coefficients for each phase were obtained through the experimental method. The equilibrium angle θ_{eq} was selected as the peak angle of each phase or the angle at which the ground reaction force was imposed.
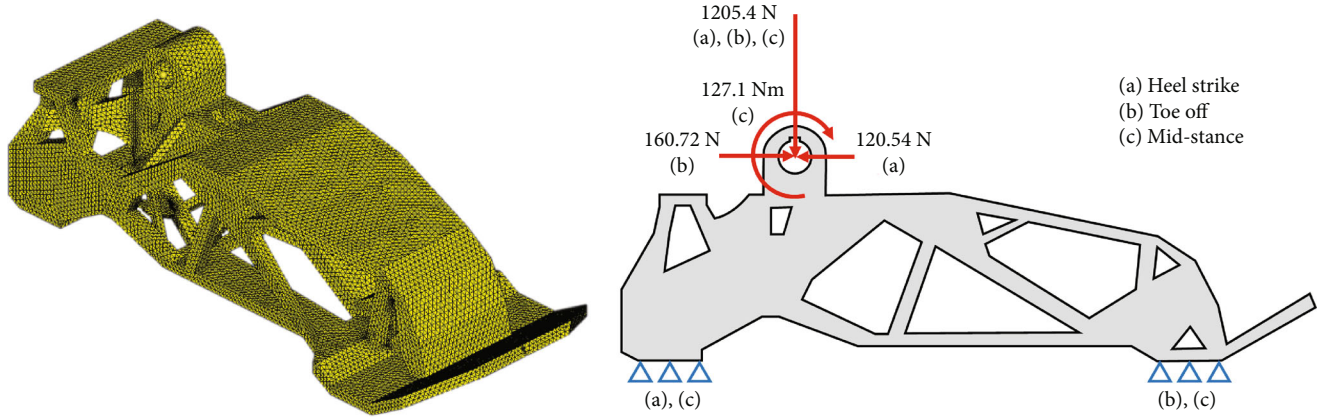
Figure 13: A 3D mesh of the foot structure and the boundary conditions.

(a) Heel strike

(b) Toe off
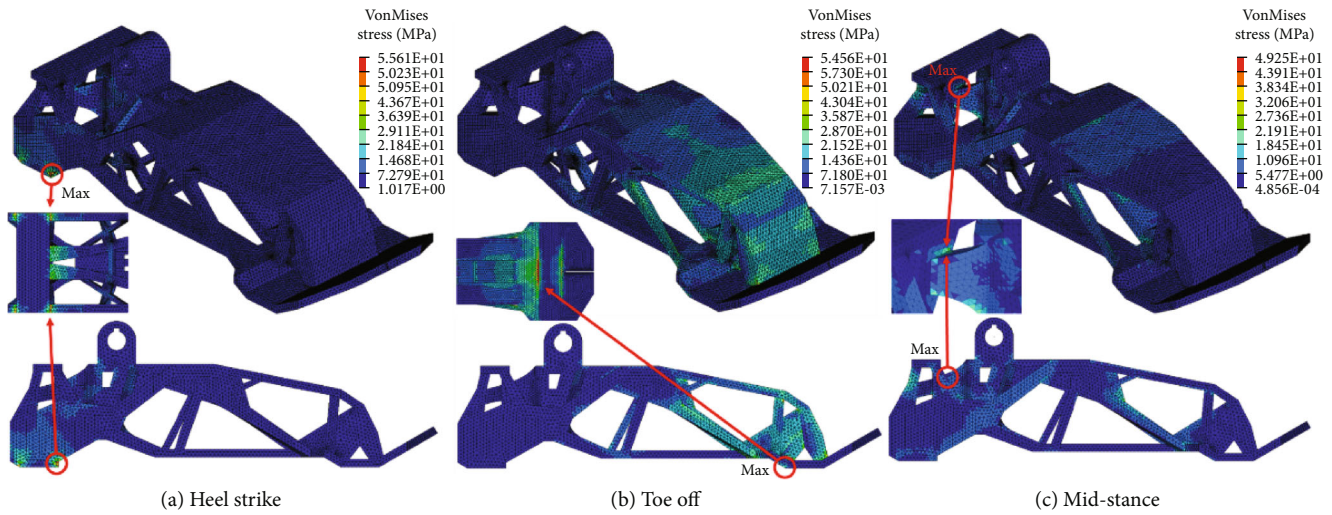
(c) Mid-stance

Figure 14: Results of the FE analysis of the foot structure.

Table 2: Peak stresses of each walking phase.

Walking phase	Max stress	Yield stress
(a) Heel strike	65.51 MPa	
(b) Toe off	64.56 MPa	75 MPa
(c) Mid-stance	49.29 MPa	

4. Discussion

4.1. Performance Evaluation of Prosthetic Leg. Consequently, an active transfemoral prosthetic leg system was developed as shown in Figure 8. The three linkage type includes certain specification disadvantages, and thus, a direct-drive type was applied to the knee joint, and a spring system was applied to the ankle joint. The structure was then designed using the optimization process. The active prosthesis was designed with two degrees of freedom in the ankle and knee. The knee joint plays an important role and is accountable for more than 50% of the walking mechanism. It consists of an AC motor system and can generate 106.57 Nm torque and proper motion in a range from 0° to 100°. The ankle joint plays an important role in supporting the torque caused by the body weight. The spring system is simple and involves a general system to generate torque without a motor system. The ankle joint was composed of a spring system to generate 127.1 Nm torque and angle.

In order to evaluate design efficiency, specifications of the prosthetic leg system and desired specifications were compared, and the comparison results are shown in Table 6. The objects of comparison included the maximum torque and operating angle of each joint, power of the knee joint, height, total weight, and maximum stress. These variables were selected for the following reasons.

First, it is necessary for the prosthetic leg to make a proper motion to mimic the gait of a normal person. Therefore, it is necessary for the prosthetic leg to implement the range of motions similar to a human leg in conjunction with supplying the necessary power to overcome obstacles that could be encountered by the amputees while walking. The range of the joint angle, target torques, and power was based on specifications listed in a previous study. The prosthetic leg was designed to meet the specification based on this design parameter.

(a) 3D mesh   (b) FE analysis
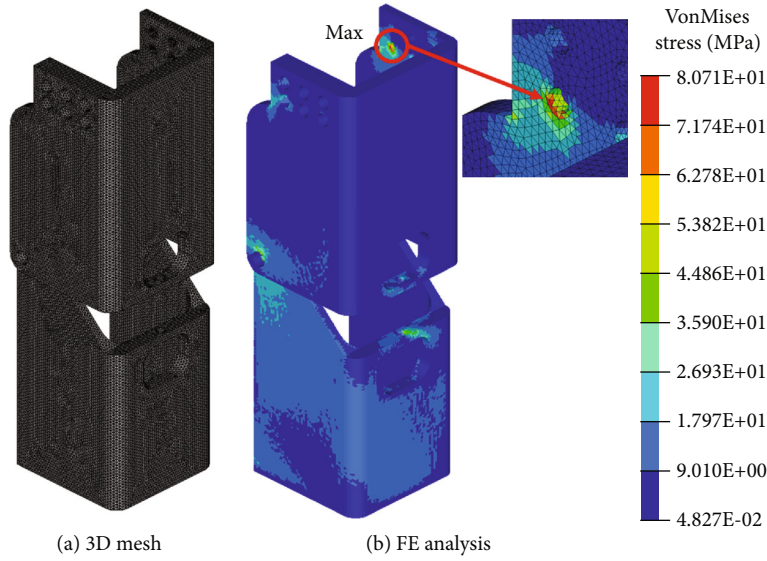
Figure 15: Result of the FE analysis of the lower-limb structure.
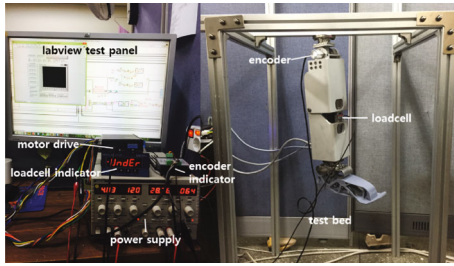
Figure 16: Experimental setup for the unlocked prosthetic leg test.

Table 3: Coefficient of controller for level walking.

Phase	k (nm/deg)	b (ns/m)	θeq (deg)
1	6	0	25
2	4	0	13
3	0.1	0.02	59
4	0.2	0.03	9

Table 4: Coefficient of controller for stair ascent.

Phase	k (nm/deg)	b (ns/m)	θeq (deg)
1	2	0	17
2	10	0	24
3	0.1	0.02	87
4	0.5	0.03	72

Second, weight is the most important factor because the user can feel fatigue or discomfort if the prosthetic leg is heavier than their original leg. Hence, it is necessary to minimize the weight to ensure the comfort of the amputees. The developed active transfemoral prosthetic leg has a total weight of 4,779 g, which corresponds to 97.3% of the target weight (4,912 g) obtained by considering the user's body size. The weight of the prosthesis is 1.150 kg for the motor,

Table 5: Coefficient of controller for stair descent.

Phase	k (nm/deg)	b (ns/m)	θeq (deg)
1	8	0	28
2	6.5	0	26
3	0.1	0.02	81
4	0.1	0.03	13

Table 6: Comparison between the desired and prosthetic leg specifications.

	Requirement	Prosthetic leg Specifications
Knee range of motion	0° to 100°	0° to 100°
Ankle range of motion	−25° to 15°	−25° to 15°
Maximum knee torque	106.6 nm	106.57 nm
Maximum ankle torque	127.1 nm	127.1 nm
Peak knee power	250 W	250 W
Height (below-knee)	438 mm	444.5 mm
Maximum total weight	4.912 kg	4.779 kg
Max. stress	Foot: 65.51/75 MPa	
Allowable stress	Lower limb: 80.71/95 MPa	

0.920 kg for the reducer, 0.209 kg for the foot, and 2.5 kg for the body (including cover and joint gear), totaling 4.779 kg. In addition, the experiment was conducted by supplying power by wire without a battery. Although the weight of the motor and gearbox exceeds 2 kgf, the total weight was effectively reduced by introducing an optimization process with respect to the structure. Similarly, it was necessary for the total length of the prosthetic leg to be similar to the length of the original leg of a user. The developed prosthetic leg had a length of 444.5 mm, which corresponded to 101.5% of the target length (438 mm).

Finally, it was necessary to ensure the safety of the user while using the prosthetic leg. Therefore, the safety factor is

(a) Level walking

(b) Stair ascent

(c) Stair descent
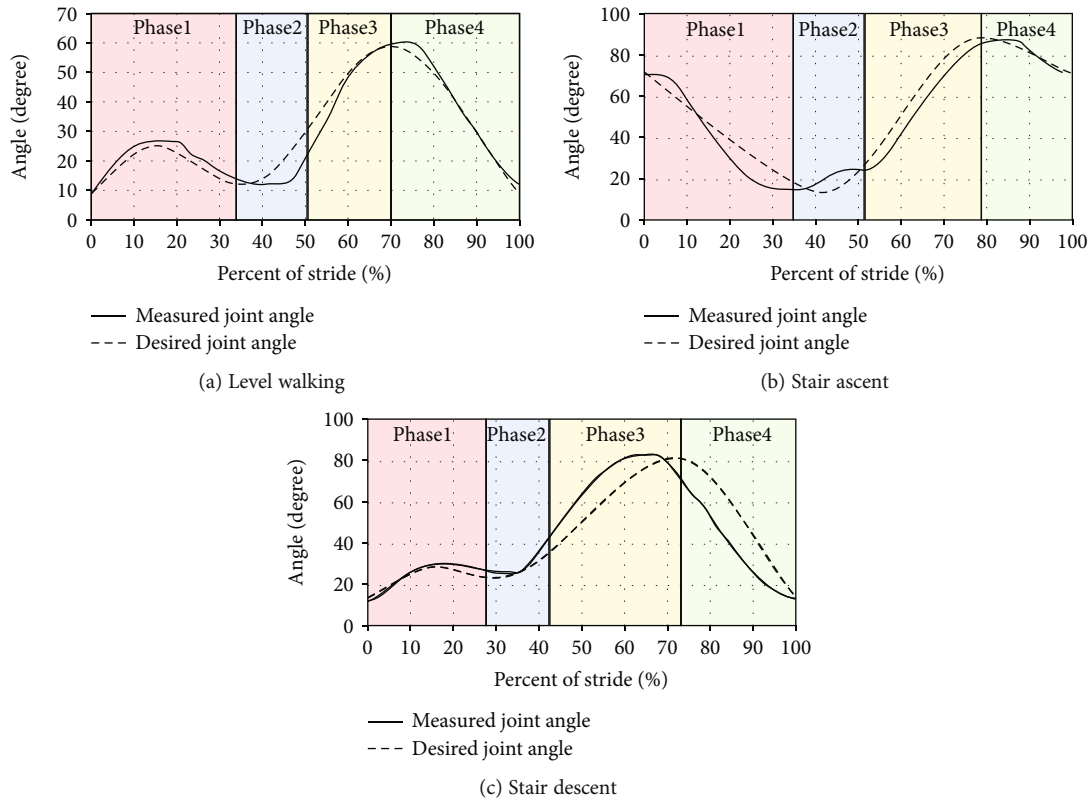
FIGURE 17: Comparison between the desired motion and the actual drive motion.

important in designing a prosthetic leg. The yield stress of the used material was compared with the maximum stress predicted by FE analysis. Plastic nylon (which is the foot structure material) has a yield strength of 75 MPa. The maximum stress of the foot structure was expected as 65.51 MPa, and the safety factor at this time was estimated as 1.15. In a similar manner, the 7075 aluminum alloy, which was used to design the material of the lower-limb structure, possesses a yield strength of 95 MPa. The maximum stress of the lower limb was expected as 80.71 MPa, and the safety factor at this time was estimated as 1.18. The maximum stresses of each part were lower than the yield strength of each material.

The developed prosthesis was heavier than the prosthesis sold on the market, although it was lighter than the dimensions of an actual human body. The weight of the motor and the gearbox exceeded 2 kg. It was necessary to introduce a suitable motor and gearbox to reduce the weight. Hence, the implementation of the research on optimizing motors and gearboxes will help in developing a better prosthesis.

4.2. Performance Evaluation of Controller. The comparison between the desired motion and the actual drive motion with the level walking controller obtained by the unlocked prosthetic leg test (Figure 17(a)). The knee angle of the prosthesis was measured while tracking the normal walking data. The actual motion of the prosthetic knee joint exhibited a similar tendency with the desired motion. The knee angle of the prosthetic leg indicated a smooth swing curve, but was relatively smaller than the desired angle and experienced a slight

delay. This phenomenon was due to the limitations of the experimental system. The supplied voltage was lower than the nominal voltage and reduced the torque below the target torque. It was considered that the torque estimated by the influence of relatively low power supply had a slight delay when compared to the objective data and would thereby affect the walking speed.

Figures 17(b) and 17(c) show the comparison between the desired motion and the actual drive motion with stair ascent and the descent controller obtained by the unlocked prosthetic leg test. They also indicated that the objective function was followed in a similar manner. However, they exhibited slight inconsistencies. It involved a position-based control, and a delay occurred when each phase went to the next phase. This appeared to be the cause of showing the actual knee motion follow slightly refracted curves.

The active prosthetic leg and controller exhibited behavior that was considerably similar to that of a normal gait. The PD controller implemented a knee motion similar to normal walking. The experimental result of control based on the position data showed the feasibility of the level and stair walking of the active prosthetic leg using the PD controller. Additionally, it allowed the framework of the walking test to mimic the motion of a normal individual.

Finally, the developed prosthetic leg was controlled by a PD controller that generated human-like walking motion, and the resulting joint kinematics were compared with a captured human gait to verify the control performance. It is expected that the study results with respect to the active transfemoral prosthetic leg will help in the rehabilitation of

amputees. Furthermore, this study can be applied to the area of biped robots that imitate the human motion.

5. Conclusions

In this study, an active transfemoral prosthetic leg was optimally designed and controlled with a PD controller. The weight of the prosthetic leg is an important factor in the design because it is related to user fatigue. An optimization process was used for foot and lower-limb structures to obtain optimal shapes and reduce the weight. Topology and shape optimization were implemented in the design. As a result, the shape of a prosthetic leg was developed without exceeding the dimensions of the human body. The optimized foot structure was produced through 3D printing to reflect the optimization result as much as possible. Finally, an optimized structure for stair walking was designed while maintaining robustness. A PD controller based on position control was used to control the developed prosthetic leg. The actual motion of the prosthetic knee joint exhibited a tendency similar to the desired motion. It is expected that the results of this study will aid in the rehabilitation of amputees by developing optimal active transfemoral prosthetic legs. Furthermore, the findings of this study can be applied to the area of biped robots wherein human motion is imitated.

Data Availability

The experimental and simulation data used in this study are included within the paper.

Conflicts of Interest

The authors declare no conflict of interest.

Acknowledgments

References

[1] F. Sup, H. A. Varol, J. Mitchell, T. J. Withrow, and M. Goldfarb, "Self-contained powered knee and ankle prosthesis: initial evaluation on a transfemoral amputee," in *2009 IEEE 11th International Conference on Rehabilitation Robotics*, pp. 638–644, Kyoto, 2009.

[2] E. C. Martinez-Villalpando and H. Herr, "Agonist-antagonist active knee prosthesis: a preliminary study in level-ground walking," *Journal of Rehabilitation Research & Development*, vol. 46, no. 3, pp. 361–373, 2009.

[3] E. Russell Esposito, J. M. Aldridge Whitehead, and J. M. Wilken, "Step-to-step transition work during level and inclined walking using passive and powered ankle–foot prostheses," *Prosthetics and Orthotics International*, vol. 40, no. 3, pp. 311–319, 2016.

[4] J. Realmuto, G. Klute, and S. Devasia, "Nonlinear passive cam-based springs for ankle prostheses," *Journal of Mecial Devices*, vol. 9, no. 1, pp. 1–10, 2015.

[5] F. Sup, H. A. Varol, and M. Goldfarb, "Upslope walking with a powered knee and ankle prosthesis: initial results with an

[6] W. C. Flowers and R. W. Mann, "An electrohydraulic knee-torque controller for a prosthesis simulator," *ASME Journal of Biomechanical Engineering*, vol. 99, no. 1, pp. 3–8, 1977.

[7] K. H. Lee, J. H. Chung, and C. H. Lee, "Design and optimization study of active trasfemoral prosthesis leg," *Korean Journal of Rehabilitation Welfare Engineering & Assistive Technology*, vol. 7, no. 2, pp. 41–46, 2013.

[8] F. Sup, A. Bohara, and M. Goldfarb, "Design and control of a powered transfemoral prosthesis," *The International journal of robotics Research*, vol. 27, no. 2, pp. 263–273, 2008.

[9] B. Lawson, H. A. Varol, A. Huff, E. Erdemir, and M. Goldfarb, "Control of stair ascent and descent with a powered transfemoral prosthesis," *IEEE Transactions on Neural Systems and Rehabilitation Engineering*, vol. 21, no. 3, pp. 466–473, 2013.

[10] S. Au, M. Berniker, and H. Herr, "Powered ankle-foot prosthesis to assist level-ground and stair-descent gaits," *neural networks*, vol. 21, no. 4, pp. 654–666, 2008.

[11] M. Grimmer et al., "A powered prosthetic ankle joint for walking and running," *Biomedical Engineering*, vol. 15, no. 3, pp. 37–52, 2016.

[12] U. J. Yang and J. Y. Kim, "Mechanical design of powered prosthetic leg and walking pattern generation based on motion capture data," *Advanced Robotics*, vol. 29, no. 16, pp. 1061–1079, 2015.

[13] R. D. Bellman, M. Holgate, and T. G. Sugar, "Design of an Active Robotic Ankle Prosthesis with Two Actuated Degrees of Freedom Using Regenerative Kinetics," in *Proceedings of the 2nd Biennial IEEE/RASEMBS International Conference on Biomedical Robotics and Biomechatronics*, pp. 511–516, Scottsdale, AZ, 2008.

[14] R. Borjian, J. Lim, M. B. Khamesee, and W. Melek, "The design of an intelligent mechanical active prosthetic knee," in *Industrial Electronics 2008. IECON 2008. 34th Annual Conference of IEEE*, pp. 3016–3021, Orlando, FL, 2008.

[15] K. H. Ha, H. A. Varol, and M. Goldfarb, "Volitional control of a prosthetic knee using surface electromyography," *IEEE Transactions on Biomedical Engineering*, vol. 58, no. 1, pp. 144–151, 2011.

[16] M. G. Bernal-Torres, H. I. Medellin-Castillo, and J. C. Arellano-Gonzalez, "Design and control of a new biomimetic transfemoral knee prosthesis using an echo-control scheme," *Journal of Healthcare Engineering*, vol. 2018, pp. 1–17, 2018.

[17] M. Omasta, D. Paloušek, T. Návrat, and J. Rosický, "Finite element analysis for the evaluation of the structural behaviour, of a prosthesis for trans-tibial amputees," *Medical Engineering & Physics*, vol. 34, no. 1, pp. 38–45, 2012.

[18] W. H. Ho, T.-Y. Shiang, C. C. Lee, and S. Y. Cheng, "Body segment parameters of young Chinese men determined with magnetic resonance imaging," *Medicine & Science in Sports & Exercise*, vol. 45, no. 9, pp. 1759–1766, 2013.

[19] R. Riener, M. Rabuffetti, and C. Frigo, "Stair ascent and descent at different inclinations," *Gait & Posture*, vol. 15, no. 1, pp. 32–44, 2002.

[20] K. H. Lee, J. H. Chung, and C. H. Lee, "Development of artificial foot of active transfemoral prosthesis system using topology optimization," in *Proceedings of the World Congress on Engineering 2015*, vol. 2, pp. 1257–1260, London, 2015.

[21] M. P. Bendsøe and N. Kikuchi, "Generating optimal topologies in structural design using a homogenization method,"

Computer Methods in Applied Mechanics and Engineering, vol. 71, no. 2, pp. 197–224, 1988.

[22] Z. Luo, N. Zhang, Y. Wang, and W. Gao, "Topology optimization of structures using meshless density variable approximants," *International Journal for Numerical Methods in Engineering*, vol. 93, no. 4, pp. 443–464, 2012.

[23] J. T. Pereira, E. A. Fancello, and C. S. Barcellos, "Topology optimization of continuum structures with material failure constraints," *Structural and Multidisciplinary Optimization*, vol. 26, no. 1-2, pp. 50–66, 2004.

[24] S. H. Cha, S. W. Lee, and S. Cho, "Experimental validation of topology design optimization," *Computational Structural Engineering Institute of Korea*, vol. 26, no. 4, pp. 241–246, 2013.

[25] M. M. Saunders, E. P. Schwentker, D. B. Kay et al., "Finite element analysis as a tool for parametric prosthetic foot design and evaluation. Technique development in the solid ankle cushioned heel (SACH) foot," *Computer Methods in Biomechanics and Biomedical Engineering*, vol. 6, no. 1, pp. 75–87, 2003.

[26] D. Levine, J. Richards, and M. W. Whittle, *Whittle's gait analysis*, Churchill Livingstone, 5th edition, 2012.

[27] F. Sup, H. A. Varol, J. Mitchell, T. J. Withrow, and M. Goldfarb, "Preliminary evaluations of a self-contained anthropomorphic transfemoral prosthesis," *IEEE/ASME Transactions on Mechatronics*, vol. 14, no. 6, pp. 667–676, 2009.

[28] W. S. Kim, S. Y. Kim, and Y. S. Lee, "Prototype development of a DC motor-based powered prosthesis and its control," in *2013 RESKO Technical Conference*, vol. 1, pp. 201–204, Seoul, 2013.

Research Article

Design and Experiment of Assistive Mechanism for Adjustment of Transrectal Ultrasound Probe

Jin-Gang Jiang [1,2] **Hui Zuo,** [1] **Yong-De Zhang,** [1,2] **Zhi-Yuan Huang,** [1] **Xiao-Wei Guo,** [1] **and Yong Xu** [3]

[1]*Key Laboratory of Advanced Manufacturing and Intelligent Technology, Ministry of Education, Harbin University of Science and Technology, Harbin 150080, China*
[2]*Robotics & its Engineering Research Center, Harbin University of Science and Technology, Harbin 150080, China*
[3]*Urinary Surgery, The General Hospital of Chinese People's Liberation Army, Beijing 100039, China*

Correspondence should be addressed to Jin-Gang Jiang; jiangjingang@hrbust.edu.cn

Transrectal ultrasound prostate biopsy is the most commonly used method for the diagnosis of prostate cancer. During the operation, the doctor needs to manually adjust the ultrasound probe for repeated adjustments, which is difficult to ensure the efficiency, accuracy, and safety of the operation. This paper presents a passive posture adjusting mechanism of transrectal ultrasound probe. The overall mechanism has 7 degrees of freedom, consisting of a position adjustment module, a posture adjustment module, and an ultrasonic probe rotation and feed module. In order to achieve the centering function, the posture adjustment module is designed based on the double parallelogram. Centering performance is verified based on SimMechanics, and remote center point error of physical prototypes is evaluated. The maximum error of the azimuth remote center point motion and the maximum error of the remote center point motion of the ultrasonic probe are 4 mm and 3.4 mm, respectively, which are less than the anus that can withstand 6 mm. Meanwhile, the analysis of measurement error shows that the random error correlation is weak in different directions, the systematic error confidence intervals of azimuth and elevation angle are less than 2.5 mm, and the maximum relative fixed point error and the maximum relative standard error are 14.73% and 14.98%, respectively. The simulation and testing results have shown the effectiveness and reliability of the propose mechanism.

1. Introduction

Nowadays, people are paying attention to their own health problems as the significant improvement in people's living standards. The American Cancer Society counts the top ten cancers with the highest cancer incidence in the United States in 2017. Prostate cancer ranks first among all high-risk cancers among men, accounting for about one-fifth of the total number of male cancer patients; thus, it will cause great pain to male patients. At the same time, the mortality rate of prostate cancer is increasing at a rate of 2% per year and showing a trend of rejuvenation [1, 2]. The most critical means of curing prostate cancer is early diagnosis [3–8]. In the clinic, the most common method for early diagnosis of prostate cancer is transrectal ultrasound prostate

biopsy. An ultrasound probe is utilized to probe the patient's rectum and puncture the prostate under ultrasound-guided guidance when the operation is performed. However, this surgery still has the following problems: the entire procedure requires the doctor to operate with an ultrasound probe, and it is necessary to repeatedly adjust the ultrasound probe, which may cause fatigue and mood swings; the ultrasound probe needs to be inserted into the patient's rectum, which will cause damage to the anus when adjusting the posture of the probe; this surgical procedure requires the cooperation of multiple nurses, resulting in wastage of personnel. Moreover, the number of prostate patients is growing, and the existing medical staff is not enough to complete such a large workload, and the traditional hand-held method is difficult to ensure the precision of the puncture intervention because

of the special location of the prostate. Therefore, it is necessary to study medical devices that assist doctors in prostate scans and biopsy gun puncture interventions.

In recent years, minimally invasive interventional robotics has gradually become one of the hotspots in the medical field, and this technology has attracted the attention of researchers. In 2007, Yan Yu of Thomas Jefferson University in the United States developed a prostate seed implantation treatment system based on ultrasound image navigation [9–11], which can automatically or manually use the rotation operation to obtain ultrasound images of lesion points. The American Engineering Research Center and Johns Hopkins University have jointly developed a robotic system that includes ultrasound image navigation and TPS to enable free movement and attitude adjustment of the biopsy needle in a vertical plane [12, 13]. An ultrasound imaging-guided prostate interventional robot was designed by Kim et al., in which 2-DOF is able to be manually adjusted for posture adjustment, and two degrees of freedom are used to adjust the movement and rotation of the ultrasound probe [14]. Vitrani et al. of the University of Pittsburgh designed an artificially operated prostate biopsy probe holder, and its structural is similar to a 6-DOF series manipulator, which uses ultrasound transrectal puncture for good stiffness and stability [15]. The Institute of Intelligent Machines of Harbin University of Science and Technology has designed the structure of an all-round prostate robot. This error of each axis of the system is kept within 0.05 mm through experiments, which has high repeat positioning accuracy and meet the surgical requirements [16–18].

At present, the active prostate interventional robot has been extensively studied; however, it is difficult to promote and apply because of its complicated system, high cost, and long training time [19]. In contrast, passive prostate-assisted interventional mechanism has relatively simple structure, a short design cycle, low cost, and is easier to promote and apply than active mechanism.

The key technology of the passive prostate-assisted interventional mechanism is the centering motion of the transrectal ultrasound probe, and the remote center mechanism (RCM) can realize the centering motion of the ultrasound probe, so that the doctor's hands are truly liberated. The concept of the RCM was first proposed by Taylor et al. at Johns Hopkins University in 1995. The designed azimuth rotation center and the pitch angle rotation center intersect at the remote center point, and the posture of the puncture needle can be arbitrarily adjusted in 2-DOF, and the purpose of adjusting the distal center position is achieved by the expansion and contraction of the link [20]. The American Computer Surgery Systems Research Center and Johns Hopkins University have developed a renal puncture robot that is able to be installed on a surgical bed. In this robot, a single-bar parallelogram RCM mechanism is used to complete the centering rotation function during the operation [21]. Jilin University developed a mirror arm of a new type of surgical robot based on RCM. This RCM uses the crank slider to realize the centering function of the actuator [22]. Kuo and Dai designed a decoupling RCM based on a parallel arm. The mechanism includes a fixed base, a motion restraining leg,

and two auxiliary drive legs. The motion-constrained leg is designed as a 3RP mechanism, which can realize the rotational motion and axial translational motion of the surgical instrument about the rotation axis [23].

From the research status, it can be found that the existing RCM can meet the surgical requirements. However, the lack of work concerning on a single-bar parallelogram mechanism, a crank slider mechanism, or a triangular mechanism is partly due to complicated structure, poor stability, and large space occupation.

This paper is aimed at studying the ultrasonic probe position and posture adjustment mechanism with centering function and passive. The range of motion of the ultrasonic probe, the operable space of the mechanism, and the design criteria were obtained accordingly to analyze the surgical procedure of prostate biopsy. The mechanism is divided into functions, and the degree of freedom of each module is allocated reasonably according to the design criteria. Next, each module of the mechanism is designed and, a three-dimensional model of the overall mechanism is drawn. This study is focused on designing the posture adjustment module with centering function in design phase. The D-H method is utilized to establish the coordinate system of the mechanism, and the joint parameters are obtained. Combined with the simulation results, the positioning error of the remote center point and the analysis of error in the actual surgical operation were tested and analyzed in the experimental part.

The transrectal ultrasound probe position-adjusting RCM will complement a large gap in the passive prostate-assisted interventional mechanism in the field of prostate intervention. The designed RCM can not only enable doctors to truly liberate their hands during the operation, but also achieve the level of planning and industrialization, improve the efficiency and precision of prostate interventional surgery, and a more practical motivation for this study is to promote the development of prostate cancer medicine.

2. Methods

2.1. Analysis of Functional Requirements of Adjustment Mechanism.
Transrectal prostate biopsy is an effective means of diagnosing prostate cancer. When the operation is performed, the doctor uses an ultrasound probe to probe the patient's rectum and puncture the prostate under the guidance of ultrasound images.

2.1.1. Motion Analysis of Ultrasonic Probe.
The prostate, which closes to the rectal wall, is located in the abdomen of the rectum. The upper end of the prostatic body has a transverse diameter of about 40 mm, a vertical diameter of about 30 mm, and anteroposterior diameter of about 25 mm. After filling with water, the volume increases by 25%. The cavity rectal ultrasound probe is invaded through the anus. During the guided puncture, the rectal ultrasound probe needs to perform position adjustment, azimuth adjustment, pitch adjustment, rotation, and feed to achieve multiangle omnidirectional scanning of the prostate. The rectal anatomy is shown in Figure 1. We found that the ampulla space inside the rectum is relatively wide; however, the anal internal
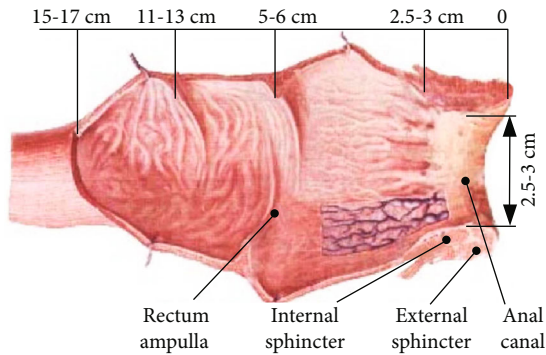
FIGURE 1: Rectum anatomy graph.
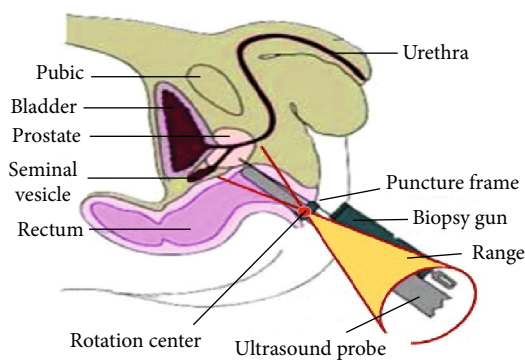
FIGURE 2: Motion scope of ultrasonic probe.

sphincter is muscle and its space is narrow, and the position is fixed.

The ultrasound probe pass through the anal canal to reach the ampulla of the rectum, and the ultrasound probe contacts with the internal sphincter of the anus at the anal canal. Therefore, the ultrasound probe should always swing with the center of the anus peripheral as the center of rotation to avoid damage to the rectum and increase the patient's pain when scanning the prostate. Figure 2 shows that the resulting range of motion is a conical space.

2.1.2. Analysis of Mechanism Operational Space. During the prostate biopsy operation, the patient adopts the left lateral position. In order to prevent the ultrasound probe from interfering with the bed during adjustment, the patient keeps knee-shouldered and the buttocks are positioned the bedside. The posture of the patient is shown in Figure 3. The longitudinal axis of the trunk is 30°~45° to the edge of the bed, the angle between the thigh and the edge of the bed is 45°~60°, and the distance between the prostate and the bed is 150~250 mm. The anus is able to be exposed according to the position of left knee flexing. Furthermore, it is convenient for the ultrasound probe to be invaded from the rectum.

2.1.3. Design Guidelines of Position and Posture Adjustment Mechanism. According to the surgical characteristics of transrectal ultrasound probe prostate biopsy surgery, the

design of the ultrasonic probe posture adjustment mechanism needs to be considered as following below criteria:

(1) *Continuous Motion*: The mechanism should continuously move, which can drive the ultrasonic probe to smoothly reach the required spatial position and posture

(2) *Reliable Locking*: In order to the safety and positioning accuracy of the operation, the mechanism needs to be securely locked when the ultrasonic probe moves to a proper posture

(3) The positioning mechanism and the posture adjustment mechanism are not interfere with each other and are completely decoupled

(4) The working range is able to cover all prostate areas without blind spots

(5) The structure is simple and reliable, and the manufacturing is easy obtained

2.2. Design of Position and Posture of Adjustment Mechanism. In order to meet the needs of different scanning range of prostate tissue by ultrasound probe during operation, the position adjustment function, posture adjustment function, rotation, and feed function of the ultrasonic probe should be realized. The 3-DOF spatial positioning mechanism, 2-DOF posture adjustment mechanism, and 2-DOF ultrasonic probe rotation and feed mechanism are adopted. The motion relationship between the three mechanisms is completely decoupled. The transrectal ultrasound probe position and posture adjustment mechanism are composed of a position adjustment module, a posture adjustment module, an ultrasonic probe rotation, and a feed module and a bottom clamping device. From the perspective of degree of freedom, this adjustment mechanism is a 7-DOF robot. Joint 7 is only a moving joint, and the other joints are rotating joints in the mechanism. The joints 1 to 4 constitute a position adjustment module; joint 5 and joint 6 constitute a posture adjustment module; joint 7 is utilized to realize the penetration movement of the ultrasonic probe along the peripheral center of the anus, and the joint 8 is utilized to realize the rotation of the ultrasonic probe around its own axis. Figure 4 shows schematic diagram of each module of the adjustment mechanism.

The centering function is implemented by the posture adjustment module. We need to consider the centering effect and the implementation of the centering function; therefore, the design of posture adjustment module is focused in design phase.

Due to the size and weight of the posture adjustment module affect the size of the position adjustment module, the specific structural size of the posture adjustment module is calculated in this section. For the posture adjustment module, the 2-DOF structure is chosen. In order to make the ultrasound probe move in two directions around the center of the anus, an RCM mechanism is considered. The posture adjustment module adopts an RCM mechanism based on double parallelograms, and its schematic diagram is shown in Figure 5. Double parallelograms are □ADCF and □BCIJ.
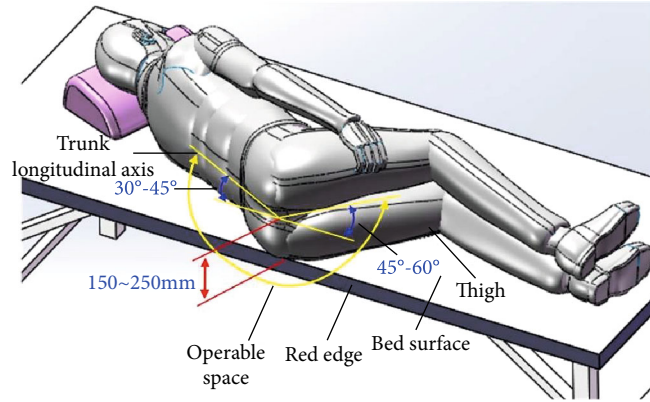
FIGURE 3: Operational space.
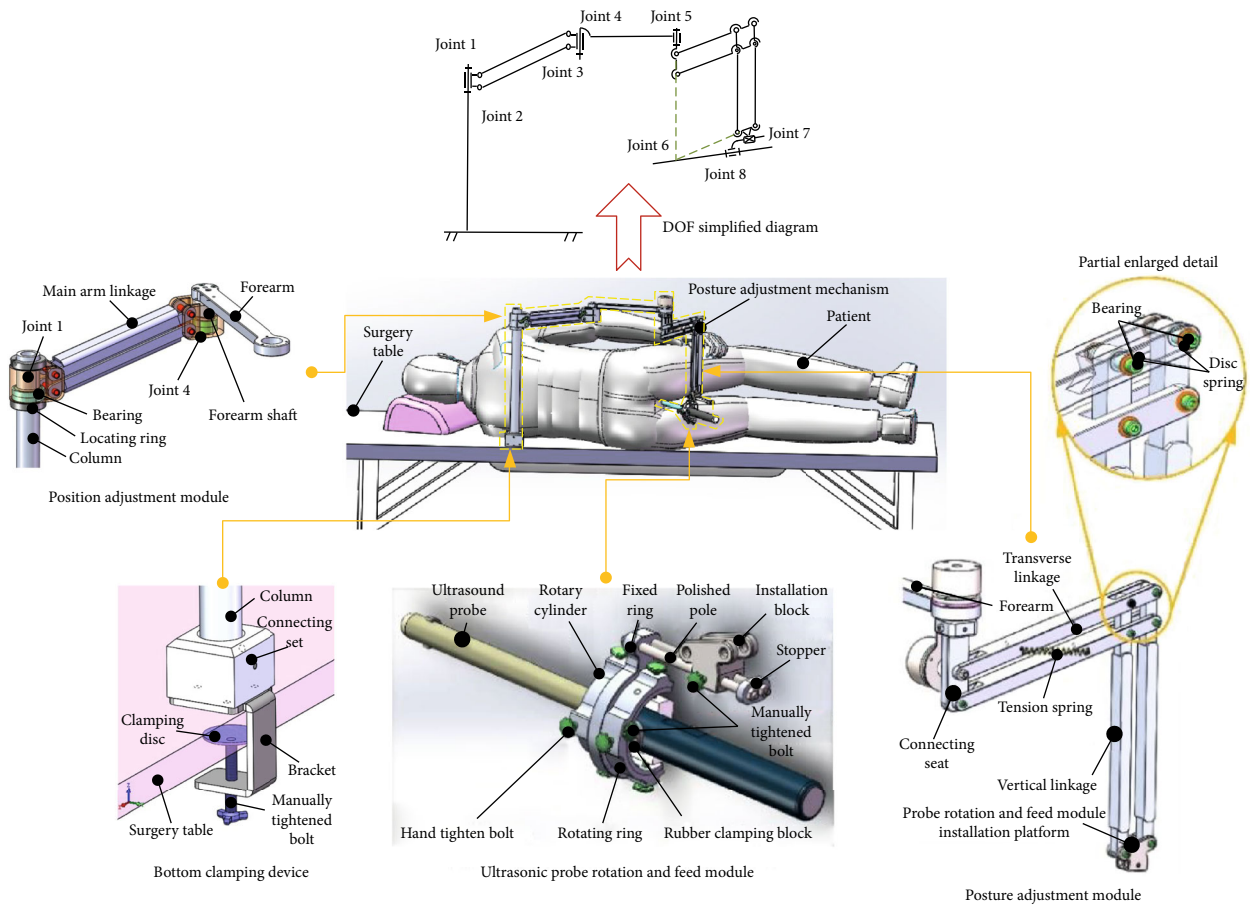
FIGURE 4: Schematic diagram of the position adjustment mechanism of the transrectal ultrasound probe and each module structure diagram.

In order to conveniently describe the characteristics of the mechanism, a local coordinate system is established in Figure 5. When the link DF swings the angle α around the point D, the double parallelogram mechanism has the following characteristics:

(1) *Parallel Characteristics*: $AD//BI//CJ$ and $AC//DF//IJ$

(2) *Centering Characteristics*: The position of the intersection H of the AD extension line and the JI extension line is always unchanged

When the doctor performs the operation, the fixed point H is always at the center point of the anus, and the AD rod is vertically above the patient's ankle. The length DH must be greater than half the width of the patient's ankle to prevent the posture adjustment module from interfering with the patient's body. According to the size of the human body, the width of the crotch is generally 300 mm~420 mm, so the length of DH needs to satisfy the equation:

$$l_{DH} > 210\text{mm}. \tag{1}$$
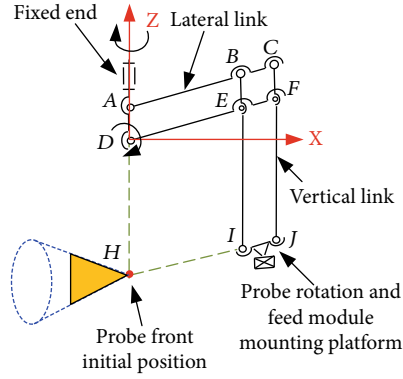
FIGURE 5: Schematic diagram of posture adjustment module.

We choose $l_{DH} = 220$mm and $l_{AD} = 30$mm, and then, the length of the longitudinal link is as follows:

$$l_{BI} = 250\text{mm}. \tag{2}$$

The size of the vertical plane of the anus peripheral center point is 120 mm away from the buttocks. In order to prevent the longitudinal link BI from interfering with the patient's body, the length HI needs to satisfy the equation:

$$l_{HI} > 120\text{mm} \tag{3}$$

Taking into account the ultrasonic probe rotation and the size occupied by the feed module, we choose $l_{DI} = 200$mm, $l_{IJ} = 30$mm, the length of the transverse link is:

$$l_{AC} = 230\text{mm} \tag{4}$$

According to the physiological characteristics of the human body, the space occupied by the prostate is generally $40\text{ mm} \times 30\text{ mm} \times 25\text{ mm}$, and Figure 6 shows the spatial state of the prostate in the left lateral position and the spatial analysis of the angle of the ultrasound probe scanning the prostate. The azimuth angle β is the swing angle of the ultrasonic probe in the transverse section, and the pitch angle γ is the swing angle of the ultrasonic probe in the longitudinal section. Due to the distance HK from the peripheral center point H of the anus to the surface of the prostate is 60 mm, the volume of the prostate is increased by 25% after filling with water, and the volume of the prostate is $50\text{ mm} \times 40\text{ mm} \times 40\text{ mm}$ when calculating the swing angle of the ultrasonic probe.

Therefore, $PK = 25$mm, $MK = NK = 40$mm, $OM = OK = 1/2MN = 1/2\sqrt{MK^2 + NK^2} = 28$mm,

$$OH = HK + OK = 88\text{mm}. \tag{5}$$

In order for the ultrasound probe to cover the entire area of the prostate, the beta and gamma angles should satisfy the following equation:
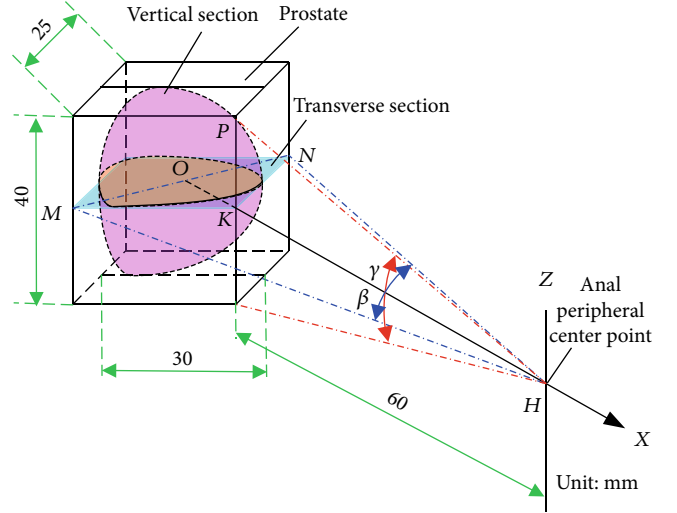
FIGURE 6: Analysis of swing angle of ultrasonic probe.

$$\tan\frac{\beta}{2} \geq \frac{OM}{OH} = \frac{28}{88},$$
$$\tan\frac{\gamma}{2} \geq \frac{PK}{HK} = \frac{25}{60}. \tag{6}$$

Solving result is $\beta \geq 35.4°$, $\gamma \geq 45.3°$.

2.3. Simulation Analysis of the Motion Performance of Adjustment Mechanism. The principle design of the ultrasonic probe position and posture adjustment mechanism determines the overall configuration of the mechanism, so that the designed mechanism is able to meet the working requirements, which meet the scanning range of the ultrasound probe during the operation to completely cover every part of the prostate. Therefore, it is necessary to utilize kinematics to analyze the mechanism to solve the motion space of the mechanism and the centering effect when the ultrasonic probe finishes the adjustment of posture.

2.3.1. Coordinate System Establishment and Joint Parameters. According to the structure of the ultrasonic probe position and posture adjustment mechanism, a schematic diagram of the mechanism is established, as shown in Figure 7. This mechanism is a six-bar linkage consisting of two parallelograms because of the posture adjustment module is not a simple open-loop kinematic chain.

In this mechanism, the rod 6 and the rod 7 are, respectively, the probe rotation and feed module mounting platform and the feeding platform, and the rod 8 is an ultrasonic probe. The coordinate system origin o_6 of the rod 6 is established at the remote center point based on the analysis of the mechanism characteristics. The coordinate system origin o_7 of the rod 7 is established at the end of the feed platform, and the coordinate system origin o_8 of the rod 8 is established at the end of the ultrasonic probe, and the directions of the x_6-axis and the x_7-axis are along the ultrasonic probe axis x_8. Therefore, the system is regarded as a simple open-loop kinematic chain to discuss and
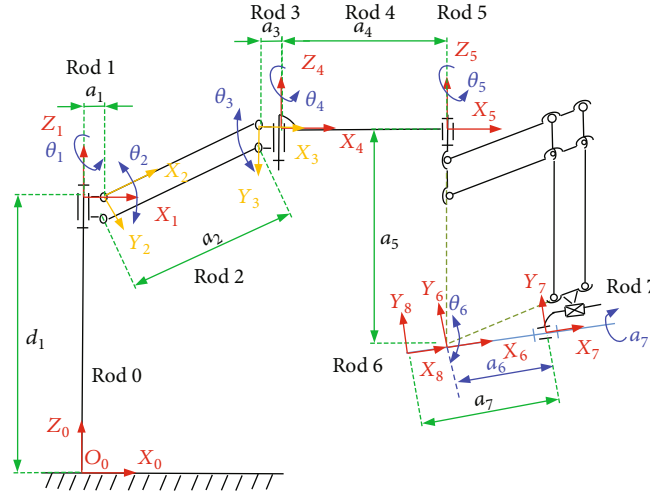
FIGURE 7: The kinematics coordinate system.

TABLE 1: D-H parameters of manipulator.

Rod i	1	2	3	4	5	6	7	8
a_{i-1} (°)	0	29.5	200	29.5	250	300	a_6	190
α_{i-1} (°)	0	-90	0	90	0	90	0	α_7
d_i (mm)	445	0	0	0	0	0	0	0
θ_i (°)	θ_1	θ_2	$-\theta_2$	θ_4	θ_5	θ_6	0	0
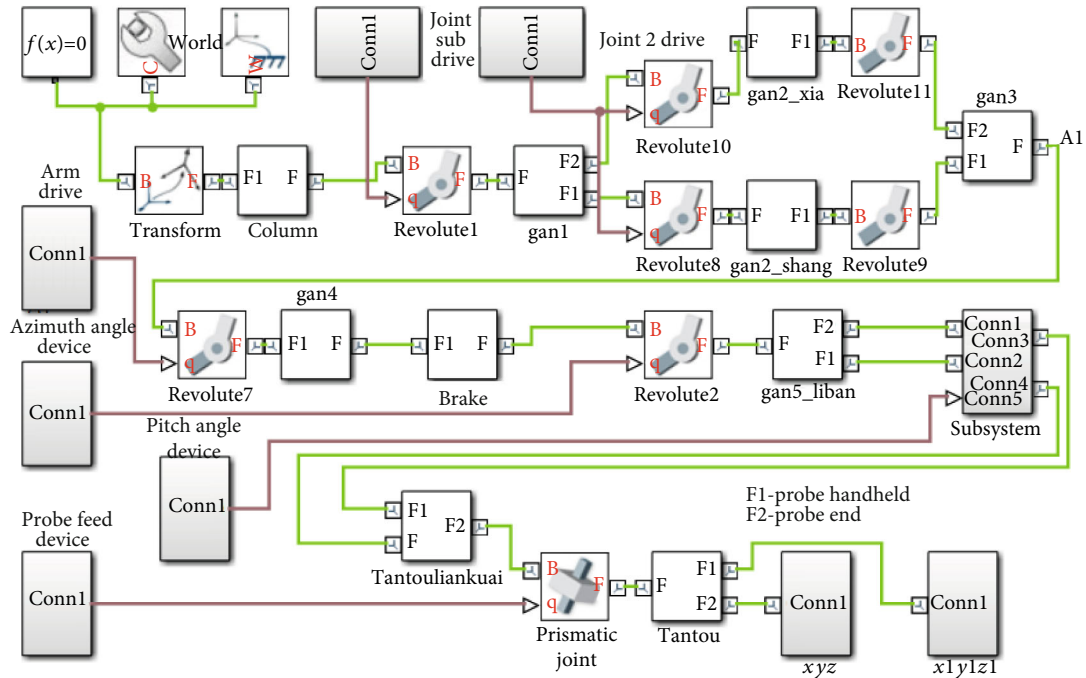
FIGURE 8: SimMechanics model of ultrasonic probe position adjustment mechanism.

research; furthermore, the D-H method is utilized to solve the kinematics of the mechanism.

The base coordinate system is $o_0 x_0 y_0 z_0$, and d_1, a_1, a_2, a_3, a_4, a_6, and a_7 are the rod lengths of the respective links, and θ_1, θ_2, θ_3, and θ_4 are the rotation angles of the respective

TABLE 2: Posture simulation parameters of ultrasonic probe at 0 mm, 30 mm, and 60 mm feeding.

θ_1 (°)	θ_2 (°)	θ_4 (°)	θ_5 (°)	θ_6 (°)	α_7 (°)
-30	20	80	-20~20	-25~25	0

(a)

(b)

(c)

(d)
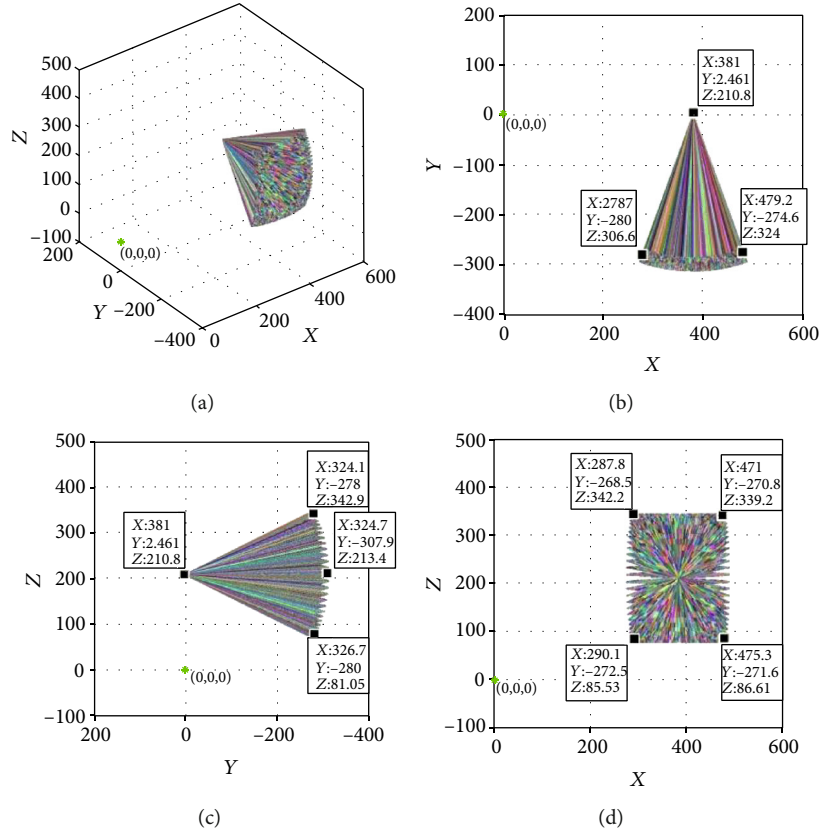
FIGURE 9: Posture of ultrasonic probe at 0 mm feeding: (a) three-dimensional map; (b) *xoy* plane projection; (c) *yoz* plane projection; and (d) *xoz* plane projection.

rotary joints of the position adjustment mechanism, respectively.

Due to the rod 2 that constitutes a parallelogram structure, $\theta_3 = -\theta_2, \theta_5, \theta_6$ are the azimuth and pitching angles of the RCM mechanism, a_7 is the feed distance of the ultrasonic probe along the x_8-axis, and α_7 is the rotation angle of the ultrasonic probe. According to the designed requirements, the organization has a total of 7 degrees of freedom, and the joint parameters are shown in Table 1.

2.3.2. Simulation of Centering Effect Based on SimMechanics. According to the mechanism diagram and the connecting rod parameters drawn in Figure 7 and Table 1, the physical model of the ultrasonic probe posture adjustment mechanism is established in the SimMechanics toolbox, the end track of the ultrasonic probe is tracked, and we output the recorded position coordinates to Workspace for drawing 3D graphics.

The model established for the ultrasonic probe pose adjustment mechanism in the SimMechanics toolbox is shown in Figure 8. The SimMechanics model mainly includes a ground module, 13 rigid body modules, 12 rotary joint modules, 1 moving joint module, 6 drive modules, and 2 sensor modules.

(1) "World" indicates the position of the base coordinate system, which is located on the bottom surface of the column

(2) The rigid body modules respectively represent 13 movable members of the posture adjustment mechanism

(3) The rotary joints respectively represent the movement relationship between the members as rotation

(4) The moving joints represent the rotation and advancement of the ultrasonic probe

(5) The movement constraint of the module relative to the posture adjustment module is provided

(6) The drive modules are respectively added to the corresponding joints

(7) The sensor modules respectively record the coordinate positions that the end position of the ultrasonic probe and the position of reached handheld

The posture adjustment module enables the ultrasonic probe to realize the centering function of swinging around a certain point and simulates the centering effect of the ultrasonic probe. Table 2 shows the setting parameters.

3. Results

3.1. Simulation Results of Centering Effect. The simulation results when the feed distance $a_6 = 0$ mm are shown in Figure 9. The posture adjustment module allows the

(a)

(b)

(c)

(d)
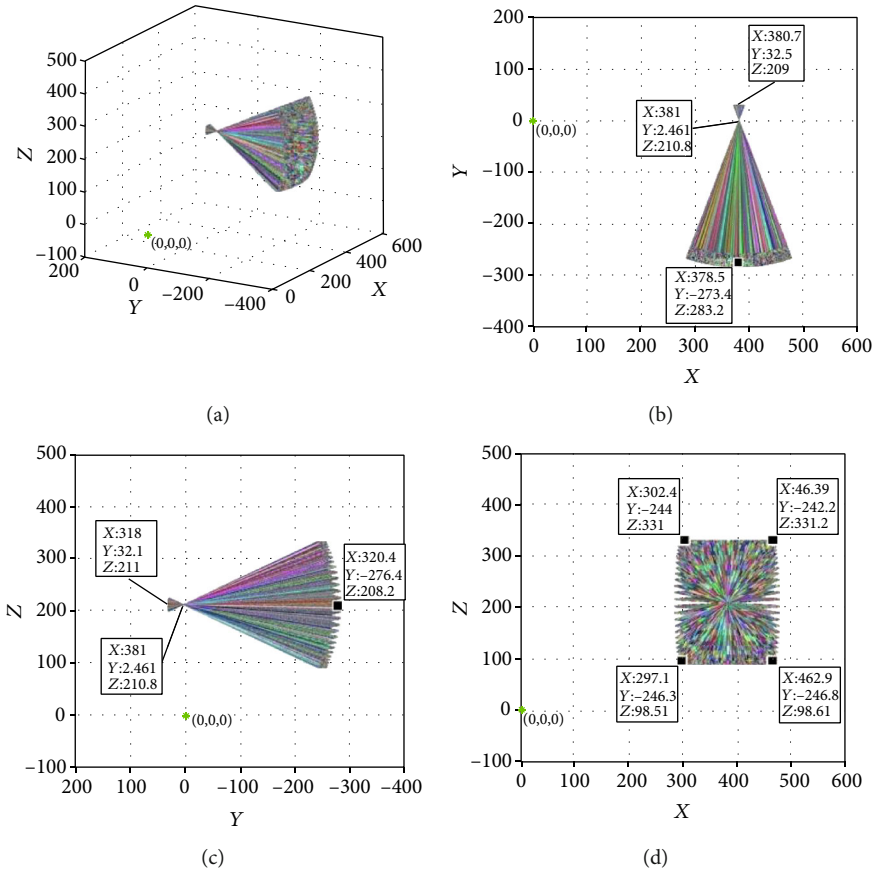
FIGURE 10: Posture of ultrasonic probe at 30 mm feeding: (a) three-dimensional map; (b) *xoy* plane projection; (c) *yoz* plane projection; and (d) *xoz* plane projection.

ultrasonic probe to realize the centering function of swinging around a certain point, and the effectiveness of centering the ultrasonic probe is simulated. The parameter settings are shown in Table 2.

The simulation results when the feed distance $a_6 = 0$ mm are shown in Figure 9. The color line segments in the figure represent the posture of the ultrasonic probe at different joint angles. The position coordinates of the remote center point of the mechanism are (381.000, 2.461, and 210.800) when $\theta_1 = -30°$, $\theta_2 = 20°$, and $\theta_4 = 80°$. The scanning end of the ultrasonic probe is always at the remote center point of the mechanism, and a cone-shaped space with the point as a vertex is formed when the azimuth and pitching angles are adjusted according to a given angle.

The omnidirectional scan of the prostate can be completed when the doctor inserts the ultrasound probe into the rectum and adjusts the azimuth, pitching angle, and the angle of rotation of the ultrasound probe. The joint parameters of the position adjustment module and the posture adjustment module are not changed in order to observe the change in the posture after the ultrasonic probe is fed. The feed distance of the ultrasonic probe was changed to $a_6 = 30$ mm. The simulation results obtained are shown in Figure 10.

Measurements showed that the coordinates of this point remained at (381.000, 2.461, and 210.800). The ultrasonic probe still changed the azimuth and pitching angles accord-

ing to the remote center point after feeding 30 mm, which meets the design requirements. We changed the feed distance of the ultrasonic probe to $a_6 = 60$ mm, while leaving the parameters of the other joints unchanged, and the posture change of the ultrasonic probe was simulated. The simulation results are shown in Figure 11. It can be seen in the figure that the coordinates of the intersections of all the line segments intersecting in space remain at (381.000, 2.461, and 210.800). This means that the azimuth and pitching angles of the ultrasonic probe remain changed according to the remote center point after feeding 60 mm, which also meets the design requirements.

The results of the simulation of the ultrasonic probe at feed rates of 0 mm, 30 mm, and 60 mm, respectively, showed that the ultrasonic probe can achieve a very stable centering effect at different feed rates and can be used for surgery.

3.2. Experiment Results of Centering Effect

3.2.1. Physical Prototype of the Posture Adjustment Mechanism of Ultrasonic Probe. Many interference factors exist because the mechanism is operated during the actual operation. This experimental section describes the simulation of the actual surgical environment and operation process. The range and continuity of each joint, reliable locking ability, position adjustment mechanism working space and

(a)

(b)

(c)

(d)
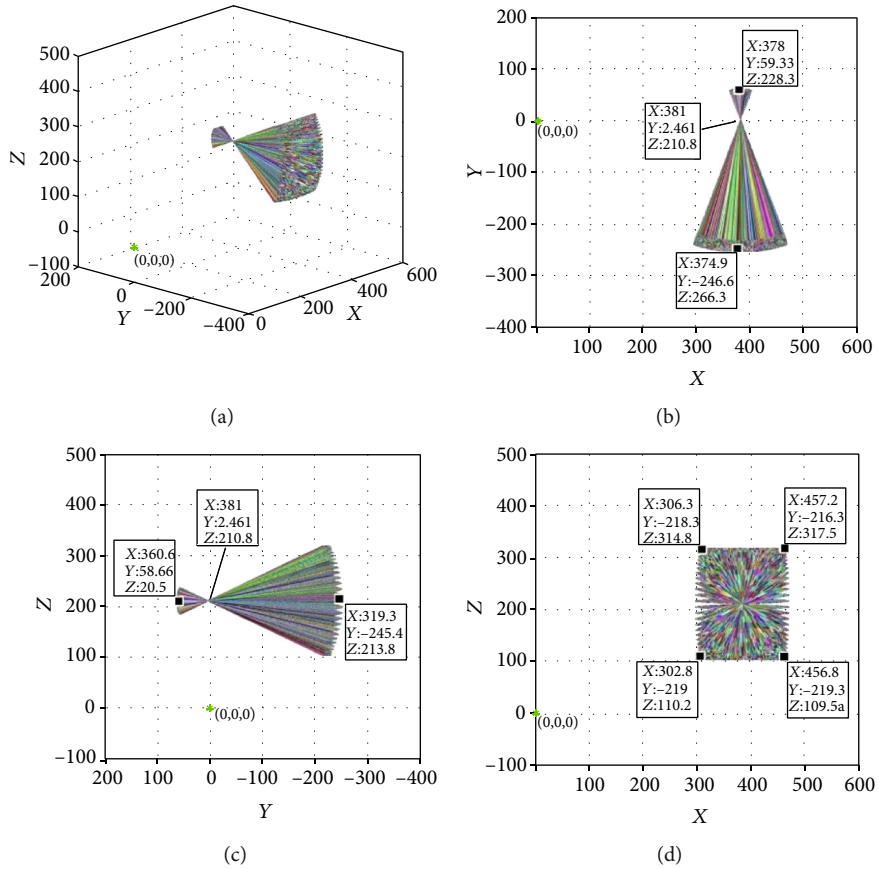
FIGURE 11: Posture of ultrasonic probe at 60 mm feeding: (a) three-dimensional map; (b) *xoy* plane projection; (c) *yoz* plane projection; and (d) *xoz* plane projection.

FIGURE 12: Physical prototype of the posture adjustment mechanism of ultrasonic probe.

positioning ability, mechanism static stiffness, RCM posture adjustment, and centering motion performance were tested to verify the rationality of these mechanisms. Figure 12 shows the physical prototype of the mechanism.

3.2.2. Remote Center Point Error Measurement. The doctor adjusts the azimuth and pitching angle of the ultrasound probe to omnidirectionally scan the prostate. To ensure the safety of the operation and reduce the damage caused to the patient by the ultrasonic probe, the ultrasonic probe needs to achieve a centering motion around the center of the anus. Therefore, it was necessary to test the RCM of the posture adjustment module to examine whether it meets the surgical requirements.

The RCM performance comprises the displacement range of the remote center point of the mechanism in the space when the ultrasonic probe performs posture adjustment. The RCM performance can be evaluated by measuring the error between the spatial fixed point and the remote center marked point under the existing experimental conditions. A fixed point in space measures only the error of the remote center point in the two-dimensional (2D) plane because the position change of the remote center point is 3D in space. Therefore, in this section, we describe two sets of experiments performed to measure the error, which is caused by changing the azimuth or pitching angle, separately.

(1) Azimuth Remote Center Point Motion Error Measurement. The azimuth angles θ_5 (-40˚, -20˚, 0˚, 20˚, and 40˚) were adjusted under different feed rates a_6 (0 mm, 30 mm, and 60 mm). The mechanism was adjusted to a certain position, and then, the joints of the position adjustment mechanism were locked. The pitch angle of the ultrasonic probe was θ_6 = 0˚, and the rotation angle of the ultrasonic probe $\alpha_7 = 0$˚. Because the azimuth is adjusted to the angle change in the horizontal plane, the wooden board with the coordinate paper was fixed directly below the ultrasonic probe (the scale of the coordinate paper was 1 mm), and then, the position of the remote center point was marked on the ultrasonic probe; a laser was used to illuminate the remote center point as a

(a) (b)
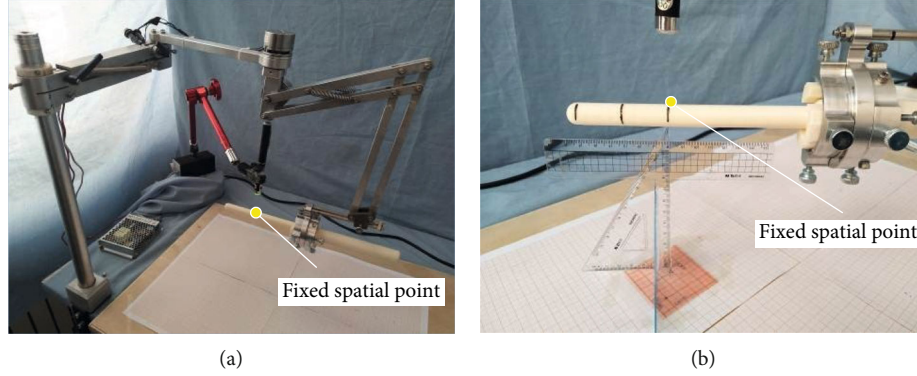
FIGURE 13: Measurement of azimuth remote center point error: (a) overall view; (b) partial magnification view.
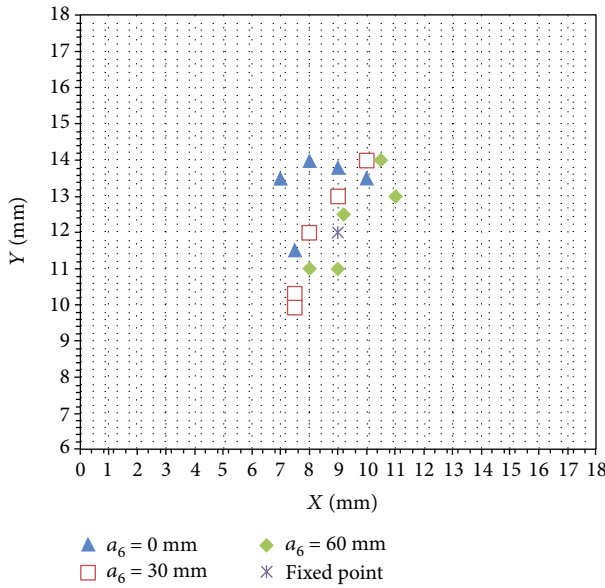
FIGURE 14: Remote center point error under the motion of azimuth angle.

fixed spatial point. Finally, the position of the fixed spatial point was marked on the coordinate paper. Figure 13 shows experimental process.

The experimental data were obtained by means of multiple measurements. The experimental results are shown in Figure 14. The points marked on the coordinate paper were enlarged and measured. The distance between the subsequent remote center point and the fixed spatial point is less than 4 mm, and the deformation of the anus is about 6 mm. Therefore, the accuracy of the remote center point under the azimuth angle meets the surgical requirements.

(2) Pitch Angle Remote Center Point Motion Error Measurement. The pitch angles θ_6 (-24°, -12°, 0°, 12°, and 24°) were adjusted under different feed rates a_6 (0 mm, 30 mm, and 60 mm). The mechanism was adjusted to a certain position, and then, the joints of the position adjustment mechanism were locked. The pitch angle of the ultrasonic probe was θ_5 = 0°, and the rotation angle of the ultrasonic probe $\alpha_7 = 0°$.

Because the azimuth is adjusted to the angle change in the vertical plane, the wooden board with the coordinate paper was fixed directly below the ultrasonic probe (the scale of the coordinate paper was 1 mm), and then, the position of the remote center point was marked on the ultrasonic probe; a laser was used to illuminate the remote center point as a fixed spatial point. Finally, the position of the fixed spatial point was marked on the coordinate paper. Figure 15 shows the experimental process. The obtained experimental data are shown in Figure 16.

The measurement of the points marked on the coordinate paper showed that the distance between the subsequent remote center points and the fixed spatial point is less than 3.4 mm, and the deformation of the anus is about 6 mm. Therefore, the accuracy of the remote center point meets the surgical requirements under the change in the pitch angle.

4. Discussion

The positioning error of the remote center point is related to the entire mechanism and is composed mainly of systematic error and random error.

The systematic error is composed of multiple error factors with deterministic changes [24–26]. Therefore, we used the measured mean and variance to consider the systematic error, and, in order to avoid the error estimation bias caused by the small number of sample repetitions, the confidence interval was used to state the systematic error limit. Then, we defined the safety factor as k_1 and $[\bar{x} - k_1 s, \bar{x} + k_1 s]$ as the confidence interval for μ, where μ is the mean, s is the measurement variance, and $\bar{x}$ is the unbiased estimator of μ. In addition, in order to determine the relative error, the relative fixed point error and the relative standard deviation (RSD) were used as the evaluation indexes in each direction. The relative fixed point error ε_0 is the error of the measured mean value with respect to the fixed point. It takes the relative error of the x-axis coordinates as an example, which is expressed as

$$\varepsilon_0 = \frac{|\bar{x} - x_0|}{x_0} \times 100\%, \qquad (7)$$

(a)

(b)
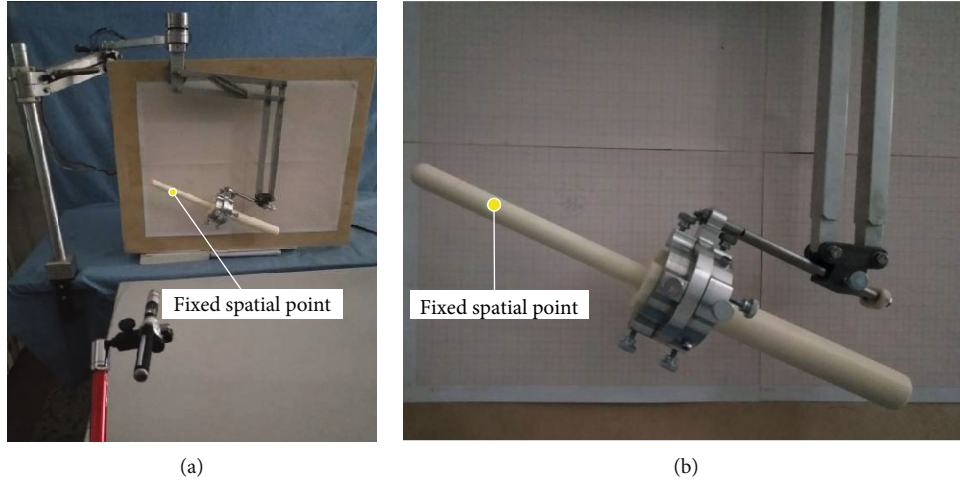
FIGURE 15: Measurement of pitching center point error: (a) overall view; (b) partial magnification view.
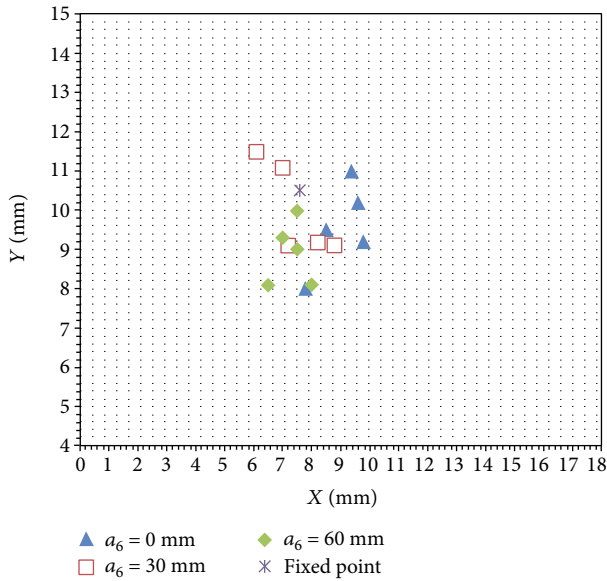
FIGURE 16: Remote center point error under the motion of pitching angle.

where $\bar{x} = \sum_{i=1}^{n} x_i/n$, and x_0 is the x-axis coordinate value of the fixed point.

The RSD can be used to verify the precision of the measurement results:

$$\text{RSD} = \frac{S}{\bar{x}} \times 100\%. \tag{8}$$

Most random errors follow a normal distribution. To reflect the spatial relationship of random stochastic processes in different spatial locations, the value of the random error parameters ranged from -1 to 1 [27, 28]. The x and y direction and the x and z directions of the azimuth and pitching angles were used as the positioning quality indicators as two sets of 2D random variables. The correlation coefficient between 2D variables is defined as

$$r = \frac{\sum_{i=1}^{n}(x_i - \bar{x})(y_i - \bar{y})}{\sqrt{\sum_{i=1}^{n}(x_i - \bar{x})^2 \sum_{i=1}^{n}(y_i - \bar{y})^2}}. \tag{9}$$

According to the theory of the above error analysis, the confidence interval was taken as 90%, and the measured mean value, relative fixed point error, relative standard error, confidence interval, and 2D variable relative parameters were calculated. The azimuth error calculation results are shown in Table 3.

As shown in Table 3, for the same probe feed distance, the width of the confidence interval between the x direction and the y direction is close, and both are stable at approximately 2.3 mm, indicating that the positioning performance is relatively stable. The relative fixed point error and RSD in different feed directions are basically stable in the x direction, and the relative fixed point error is larger in the y direction, except in the case of the 0 mm feed distance. However, for the remaining feed distances, the error remains stable below 15%, and the error can be controlled within 1.8 mm. The relative error parameters of the x and y directions under different feed distances are relatively low, indicating that the correlation between the two parameters is not strong. It is proved that the measurement value in the y direction cannot be determined by measuring the x direction. The results show that the azimuth centering performance is stable, and the accuracy meets the requirements. Similarly, an error analysis of the remote center point measurement data was performed. The analysis results are shown in Table 4.

5. Conclusions

This study is aimed at designing a passive ultrasound probe position and posture adjustment mechanism to assist doctors performing prostate scans and puncture interventions. In this paper, the forward kinematics analysis of the mechanism, the simulation of the centering effect, the development of the physical prototype, and related experimental research were presented. The main findings are as follows.

TABLE 3: Analysis result of azimuth angle of remote center point error.

| Probe feed distance/mm | x direction | | | | y direction | | | | x and y directional random error relative parameter |
	μ (mm)	ε_0 (%)	RSD (%)	Confidence interval	μ (mm)	ε_0 (%)	RSD (%)	Confidence interval	
0	8.30	7.78	14.40	(7.15, 9.44)	13.26	10.50	7.50	[12.30, 14.21]	0.342
30	8.40	6.67	12.80	(7.36, 9.43)	11.86	1.16	14.41	(11.22, 13.49)	0.758
60	9.54	6.00	12.50	(8.38, 10.69)	12.30	2.50	10.50	(11.05, 13.54)	0.840

TABLE 4: Analysis result of pitching angle of remote center point error.

| Probe feed distance/mm | x direction | | | | z direction | | | | x and z directional random error relative parameter |
	μ (mm)	ε_0 (%)	RSD (%)	Confidence interval	μ (mm)	ε_0 (%)	RSD (%)	Confidence interval	
0	8.72	14.73	12.97	(7.56, 9.95)	9.58	8.76	11.69	(8.50, 10.65)	0.741
30	7.46	1.84	14.98	(6.45, 8.46)	10.20	2.85	11.56	(9.16, 11.23)	-0.873
60	7.30	3.94	7.80	(6.75, 8.84)	8.90	15.23	9.10	(8.12, 10.67)	0.108

(1) The moving shape of the ultrasonic probe is the conical space around the center of rotation of the anus. The design requirements are determined by analyzing the surgical procedure; the posture adjustment module is designed such that the double parallel quadrilateral RCM mechanism allows the ultrasonic probe to achieve the centering function

(2) SimMechanics was used to simulate the effectiveness of centering the ultrasonic probe when adjusting the posture under different feed distances. The study results showed that the ultrasonic probe is centered and stable, which verifies that the position adjustment of the ultrasonic probe meets the design requirements

(3) A physical prototype was developed and debugged. The effectiveness of the centering of the remote center point was measured when adjusting the posture of the ultrasonic probe, and the displacement range of the remote center point in space was obtained. The experimental results show that the maximum error of the azimuth remote center point motion and the maximum error of the remote center point motion of the ultrasonic probe are 4 mm and 3.4 mm, respectively, that is, less than a 6 mm anus can withstand. The random error correlation in different directions is weak, the systematic error confidence intervals of the azimuth and elevation angle are less than 2.5 mm, and the maximum relative fixed point error and the maximum relative standard error are 14.73% and 14.98%, respectively

The system meets the surgical requirements of a passive medical mechanism to be applied in actual surgical procedures.

Data Availability

The data used to support the findings of this study are available from the corresponding author upon request.

Conflicts of Interest

Authors declare that there is no conflict of interest.

Acknowledgments

References

[1] R. L. Siegel, K. D. Miller, and A. Jemal, "Cancer statistics, 2020," Ca A Cancer Journal for Clinicians, vol. 70, no. 1, pp. 7–30, 2020.

[2] K. A. Cronin, A. J. Lake, S. Scott et al., "Annual Report to the Nation on the Status of Cancer, part I: National cancer statistics," Cancer, vol. 124, no. 13, pp. 2785–2800, 2018.

[3] Z. F. Ma, "How to find prostate cancer early," Health Guide, vol. 21, no. 2, pp. 14-15, 2015.

[4] C. H. Pernar, E. M. Ebot, K. M. Wilson, and L. A. Mucci, "The epidemiology of prostate cancer," Cold Spring Harbor Perspectives in Medicine, vol. 8, no. 12, p. a030361, 2018.

[5] K. J. Harrington, C. Spitzweg, A. R. Bateman, J. C. Morris, and R. G. Vile, "Gene therapy for prostate cancer: current status and future prospects," Journal of Urology, vol. 166, no. 4, pp. 1220–1233, 2001.

[6] M. M. Pomerantz, M. L. Freedman, and P. W. Kantoff, "Genetic determinants of prostate cancer risk," BJU International, vol. 100, no. 2, pp. 241–243, 2018.

[7] D. D. Sjoberg, A. J. Vickers, M. Assel et al., "Twenty-year risk of prostate cancer death by midlife prostate-specific antigen and a panel of four kallikrein markers in a large population-based cohort of healthy men," European Urology, vol. 73, no. 6, pp. 941–948, 2018.

[8] J. Jiang, Z. Min, Y. Zhang, X. Guo, and Y. Xu, "Design and performance evaluation of passive interlocking posture adjustment mechanism for transrectal ultrasound probe," *Journal of Mechanics in Medicine and Biology*, vol. 19, no. 7, article 1940035, 2019.

[9] K. G. Yan, T. Podder, Y. Yu, T.-I. Liu, C. W. S. Cheng, and W. S. Ng, "Flexible needle-tissue interaction modeling with depth-varying mean parameter: preliminary study," *IEEE Transactions on Biomedical Engineering*, vol. 56, no. 2, pp. 255–262, 2009.

[10] Y. Yu, T. K. Podder, Y. D. Zhang et al., "Robotic system for prostate brachytherapy," *Brachytherapy*, vol. 7, no. 6, pp. 100-101, 2010.

[11] Y. Yu, T. Podder, Y. Zhang et al., "Robot-assisted prostate brachytherapy," in *International Conference on Medical Image Computing & Computer-assisted Intervention*, pp. 41–49, Copenhagen, Denmark, 2006.

[12] M. A. Meltsner, N. J. Ferrier, and B. R. Thomadsen, "Observations on rotating needle insertions using a brachytherapy robot," *Physics in Medicine & Biology*, vol. 52, no. 19, pp. 6027–6037, 2007.

[13] G. Fichtinger, J. P. Fiene, C. W. Kennedy et al., "Robotic assistance for ultrasound-guided prostate brachytherapy," *Medical Image Analysis*, vol. 12, no. 5, pp. 535–545, 2008.

[14] C. Kim, F. Schäfer, D. Chang, and D. Petrisor, "Robot for ultrasound-guided prostate imaging and intervention," in *2011 IEEE/RSJ International Conference on Intelligent Robots and Systems*, pp. 943–948, San Francisco, CA, USA, 2011.

[15] M.-A. Vitrani, M. Baumann, D. Reversat, G. Morel, A. Moreau-Gaudry, and P. Mozer, "Prostate biopsies assisted by comanipulated probe-holder: first in man," *International Journal of Computer Assisted Radiology and Surgery*, vol. 11, no. 6, pp. 1153–1161, 2016.

[16] J. Y. Li, *Design on Control System of Five Degrees of Freedom Prostate Biopsy Robot*, Harbin University of Science and Technology, 2013.

[17] Y. D. Zhang, J. C. Peng, Z. Liu, J. G. Jiang, and Y. J. Zhao, "Research on the segmentation method of prostate magnetic resonance image based on level set," *Chinese Journal of Scientific Instrument*, vol. 38, no. 2, pp. 416–424, 2017.

[18] Y. D. Zhang, W. X. Zhang, Y. Liang, and Y. Xu, "Research on mechanism and strategy of high accuracy puncture of prostate," *Chinese Journal of Scientific Instrument*, vol. 38, no. 6, pp. 1405–1412, 2017.

[19] M. E. Karar, "A simulation study of adaptive force controller for medical robotic liver ultrasound guidance," *Arabian Journal for Science and Engineering*, vol. 43, no. 8, pp. 4229–4238, 2018.

[20] R. H. Taylor, J. Funda, B. Eldridge et al., "A telerobotic assistant for laparoscopic surgery," *IEEE Engineering in Medicine and Biology Magazine*, vol. 14, no. 3, pp. 279–288, 1993.

[21] E. M. Boctor, R. J. Webster III, H. Mathieu, A. M. Okamura, and G. Fichtinger, "Virtual remote center of motion control for needle placement robots," *Computer Aided Surgery*, vol. 9, no. 5, pp. 175–183, 2010.

[22] G. Y. Dong, *The Design and Research of the Robot Arm for Celiac Minimally Invasive Surgery*, Jil-in University, 2016.

[23] C. H. Kuo and J. S. Dai, "Kinematics of a fully-decoupled remote center-of-motion parallel manipulator for minimally invasive surgery," *Journal of Medical Devices*, vol. 6, no. 2, pp. 211–214, 2012.

[24] M. Yi, X. J. Zou, L. F. Luo et al., "Error analysis of dynamic localization tests based on binocular stereo vision on litchi harvesting manipulator," *Transactions of the Chinese Society of Agricultural Engineering (Transactions of the CSAE)*, vol. 32, no. 5, pp. 50–56, 2016.

[25] H. Wei and C. Cheng, "The error analysis of the localization result caused by the installation errors of a seabed array of magnetometers," in *2016 IEEE Chinese Guidance, Navigation and Control Conference (CGNCC)*, pp. 16–19, Nanjing, China, 2017.

[26] Y. Cheng, S. Yin, X. Wang, L. An, and H. Liu, "Design and analysis of double-side meshing and dual-phase driving timing silent chain system," *Strojniski Vestnik - Journal of Mechanical Engineering*, vol. 62, no. 2, pp. 127–136, 2016.

[27] M. Pola and P. Bezoušek, "Pseudorange error analysis for precise indoor positioning system," *Journal of Electrical Engineering*, vol. 68, no. 3, pp. 206–211, 2017.

[28] J. Chang, A. Delaigle, P. Hall, and C. Y. Tang, "A frequency domain analysis of the error distribution from noisy high-frequency data," *Biometrika*, vol. 105, no. 2, pp. 353–369, 2018.

Research Article

Leg Locomotion Adaption for Quadruped Robots with Ground Compliance Estimation

Songyuan Zhang ⬤**, Hongji Zhang, and Yili Fu**

State Key Laboratory of Robotics and System, Harbin Institute of Technology, 150001, China

Correspondence should be addressed to Songyuan Zhang; zhangsy@hit.edu.cn

Locomotion control for quadruped robots is commonly applied on rigid terrains with modelled contact dynamics. However, the robot traversing different terrains is more important for real application. In this paper, a single-leg prototype and a test platform are built. The Cartesian coordinates of the foot-end are obtained through trajectory planning, and then, the virtual polar coordinates in the impedance control are obtained through geometric transformation. The deviation from the planned and actual virtual polar coordinates and the expected force recognized by the ground compliance identification system are sent to the impedance controller for different compliances. At last, several experiments are carried out for evaluating the performance including the ground compliance identification, the foot-end trajectory control, and the comparison between pure position control and impedance control.

1. Introduction

Currently, the main forms of locomotion robots include legged robots and tracked/wheeled robots. Compared with a tracked or wheeled robot, legged robots can easily adapt to and walk on rough terrain [1]. Legged robots can choose contact points with environment for overcoming obstacles and finding the feasible stable region [2]. For example, Boston Dynamics developed a hydraulic driven BigDog robot, which aimed at building an unmanned legged robot with rough-terrain mobility [3]. MIT Cheetah was designed with proprioceptive actuator for impact mitigation and high-bandwidth physical interaction [4]. In our previous research, inspired by the proprioceptive actuator [5], we designed a single-leg platform for high-speed locomotion. ANYmal used the complicated actuator which makes the robot impact with high torque control accuracy [6]. Overall, the hydraulic actuator has the feature of naturally robust against impulsive loads with a high-power density [7, 8]. However, legged robots with hydraulic actuators such as Bigdog developed by Boston Dynamics are difficult to be scaled down and will generate large noise [9]. Different from that, the electric actuator with

proprioceptive design allows the force proprioception which can deliver the desired force with motor current sensing [10].

For quadruped robot to achieve better performance, foot trajectory planning is crucial. Two factors should be considered in the design of the foot trajectory. One is that the great impact should be avoided when the feet land on the ground; another is that the leg structure should have enough ground clearance for avoiding obstacles [11]. The foot trajectory also requires continuous velocity and acceleration for stability. There are three main methods to plan the trajectory of a quadruped robot, i.e., Bézier curve trajectory, cubic trajectory, and sinusoidal trajectory [11]. Among them, the Bézier curve meets the above requirements perfectly. After the foot trajectory planning, the behaviour that the robot interacts with irregular ground should be considered. Quadruped robots which can adjust the foot-end dynamic behaviour to deal with the unstructured terrains are important on real application. For example, Semini et al. implemented an impedance controller to control the electrohydraulically driven leg of HyQ [12]. Hyun et al. realized the virtual leg compliance of the MIT Cheetah with proprioceptive impedance control to deal with the external disturbance. After
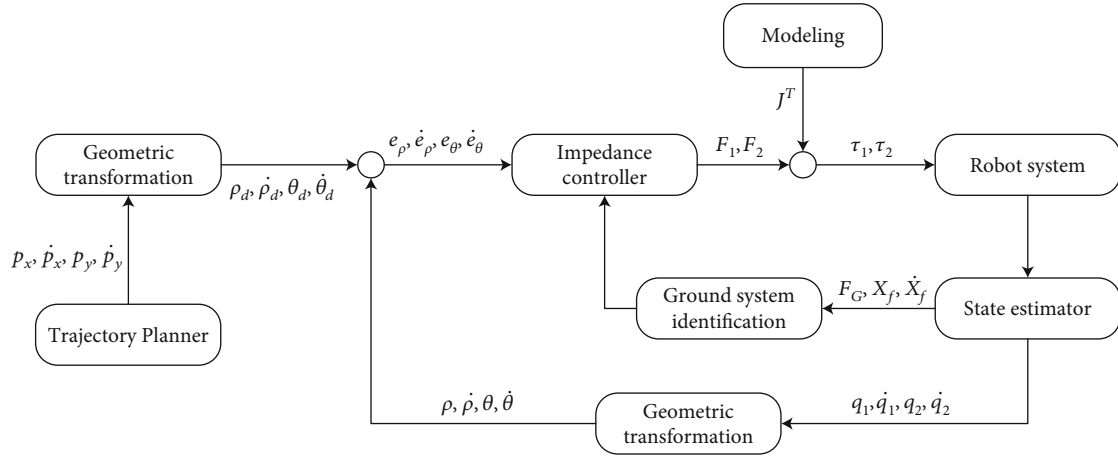
Figure 1: Overall of the control diagram.
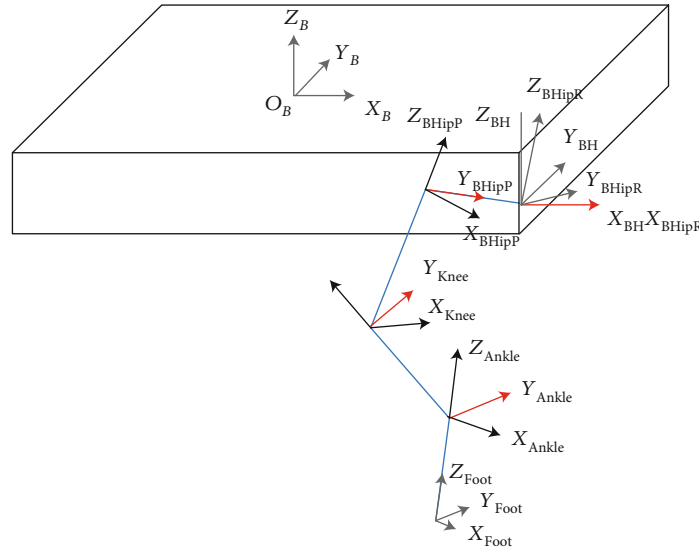
Figure 2: Link coordinate systems for the right front leg of the quadruped robot.

knowing the coordinates in the Cartesian coordinate system, the joint coordinates are obtained by inverse kinematic transformation, and the joint motion trajectory is obtained. Moreover, the whole leg movement of quadruped robots will be divided into stance phase with impedance control and swing phase with position control [13]. However, rigid ground assumption is applied for most researches. The different contact dynamics between the rigid assumption and soft contact will affect the performance and stability of robots. In contrast to that, Kim et al. penalizing the contact interaction in the cost function during the design of the whole-body controller [14]. Neunert et al. used the soft contact model combined with MPC controller [15]. Bosworth et al. designed a controller which can be tuned for different ground types [16]. Different from that, in our study, the least-squares method is applied to estimate the ground compliance parameters. The method is a soft terrain adaption algorithm which can achieve a transition between hard and soft ground with a real-time terrain-aware. For real leg locomotion adaption,

the estimated stiffness of ground will be used for adjusting the parameters of impedances controller.

This paper is structured as follows: Section 2 introduces the kinematic modelling method for the leg. In Section 2, the foot trajectory of the leg is designed utilizing the Bézier curve and sinusoidal waves. The detailed implementation of impedance control and ground compliance identification will be introduced in Section 2. The experimental results are provided in Section 3. At last, the conclusions are given.

2. Materials and Methods

The detailed leg design with three-joint leg structure can be found in our previous research [5]. The overall of the control diagram is shown in Figure 1. During the movement of robots, the Cartesian coordinates of the foot-end are obtained through trajectory planning, and then, the virtual polar coordinates in the impedance control are obtained
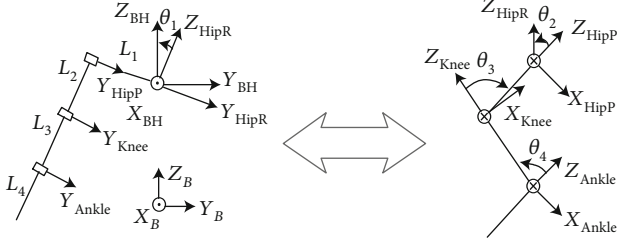
FIGURE 3: One leg kinematic model of the quadruped robot.

through geometric transformation. The deviation from the planned and actual virtual polar coordinates and the expected force recognized by the ground identification system is sent to the impedance controller. Finally, the desired foot-end force is obtained and then, the joint torque can be calculated by the change of the Jacobian matrix and sent to the robot system. The status of the robot system is also fed back to the previous process.

2.1. One Leg Kinematic Analysis. For realizing the foot trajectory control of the leg, the kinematics formula should be derived first. To simplify the subsequent analysis of the motion control problems, the first step is to establish a complete coordinate system for a quadruped robot. Since the configuration of the four legs of the robot is identical, the only difference is the position of the hip joint relative to the centre of mass (COM) of the robot. Therefore, the kinematics analysis of the foot-end with the hip coordinate system is consistent for all four legs. Here, only the right front leg is selected for the analysis in this section. The following joint coordinate systems are established according to the Denavit-Hartenberg (D-H) method: the hip rolling coordinate system $\sum_{\text{HipR}}$, the hip pitch coordinate system $\sum_{\text{HipP}}$, the knee pitch coordinate system $\sum_{\text{Knee}}$, the ankle pitch coordinate system $\sum_{\text{Ankle}}$, and the foot-end coordinate system $\sum_{\text{Foot}}$ are shown in Figure 2. The blue line in the figure shows the three links of the leg; the red line shows the axes of the leg rotating joints.

The coordinate system of each link, as well as four joint angles, is shown in Figure 3 in detail. The left picture is the front view, where the X_{BH} axis of the hip torso coordinate system is perpendicular to the paper surface. The right picture is a schematic plan view of the right front leg, the rotation axes of the hip pitch, knee pitch, and ankle pitch joints which are oriented perpendicular to the paper in. In addition, according to the right-hand rule, from the foot-end to the hip joint, the ankle pitch joint θ_4, knee pitch joint θ_3, hip pitch joint θ_2, and hip roll joint θ_1 are defined.

According to the given kinematic model of the quadruped robot, from the hip pitch coordinate system $\sum_{\text{BH}}$ to the foot-end coordinate system $\sum_{\text{Foot}}$, the homogeneous transformation matrix between the neighbouring link coordinate systems can be derived. Firstly, the homogeneous transformation matrix of the hip rolling coordinate system relative to the hip torso coordinate system is

$$\substack{BH \\ HipR}T = \begin{bmatrix} 1 & 0 & 0 & 0 \\ 0 & \cos(-\theta_1) & -\sin(-\theta_1) & 0 \\ 0 & \sin(-\theta_1) & \cos(-\theta_1) & 0 \\ 0 & 0 & 0 & 1 \end{bmatrix}. \tag{1}$$

The homogeneous transformation matrix of the hip pitch coordinate system relative to the hip rolling coordinate system is

$$\substack{HipR \\ HipP}T = \begin{bmatrix} \cos(\theta_2) & 0 & \sin(\theta_2) & 0 \\ 0 & 1 & 0 & -L_1 \\ -\sin(\theta_2) & 0 & \cos(\theta_2) & 0 \\ 0 & 0 & 0 & 1 \end{bmatrix}. \tag{2}$$

The homogeneous transformation matrix of the knee pitch coordinate system relative to the hip pitch coordinate system is

$$\substack{HipP \\ Knee}T = \begin{bmatrix} \cos(-\theta_3) & 0 & \sin(-\theta_3) & 0 \\ 0 & 1 & 0 & 0 \\ -\sin(-\theta_3) & 0 & \cos(-\theta_3) & -L_2 \\ 0 & 0 & 0 & 1 \end{bmatrix}. \tag{3}$$

The homogeneous transformation matrix of the ankle pitch coordinate system relative to the knee pitch coordinate system is

$$\substack{Knee \\ Ankle}T = \begin{bmatrix} \cos(\theta_4) & 0 & \sin(\theta_4) & 0 \\ 0 & 1 & 0 & 0 \\ -\sin(\theta_4) & 0 & \cos(\theta_4) & -L_3 \\ 0 & 0 & 0 & 1 \end{bmatrix}, \tag{4}$$

The homogeneous transformation matrix of the foot-end coordinate system relative to the ankle pitch coordinate system is

$$\substack{Ankle \\ Foot}T = \begin{bmatrix} 1 & 0 & 0 & 0 \\ 0 & 1 & 0 & 0 \\ 0 & 0 & 1 & -L_4 \\ 0 & 0 & 0 & 1 \end{bmatrix}. \tag{5}$$

At last, by integrating these transformation matrixes, the (6) and (7) can be derived

$$\substack{BH \\ Foot}T = \substack{BH \\ HipR}T \cdot \substack{HipR \\ HipP}T \cdot \substack{HipP \\ Knee}T \cdot \substack{Knee \\ Ankle}T \cdot \substack{Ankle \\ Foot}T, \tag{6}$$

$$
{}^{BH}_{Foot}T = \begin{bmatrix} c_{2-3+4} & 0 & s_{2-3+4} & -L_4 s_{2-3+4} - L_3 s_{2-3} - L_2 s_2 \\ -s_1 s_{2-3+4} & c_1 & s_1 c_{2-3+4} & -L_1 c_1 - (L_2 c_2 + L_3 c_{2-3} + L_4 c_{2-3+4}) s_1 \\ -c_1 s_{2-3+4} & -s_1 & c_1 c_{2-3+4} & L_1 s_1 - (L_2 c_2 + L_3 c_{2-3} + L_4 c_{2-3+4}) c_1 \\ 0 & 0 & 0 & 1 \end{bmatrix},
$$

$$(7)$$

where c_1 represents $\cos \theta_1$, s_1 represents $\sin \theta_1$, c_2 represents $\cos \theta_2$, c_{2-3} represents $\cos (\theta_2 - \theta_3)$, s_{2-3} represents $\sin (\theta_2 - \theta_3)$, c_{2-3+4} represents $\cos (\theta_2 - \theta_3 + \theta_4)$, and s_{2-3+4} represents $\sin (\theta_2 - \theta_3 + \theta_4)$.

Therefore, according to the positive kinematic analysis, in the case of the known joint angle $\theta_1, \theta_2, \theta_3, \theta_4$, the position and orientation of the foot-end relative to the hip torso coordinate system can be obtained. For calculating the inverse solution, the solvability should be considered for avoiding the no solution or multiple solutions. Usually, solving robot kinematic equations by the inverse operation is a nonlinear problem, and solving forward kinematic problems is to check whether the target point is in the working space. Therefore, for deciding the existence of the robot inverse kinematics solution, the robot leg's workspace should be calculated. For ensuring that the inverse kinematic is solvable, the foot of the quadruped robot must be within the workspace of the leg joint. According to the design index $\theta_1 \in [-20^\circ, 20^\circ]$, $\theta_2 \in [-50^\circ, 50^\circ]$, $\theta_3 \in [-120^\circ, 120^\circ]$, a series of coordinate points can be obtained with different joint angles. A point cloud map indicting the whole working space of the leg is shown in Figures 4 and 5.

For the solution of inverse kinematic problems, there are mainly two types of closed-form solutions (analytic solutions) and numerical solutions. In this paper, the closed solution method is used to solve the analytical solution. Because the quadruped robot has the same leg configuration, only the right front leg is considered to establish its inverse kinematics model. From equation (7), we can get

$$
{}^{BH}P_x^2 + {}^{BH}P_y^2 + {}^{BH}P_z^2 = L_1^2 + L_2^2 + L_3^2 + L_4^2 + 2L_2 L_3 \cos \theta_3 \\ + 2L_3 L_4 \cos \theta_4 + 2L_2 L_4 \cos (\theta_3 - \theta_4).
$$

$$(8)$$

Because of the parallelogram structure, it is structurally guaranteed that the (8) simplifies to

$$
{}^{BH}P_x^2 + {}^{BH}P_y^2 + {}^{BH}P_z^2 = L_1^2 + L_2^2 + L_3^2 + L_4^2 \\ + 2(L_2 L_3 + L_3 L_4) \cos \theta_3 + 2L_2 L_4.
$$

$$(9)$$

So, we can obtain

$$
\theta_3 = \theta_4 = \arccos \left(\frac{{}^{BH}P_x^2 + {}^{BH}P_y^2 + {}^{BH}P_z^2 - L_1^2 - L_2^2 - L_3^2 - L_4^2 - 2L_2 L_4}{2(L_2 L_3 + L_3 L_4)} \right).
$$

$$(10)$$

From equation (7), we get

$$
\frac{{}^{BH}P_y + L_1 \cos \theta_1}{{}^{BH}P_z + L_1 \sin \theta_1} = \frac{\sin \theta_1}{\cos \theta_1}.
$$

$$(11)$$

Further,

$$
\frac{-{}^{BH}P_z}{\sqrt{{}^{BH}P_y^2 + {}^{BH}P_z^2}} \sin \theta_1 - \frac{-{}^{BH}P_y}{\sqrt{{}^{BH}P_y^2 + {}^{BH}P_z^2}} \cos \theta_1 \\ = \frac{-L_1}{\sqrt{{}^{BH}P_y^2 + {}^{BH}P_z^2}}.
$$

$$(12)$$

So,

$$
\theta_1 = \arcsin \frac{-L_1}{\sqrt{{}^{BH}P_y^2 + {}^{BH}P_z^2}} + \arctan \frac{{}^{BH}P_y}{{}^{BH}P_z}.
$$

$$(13)$$

From equation (7), we can also get

$$
{}^{BH}P_x = -(L_4 + L_2 + L_3 \cos \theta_3) \sin \theta_2 + L_3 \sin \theta_3 \cos \theta_2.
$$

$$(14)$$

Since θ_3 has been given by equation (10), so

$$
\theta_2 = \arcsin \frac{{}^{BH}P_x}{\sqrt{(L_4 + L_2 + L_3 \cos \theta_3)^2 + (L_3 \sin \theta_3)^2}} \\ + \arctan \frac{L_3 \sin \theta_3}{L_4 + L_2 + L_3 \cos \theta_3}.
$$

$$(15)$$

Formula (10), formula (13), and formula (15) are the inverse kinematic equations of the leg, and the inverse solution is the only solution. Thus, if we know the coordinates of the foot-end of any leg in the hip joint body coordinate system, we can solve the requirement of each joint angle.

2.2. *Velocity Jacobian Matrix.* In this section, the velocity Jacobian matrix is derived which is useful for further leg control such as the transformation of forces and torques from the foot-end to the joints. The definition of the Jacobian matrix is as follows:

$$
J = \begin{bmatrix} \dfrac{\partial {}^{BH}P_x}{\partial \theta_1} & \dfrac{\partial {}^{BH}P_x}{\partial \theta_2} & \dfrac{\partial {}^{BH}P_x}{\partial \theta_3} \\ \dfrac{\partial {}^{BH}P_y}{\partial \theta_1} & \dfrac{\partial {}^{BH}P_y}{\partial \theta_2} & \dfrac{\partial {}^{BH}P_y}{\partial \theta_3} \\ \dfrac{\partial {}^{BH}P_z}{\partial \theta_1} & \dfrac{\partial {}^{BH}P_z}{\partial \theta_2} & \dfrac{\partial {}^{BH}P_z}{\partial \theta_3} \end{bmatrix}.
$$

$$(16)$$
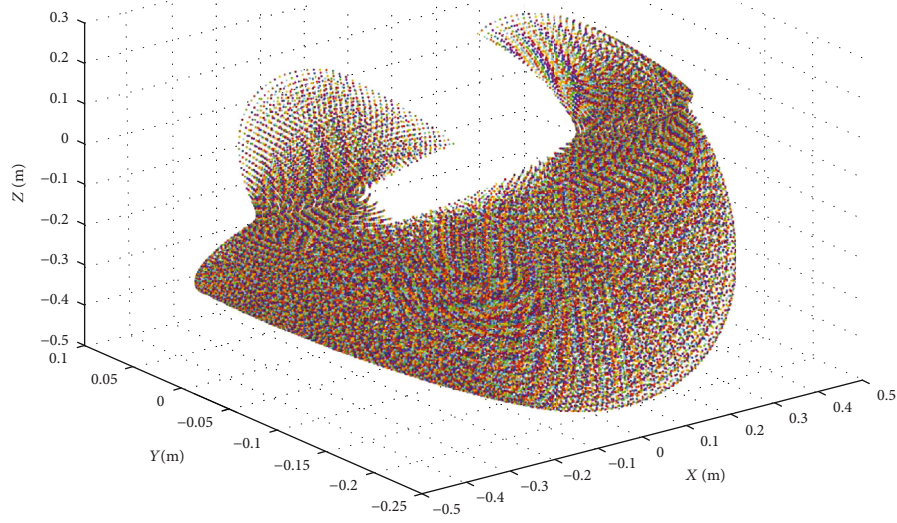
FIGURE 4: 3D workspace point map of one leg.
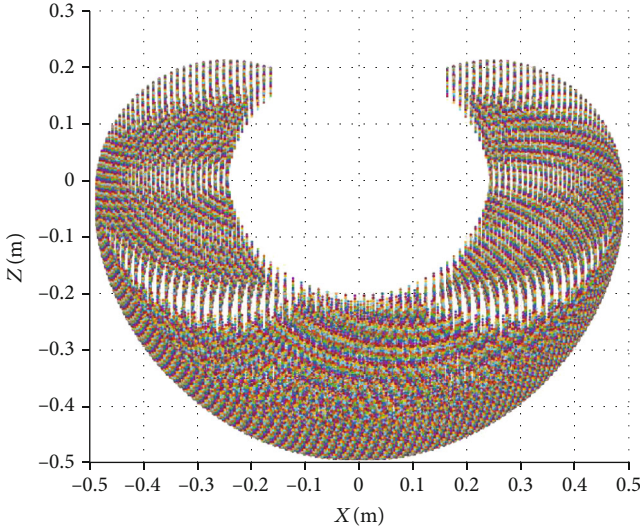
FIGURE 5: $X_{\mathrm{HipR}}Z_{\mathrm{HipR}}$-plane workspace point map.

TABLE 1: The twelve control points of the Bézier curve.

	x (mm)	y (mm)
c_0	-170	460
c_1	-280.5	460
c_2	-300	361.1
c_3	-300	361.1
c_4	-300	361.1
c_5	0	361.1
c_6	0	361.1
c_7	0	321.4
c_8	303.2	321.4
c_9	303.2	321.4
c_{10}	282.6	460
c_{11}	170	460

Then, according to the equation of positive kinematics, the Jacobian matrix of the velocity from the leg joint coordinates to the foot can be obtained as

$$
J = \begin{bmatrix} 0 & l_2 c_2 + l_3 c_{23} & l_3 c_{23} \\ l_1 s_1 + l_2 c_1 c_2 + l_3 c_1 c_{23} & -s_1(l_3 s_{23} + l_2 s_2) & -l_3 s_1 s_{23} \\ -l_1 c_1 + l_2 s_1 c_2 + l_3 s_1 c_{23} & c_1(l_3 s_{23} + l_2 s_2) & l_3 c_1 s_{23} \end{bmatrix}.
\tag{17}
$$

2.3. *Foot-End Trajectory Planning.* For obtaining better performance of the robot, we should design the foot-end trajectory properly. During the swing phase, the leg is not affected by contact force, so a higher speed and acceleration can be achieved. During the stance phase, the exten-

sive loadings will be added on the legs; it will cause a great rigid impact with only position control. Since the swing phase and the stance phase have different dynamic characteristics, the trajectories of the two phases are designed individually.

Later, for tracking the trajectory, two control methods will be compared which are position control and impedance control.

The swing-phase trajectories are designed from a Bézier curve defined by twelve control points, and stance-phase trajectories are designed as part of sinusoidal wave which has a good performance in smoothness and was also used in other robots [17].

2.3.1. *Trajectory Design for the Swing Phase.* The swing-phase trajectory design should guarantee enough ground clearance for avoiding obstacles and reduce energy losses
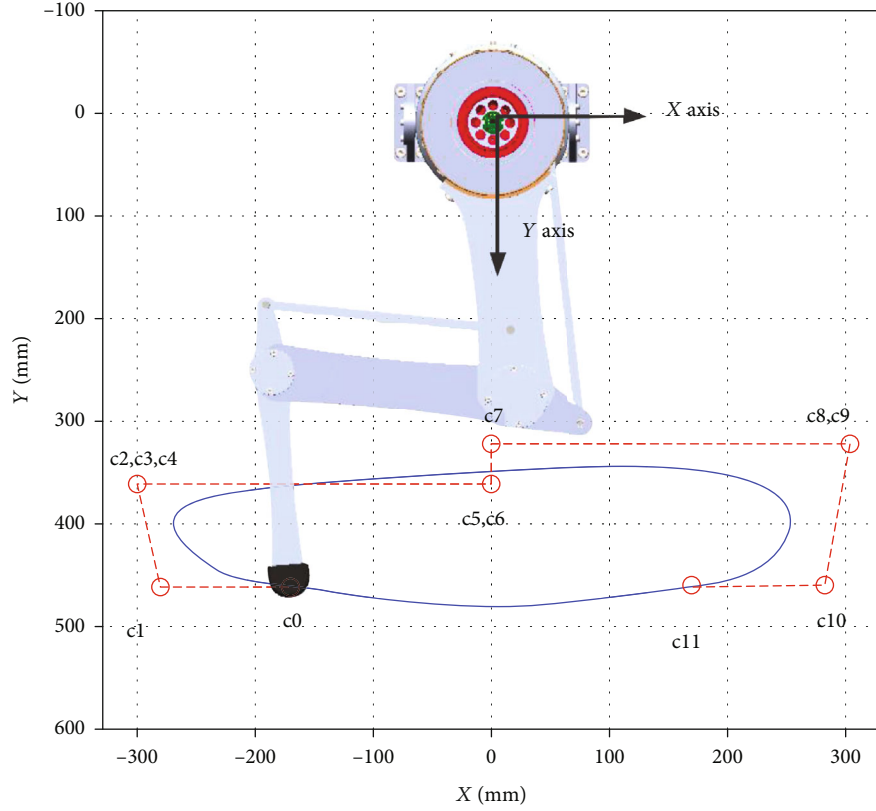
FIGURE 6: The desired trajectory decided by 12 control points of the Bézier curve.
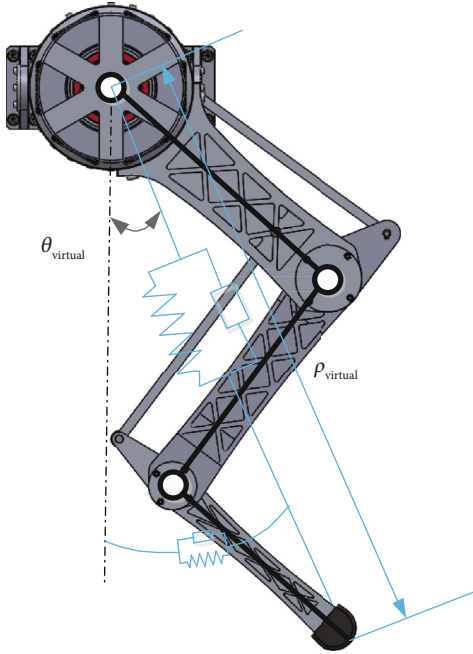
FIGURE 7: Virtual impedance model of the leg.

during touchdown motion [18]. The design of the swing-phase trajectory should not only approximate the natural behaviour of the leg but also satisfy ground clearance,

which can avoid obstacles in the swing phase. The Bézier curve formula determined by the normalization parameter $S^{SW}(t) \in [0, 1]$ is

$$p^{sw}(t) = p^{sw}(S^{sw}(t)) = \sum_{k=0}^{n} C_n^k (1 - S^{sw})^{n-k} (S^{sw})^k c_k,$$

$$v^{sw}t = \frac{dp^{sw}}{dS^{sw}} \frac{dS^{sw}}{dt} = \frac{dp^{sw}}{dS^{sw}} \frac{1}{T_{sw}}, \quad (18)$$

where C_n^k represents the number of unordered collection in which k elements are taken from n elements, $(n + 1)$ is the number of control points, c_k is a kth two-dimensional control point where $k \in \{0, \cdots\cdots, 11\}$. The curve can be generated by twelve control points as shown in Table 1, and the trajectory shape is shown in Figure 6.

2.3.2. Trajectory Design for the Stance Phase. The stance-phase control of each leg will affect the performance of quadruped locomotion via interaction with the ground. Therefore, the planned trajectory should not only consider the motion requirements but also the interactive force requirements.

The stance-phase trajectory is proposed to simply as a sinusoidal wave with two parameters: the half of the stroke length L_{span}, and the amplitude variable δ. As with the swing
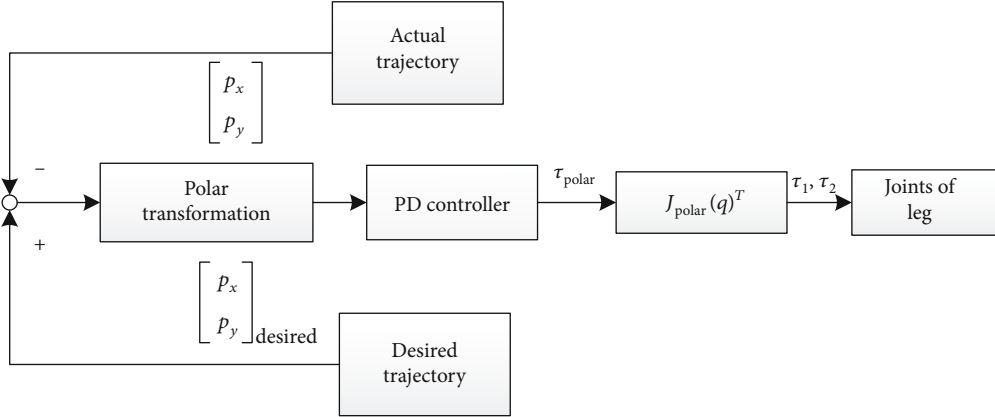
FIGURE 8: Block diagram for impedance controller.

phase, the stance-phase trajectory equation is also determined by the normalized parameters, $S^{st} \in [0,1]$

$$p_x^{st}(t) = L_{span}\left(1 - 2S^{st}(t)\right) + P_{0,x},$$

$$p_y^{st}(t) = \delta \cos\left(\frac{\pi}{2L_{span}}p_x^{st}(t)\right) + P_{0,y},$$

$$v_x^{st}(t) = \frac{dp_x^{st}}{dS^{st}}\frac{dS^{st}}{dt} = -\frac{2L_{span}}{T_{st}},$$

$$v_y^{st}(t) = \frac{dp_y^{st}}{dp_x^{st}}\frac{dp_x^{st}}{dt} = \frac{\delta\pi}{T_{st}} \sin\left(\frac{\pi}{2L_{span}}p_x^{st}(t)\right). \tag{19}$$

Considering that the robot's leg will touch the ground and bear an impact, therefore, an impedance control should be used to resist the impact during the stance phase and will be introduced in the next part.

2.4. Impedance Controller Design. In the previous section, we discussed the planning for robot's foot-end trajectory. If the robot has no contact with the external environment, pure motion control is enough for trajectory tracking. However, quadruped robots are high dynamic robots that their feet will contact the ground frequently during the movement. In this case, the space constraint brought by the environment will hinder the tracking movement of the robot end effector. Therefore, for ensuring the compliance during the movement, the impedance control is used where the leg will be imitating mass, spring, and damper properties. Based on this, the robot will present virtual mass, stiffness, and damping characteristics during movement [4].

A schematic diagram of a one-dimensional mass-damping-spring model is shown in Figure 7. Impedance is used to describe the behavior of a robot. Different impedance parameters can be set to give different dynamic characteristics of the robot.

The dynamics for a one-dof robot rendering an impedance can be written

$$m\ddot{x} + b\dot{x} + kx = f, \tag{20}$$
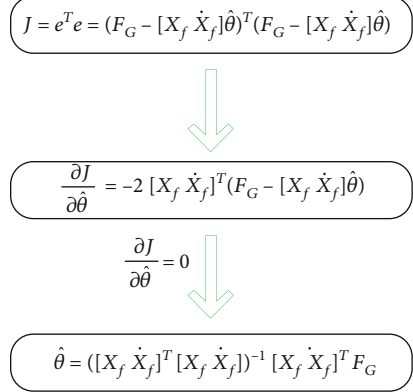
FIGURE 9: Derivation block diagram of the least-squares method.

where x is the position, m is the mass, b is the damping, k is the stiffness, and f is the force applied by the user. If b or k in the impedance coefficient is set to be large, it is called high impedance; if b or k is set small, it becomes low impedance. In this paper, virtual leg impedance is created in the polar coordinate as shown in Figure 7.

The control formula can be derived as

$$f_{control} - f_{est} = m(\ddot{x}_d - \ddot{x}) + b(\dot{x}_d - \dot{x}) + k(x_d - x), \tag{21}$$

where $f_{control}$ is the control force sent to the controller; f_{est} is the estimated ground reaction force; $\ddot{x}_d, \dot{x}_d, x_d$ are desired acceleration, velocity, and position; and $\ddot{x}, \dot{x}, x$ are actual acceleration, velocity, and position. Considering that the virtual mass has no significant effect on the impedance effect of the robot's legs, no virtual mass term is added to the control algorithm in this paper.

The Jacobian from the hip/shoulder to foot-end in the polar coordinate system is obtained by the transformation. The position relationship between the Cartesian coordinate system and the polar coordinate system is

$$\begin{bmatrix} \rho_{virtual} \\ \theta_{virtual} \end{bmatrix} = \begin{bmatrix} \sqrt{x^2 + y^2} \\ \arctan(x/y) \end{bmatrix}. \tag{22}$$

(a)   (b)
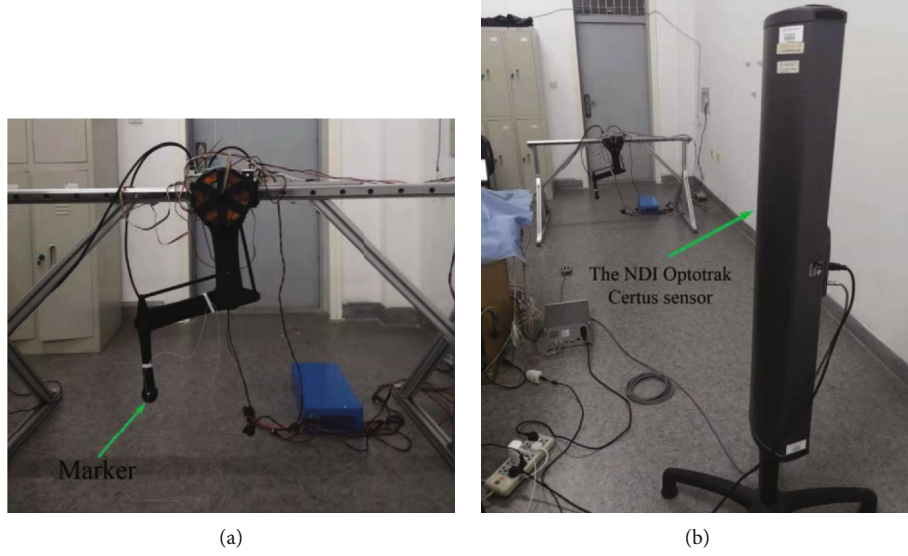
FIGURE 10: Experimental platform. (a) One leg experimental platform. (b) Trajectory measurement with the NDI Optotrak Certus sensor.
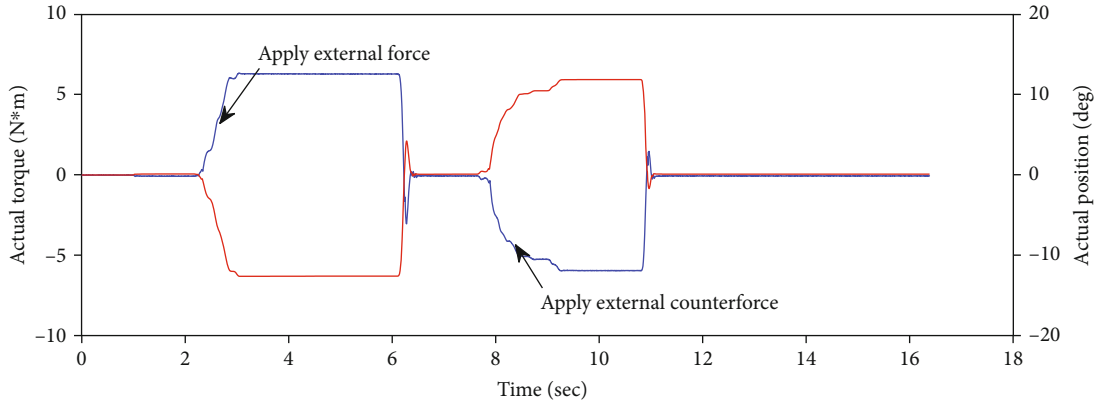
FIGURE 11: The actual torque and position of the hip joint change after applying force.

So the Jacobian from the Cartesian coordinate system to the polar coordinate system is

$$J_{\mathrm{polar}}(x, y) = \begin{bmatrix} \dfrac{x}{\sqrt{x^2 + y^2}} & \dfrac{y}{\sqrt{x^2 + y^2}} \\ \dfrac{1}{y(x^2/y^2 + 1)} & \dfrac{-x}{y^2(x^2/y^2 + 1)} \end{bmatrix}. \tag{23}$$

Then, impedance control law can be derived as

$$\begin{bmatrix} \tau_1 \\ \tau_2 \end{bmatrix} = J_{\mathrm{polar}}(q)^T \begin{bmatrix} k_\rho e_\rho + b_\rho \dot{e}_\rho \\ k_\theta e_\theta + b_\theta \dot{e}_\theta \end{bmatrix}, \tag{24}$$

where e_ρ, $\dot{e}_\rho$, e_θ, and $\dot{e}_\theta$ are radial position error, radial velocity error, angular position error, and angular velocity error between the actual trajectory with designed trajectory, respectively. $J_{\mathrm{polar}}(q)$ is the Jacobian from hip/shoulder to foot-end in the polar coordinate system, and $J_{\mathrm{polar}}(q) =$

$J_{\mathrm{polar}}(x, y)J_{\mathrm{Cartesian}}(q)$. And the block diagram for the impedance controller can be shown in Figure 8.

2.5. Ground Compliance Estimation.
For the above analysis, we assumed that the ground is completely rigid, but for a real application, the assumption is limited. For example, if the robot is moving on a concrete floor or an asphalt road, we can think that the assumption is completely valid. But when the robot moves in an environment like grass, marshes, and snow, there will be a big difference. Therefore, the identification of ground compliance is important. Through the system identification method, we can get the stiffness and damping characteristics of the contact ground, and then, further operations to achieve the corresponding impedance characteristics can be implemented.

Among the system identification theory, the least-squares method is widely used, and the effect is also excellent. Therefore, we use the least-squares method to estimate the ground compliance parameters.
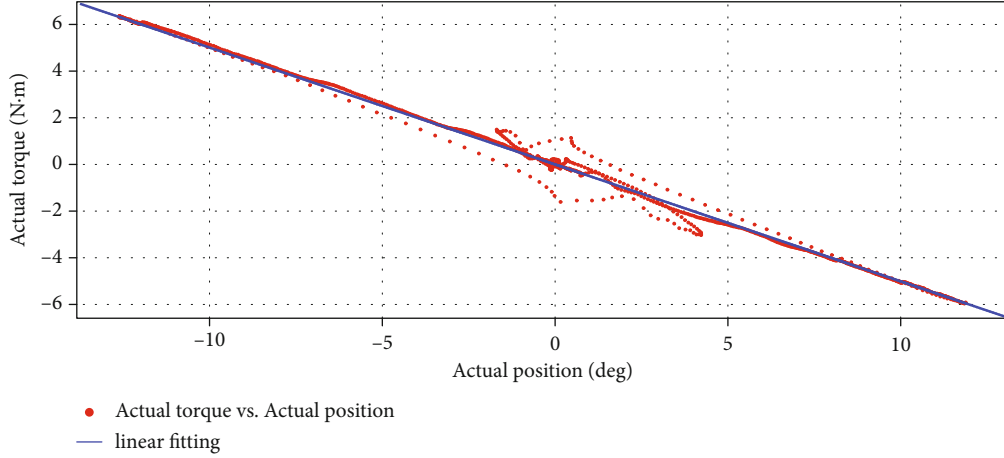
FIGURE 12: The actual torque change with the position of the hip joint and the fitting straight line.
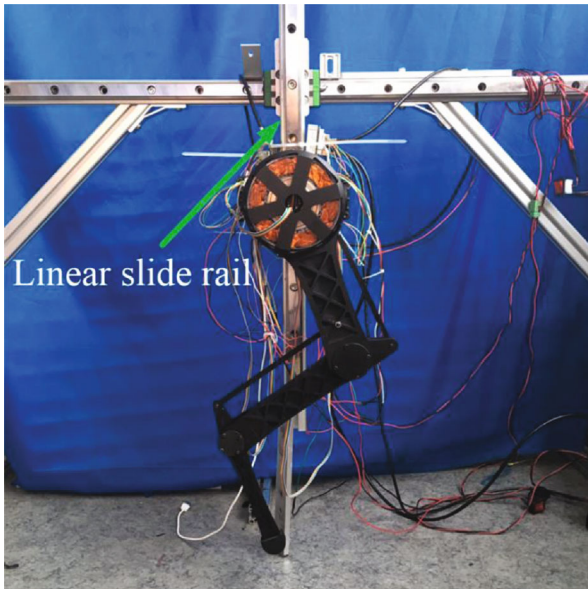
FIGURE 13: Diagram of free dropping apparatus of the single-leg prototype.

Taking into account the storage performance and computational performance of industrial controllers, we estimate the ground parameters using the least squares method in limited memory, which limit the estimated range. The ground reaction force (GRF) is described as

$$f_G = k_G x_f + b_G \dot{x}_f, \tag{25}$$

where k_G and b_G are ground stiffness and damping coefficients; that is, the values we need to identify by the system identification x_f and f_G are the depth and the ground reaction force. Then, we can estimate the ground parameters by the least squares method in limited memory.

At every time instant n, we gather samples from the previous k time instances and compute the ground parameters. By choosing the appropriate k value, i.e., the defined range,

a good parameter estimate can be obtained and the data saturation phenomenon can be effectively improved.

To implement the estimation of parameters, we construct the following dataset

$$F_G = [f_G(n)f_G(n-1) \cdots f_G(n-k)]^T,$$
$$X_f = [x_f(n)x_f(n-1) \cdots x_f(n-k)]^T, \tag{26}$$
$$\dot{X}_f = [\dot{x}_f(n)\dot{x}_f(n-1) \cdots \dot{x}_f(n-k)]^T.$$

By estimating $\widehat{\theta}$ and $\widehat{F}_G$ as the optimal estimate of $\theta = [k_G \ b_G]^T$ and F_G, we can get

$$\widehat{F}_G = \begin{bmatrix} X_f & \dot{X}_f \end{bmatrix} \widehat{\theta}. \tag{27}$$

Then, by defining $e = F_G - \widehat{F}_G$ and $J = e^T e$, and from that, the least-squares estimation requires that the sum of the squares of the residuals be the smallest; we can obtain the parameters as shown in Figure 9.

Moreover, considering that recent samples make more great impact on the results, we use a weighting matrix $Q \in \mathbb{R}^{k \times k}$ to penalize the error on most recent sample compared to the less recent ones and thus, giving more importance to the most recent samples. And the result is

$$\widehat{\theta} = \left(\begin{bmatrix} X_f & \dot{X}_f \end{bmatrix}^T Q \begin{bmatrix} X_f & \dot{X}_f \end{bmatrix} \right)^{-1} \begin{bmatrix} X_f & \dot{X}_f \end{bmatrix}^T F_G. \tag{28}$$

According to the estimates $\widehat{\theta} = [\widehat{k}_G \quad \widehat{b}_G]^T$, we can acquire

$$\widehat{f}_G = \widehat{k}_G x_f + \widehat{b}_G \dot{x}_f. \tag{29}$$
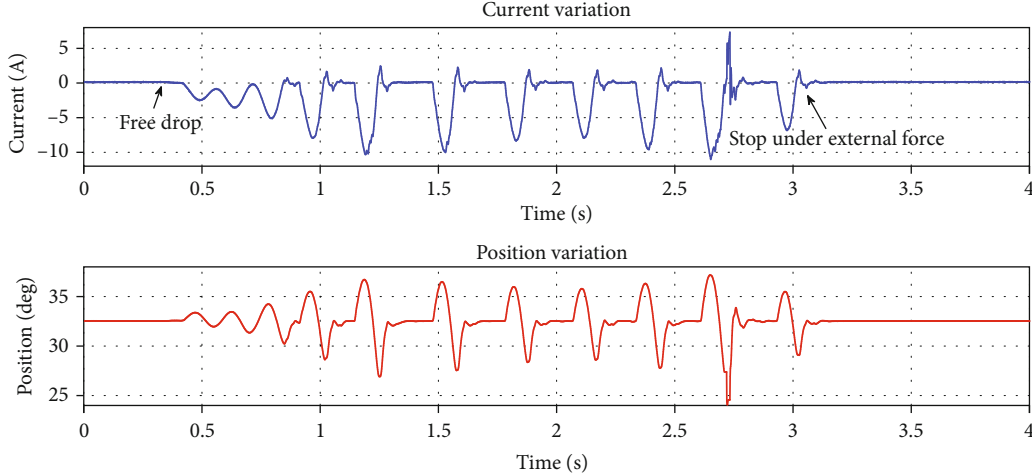
FIGURE 14: The current and position variation of the knee motor under pure position control.

TABLE 2: Comparison between pure position control and impedance control.

Control mode	Stability	Position steady-state error (deg)	Peak current (A)	Compliance
Impedance control	Stable	11.4	4.309	Soft
Position control	Unstable	—	11.03	Hard
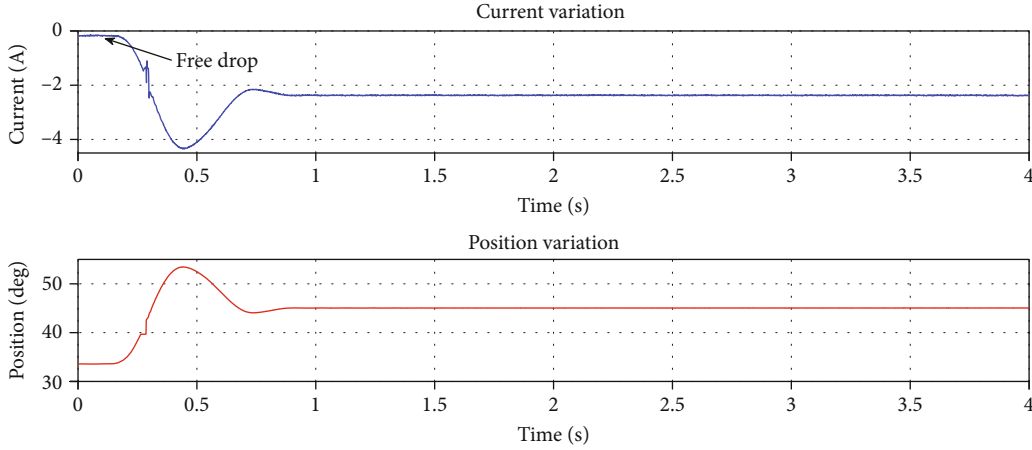
FIGURE 15: The current and position variation of the knee motor under impedance control.

Then, in the stance phase, for getting better impedance characteristics for the robot, we apply this force to the impedance control formula (21), and we can get

$$f_{\text{control}} - \widehat{f}_G = m(\ddot{x}_d - \ddot{x}) + b(\dot{x}_d - \dot{x}) + k(x_d - x). \quad (30)$$

By the least-squares estimation method with limited memory and fading memory for ground parameters, we reasonably introduced the estimated value of GRF. Applying the estimated GRF to the f_{desired} impedance controller, the value will change with different ground conditions, allowing the robot to adapt to different ground conditions with suitable compliance.

3. Experimental Results

3.1. Foot-End Trajectory Experiment. For ensuring that the robot can well perform the planned motion characteristics, an experiment was carried out to verify the robot's performance of foot-end trajectory tracking.

The experimental platform was constructed as shown in Figure 10. The NDI Optotrak Certus was used to trace the presticked marker on the endpoint of the leg, and the actual trajectories can be obtained. The accuracy that NDI Optotrak Certus can achieve is 0.01 mm and its sampling frequency is 100 Hz, which is sufficient for our trajectory following the acquisition.

Because the data collected by the NDI Optotrak Certus is three-dimensional coordinates of a point on its body, and the trajectory points we plan are the two-dimensional coordinates with the axis of the hip joint motor as the origin; it is necessary to compare the trajectories after the coordinate transformation.

The first step is to find the homogeneous transformation matrix $^{O}T_{A}$ from the NDI Optotrak Certus coordinate system A to the robot coordinate system O.

In the coordinate system O, four scattered coordinate points were selected that the foot-end of the robot can reach. Suppose the leg motion is strictly in a plane, and $z = 0$, then assume that the coordinates of the selected four points are $(^{O}x_{1}, ^{O}y_{1}, ^{O}z_{1})$, $(^{O}x_{2}, ^{O}y_{2}, ^{O}z_{2})$, $(^{O}x_{3}, ^{O}y_{3}, ^{O}z_{3})$, and $(^{O}x_{4}, ^{O}y_{4}, ^{O}z_{4})$.

Simultaneously, the four points are collected by the NDI Optotrak Certus, and the coordinates under frame A are $(^{A}x_{1}, ^{A}y_{1}, ^{A}z_{1})$, $(^{A}x_{2}, ^{A}y_{2}, ^{A}z_{2})$, $(^{A}x_{3}, ^{A}y_{3}, ^{A}z_{3})$, and $(^{A}x_{4}, ^{A}y_{4}, ^{A}z_{4})$.

So

$$\begin{bmatrix} ^{O}x_{1} \\ ^{O}y_{1} \\ ^{O}z_{1} \\ 1 \end{bmatrix} = {}^{O}T_{A} \begin{bmatrix} ^{A}x_{1} \\ ^{A}y_{1} \\ ^{A}z_{1} \\ 1 \end{bmatrix}. \tag{31}$$

After making the same transformation of all four coordinates and transforming the final matrix equation appropriately, we can get

$$^{O}T_{A} = \begin{bmatrix} ^{O}x_{1} & ^{O}x_{2} & ^{O}x_{3} & ^{O}x_{4} \\ ^{O}y_{1} & ^{O}y_{2} & ^{O}y_{3} & ^{O}y_{4} \\ ^{O}z_{1} & ^{O}z_{2} & ^{O}z_{3} & ^{O}z_{4} \\ 1 & 1 & 1 & 1 \end{bmatrix} \cdot \begin{bmatrix} ^{A}x_{1} & ^{A}x_{2} & ^{A}x_{3} & ^{A}x_{4} \\ ^{A}y_{1} & ^{A}y_{2} & ^{A}y_{3} & ^{A}y_{4} \\ ^{A}z_{1} & ^{A}z_{2} & ^{A}z_{3} & ^{A}z_{4} \\ 1 & 1 & 1 & 1 \end{bmatrix}^{-1}. \tag{32}$$

After finding the homogeneous transformation matrix $^{O}T_{A}$, the points collected by the NDI Optotrak Certus are homogeneously transformed to obtain the actual trajectory in the O coordinate system and compared with the planned trajectory.

3.2. Impedance Control Experiment.
For the experiment, the impedance control is based on the control in the torque mode. Therefore, the controller should first be switched to the torque mode at first. In our study, the controller (C6015, Beckhoff) was chosen with EtherCAT connection to each motor.

We observed the relationship between the real-time position, the real-time torque, and time by applying external torque to the hip joint, as shown in Figure 11. Then, we fit the torque position and get the result as shown in Figure 12.
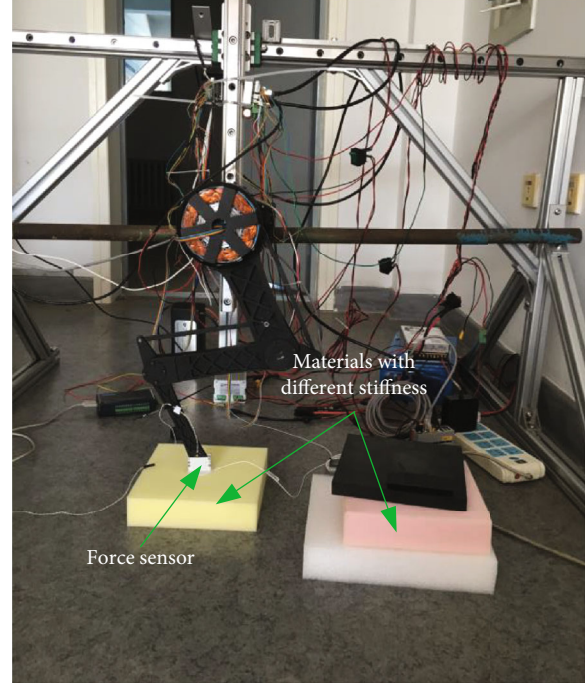
FIGURE 16: Diagram of the identification of various ground materials.

And the fitting equation is

$$y = -0.501x - 0.0003333. \tag{33}$$

3.3. Comparison between Pure Position Control and Impedance Control.
As we know, the essence of impedance control is to control the dynamic relationship between force and position. The pure position control is mainly to achieve an accurate position and does not consider the interaction with the outside world. To better understand impedance control and pure position control, we have done experiments to compare the characteristics of the two control methods. According to the characteristics of the two control methods, we can determine which way is more suitable in the locomotion of the quadruped robot.

In the previous analysis, we have also seen that in the swing phase, since the foot-end point of the single-leg prototype has no contact with the ground, the effects of impedance control and pure position control are similar. But in the stance phase, the foot-end point of the single-leg prototype contacts the ground, and there will be a large impact at the moment of contact. If the control strategy does not have a certain cushioning effect, it will be harmful to the motor. Therefore, it is necessary to test and analyse the control effect of pure position control and impedance control.

As shown in Figure 13, the experimental procedure is to set a fixed desired position through the impedance control and pure position control in the single-leg prototype in the suspended state (here, the desired force in the impedance control is set to 0). Then, at a certain height, the single-leg prototype was dropped freely, and the current and position change of the single-leg prototype motor were observed.
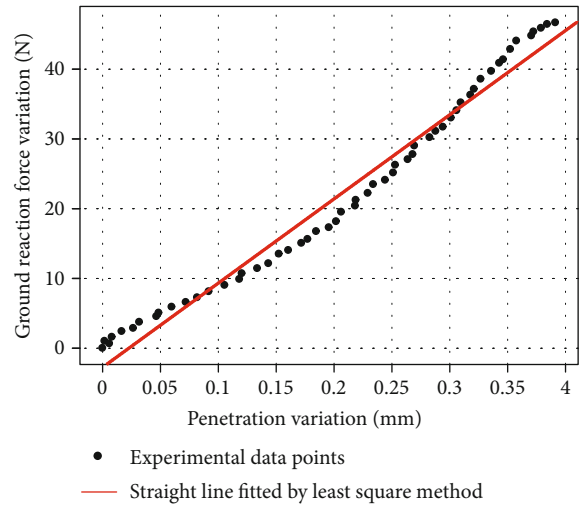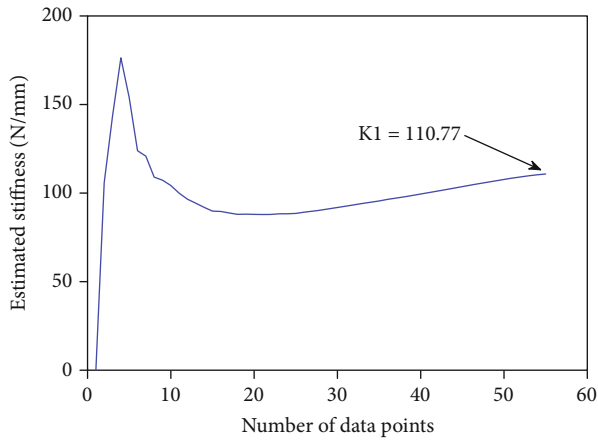
(a)
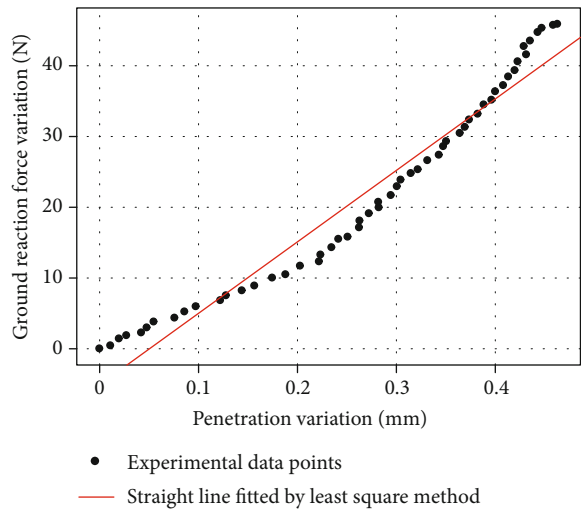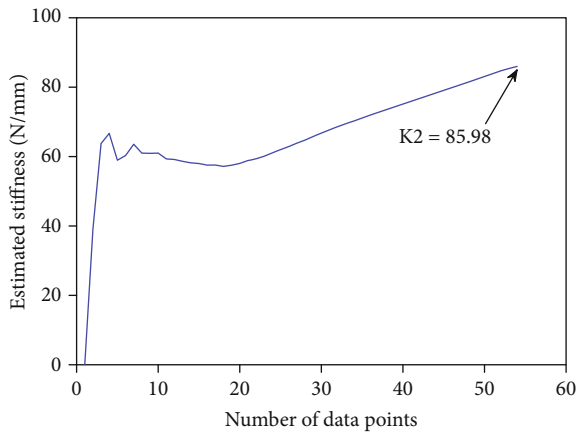
(b)
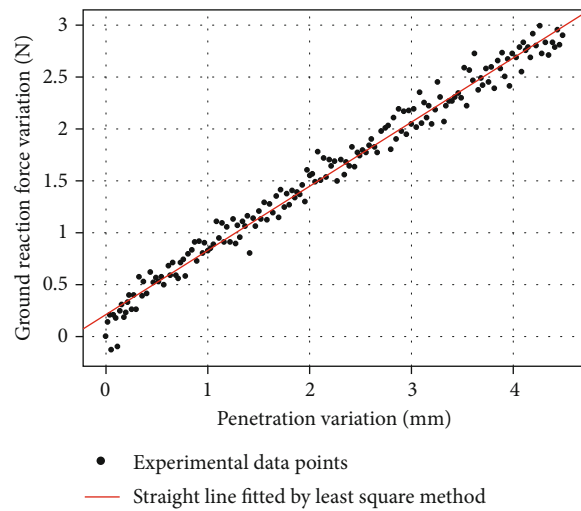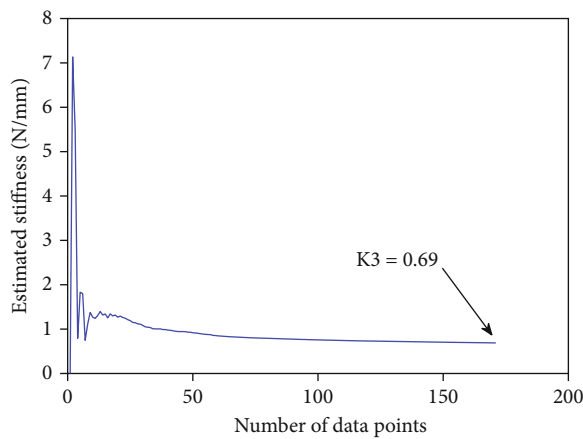
(c)

Figure 17: Continued.

(d)

(e)
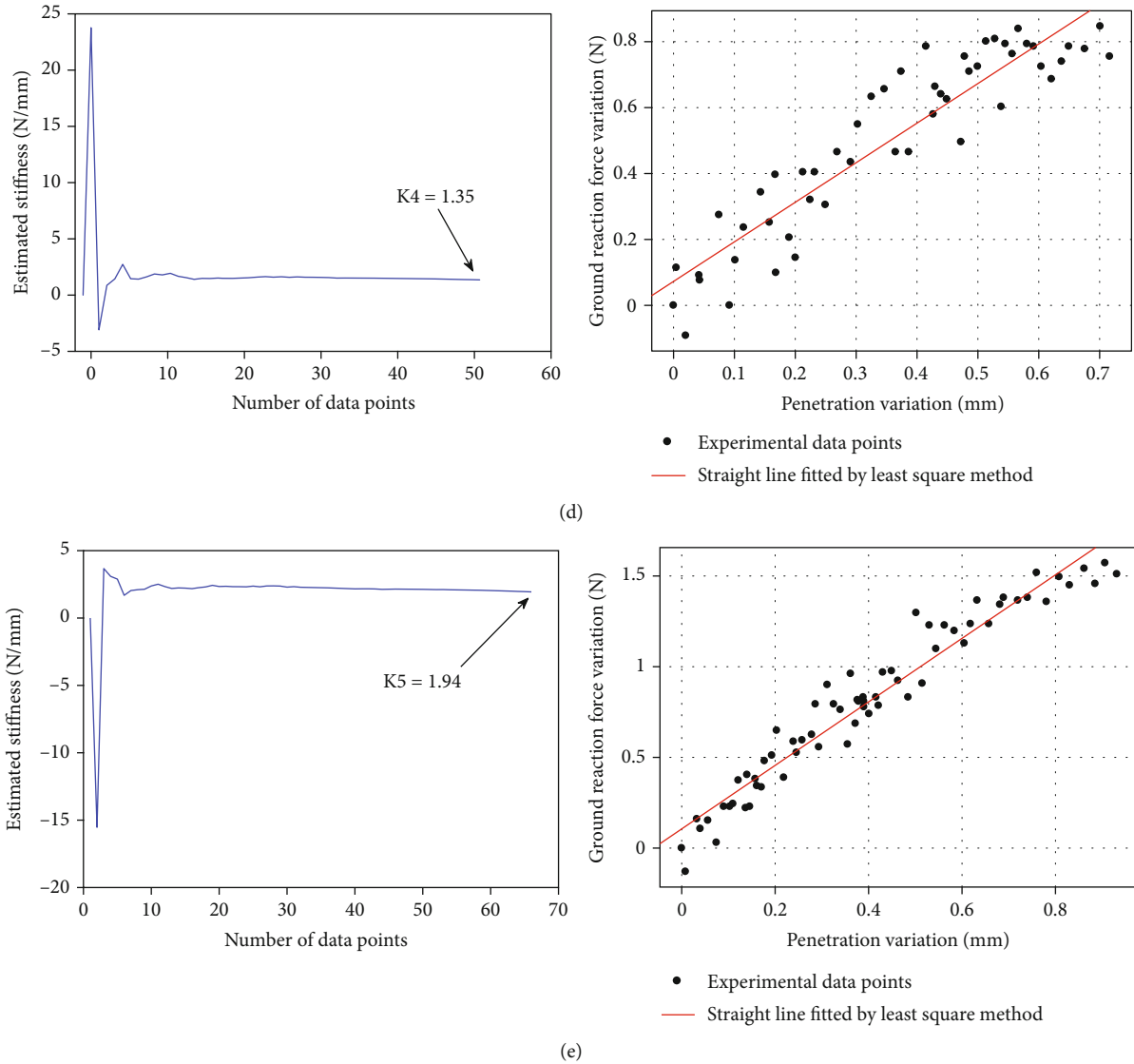
FIGURE 17: The recursive change process of stiffness and the fitting straight line. (a) Medium hard rubber. (b) High durometer rubber. (c) Low hardness sponge. (d) Medium hardness sponge. (e) High hardness sponge.

It should be noted that the drop height under the impedance control is 44 mm. Therefore, in the pure position control, the drop height was also set to 44 mm at first, but it is impossible to collect appropriate experimental data with high impact. At last, the drop height was determined to be 10 mm. In addition, through the data measurement and analysis of the two joint motors, the variation of current and position values of the hip motor during the falling process is not particularly obvious. Therefore, we did not collect the data on hip joint motor, but only current and position acquisition of the knee motor.

By analyzing the experimental data in Figure 14, we can know that in the pure position control, even if it drops from a height of 10 mm, the position and current value of the motor show a tendency to disperse, that is, an unstable state. And the peak current during the whole process is 11.03 A as shown in Table 2. In the final stage, to avoid serious damage

to the motor and the outside world, it is necessary to add external force to force the single-leg prototype to stop beating.

In the impedance control as shown in Figure 15, we can see that although the drop height is 44 mm, which is 4.4 times in the above example, the peak current during the whole drop process is only 4.309 A as shown in Table 2, which effectively solves the impact on the motor during the dropping process.

3.4. Ground Compliance Identification. Through the previous analysis, we set up the corresponding experiments to identify the stiffness of the ground of various materials.

A portion of the experimental setup is similar to the previous motion control experiment where the motion capture system is used to capture the depth of the foot into the material. Since the stiffness is defined as the force acting on the unit displacement, it is also necessary to place a force sensor

as shown in Figure 16 at the foot-end to measure the ground reaction force when the foot-end is in contact with the ground.

The experimental procedure consists of designing a control program that allows the foot-end point of the single-leg prototype to move vertically downward from above the ground material and penetrate the material, and the NDI Optotrak Certus and the force sensor collect the displacement and force information of the foot-end in real-time. Then, by observing the data of the collected foot-end force, we can judge the moment when the foot-end is in contact with the material, and then based on the displacement information at that moment, the penetration value data of the foot-end is obtained. With the penetration value and the foot-end force information, the stiffness of various ground materials can be identified by the recursive least squares method.

In the experiment, we selected five different materials, namely, material 1 is medium hardness rubber, material 2 is reinforced rubber, material 3 is low hardness sponge, material 4 is medium hardness sponge, and material 5 is high hardness sponge. The stiffness of the above five materials was obtained by the above experimental method, as shown in Figure 17.

4. Conclusion

Locomotion adaption for quadruped robots with ground compliance estimation is important, especially for high-speed locomotion. In this paper, the Cartesian coordinates of the foot-end are obtained through trajectory planning, and then the virtual polar coordinates in the impedance control are obtained through geometric transformation. The deviation from the planned and actual virtual polar coordinates and the expected force recognized by the ground identification system is sent to the impedance controller. The desired foot-end force is obtained and then the joint torque is obtained by the change of the Jacobian matrix and sent to the robot system. The status of the robot system is also fed back to the previous process. At last, several experiments are carried out for evaluating the performance including the ground compliance identification, the motion control and the comparison between pure position control and impedance control. In the future, the prosed control framework will be used on our quadruped robots for testing the robust when traversing on a wide variety of terrains.

Data Availability

All data were experimentally obtained.

Conflicts of Interest

The authors declare that there is no conflict of interest regarding the publication of this paper.

Acknowledgments

References

[1] J. Hwangbo, J. Lee, A. Dosovitskiy et al., "Learning agile and dynamic motor skills for legged robots," *Science Robotics*, vol. 4, no. 26, pp. 1–13, 2019.

[2] R. Orsolino, M. Focchi, S. Caron et al., "Feasible region: an actuation-aware extension of the support region," *IEEE Transactions on Robotics*, vol. 36, no. 4, pp. 1239–1255, 2020.

[3] L. Ding, H. Gao, Z. Deng et al., "Foot-terrain interaction mechanics for legged robots: Modeling and experimental validation," *The International Journal of Robotics Research*, vol. 32, no. 12, pp. 1585–1606, 2013.

[4] P. M. Wensing, A. Wang, S. Seok, D. Otten, J. Lang, and S. Kim, "Proprioceptive actuator design in the MIT cheetah: impact mitigation and high-bandwidth physical interaction for dynamic legged robots," *IEEE Transactions on Robotics*, vol. 33, no. 3, pp. 509–522, 2017.

[5] X. Zeng, S. Zhang, H. Zhang, X. Li, H. Zhou, and Y. Fu, "Leg trajectory planning for quadruped robots with high-speed trot gait," *Applied Sciences*, vol. 9, no. 7, p. 1508, 2019.

[6] M. Hutter, C. Gehring, D. Jud et al., "ANYmal - a highly mobile and dynamic quadrupedal robot," in *2016 IEEE/RSJ International Conference on Intelligent Robots and Systems (IROS)*, pp. 38–44, Daejeon, South Korea, 2016.

[7] X. Li, H. Zhou, H. Feng, S. Zhang, and Y. Fu, "Design and experiments of a novel hydraulic wheel-legged robot (WLR)," in *2018 IEEE/RSJ International Conference on Intelligent Robots and Systems (IROS)*, pp. 3292–3297, Madrid, Spain, 2018.

[8] X. Li, H. Zhou, S. Zhang, H. Feng, and Y. Fu, "WLR-II, a hose-less hydraulic wheel-legged robot," in *2019 IEEE/RSJ International Conference on Intelligent Robots and Systems (IROS)*, pp. 4339–4346, Macau, China, China, 2019.

[9] M. Raibert, K. Blankespoor, G. Nelson, and R. Playter, "Big-dog, the rough-terrain quadruped robot," *IFAC Proceedings Volumes*, vol. 41, no. 2, pp. 10822–10825, 2008.

[10] S. Seok, A. Wang, D. Otten, and S. Kim, "Actuator design for high force proprioceptive control in fast legged locomotion," in *2012 IEEE/RSJ International Conference on Intelligent Robots and Systems*, pp. 1970–1975, Vilamoura, Portugal, 2012.

[11] N. Hu, S. Li, D. Huang, and F. Gao, "Crawling gait planning for a quadruped robot with high payload walking on irregular terrain," *IFAC Proceedings Volumes*, vol. 47, no. 3, pp. 2153–2158, 2014.

[12] C. Semini, V. Barasuol, J. Goldsmith et al., "Design of the hydraulically actuated, torque-controlled quadruped robot HyQ2Max," *IEEE/ASME Transactions on Mechatronics*, vol. 22, no. 2, pp. 635–646, 2017.

[13] S. Jung, T. C. Hsia, and R. G. Bonitz, "Force tracking impedance control of robot manipulators under unknown environment," *IEEE Transactions on Control Systems Technology*, vol. 12, no. 3, pp. 474–483, 2004.

[14] D. Kim, S. Jorgensen, J. Lee, J. Ahn, J. Luo, and L. Sentis, "Dynamic locomotion for passive-ankle biped robots and

humanoids using while-body locomotion control," 2019, https://arxiv.org/abs/1901.08100.

[15] M. Neunert, M. Stauble, M. Giftthaler et al., "Whole-body nonlinear model predictive control through Contacts for quadrupeds," *IEEE Robotics and Automation Letters*, vol. 3, no. 3, pp. 1458–1465, 2018.

[16] W. Bosworth, J. Whitney, S. Kim, and N. Hogan, "Robot locomotion on hard and soft ground: measuring stability and ground properties in-situ," in *2016 IEEE International Conference on Robotics and Automation (ICRA)*, pp. 3582–3589, Stockholm, Sweden, 2016.

[17] Y. H. Lee, Y. H. Lee, H. Lee et al., "Trajectory design and control of quadruped robot for trotting over obstacles," in *2017 IEEE/RSJ International Conference on Intelligent Robots and Systems (IROS)*, pp. 4897–4902, Vancouver, BC, Canada, 2017.

[18] M. Haberland, J. G. D. Karssen, S. Kim, and M. Wisse, "The effect of swing leg retraction on running energy efficiency," in *2011 IEEE/RSJ International Conference on Intelligent Robots and Systems*, pp. 3957–3962, San Francisco, CA, USA, 2011.

Research Article

Prediction of Passive Torque on Human Shoulder Joint Based on BPANN

Shuyang Li,[1] Paolo Dario,[1,2] and Zhibin Song [1]

[1]*Key Laboratory of Mechanism Theory and Equipment Design of Ministry of Education, Tianjin University, Tianjin 300072, China*
[2]*The BioRobotics Institute, Scuola Superiore Sant'Anna, Polo Sant'Anna Valdera, V.le R. Piaggio 34, Pontedera 56025, Italy*

Correspondence should be addressed to Zhibin Song; songzhibin@tju.edu.cn

In upper limb rehabilitation training by exploiting robotic devices, the qualitative or quantitative assessment of human active effort is conducive to altering the robot control parameters to offer the patients appropriate assistance, which is considered an effective rehabilitation strategy termed as assist-as-needed. Since active effort of a patient is changeable for the conscious or unconscious behavior, it is considered to be more feasible to determine the distributions of the passive resistance of the patient's joints versus the joint angle in advance, which can be adopted to assess the active behavior of patients combined with the measurement of robotic sensors. However, the overintensive measurements can impose a burden on patients. Accordingly, a prediction method of shoulder joint passive torque based on a Backpropagation neural network (BPANN) was proposed in the present study to expand the passive torque distribution of the shoulder joint of a patient with less measurement data. The experiments recruiting three adult male subjects were conducted, and the results revealed that the BPANN exhibits high prediction accurate for each direction shoulder passive torque. The results revealed that the BPANN can learn the nonlinear relationship between the passive torque and the position of the shoulder joint and can make an accurate prediction without the need to build a force distribution function in advance, making it possible to draw up an assist-as-needed strategy with high accuracy while reducing the measurement burden of patients and physiotherapists.

1. Introduction

For patients suffering impaired upper limb function after stroke, adopting rehabilitation robots for rehabilitation exercise can reduce labor burden of therapists, with more accurate measurement of the position and force information in the rehabilitation training. Thus, the quantitative assessment of the patient's health state can be achieved. Recently, the research and application of the rehabilitation robotics has been increasingly common [1, 2]. In therapeutic practice, not all patients lost all their active motion abilities; thus, patients retaining part of the motion abilities can achieve significantly improved training effect of their active participation in the rehabilitation training [3]. As revealed from existing studies, overdose robotic assistance will reduce the patient's active force output and energy consumption in rehabilitation training, and the patient's limbs appear to be "slacking," probably reducing the efficiency of rehabilitation

[4]. Thus, compared with the stiff control strategy that moves the patient's limbs along a desired trajectory in the training process given the patient's active motion ability, the so-called "assist-as-needed" strategy that provides only the minimum assistance required to maximize the patient's active participation can enhance the efficiency of rehabilitation [5].

One of the critical problems of the assist-as-needed rehabilitation strategy refers to the methods to assess the patient's active motion state, which will generate feedback to the robotic therapy devices to modify the control strategy. A common method complies with the surface electromyographic (sEMG), as collected in real time in the rehabilitation training and analyzed online to extract the patient's movement intention [6, 7]. However, applying sEMG to calculate the joint torque usually requires the integration of a complex musculoskeletal model that contains numerous parameters difficult to measure in vivo. Moreover, for patients with neurological impairment due to stroke, the sEMG can be

significantly inconsistent with that of the healthy people, and the real movement intention of the mentioned patients may be difficult to successfully extract with the sEMG. There is another type of active motion state assessment method, calculating the patient's active force/moment based on the dynamic model of the human-robot interaction system and the determined value of the robotic device sensor. Obviously, the patients' active force/torque intuitively manifests their motion intention. In fact, the patient's active force/torque is changeable for both of the conscious and unconscious behaviors in the rehabilitation training. Furthermore, unlike the changeable active motion state, a stable nonlinear torque-angle relationship is identified between the passive components of the human joint (e.g., passive resistance of the soft tissues and gravitational torque, as well as the posture of limb for a patients). Thus, a measurement before rehabilitation training to distribute passive components of force/torque of the human shoulder joint is critical to assess active motion states based on dynamic models.

In general, the upper limb is affected by gravitational force/torque, passive resistance force/torque generated by joint biological tissue, active muscle force/torque, and assisted force/torque provided by the rehabilitation device during rehabilitation exercise. In addition, the influence of centrifugal force and inertial force should also be taken into account when the movement speed and acceleration is large. However, considering the safety and comfort of patients, the speed and acceleration of rehabilitation training are usually small; thus, the centrifugal force and inertial force can be neglected. Since the main motion form of the upper limb joints is rotation, the torque is usually concerned rather than the force. Passive torque of the shoulder joint is mainly composed of the gravitational torque and the joint resistance torque. The gravitational torque is determined by inertia parameters such as mass and centroid position. And the joint resistance torque is mainly determined by the viscoelastic characteristics of joint biological tissue. In 1980, the shoulder joint resistance torque of 3 subjects under several simple movement that was measured of upper arm was measured by Engin et al. [8]. The results showed that the magnitude of the shoulder joint resistance torque is obviously different between subjects, but the trend of the torque-angle curves of different subjects is similar. Then, in 1986, Engin et al. measured the shoulder joint resistance torque of the shoulder joint of 10 subjects beyond the active range of motion of each subject, and a statistical database of the torque-angle relationship was formed which can be used in realistic dynamic simulations of human shoulder joint [9]. However, gravitational influence on the shoulder was factored out in their research by making the experimental motion performed only in a horizontal equigravitational plane, which is not easy to realize in actual rehabilitation state. In 2009, an upper limb dynamic model is established by Zhang et al., where each segment of the upper limb was regarded as a rigid body link, and the joint elastic resistance torque and gravitational torque are treated as a whole passive torque [10]. The rate of change of the joint rotation angle according to the dynamic force was defined as joint stiffness. The measurement experiment found that the joint stiffness of the subjects after stroke was significantly increased compared with that of healthy subjects. However, the stiffness value in this study was regarded as a constant value, without considering the change of joint stiffness with a joint rotation angle. In 2019, the passive torque of shoulder joint during external rotation and internal rotation was measured by Wight et al., and the slope of the best-fit line of the torque-angle curve was defined as stiffness [11]. However, in their study, the upper limb rotation was carried out in a fixed plane without considering the distribution of passive torque in other planes. Obtaining the distribution of shoulder passive torque in a wider range is beneficial to evaluating health status and drawing up the rehabilitation strategies, but the measurement of the joint passive torque over the entire joint range of motion may take a long time and make the patients fatigued. Thus, the joint passive torque assessment method with less measurement data can be beneficial.

Since the artificial neural network (ANN) is capable of approximating any rational function without the cognition of the system constitutive model, a prediction method of the shoulder passive torque, as caused both by the gravity and the joint soft tissues, was proposed in the present study based on BPANN, making the expansion of the passive torque distribution of shoulder joint possible.

A passive upper limb abduction experiment was executed with the 7-DoF lightweight collaborative robot KUKA lbr iiwa extensively applied in the human-robot interaction experiments [12]. The position and the force/torque applied to the robot by human upper limb were recorded by the robot sensor in the experimental motion. Subsequently, the kinematic analysis and static force analysis of the upper limb were conducted to calculate the motion and the resistance torque of the shoulder joint. Some of the mentioned angle-torque results were given into a three-layer BPANN as training data. Next, the trained BPANN was adopted to assess the passive torque of the rest joint posture data collected from the identical subject. Afterwards, the torque assessed by BPANN was compared with the torque calculated by static force analysis. The result suggested that the BPANN can accurately assess the spatial distribution of shoulder passive torque.

Results showed that the BPANN assessment method proposed in this study can predict the passive torque of the shoulder joint during the upper limb abduction with high accuracy and make it possible to obtain more passive torque-angle distribution through less measurement data, which is critical to reduce the burden on patients.

2. Methods

2.1. Subjects. Three healthy male adults were recruited from the identical institution where the experiments of this study were conducted. All subjects were voluntary to participant in the experiment; they were right-handed, with no history of shoulder disease.

2.2. Experimental Protocol. The subjects were seated at a high chair. The subject's right upper limb was connected to the end tool flange of the robot through the orthosis (Figure 1). To avoid the effect of forearm movement, the elbow joint of
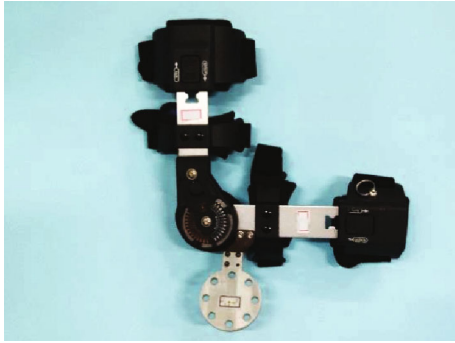
Figure 1: The orthosis of right upper limb.

Figure 2: World frame and flange frame of the robot.

the orthosis was locked in a 90° posture, while the shoulder joint movement was not restricted by the orthosis. The subjects were required to maintain the stability of their trunk and avoid the rotation of their upper arm while their right upper limb being dragged by the robot to complete abduction movement in different planes of elevation.

The motion path of the robot was generated by dragging teaching method. In the preliminary stage, the robot was set to a low-stiffness impedance control mode, thus making it possible for the robot to follow the subject's movement. In the dragging stage, the subject was required to move his upper limb along the specified abduction trajectory actively and dragging the compliant robot. The robot recorded the rotation angle of each axis at a frequency of 100 Hz during the dragging step automatically. Subsequently, the trajectory reproduction step was executed in the passive upper limb abduction, in which the robot was set to a impedance control mode with higher stiffness, and the axes angle data recorded in the dragging step was transferred to the controller as the position parameter successively. Thus, the robot can regenerate a similar trajectory of the dragging step. Though the impedance control mode in trajectory reproduction step may lose some positioning accuracy compared with the position control mode for the effect of human upper limb, it can comply with the natural movement trajectory of the upper limbs better, ensuring the safety of the robot and the subjects. Moreover, its compliant properties also helps avoid the sudden change of the joint torque of the robot attributed to the human upper limb as an uncertain load. Accordingly, the impedance control mode is chosen for the passive abduction experiment in the present study. To ensure the safety of rehabilitation training, usually the speed during the motion is slow. Thus, this study only focused on the shoulder resistance performance at low speed, and the speed of each axis of the robot was also limited to 1/10 of its maximum speed.

Before the start of the experiment, the subjects were required to fully warm up the upper limbs. During the passive abduction, the upper limbs of the subjects should not feel being pulled or pushed by the robot obviously. To ensure the stability of the passive torque, all subjects were required to participate in the preexperiment before the formal experiment to determine their muscle relaxation level in the passive abduction. Besides, the sEMG signals of the upper limb muscles related to the active motion were harvested to monitor their muscle activity. As revealed from the results of preexperiment results, the subjects can maintain muscle relaxation during passive exercise. To avoid the interference of the electrode patches and the wires on the subject's motion, no sEMG signal was harvested in the formal passive exercise experiment.
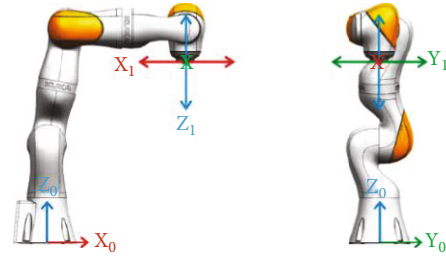
The identical passive abduction trajectory was repeated 2 times in a single experiment. If significant difference is identified between the determined values of the two motion along the identical trajectory, the data will be considered invalid. The position data (axes angle) and force data of the experiment were recorded with the DataRecorder function built in the robot control software; thus, the data of the operation of the robot at the specified frequency (50 Hz in the present study) can be recorded.

2.3. Kinematics. The motion and force of real human upper limbs can be significantly complicated, and it is acceptable to make a reasonable simplification when performing kinematic analysis. In the present study, the following assumptions were made:

(1) The flexibility of the biological tissue is not considered. The hand takes up a small proportion in the upper limb, and the effect of its motion on the upper limb is negligible. The elbow motion is locked by the orthosis. In the mentioned case, the entire upper limb and the connected orthotics can be considered a whole rigid body for kinematic analysis

(2) The shoulder joint is simplified as a ball and socket joint rotating around a fixed point on the human body, and the spatial position of the center of the shoulder joint is assessed with the least-square sphere-fitting method

Thus, the upper limb is considered a rigid body that rotates around the ball and socket joint at a fixed center. Subsequently, the shoulder joint posture can be calculated from the robot position data recorded by the DataRecorder function. The robot axes angle can be adopted to calculate the position and posture of the flange frame relative to the world coordinate system of the robot by robot forward kinematics. Besides, the world and the flange frames of the robot are illustrated in Figure 2.

To quantitatively express the movement of the shoulder joint, the local frame of the shoulder (Figure 3) was built according to the ISB recommendation [13] at its rotation
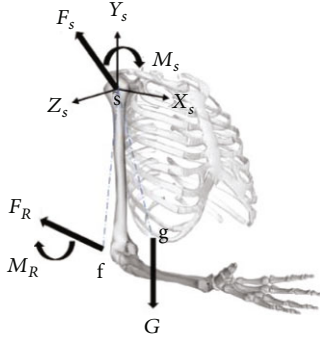
FIGURE 3: Shoulder joint frame system and upper limb stress.

FIGURE 4: Projection of motion trajectory on XZ plane.

center. In the preliminary stage of the experiment, the subjects altered their sitting posture as guided by the experiment supervisor, thereby making the coronal, sagittal, and vertical axes of their body parallel to the X_0-axis, Y_0-axis, and Z_0-axis of the robot world frame, respectively.

The upper limb and the orthosis are considered a rigid body, and the orthosis is rigidly fixed on the robot flange, so the homogeneous transformation matrix between the robot flange frame and the shoulder frame is considered invariant with upper limb motion. The actual value of the transformation matrix was determined, to be specific, the robot axes angle when the shoulder joint was on its initial posture where shoulder abduction/adduction angle, flexion/extension angle, and internal rotation/external rotation angle were 0° on the whole. Subsequently, the position and posture of the flange frame could be calculated, while the shoulder frame posture was already known (all rotation angle was 0°). Thus, the rotation matrix between the two frames was calculated. Besides, by employing the radius from the shoulder rotation center sphere-fitting, the translation vector between the two frames was calculated. With the rotation matrix and the translation vector, the homogeneous transformation matrix between the robot flange frame and the shoulder joint frame was determined, which can be adopted to calculate the posture of shoulder frame from the robot axes angle as expressed Equation (1), where T_s denotes the homogeneous transformation matrix of shoulder joint frame relative to the robot world frame, T_F represents the homogeneous transformation matrix of robot flange frame calculated by forward kinematics relative to the robot world frame, and $^R_F T$ indicates the homogeneous transformation matrix of the shoulder joint frame relative to the robot flange frame.

$$T_s = T_F {}^R_F T \tag{1}$$

Overall, the posture of rigid body is not expressed by the rotation matrix which contains 9 elements directly, whereas it is decomposed into 3 rotation angles in a certain order. The ISB recommended by adopting the YXY order Euler angle to present the shoulder joint (GH joint, actually) posture. However, some existing studies suggested that the YXY sequence Euler angles gives gimbal deadlock problem, and the clinical amplitude coherence is poor [14]. In the
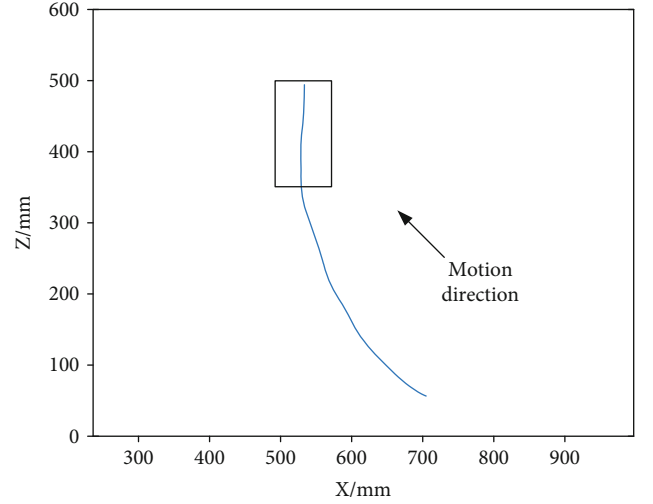
present study, the two angles globographic method was adopted to describe the shoulder motion, excluding the rotational effect of the upper arm. The globographic angles were calculated by a landmark point fixed on upper arm, which was taken as the elbow point. The elbow point was obtained by manual measurement.

Though the subjects were required to move their upper limb within a single plane in the passive abduction movement experiments, the elbow joint sampling points did not exhibit the single plane distribution. The mentioned finding is because the movement trajectories were generated by the subjects themselves and because the designated primary movement tended to be accompanied by an unconscious "secondary movement" [15].

It was found in the experiments that the results of sphere fitting were quite different at different stages of a same movement, especially at the end stage. For example, the projection of an abduction trajectory in 0° plane of elevation of subject S1 on the XY plane was shown in Figure 4. The trajectory curve displays a significantly different curvature between the initial and final stages. This is primarily attributed to the translation of the shoulder joint center and for the rigid connection between upper limb and robot that made the rotation of the robot axis more difficult under the larger rotation angle; the effect of the center translation was more obvious than in human natural voluntary movement. Accordingly, for the data of each motion trajectory, the former part was taken for sphere fitting, and the shoulder joint angle was calculated by the intersection point of the line connecting the sample point and the fitting sphere center and the fitting sphere. The fitting sphere with the same trajectory shown in Figure 4 and its corresponding intersection point on the sphere is illustrated in Figure 5.

2.4. Static Force Analyses. The passive abduction experiment in the present study was conducted at a slow speed, so the human-robot system is considered quasi-static, and the effect of inertial force was ignored. Moreover, low-speed also reduced the effect of velocity-related viscous part in the passive torque of the shoulder joint.

○ Sample point
— Intersection point
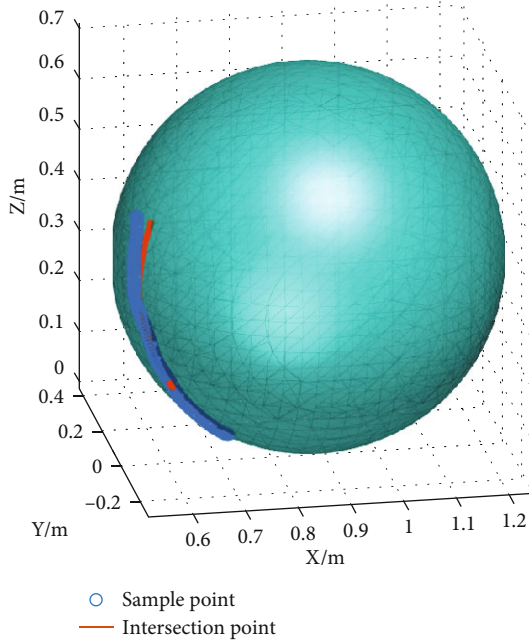
Figure 5: Sphere-fitting results.

Figure 6: The topological structure of BPANN.

The force/torque applied on the upper limb under quasi-static is illustrated in Figure 3. The robot applies an assist force F_R on the original point of the flange frame and an assist torque M_R to the upper limb through the orthosis. The shoulder joint generated a resistance force F_s applied on its rotation center and a resistance torque M_s. The gravity G was applied on the center of mass of the upper limb. Furthermore, the gravity G and assist force F_R would generate torque M_G and M_{FR} at the shoulder rotation center, respectively.

In fact, the rigidly connected robot flange provided constraints of all 6 DoF for the upper limb, and the shoulder joint, which was approximated as a ball and socket joint, generated additional constraints for the upper limb; thus, the upper limb static force system became an overdetermined problem. For this reason, there are infinite sets of solutions for the static equilibrium state of the system in theory. However, an ideal ball and socket joint would only provide force constraints without torque constraints. Likewise, in a specific joint angle, the resistance force F_s of shoulder joint may change following the external force/torque, whereas the resistance torque M_s is relatively stable, primarily determined by the joint tissue characteristics. Moreover, the experimental results revealed that the high repeatability of M_R and F_R of a specific subject in the identical trajectory.

The static equilibrium equation is written in Equation (3).

$$\mathrm{F_s + F_R + G = 0,} \tag{2}$$

$$M_s + M_R + M_G + M_{FR} = 0. \tag{3}$$

The robot assist force F_R and assist torque M_R were calculated by the robot joint external torque by Equation (4) derived from the principle of virtual work, where f denotes the generalized force of the robot, τ_e represents the external torque on the robot joint calculated by the robot based on its torque sensor measurements with the built-in dynamic model, and J^+ indicates the pseudo-inverse matrix of the 7×6 robot Jacobian matrix. The external torque data were smoothed with a moving average filter to reducing the influence of high-frequency noise.
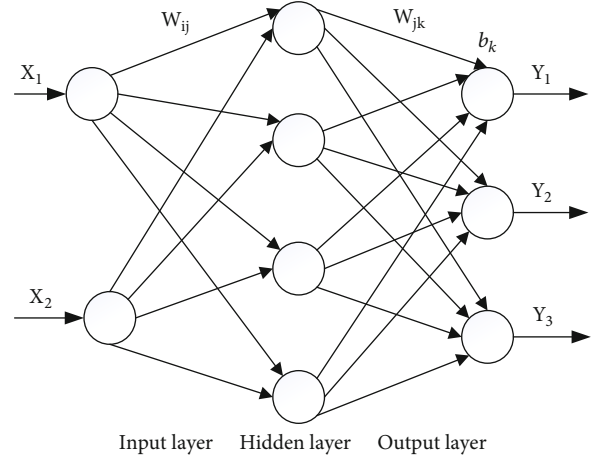
$$f = \begin{bmatrix} F_R \\ M_R \end{bmatrix} = J^+ \tau_e. \tag{4}$$

The gravity and the center of mass of the orthosis was determined in advance; its effect was removed from the result. The passive torque of shoulder joint M_P can be calculated as Equation (5).

$$M_P = M_s + M_G = -M_R - M_{FR}. \tag{5}$$

2.5. ANN Prediction. Unlike conventional function fitting methods, the ANN expresses the mapping relationship between input data and output data through the structure and parameters (e.g., weights and biases here) of the layered network. A three-layer feedforward ANN was used here to express the torque-angle relationship of shoulder joint. The number of units of the input layer was two and that of the output layer was three. The number of the hidden units was determined initially by an empirical equation and altered according to assessed effects. After the network structure was determined, the weights and biases of the network could be altered by training. Backpropagation (BP) algorithm is commonly used in ANN training, calculating the gradient of the error with respect to the weights for a given input by propagating error backwards through the network [16]. The topological structure of BPANN is illustrated in Figure 6.

Two globographic angles were selected as the input data and the three components of shoulder passive torque relative to the direction of robot world frame calculated in section 2.4. The activation functions of the hidden and output units were sigmoid. All data were normalized before being transferred to a neural network. The training of the BPANN was carried out in the Neural Network Toolbox of MATLAB. In

(a)

(b)
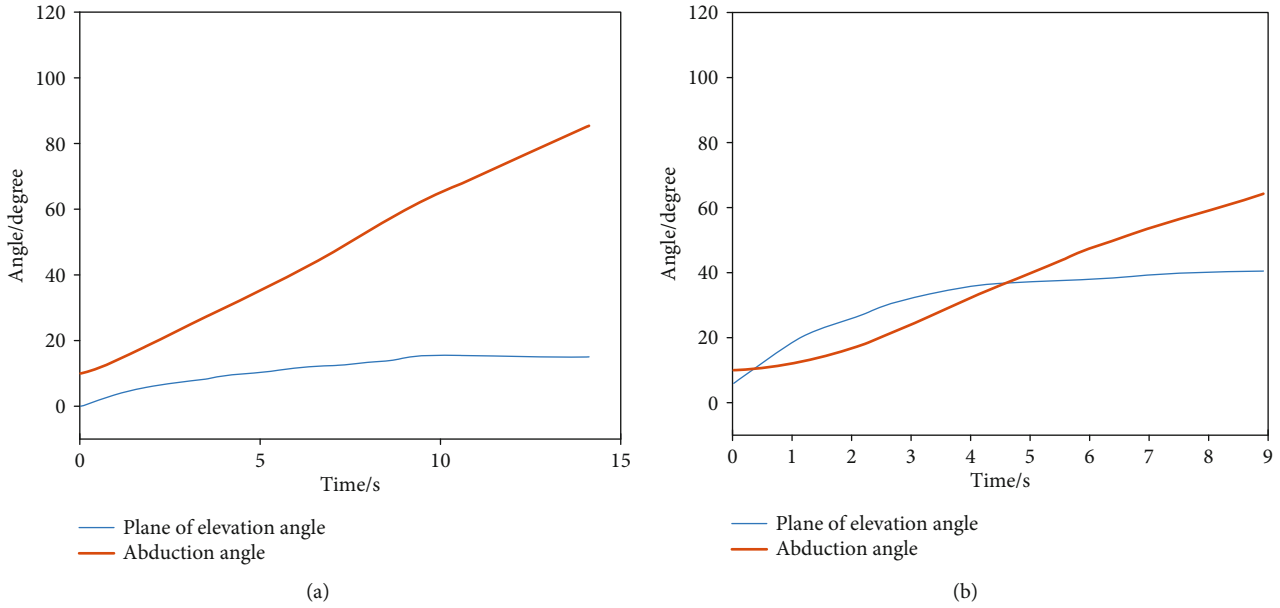
FIGURE 7: Globographic angle results. (a) Globographic angle of abduction in 0° plane of elevation. (b) Globographic angle of abduction in 30° plane of elevation.

(a)

(b)
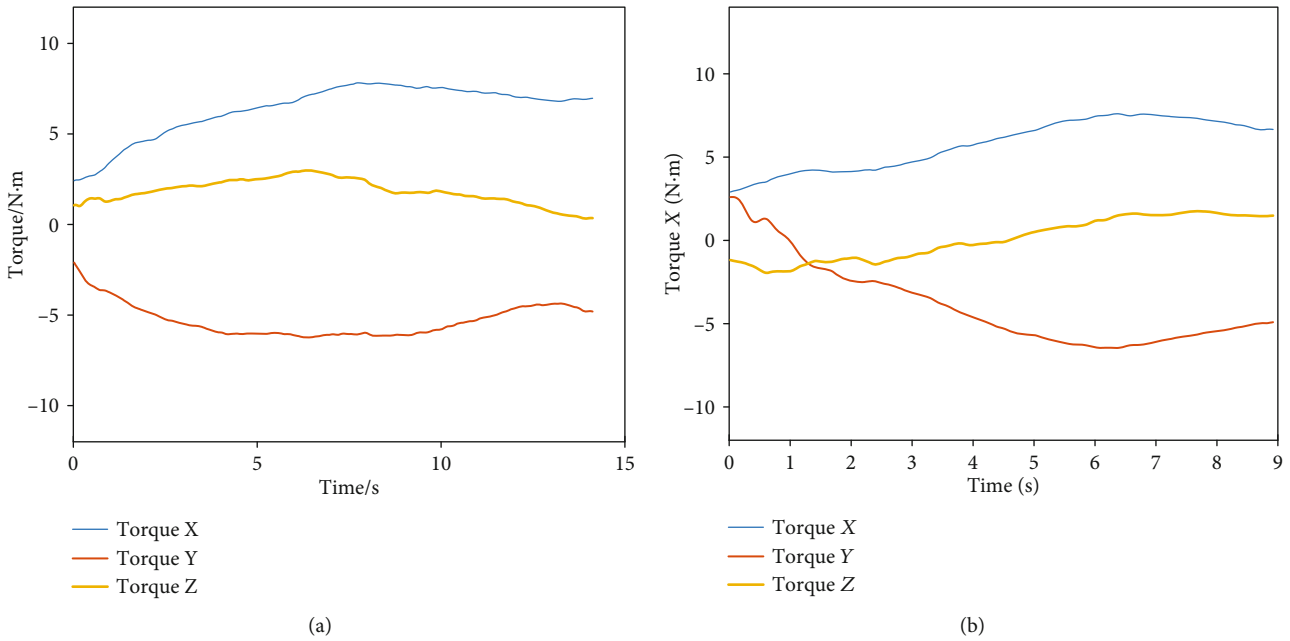
FIGURE 8: Shoulder joint passive torque results. (a) Passive torque components of abduction in 0° plane of elevation. (b) Passive torque components of abduction in about 30° plane of elevation.

terms of the training parameters, the maximum number of training epochs was 1000, the performance goal is 0.001 where the performance was measured by the mean square error (MSE) of the network output, and the learning rate is 0.01. The Levenberg-Marquardt optimization was chosen to be the backpropagation algorithm due to its faster training speed.

3. Results

3.1. Kinematics. The globographic angle results of the abduction trajectories in 0° plane of elevation and 30° plane of ele-

vation of subject S1 were shown in Figures 7(a) and 7(b), respectively. The angle curves suggested that a secondary movement took place, especially in the moment as presented in Figure 7(b).

3.2. Shoulder Passive Torques. The passive torque calculation results of the two moments in Figure 7 are, respectively, shown in Figures 8(a) and 8(b). It can be seen that the passive torque on the shoulder joint is quite different in different motion trajectories of the same subject.
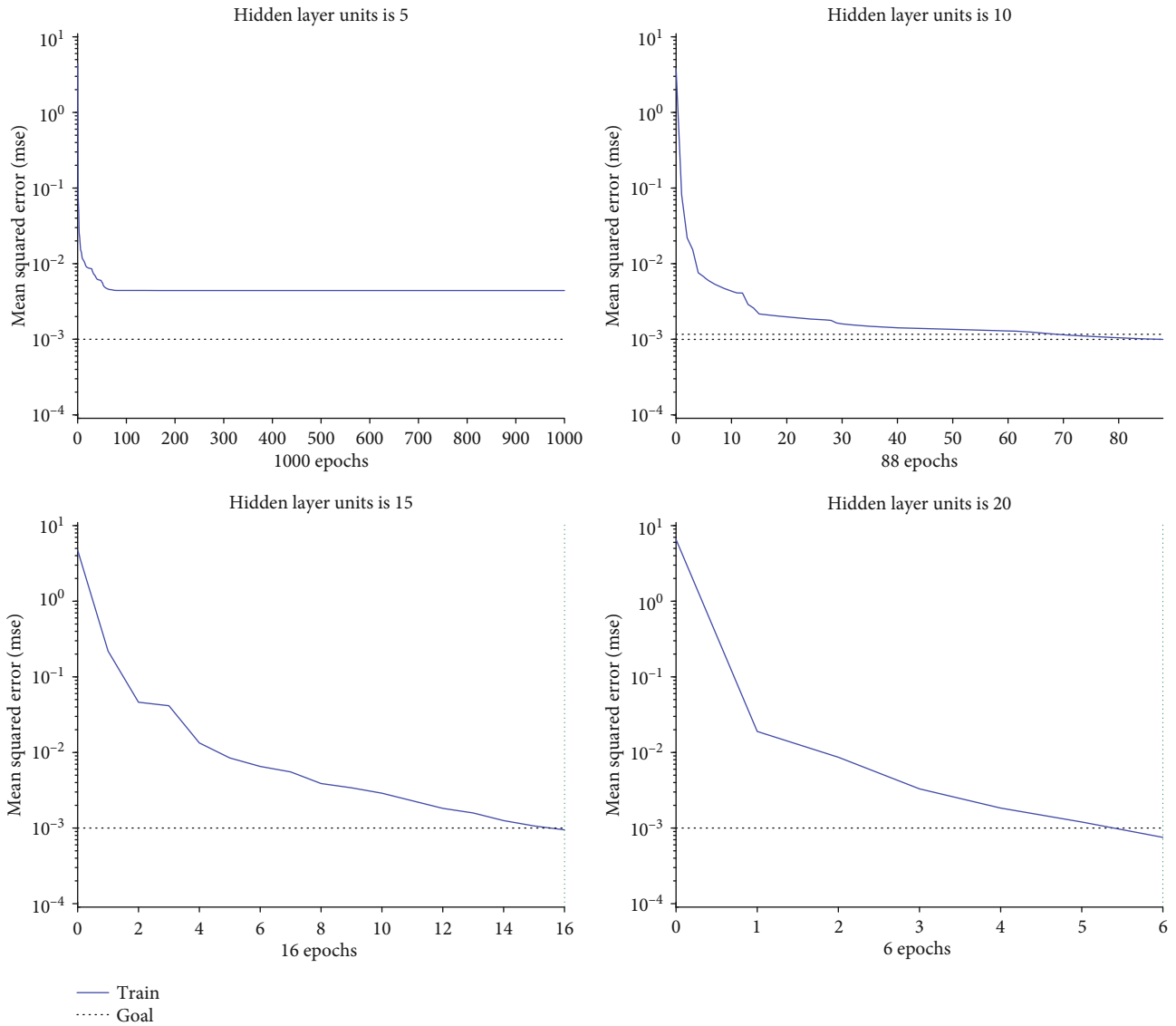
FIGURE 9: Performance of the BPANN with different hidden layer units.

3.3. BPANN Prediction. In the two motions of subject S1 as presented in Figure 7, 1123 groups of angle-torque data were collected. First, 500 groups of data were selected randomly to train the BPANN, and the rest groups of data acted as test set to verify the prediction effect of the network.

The number of hidden layer units impacted the prediction effect of the BPANN. Generally, with the increase of the number of neural network layers and hidden layer elements, the nonlinear fitting ability of neural network is enhanced. However, too complicated network structure will increase the calculate complexity and may lead to over-fitting, thus reducing the generalization ability of the BPANN. Therefore, the network structure should be determined according to the prediction effect in practical application. In this paper, the training performance of the network with 5~20 hidden layer units was tested, and the training curves of the networks with different hidden layer units were shown in Figure 9. It can be seen that when the number of the units

is small, the network needs more training epochs to achieve the performance goal. Especially when the number of units is very small, the network cannot meet the performance goal, even after more training epochs than 1000. For example, when the number of hidden layer units is 5, the network performance hardly changed with iterative calculation after 84 training epochs, which can not meet the set accuracy goal (0.001). However, although more units can make the network reach the specified accuracy with fewer training epochs, the computational complexity of each epoch is larger. In this paper, the number of the hidden layer units was chosen to be 9, with which the structure of the network will not be too complicated, and at the same time, the accuracy target can be achieved at a relatively fast speed.

The passive torque prediction error of the test set data in each direction was shown in Figure 10. For clarity of illustration, not all sample points in the test set were shown in Figure 10, and one point was taken for every 5 points for
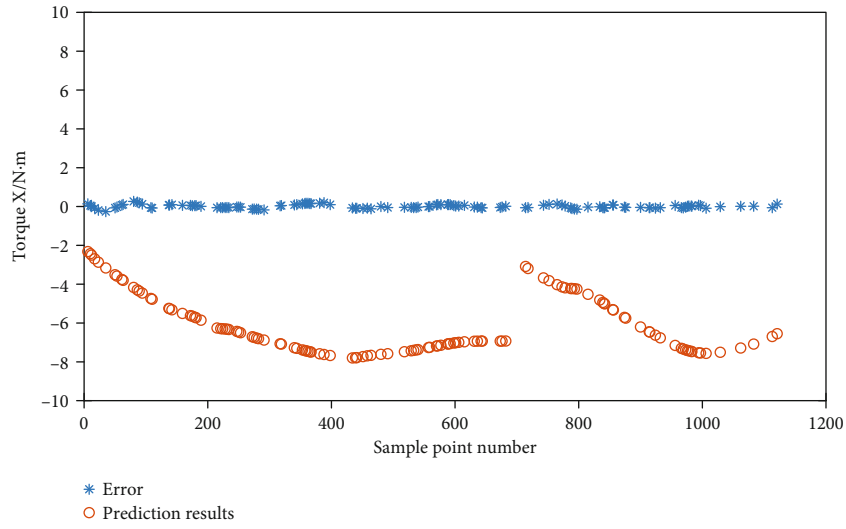
(a)
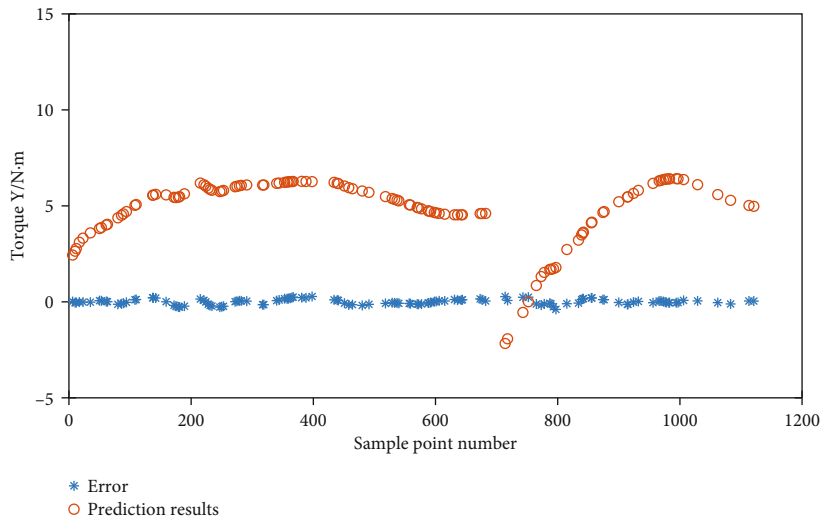
(b)
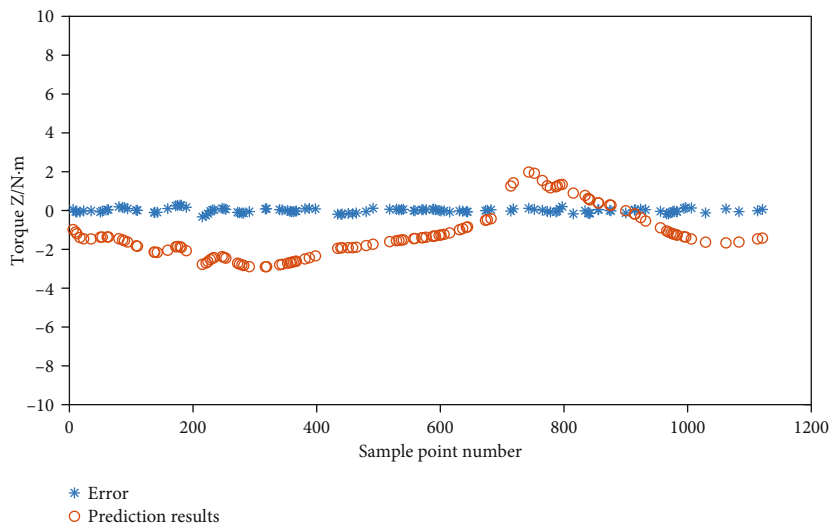
(c)

FIGURE 10: Assessment results and errors in each direction.

TABLE 1: MAV and MSE of ANN assessment.

	MAV[N·m]	MSE[N·m]	RE
X	6.399	0.093	0.0145
Y	5.172	0.139	0.0269
Z	1.728	0.104	0.0602

plotting. It can be seen that the prediction error was small compared with the magnitude of each passive torque component, and the specific mean absolute value (MAV) and mean square error (MSE) of the passive torque prediction are listed in Table 1. The relative error (RE) is defined as the ratio of the MSE to MAV. The results showed that the BPANN can predict the torque of the shoulder joint with high accuracy.

For subject S2 and S3, similar accurate passive torque perditions can be conducted by BPANN, which was not repeated in this paper for the sake of length. Although the upper limb is often treated as a rigid body link system, in fact, the biological tissue is not rigid and its characteristics, such as inertial parameters and elastic characteristics, will change with the limb motion. Especially for the shoulder joint, its actual motion is coupled by the common motion of the glenohumeral joint, the acromioclavicular joint, the sternoclavicular joint, and the scapulothoracic joint, making the motion and the passive torque on the joint complicated and nonlinear. The coupling motion and passive torque of the shoulder joint has large differences between individuals, but for a specific individual, the relatively stable regularity of shoulder joint motion and passive torque can be found [8, 17]. Considering the BPANN has the ability to learn any nonlinear relation between independent variables and dependent variables, it is suitable for learning the nonlinear relationship between passive moment and joint angle of shoulder joint of a specific individual and expanding the torque-angle distribution. The results showed that the BPANN above can predict the passive torque of a joint angle which is not in the training set with high accuracy.

4. Conclusion

In the present study, a shoulder passive torque prediction method based on BPANN was proposed to expand the shoulder passive torque-angle relationship. Experiments were carried out to measure the kinematics and torques on the shoulder joint of 3 healthy subjects, and the measurement data was used as training set and testing set of a three-layer BPANN to test the prediction effect. The results revealed that the BPANN can learn the nonlinear relationship between the passive torque and the position of the shoulder joint and make accurate prediction without the need to build a force distribution function in advance, which is required in conventional curve fitting methods. The prediction method can expand the spatial distribution of the passive torque on shoulder joint with less measurement data, making it possible to draw up an assist-as-needed strategy with high accuracy while reducing the measurement burden of patients and physiotherapists. That is, the BPANN is capable of learning the regularity between the shoulder joint passive torque and the joint position for a specific individual and expand the spatial distribution with less measurement data.

Data Availability

The position data and force/torque data used to support the findings of this study are included within the article.

Conflicts of Interest

The authors declare there is no conflict of interest regarding this publication.

Acknowledgments

References

[1] R. Colombo, F. Pisano, S. Micera et al., "Upper limb rehabilitation and evaluation of stroke patients using robot-aided techniques," in *9th International Conference on Rehabilitation Robotics, 2005. ICORR 2005*, Chicago, IL, USA, July 2005.

[2] L. L. Cai, A. J. Fong, Y. Liang, J. W. Burdick, and V. R. Edgerton, "Assist-as-needed training paradigms for robotic rehabilitation of spinal cord injuries," in *International conference on robotics and automation*, Orlando, FL, USA, May 2006.

[3] L. L. Cai, A. J. Fong, C. K. Otoshi et al., "Implications of assist-as-needed robotic step training after a complete spinal cord injury on intrinsic strategies of motor learning," *The Journal of Neuroscience*, vol. 26, no. 41, pp. 10564–10568, 2006.

[4] E. T. Wolbrecht, V. Chan, D. J. Reinkensmeyer, and J. E. Bobrow, "Optimizing compliant, model-based robotic assistance to promote neurorehabilitation," *IEEE Transactions on Neural Systems and Rehabilitation Engineering*, vol. 16, no. 3, pp. 286–297, 2008.

[5] D. J. Reinkensmeyer, E. T. Wolbrecht, V. Chan, C. Chou, S. C. Cramer, and J. E. Bobrow, "Comparison of Three-Dimensional, assist-as-needed robotic arm/hand movement training provided with pneu-wrex to conventional Tabletop therapy After chronic stroke," *American Journal of Physical Medicine & Rehabilitation*, vol. 91, 11 Suppl 3, pp. S232–S241, 2012.

[6] L. Peng, Z.-G. Hou, L. Peng, and W.-Q. Wang, "Experimental study of robot-assisted exercise training for knee rehabilitation based on a practical EMG-driven model," in *2016 6th IEEE International Conference on Biomedical Robotics and Biomechatronics (BioRob)*, Singapore, Singapore, June 2016.

[7] Q. Ai, B. Ding, Q. Liu, and W. Meng, "A subject-specific emg-driven musculoskeletal model for applications in lower-limb rehabilitation robotics," *International Journal of Humanoid Robotics*, vol. 13, no. 3, p. 1650005, 2016.

[8] A. E. Engín, "On the biomechanics of the shoulder complex," *journal of biomechanics*, vol. 13, no. 7, pp. 575–590, 1980.

[9] A. E. Engin and S.-M. Chen, "Statistical data base for the biomechanical properties of the human shoulder complex—ii: passive resistive properties beyond the shoulder complex sinus," *Journal of Biomechanical Engineering*, vol. 108, no. 3, pp. 222–227, 1986.

[10] L. Q. Zhang, H. S. Park, and Y. Ren, "Shoulder, elbow and wrist stiffness in passive movement and their independent control in voluntary movement post stroke," in *2009 IEEE International Conference on Rehabilitation Robotics*, Kyoto, Japan, June 2009.

[11] J. T. Wight, M. D. Tillman, G. B. Grover, J. W. Chow, and K. Larkin-Kaiser, "Pitching shoulder passive flexibility: torque-angle analysis for external rotation and internal rotation," *Sports Biomechanics*, pp. 1–13, 2020.

[12] D. Panariello, T. Caporaso, S. Grazioso, G. D. Gironimo, and P. Klimant, "Using the KUKA LBR iiwa Robot as Haptic Device for Virtual Reality Training of Hip Replacement Surgery," in *2019 Third IEEE International Conference on Robotic Computing (IRC)*, Naples, Italy, Italy, February 2019.

[13] G. Wu, F. C. Der Helm, H. E. Veeger et al., "ISB recommendation on definitions of joint coordinate systems of various joints for the reporting of human joint motion—Part II: shoulder, elbow, wrist and hand," *Journal of Biomechanics*, vol. 38, no. 5, pp. 981–992, 2005.

[14] M. Senk and L. Cheze, "Rotation sequence as an important factor in shoulder kinematics," *Clinical biomechanics*, vol. 21, pp. S3–S8, 2006.

[15] A. Assi, Z. Bakouny, M. Karam, A. Massaad, W. Skalli, and I. Ghanem, "Three-dimensional kinematics of upper limb anatomical movements in asymptomatic adults: Dominant vs. non-dominant," *Human Movement Science*, vol. 50, pp. 10–18, 2016.

[16] G. P. Miller, P. M. Todd, and S. U. Hegde, "Designing neural networks using genetic algorithms," *International conference on genetic algorithms*, 1989.

[17] C. Högfors, B. Peterson, G. Sigholm, and P. Herberts, "Biomechanical model of the human shoulder joint—ii. The shoulder rhythm," *Journal of Biomechanics*, vol. 24, no. 8, pp. 699–709, 1991.